

A STUDY OF THE PROPERTIES OF LAYERED LITHIUM-RICH  
TRANSITION METAL OXIDE POSITIVE ELECTRODE MATERIALS FOR  
LITHIUM-ION BATTERIES

by

Ramesh Shunmugasundaram

Submitted in partial fulfilment of the requirements  
for the degree of Doctor of Philosophy

at

Dalhousie University  
Halifax, Nova Scotia  
October 2016

© Copyright by Ramesh Shunmugasundaram, 2016

எப்பொருள் யார்யார்வாய்க் கேட்பினும் அப்பொருள்

மெய்ப்பொருள் காண்ப தறிவு

- திருவள்ளுவர்

*To discern the truth in everything, by whomsoever spoken, is wisdom.*

- Thiruvalluvar

*Dedicated To*

*Amma, Appa, Rajee and Sherwin*

# Table of Contents

<b>List of Tables .....</b>	<b>viii</b>
<b>List of Figures.....</b>	<b>x</b>
<b>Abstract.....</b>	<b>xvii</b>
<b>List of Symbols and Abbreviations Used .....</b>	<b>xix</b>
<b>Acknowledgements .....</b>	<b>xxiv</b>
<b>Chapter 1 Introduction.....</b>	<b>1</b>
1.1 Lithium-ion battery .....	1
1.2 Positive electrode materials.....	5
1.3 Layered lithium transition metal oxides (LLTMO) .....	7
1.3.1 Li[M]O <sub>2</sub> .....	9
1.3.2 Li[M <sup>†</sup> <sub>x</sub> M <sup>††</sup> <sub>1-x</sub> ]O <sub>2</sub> (binary) and Li[M <sup>†</sup> <sub>x</sub> M <sup>††</sup> <sub>y</sub> M <sup>†††</sup> <sub>1-x-y</sub> ]O <sub>2</sub> (ternary) .....	10
1.3.3 Layered lithium-rich transition metal oxides (LLRTMO).....	13
1.4 Scope of this thesis.....	21
<b>Chapter 2 Experimental .....</b>	<b>23</b>
2.1 Materials synthesis .....	23
2.1.1 Co-precipitation synthesis of mixed transition metal carbonates.....	23
2.1.2 Synthesis of layered lithium transition metal oxides.....	26
2.2 Materials characterization .....	28
2.2.1 X-Ray diffraction (XRD) .....	28

2.2.2	Scanning electron microscopy (SEM).....	31
2.2.3	Inductively coupled plasma – optical emission spectroscopy (ICP-OES).....	31
2.2.4	Brunauer-Emmett-Teller (BET) surface area analysis.....	32
2.2.5	Crystallographic density measurement (Pycnometer).....	34
2.2.6	Solid-state nuclear magnetic resonance spectroscopy (Solid-state NMR).....	36
2.3	Electrochemical characterization .....	40
2.3.1	Preparation of working electrodes.....	41
2.3.2	Construction of coin cells.....	42
2.3.1	Electrochemical testing .....	43
<b>Chapter 3 Structural characterization of layered lithium-rich transition metal</b>		
	<b>oxides .....</b>	<b>44</b>
3.1	Introduction .....	44
3.2	Superlattice ordering in layered lithium-rich transition metal oxides.....	44
3.3	Transition metal layer stacking in $\text{Li}_2\text{MnO}_3$ .....	45
3.4	FAULTS.....	50
3.5	Stacking faults in $\text{Li}_2\text{MnO}_3$ .....	51
3.6	Superlattice peak positions in $\text{Li}[\text{Li}_{1/3-2x/3}\text{Ni}_x\text{Mn}_{2/3-x/3}]\text{O}_2$ .....	58
3.7	Superlattice peak broadening in $\text{Li}[\text{Li}_{1/3-2x/3}\text{Ni}_x\text{Mn}_{2/3-x/3}]\text{O}_2$ .....	63
3.8	Conclusions .....	66
<b>Chapter 4 Effect of lithium content on the first-cycle irreversible capacity loss of</b>		
<b>layered lithium-rich transition metal oxides .....</b>		
	<b>68</b>	
4.1	Introduction .....	68



4.2	First charge-discharge cycle.....	70
4.3	Effect of spinel impurity .....	74
4.4	Synthesis by quenching.....	81
4.5	Effect of surface area.....	84
4.6	ICP results .....	87
4.7	Predicting metal-site vacancies .....	89
4.8	Density measurements.....	90
4.9	Constant current charge-discharge.....	93
4.10	Conclusions .....	94

**Chapter 5 Search for low-irreversible capacity layered lithium-rich transition metal oxides in the Li-Ni-Mn-Co-O pseudo-quaternary system .....95**

5.1	Introduction .....	95
5.2	Single phase low-irreversible capacity materials .....	103
5.3	Two-phase low- irreversible capacity materials.....	113
5.4	Conclusion.....	119

**Chapter 6 Understanding irreversible capacity behavior in layered lithium-rich transition metal oxides.....120**

6.1	Introduction .....	120
6.2	<sup>7</sup> Li NMR studies on layered lithium-rich transition metal oxides.....	120
6.3	Effect of metal composition .....	125
6.4	Effect of TM migration .....	136
6.5	Conclusion.....	142

<b>Chapter 7</b>	<b>Conclusions and suggested future work</b>	<b>144</b>
7.1	Conclusions	144
7.1.1	Structural characterization (Chapter 3)	145
7.1.2	Effect of lithium content (Chapter 4)	146
7.1.3	Effect of transition metal composition (Chapter 5)	147
7.1.4	Understanding the irreversible capacity loss in layered lithium-rich transition metal oxides (Chapter 6)	148
7.1.5	Low-IRC behavior in core-shell positive electrode materials	150
7.2	Suggested future work	150
7.2.1	Presence of Mn <sup>3+</sup> in the low-irreversible capacity samples	150
7.2.2	Effect of the nature of precursor on the low-irreversible capacity behavior	151
7.2.3	Long-term electrochemical properties of low-irreversible capacity materials	152
7.2.4	FAULTS and Neutron diffraction in LLRTMO with metal-site vacancies	153
7.2.5	Origin of metal-site vacancies in Li-Ni-Mn-O vs Li-Ni-Mn-Co-O systems	154
7.2.6	Layered NMC materials with metal-site vacancies	156
7.2.7	Effect of metal-site vacancies on the reversible anionic redox properties	157
7.2.8	Eye to reality	159
	<b>References</b>	<b>160</b>
	<b>Appendix A: Two-phase behavior vs. stacking faults</b>	<b>169</b>
	<b>Appendix B: Rietveld refinement of the XRD patterns</b>	<b>171</b>
	<b>Appendix C: XRD patterns of samples A1 to O2</b>	<b>172</b>

<b>Appendix D: Table of lattice constants of samples A1 to O2 .....</b>	<b>187</b>
<b>Appendix E: First charge-discharge profiles of samples A1 to O2 .....</b>	<b>189</b>
<b>Appendix F: Copyright information .....</b>	<b>197</b>

## List of Tables

Table 3.1 Starting and resulting hexagonal variants from possible translations.....	49
Table 3.2 Translation vectors that define the translation from one type of TM Layer to another, their probabilities and the corresponding amount of stacking faults .....	53
Table 3.3 ICP-OES compositions for the studied samples in the $\text{Li}[\text{Li}_{1/3-2x/3}\text{Ni}_x\text{Mn}_{2/3-x/3}]\text{O}_2$ series .....	58
Table 3.4 (020) and (33-1) peak positions ( $C2/m$ ) obtained from the XRD patterns ( $\text{Cu K}\alpha$ ) of the studied samples in the $\text{Li}[\text{Li}_{1/3-2x/3}\text{Ni}_x\text{Mn}_{2/3-x/3}]\text{O}_2$ series.....	61
Table 4.1 Nominal compositions of the precursors and the LLRTMO samples A1 to A3	70
Table 4.2 Structural parameters obtained from Rietveld refinement of the XRD patterns of samples A1, A2 and A3 .....	73
Table 4.3 BET surface area of the samples A1, A2, A3, A3Q and GA1 .....	84
Table 4.4 Sample, target composition, number of moles of lithium required to get a formula unit of target material, number of moles of lithium originally added including extra 5 wt % for compensating Li loss to get a formula unit of target composition, composition observed from chemical analysis (ICP-OES).....	87
Table 4.5 Sample, calculated vacancies based on ICP-OES compositions and oxidation state rules, composition of formula units with calculated vacancies, calculated densities based on ICP-OES compositions and calculated vacancy content, densities determined from He-Pycnometer, calculated densities based on ICP-OES compositions and measured lattice parameters assuming no vacancies.....	91
Table 5.1 Sample, nominal precursor composition, calculated [Li] to make one mole of the corresponding stoichiometric $\text{LiMO}_2$ , observed [Li] in one mole of synthesized	

LiMO <sub>2</sub> derived from ICP-OES, % Li deficiency, first charge specific capacity, first discharge specific capacity, % IRC relative to the first charge specific capacity and layered single phase purity of the sample. ....	99
Table 5.2 Rietveld refinement results of samples from D and K series .....	104
Table 5.3 Sample ID, ICP-OES metal ratio, calculated no. of moles of vacancies in one mole of synthesized LiMO <sub>2</sub> , calculated formula unit with metal-site vacancies, layered single phase purity, measured density from a He pycnometer, calculated density assuming metal-site vacancies and calculated density assuming no vacancies of single-phase low-IRC materials .....	106
Table 6.1 Combined <sup>7</sup> Li NMR- and ICP-OES derived Li populations of selected LLRTMO materials .....	124
Table 6.2 ICP-OES metal composition, structural parameters, surface area and density of samples A2, A2 <sup>†</sup> and A2 <sup>††</sup> .....	127
Table 6.3 ICP-OES formula unit and the precursor compositions of samples E1, A1, B1, C1, D1 and H1 .....	129
Table 6.4 Sloping region, plateau region and the total capacities observed during the first charge of samples E1, A1, B1, C1, D1 and H1 (refer Figure 6.7).....	133
Table 6.5 Comparison of properties of A1 and Fe-A1 .....	138
Table 7.1 Examples of recent thesis works done in LLRTMO materials.....	144

## List of Figures

Figure 1.1 Schematic of a Li-ion Cell.....	2
Figure 1.2 Schematic of the voltage-capacity profile of a Li-ion cell during discharge.....	5
Figure 1.3 Crystal structure of LiCoO <sub>2</sub> projected along [110] plane.....	8
Figure 1.4 Pseudo-ternary composition diagram for LiNiO <sub>2</sub> -LiMnO <sub>2</sub> -LiCoO <sub>2</sub> system ....	12
Figure 1.5 Structure of Li <sub>2</sub> MnO <sub>3</sub> (Li[Li <sub>1/3</sub> Mn <sub>2/3</sub> ]O <sub>2</sub> ) projected along (100) (left) direction and the superlattice ordering between Mn <sup>4+</sup> ions and Li <sup>+</sup> ions from (001) direction (right) .....	15
Figure 1.6 XRD pattern of Li[Li <sub>0.2</sub> Ni <sub>0.2</sub> Mn <sub>0.6</sub> ]O <sub>2</sub> .....	16
Figure 1.7 Voltage-specific capacity profile of Li <sub>1.200</sub> Mn <sub>0.533</sub> Co <sub>0.133</sub> Ni <sub>0.133</sub> O <sub>2</sub> .....	18
Figure 2.1 Schematic of a continuously-stirring tank reactor.....	24
Figure 2.2 Continuously-stirring tank reactor.....	25
Figure 2.3 Temperature profile for the solid-state synthesis of LLRTMO.....	28
Figure 2.4 Schematic of a Bragg-Brentano diffractometer.....	29
Figure 2.5 Schematic of pycnometer .....	35
Figure 2.6 Schematic of the three basics steps of a NMR experiment. ....	38
Figure 2.7 Schematic of the conversion of FID into a NMR spectrum .....	39
Figure 2.8 <sup>6</sup> Li NMR spectrum of LLRTMO materials .....	40
Figure 2.9 Electrode spread making .....	41
Figure 2.10 Coin-cell assembly .....	42
Figure 3.1 Superlattice ordering in the TM layer of Li <sub>2</sub> MnO <sub>3</sub> .....	45
Figure 3.2 Structure of Li <sub>2</sub> MnO <sub>3</sub> .....	46

Figure 3.3. TM layers of $\text{Li}_2\text{MnO}_3$ made up of pink (Mn) and green (Li) balls (A1), triangles (B1) and stars (C1). Top panel: Triangular lattice plane A1, Bottom left panel: A1 to B1 translation. Bottom right panel: B1 to C1 translation. The black, red and the blue hexagonal 2-D unit cells correspond to the A1, B1 and C1 TM layers. ....	47
Figure 3.4 TM layers of $\text{Li}_2\text{MnO}_3$ showing A1 to B2 translation (left panel) and A1 to B3 translation (right panel).....	48
Figure 3.5 FAULTS -Simulated XRD pattern of $\text{Li}_2\text{MnO}_3$ with 0 % stacking faults. ....	51
Figure 3.6 FAULTS Simulated XRD patterns of $\text{Li}_2\text{MnO}_3$ from $10^\circ$ to $90^\circ$ with varying stacking fault probabilities.....	54
Figure 3.7 Enlarged view of the FAULTS simulated XRD patterns of $\text{Li}_2\text{MnO}_3$ from $20^\circ$ to $34^\circ$ with varying stacking fault probabilities.....	55
Figure 3.8 XRD patterns of $\text{Li}_2\text{MnO}_3$ synthesized at $900^\circ\text{C}$ (LM900) and $1100^\circ\text{C}$ (LM1100). Inset: Enlarged view in the range of $20^\circ$ to $33^\circ$ .....	56
Figure 3.9 Experimental (red points), the calculated (black line) XRD patterns of LM900 (a) and LM1100 (b) obtained from FAULTS refinement and their difference (green line).....	57
Figure 3.10 XRD of the studied samples in the $\text{Li}[\text{Li}_{1/3-2x/3}\text{Ni}_x\text{Mn}_{2/3-x/3}]\text{O}_2$ series. Right panel: Expanded view of (001) peak corresponding to $C2/m$ spacegroup.....	59
Figure 3.11 XRD patterns showing only the superlattice peaks in the range of $20^\circ$ to $25^\circ$ of the studied samples in the $\text{Li}[\text{Li}_{1/3-2x/3}\text{Ni}_x\text{Mn}_{2/3-x/3}]\text{O}_2$ series. The black dotted line shows the shift in (020) peak corresponding to the $C2/m$ spacegroup.....	60
Figure 3.12 $d$ -spacings of $C2/m$ peaks ( $33-I$ ) vs. (020) of the studied samples in the $\text{Li}[\text{Li}_{1/3-2x/3}\text{Ni}_x\text{Mn}_{2/3-x/3}]\text{O}_2$ series. ....	62

Figure 3.13 Experimental (red points) and the FAULTS fitted (black line) XRD patterns of the studied samples in the $\text{Li}[\text{Li}_{1/3-2x/3}\text{Ni}_x\text{Mn}_{2/3-x/3}]\text{O}_2$ series.....	64
Figure 3.14 Experimental (red points) and the FAULTS fitted (black line) XRD patterns in the superlattice region ( $20^\circ$ to $28^\circ$ ) of the studied samples in the $\text{Li}[\text{Li}_{1/3-2x/3}\text{Ni}_x\text{Mn}_{2/3-x/3}]\text{O}_2$ series.....	65
Figure 3.15 Stacking fault probabilities ( $s$ ) versus Ni content ( $x$ ) of the studied samples in the $\text{Li}[\text{Li}_{1/3-2x/3}\text{Ni}_x\text{Mn}_{2/3-x/3}]\text{O}_2$ series. ....	66
Figure 4.1 First-cycle voltage vs specific capacity profiles of samples: A1, A2 and A3. .	71
Figure 4.2 Left Panel: X-ray diffraction patterns of samples A1, A2 and A3. Right panel: Enlarged view between $17^\circ$ and $20^\circ$ showing the (003) peak corresponding to $R-3m$ spacegroup. ....	72
Figure 4.3. SEM images of sample S (nano-sized $\text{LiNi}_{0.5}\text{Mn}_{1.5}\text{O}_4$ ).....	74
Figure 4.4 X-ray diffraction patterns of samples A1, A1 + 5% Spinel, A1 + 10% Spinel and pure Spinel .....	75
Figure 4.5 X-ray diffraction patterns in the range of $35^\circ$ to $39^\circ$ for A1, A2, A3, A1 + 5% Spinel, A1 + 10% Spinel.....	76
Figure 4.6 Left panel: $dQ/dV$ versus $V$ for samples A1, A1 + 5% Spinel and A1 + 10% Spinel in the voltage range between 2 and 4.8 V. Right panel: The green bordered portion between 2.6 and 3 V has been enlarged and is shown separately for clarity .....	77
Figure 4.7 $dQ/dV$ versus $V$ for samples A1, A2, A3, A1 + 5% Spinel and A1 + 10% Spinel. ....	78
Figure 4.8 Left panel: X-ray diffraction patterns of samples A1, A2 and A3. Bottom panel: Right panels: The green bordered portion between $14^\circ$ and $17^\circ$ and $17^\circ$ and $20^\circ$ has been enlarged and is shown separately for clarity. ....	79



Figure 4.9 First. cycle voltage - specific capacity profiles of samples, A1, A1+10 wt. % spinel and A3 .....	80
Figure 4.10 XRD patterns of A3 and A3Q (Quenched) .....	81
Figure 4.11 First cycle voltage-capacity profile of samples A3 and A3Q.....	82
Figure 4.12 Top panel: dQ/dV versus V for samples A3 and A3Q (prepared by quenching). Bottom panel: The pink bordered portion between 2.2 and 3 V has been enlarged and is shown separately for clarity. ....	83
Figure 4.13 Scanning electron micrograph images of samples A1, A2, A3 and GA1 (ground sample) .....	85
Figure 4.14 First-cycle charge-discharge voltage profiles of samples A1 and GA1 (ground sample).....	86
Figure 4.15 Plot of first charge sloping region capacity vs % Mn in +3 oxidation state and total charge of the cations vs % Mn in +3 oxidation state for A3Q.....	88
Figure 4.16 First-cycle charge-discharge voltage profiles of A1, A2, A3 and A3Q during constant time (25 h) first charge protocol. ....	93
Figure 5.1 Ni-Mn-Co ternary diagram with every point representing $Ni_xMn_yCo_{1-x-y}$ precursor composition (e.g. $Ni_{0.4}Mn_{0.2}Co_{0.4}CO_3$ ) .....	96
Figure 5.2 Scanning electron micrograph images of selected precursors A, C, H, J, L and O.....	102
Figure 5.3 XRD patterns of few single phase low-IRC materials (samples C4, D4, K2 and L2) between $20^\circ$ to $70^\circ$ .....	103
Figure 5.4 Calculated densities assuming metal-site vacancies (black) and no vacancies (red) vs measured densities (using a He-pycnometer) .....	107

Figure 5.5 Density difference between the calculated (no vacancy case) and the measured densities (from He pycnometer) vs the calculated metal-site vacancy content .....	109
Figure 5.6 First cycle charge-discharge voltage vs specific capacity profiles of few single phase low-IRC materials represented in Figure 5.3 .....	110
Figure 5.7 First cycle charge-discharge differential capacity profiles of few single phase low-IRC materials represented in Figure 5.3 .....	112
Figure 5.8 XRD patterns of samples H1, H2 and H3. Green arrows indicate the secondary spinel phase .....	113
Figure 5.9 First cycle charge-discharge voltage vs specific capacity profiles of H series. H1 and H2 are two-phase low-IRC materials. ....	114
Figure 5.10 (a) Irreversible capacity vs. vacancy content and (b) first discharge capacity vs. vacancy content showing single phase (black circles or diamonds) and two phase (red circles or diamonds) samples. ....	116
Figure 5.11 (a) Fraction IRC vs. Li excess showing single (black points) and two phase (red points) samples, (b) Co content vs. Li excess (fraction of IRC represented as size of the data points) and (c) Co content vs. Li excess showing whether a sample is single phase (Y) or not (N). ....	117
Figure 6.1 $^7\text{Li}$ NMR spectrograph of $\text{Li}_2\text{MnO}_3$ . ....	121
Figure 6.2 $^7\text{Li}$ NMR spectrographs of A1, A2, A3Q, K1, K2, L1, L2, N1, N2, O1 and O2 (refer Table 6.1) .....	122
Figure 6.3 XRD patterns of samples A2, A2 $\dagger$ and A2 $\dagger\dagger$ between $10^\circ$ to $70^\circ$ .....	127
Figure 6.4 SEM images of samples A2, A2 $\dagger$ and A2 $\dagger\dagger$ .....	128
Figure 6.5 XRD patterns of samples E1, A1, B1, C1, D1 and H1 between $10^\circ$ and $70^\circ$ Right panel: Enlarged view of the superlattice peaks between $20^\circ$ and $24^\circ$ .....	130

Figure 6.6 Lattice parameters $a$ and $c$ vs. the amount of Co for samples E1, A1, B1, C1, D1 and H1 .....	131
Figure 6.7 First cycle voltage-capacity profiles of samples E1, A1, B1, C1, D1 and H1 between 2.0 V and 4.8 V .....	132
Figure 6.8 Differential voltage-capacity profiles during the first cycle of samples E1, A1, B1, C1, D1 and H1 .....	134
Figure 6.9 Irreversible capacity vs. 4.5 V plateau capacity of samples E1, A1, B1, C1, D1 and H1 .....	135
Figure 6.10 XRD pattern of sample Fe-A1 .....	137
Figure 6.11 First cycle voltage-specific capacity profiles of samples A1 (blue) and Fe-A1 (red) between 4.8 V and 2.0 V .....	139
Figure 6.12 Voltage-specific capacity profiles obtained from step-wise charge-discharge cycles between 2.0 V and upper cut-off voltages 4.0 V(black), 4.4 V(blue), 4.6 V(pink) and 4.8 V(green). .....	140
Figure 7.1 First cycle charge-discharge profiles of $\text{Li}[\text{Li}_{0.166}\text{Ni}_{0.250}\text{Mn}_{0.583}]\text{O}_2$ synthesized from sol-gel method, hydroxide co-precipitation and carbonate co-precipitation.....	151
Figure 7.2 Top panels: Discharge specific capacity vs cycle number and bottom panels: Average discharge voltage vs. cycle number of samples A1, A2, B1 and B2.....	153
Figure 7.3 XRD pattern of the compound $\text{Li}[\text{Ni}_{1/6}\text{Mn}_{2/3}]\text{O}_2$ .....	155
Figure 7.4 Left panel: Voltage-specific capacity profiles of $\text{Li}[\text{Ni}_{1/6}\text{Mn}_{2/3}]\text{O}_2$ and right panel: $dQ/dV$ vs. $V$ plots for several cycles.....	156
Figure 7.5 First cycle charge-discharge profiles of samples K1 and K2 (left panel) and N1 and N2 (right panel) .....	157

Figure 7.6 Local Li-excess environments around O atoms in LLRTMO materials (top panel) and LLRTMO with metal-site vacancies (bottom panels)..... 158

## Abstract

High energy density lithium-ion batteries are desired for applications such as electrified vehicles. Hence, developing high energy density positive electrode materials is important. Layered lithium-rich transition metal oxides can deliver high specific capacity. However, they have several characteristic issues such as large first-cycle irreversible capacity loss that prevent their use in high-energy lithium-ion batteries. Studies to understand the properties of layered lithium-rich transition metal oxides are necessary to find solutions to those issues. Hence, this thesis is devoted to study some of the important structural and electrochemical properties of lithium-rich transition metal oxides.

Layered lithium-rich transition metal oxides have two types of metal layers, which are made of (i) only  $\text{Li}^+$  ions (Li layer) and (ii) both  $\text{Li}^+$  ions and transition metal ions such as  $\text{Mn}^{4+}$ ,  $\text{Ni}^{2+}$  and  $\text{Co}^{3+}$  (transition metal layer). The larger  $\text{Li}^+$  ions and smaller  $\text{Mn}^{4+}$  ions tend to show superlattice ordering in the transition metal layers causing superlattice peaks in the X-ray diffraction patterns. A shift in the superlattice peak positions to lower scattering angles with increasing Ni content in  $\text{Li}[\text{Li}_{1/3-2x/3}\text{Ni}_x\text{Mn}_{2/3-x/3}]\text{O}_2$  series confirmed a solid-solution behavior.  $\text{Ni}^{2+}$  ions in the transition metal layers affect the superlattice ordering, which in turn causes stacking disorder (stacking faults) of the transition metal layers along the *c*-axis and hence broadens the superlattice peaks. The probabilities of stacking faults between adjacent layers in the  $\text{Li}[\text{Li}_{1/3-2x/3}\text{Ni}_x\text{Mn}_{2/3-x/3}]\text{O}_2$  series were determined with a XRD fitting program called FAULTS. The results showed that stacking fault probability increased with increasing Ni content.

First-cycle irreversible capacity in layered Li-rich transition metal oxides is affected by several factors such as the total amount of Li in the structure. Layered lithium rich transition metal oxides with slightly smaller amount of Li than that required for stoichiometric balance were synthesized and the first-cycle irreversible capacity was measured. Compared to samples with a stoichiometrically balanced amount of Li, the Li-deficient materials had lower irreversible capacity loss. Investigating the metal compositions, true densities in combination with oxidation state rules revealed that Li-deficient materials had metal-site vacancies, which apparently reduced the high irreversible capacity. Further, a search for low-irreversible capacity materials in the Li-Ni-Mn-Co-O pseudo-quaternary system resulted in the identification of several low-irreversible capacity materials that have different Ni-Mn-Co compositions.

$^7\text{Li}$  solid-state NMR experiments conducted on several low-irreversible capacity materials suggested that the metal-site vacancies predominantly occupy the Li layer. Experiments to probe the cause for the high irreversible capacity were also conducted on materials with and without metal-site vacancies. It was found that oxygen-release occurring during the first charge was not the only reason for high irreversible capacity and that the migration of transition metal ions from the transition metal layers to the Li layer may also contribute significantly to the high irreversible capacity.

## ஆய்வேடு சுருக்கம்

மின்மயமாக்கப்பட்ட வாகனங்கள் போன்ற பயன்பாடுகளில் உயர் ஆற்றல் அடர்த்தி லித்தியம்-அயனி மின்கலங்கள் தேவைப்படுகின்றன. எனவே, உயர் ஆற்றல் அடர்த்தி நேர்மின்முனை பொருட்களை அபிவிருத்தி செய்வது முக்கியத்துவம் வாய்ந்தது. அடுக்கு லித்தியம்-மிகை இடைநிலை உலோக ஆக்சைடுகள் போன்ற நேர்மின்முனை பொருட்கள் மிகுந்த எடை திறன் வழங்கவல்லவை. இருந்தபோதிலும், அவைகளுக்கு அதிக முதல்-சுற்று மீள இயலா திறன் போன்ற தனித்துவமான பிரச்சினைகள் இருக்கின்றன. ஆதலால் லித்தியம்-மிகை இடைநிலை உலோக ஆக்சைடுகளின் உயர் ஆற்றல் லித்தியம்-அயனி மின்கல பயன்பாடுகள் தடுக்கப்படுகின்றன. இப்பிரச்சினைகளுக்கு தீர்வு காணும் வகையில், லித்தியம்-மிகை இடைநிலை உலோக ஆக்சைடுகளின் பண்புகளை புரிந்து கொள்ளக்கூடிய ஆய்வுகள் தேவை என கருதப்படுகிறது.

லித்தியம்-மிகை இடைநிலை உலோக ஆக்சைடுகளில் இரண்டு வகையான உலோக தளங்கள் உள்ளன - (i) லித்தியம்-அயனிகளை ( $Li^+$ ) மட்டும் உள்ளடக்கிய தளம் (லித்தியம் தளம்) மற்றும் (ii) லித்தியம் மற்றும்  $Mn^{4+}$ ,  $Ni^{2+}$  and  $Co^{3+}$  போன்ற இடைநிலை உலோக அயனிகளை உள்ளடக்கிய தளம் (இடைநிலை உலோக தளம்). இடைநிலை உலோக தளங்களில் உள்ள பெரிய  $Li^+$  அயனிகளும் சிறிய  $Mn^{4+}$  அயனிகளும் சிறப்பு அணிக்கோவை வடிவமைப்பில் ஈடுபடுகின்றன. அதன் விளைவாக லித்தியம்-மிகை இடைநிலை உலோக ஆக்சைடுகளின் X-கதிர் எதிரொளிப்பு படிவங்களில் சிறப்பு அணிக்கோவை முகடுகள் தோன்றுகின்றன.  $Li[Li_{1/3-2x/3}Ni_xMn_{2/3-x/3}]O_2$  பொருட்களில் உள்ள Ni அளவை அதிகரிக்கும்பட்சத்தில், அவைகளின் சிறப்பு அணிக்கோவை முகடுகள் கீழ் சிதறு கோணங்களுக்கு நகரும் தன்மை, அப்பொருட்களின் திண்ம-கரைசல் பண்பினை உறுதி செய்கிறது.  $Li[Li_{1/3-2x/3}Ni_xMn_{2/3-x/3}]O_2$  பொருட்களின் இடைநிலை உலோக தளங்களில் உள்ள  $Ni^{2+}$  அயனிகள் சிறப்பு அணிக்கோவை வடிவமைப்பை சீர்குலைக்கும் பண்பை உடையவை. அதன் விளைவாக இடைநிலை உலோக தளங்களை c-அச்ச நெடுகில் அடுக்கும் முறையில் கோளாறு (அடுக்கு தவறுகள்) ஏற்பட்டு, சிறப்பு அணிக்கோவை முகடுகள் அகன்று காணப்படுகின்றன.  $Li[Li_{1/3-2x/3}Ni_xMn_{2/3-x/3}]O_2$  பொருட்களில் உள்ள அடுத்தடுத்த இடைநிலை உலோக தளங்களில் ஏற்படும் அடுக்கு தவறுகளின் நிகழ்தகவுகள், பால்ட்ஸ் (FAULTS) என்றழைக்கப்படும் X-கதிர் எதிரொளிப்பு படிவங்களை பொருத்தும் திட்டத்தின் மூலம் தீர்மானிக்கப்பட்டன. அத்திட்டத்தின் முடிவுகள், Ni அளவை அதிகரிக்கும்பட்சத்தில் அடுக்கு தவறுகளின் நிகழ்தகவுகள் அதிகரிப்பதை எடுத்துக்காட்டின.

லித்தியம்-மிகை இடைநிலை உலோக ஆக்சைடுகளின் படி அமைப்பில் உள்ள லித்தியத்தின் மொத்த அளவு போன்ற பல்வேறு காரணிகள் முதல்-சுற்று மீள இயலா திறனை பாதிக்கின்றன. வேதிவினை சமனுக்கு தேவையான அளவை விட சற்று குறைவான லித்தியம் பயன்படுத்தி, லித்தியம்-மிகை இடைநிலை உலோக ஆக்சைடுகள் தயாரிக்கப்பட்டு, அவைகளின் முதல்-சுற்று மீள இயலா திறன் அளக்கப்பட்டது. வேதிவினை சமனுக்கு தேவையான லித்தியத்தை கொண்ட மாதிரிகளை ஒப்பிடுகையில், சற்று குறைவான லித்தியம் பெறும் மாதிரிகள் குறைந்த முதல்-சுற்று மீள இயலா திறனை வெளிப்படுத்தின. லித்தியம்-குறைவு மாதிரிகளின் உலோக தொகுப்புகள், மெய் அடர்த்திகள் மற்றும் ஒக்ஸிஜனேற்ற விதிகளை ஆராய்கையில், அவைகளின் படி அமைப்பில் உள்ள உலோக-அயனிகளின் சில இடங்களை வெற்றிடங்கள் ஆக்கிரமித்திருப்பது தெரியவந்தது. அதன் விளைவாகவே, முதல்-சுற்று மீள இயலா திறன் குறைந்திருப்பதும் கண்டறியப்பட்டது. மேலும் Li-Ni-Mn-Co-O போலி-நான்குமுனை அமைப்பில் குறைந்த மீள இயலா திறன் கொண்ட பொருட்கள் தேடப்பட்ட முடிவில், வெவ்வேறு Ni-Mn-Co தொகுப்புகளை கொண்ட பல குறைந்த மீள இயலா திறன் கொண்ட பொருட்கள் இருப்பது கண்டறியப்பட்டன.

பல குறைந்த மீள இயலா திறன் கொண்ட பொருட்களில் நடத்தப்பட்ட  $^7Li$  திண்ம-நிலை அணுக்கரு காந்த ஒத்திசைவு சோதனைகளின் முடிவுகள், அப்பொருட்களில் உள்ள உலோக-அயனி இட வெற்றிடங்கள் லித்தியம்-தளங்களையே ஆக்கிரமித்திருப்பதை பரிந்துரைத்தது. லித்தியம்-மிகை இடைநிலை உலோக ஆக்சைடுகளில் ஏற்படும் அதிக மீள இயலா திறனுக்கான காரணிகளை கண்டறியும் சோதனைகள் உலோக-அயனி இட வெற்றிடங்களை உடைய மற்றும் அவை இல்லாத பொருட்களில் நடத்தப்பட்டன. முதல் ஆற்றல் ஏற்றத்தில் ஏற்படும் ஒக்ஸிஜன்-வெளியீடு மட்டுமே மீள இயலா திறனுக்கான ஒரே காரணி இல்லை என்பதும் இடைநிலை உலோக அயனிகள் அவற்றிற்கான தளங்களில் இருந்து லித்தியம் தளங்களுக்கு இடம்பெயர்வதும் முதல்-சுற்று மீள இயலா திறனுக்கு மிக முக்கிய காரணி எனவும் அம்முடிவுகள் தெரிவித்தன.

## List of Symbols and Abbreviations Used

$\alpha, \beta, \gamma$	angles between the principle axes of the unit cell
$a, b, c$	lattice constants
$A$	area of each adsorbed molecule (BET method)
BET	Brunauer-Emmett-Teller method
BSE	back scattered electrons
$C$	BET constant
CSTR	continuously-stirring tank reactor
$\delta$	chemical shift
$\delta_{iso}$	isotropic chemical shift
$d$	distance between particular planes of an unit cell
$\Delta$	sum of weighted squared difference between observed and calculated intensities (Rietveld refinement)
DEC	diethyl carbonate
DEMS	Differential electrochemical mass spectrometry
$E$	Energy
EC	Ethylene carbonate

EPR	Electron paramagnetic resonance
EXAFS	Extended X-ray absorption fine structure
$F$	Faraday constant
FCC	Face-centered cubic
FID	Frequency induction decay
FT	Fourier Transformation
ICP-OES	Inductively coupled plasma-optical emission spectroscopy
IRC	Irreversible capacity loss
$\lambda$	Wavelength
LLRTMO	Layered Li-rich transition metal oxide
LLTMO	Layered lithium transition metal oxide
$\mu_{Li}^+$	chemical potential of Li in the positive electrode
$\mu_{Li}^-$	chemical potential of Li in the negative electrode
$M$	molar mass
MAS	magic angle spinning
$n$	order of diffraction
$n_c$	number of moles of gas in the sample cell chamber of pycnometer



$N_A$	Avogadro number
NCA	lithium nickel cobalt aluminum oxide ( <i>e.g.</i> $\text{Li}[\text{Ni}_{0.85}\text{Co}_{0.1}\text{Al}_{0.05}]\text{O}_2$ )
NMC	lithium nickel manganese cobalt oxide ( <i>e.g.</i> $\text{Li}[\text{Ni}_{0.333}\text{Mn}_{0.333}\text{Co}_{0.333}]\text{O}_2$ )
NMR	nuclear magnetic resonance
O	octahedral site
OCV	open-circuit voltage
$p'$	mole fraction of Li in the studied LLRTMO compounds
$P$	partial vapor pressure of adsorbate gas in equilibrium with the surface at 77.4 K (boiling point of liquid $\text{N}_2$ ), in pascals
$P_0$	saturated pressure of the adsorbate gas, in pascals
$P_a$	ambient pressure
P	prismatic site
$P_1$	elevated pressure in the sample cell chamber of pycnometer
$P_2$	intermediate pressure in the sample cell (or expansion) chamber of pycnometer
$P_{11}$	probability of (1/3, 1/3, 1/3) translation (FAULTS)
PVDF	polyvinylidene fluoride
$Q$	capacity

$q$	fraction of vacancies in the studied LLRTMO compounds
$R$	gas constant
$R_B$	Bragg agreement factor in the Rietica program
RF	radio frequency
rpm	rotations per minute
$S$	surface area (Chapter 2)
$S$	stacking fault probability (Chapter 3)
SE	secondary electrons
SEM	scanning electron microscopy
SL	superlattice
SSA	specific surface area
STP	standard temperature and pressure
$\theta$	scattering angle
T	tetrahedral site
$T_a$	ambient temperature
TEM	transmission electron microscopy
TM	transition metal

$v_a$	volume of gas adsorbed at STP, in mL
$v_m$	volume of gas (STP) required to form adsorbed monolayer on the sample surface, in mL
$V$	voltage
$V_{exp}$	volume of the expansion cell chamber of pycnometer
$V_{cell}$	volume of the sample cell chamber of pycnometer
$V_{samp}$	volume of the sample in the pycnometer
$V_m$	molar volume
$W_i$	statistical weight (Rietveld refinement)
XPS	X-ray photoelectron spectroscopy
XRD	X-ray diffraction
$y_i(obs)$	observed intensity (Rietveld refinement)
$y_i(cal)$	calculated intensity (Rietveld refinement)

## Acknowledgements

I would like to thank my supervisor Dr. Jeff Dahn for his mentorship, guidance, and support during my PhD years at Dalhousie. I have learnt innumerable things from Jeff but still a lot remains to be learnt. I also want to thank my committee members Dr. Mary Anne White, Dr. Mark Obrovac and Dr. Heather Andreas for their valuable advice over these years.

I am thankful to several Dahn-lab alumni - Dr. Eric McCalla, Dr. John Camardese, Dr. Aaron Rowe and Dr. Remi Petibon for their help and teachings. I would also like to thank Dr. Robbie Sanderson and Dr. David Stevens for their numerous help. Special thanks to the positive (materials) guys Dr. Jing Li, Stephen Glazier and Aaron Liu for their precious help and collaboration. I want to sincerely thank my lab-mates – Tim Crowtz, Deijun Xiong, Lin Ma, Jian Xia, Xiawei Ma, Kathlyne Nelson, Leah Ellis, and Alexander Louli, who were quite supportive and made my time very fruitful.

Thanks to Dr. Gillian Goward and Dr. Kris Harris from McMaster University for their help in solid-state NMR experiments. I would like to thank Simon Trussler for equipments, Andy George and Patricia Scallion for SEM experiments, Susan Batchilder for ICP-OES and Kevin Borgel and John Noddin for machine shop works. Thanks to Chemistry-mates Dr. Paul Duchense, Dan Chevrier, Alex Paterson and Dr. Carl Romao for useful discussions. I want to thank Gisselle Andrews for all the administrative help in the Department of Chemistry.

I want to thank my parents Shunmugasundaram Ramaiah and Ahila Shunmugasundaram and my brother Prakash Shunmugasudaram, whose moral support was invaluable. Finally, I want to thank my wife Rajalakshmi Senthil Arumugam, who is a great partner, not only in my life, but also in my research projects. Without your support and encouragement, I would not have made it to this stage.

# Chapter 1 Introduction

## 1.1 Lithium-ion battery

A lithium-ion (Li-ion) rechargeable battery is comprised of a large number of identical Li-ion cells connected to one another. A Li-ion cell has a positive electrode (*e.g.* lithium cobalt oxide ( $\text{LiCoO}_2$ )), a negative electrode (*e.g.* graphite) and an electrolyte. Lithium hexafluorophosphate ( $\text{LiPF}_6$ ) salt dissolved in a mixture of solvents such as ethylene carbonate (EC) and diethyl carbonate (DEC) is a typical electrolyte<sup>1</sup> that can be used in Li-ion cells. While the electrolyte is an ionic conductor, the electrodes act both as ionic and electronic conductors.

Figure 1.1 shows a schematic of a Li-ion cell with a  $\text{LiCoO}_2$  positive electrode and a graphite negative electrode. In Figure 1.1, the liquid electrolyte, which wets all the parts inside a Li-ion cell, is represented by the yellow region and the  $\text{Li}^+$  ions in the electrolyte as well as in the electrodes are represented by green balls.  $\text{Li}^+$  ions within the structure of an electrode are equivalent to Li atoms with electrons and hence the term “Li atoms” is used in the place of “ $\text{Li}^+$  ions”. However, irrespective of the location, the term “ $\text{Li}^+$  ions” is adopted in this thesis to match several authors such as Whittingham et al.<sup>2</sup>, Julien et al.<sup>3</sup>, and Hy et al.<sup>4</sup>

A microporous separator (dashed line between positive and negative electrodes in Figure 1.1), usually made of a polymer (*e.g.* polyethylene<sup>5</sup>), prevents electrical short-circuit between the two electrodes. It provides an ionic path for the  $\text{Li}^+$  ions through its pores. Aluminum and copper foils serve as current collectors for positive and negative electrodes respectively and are not shown in Figure 1.1.

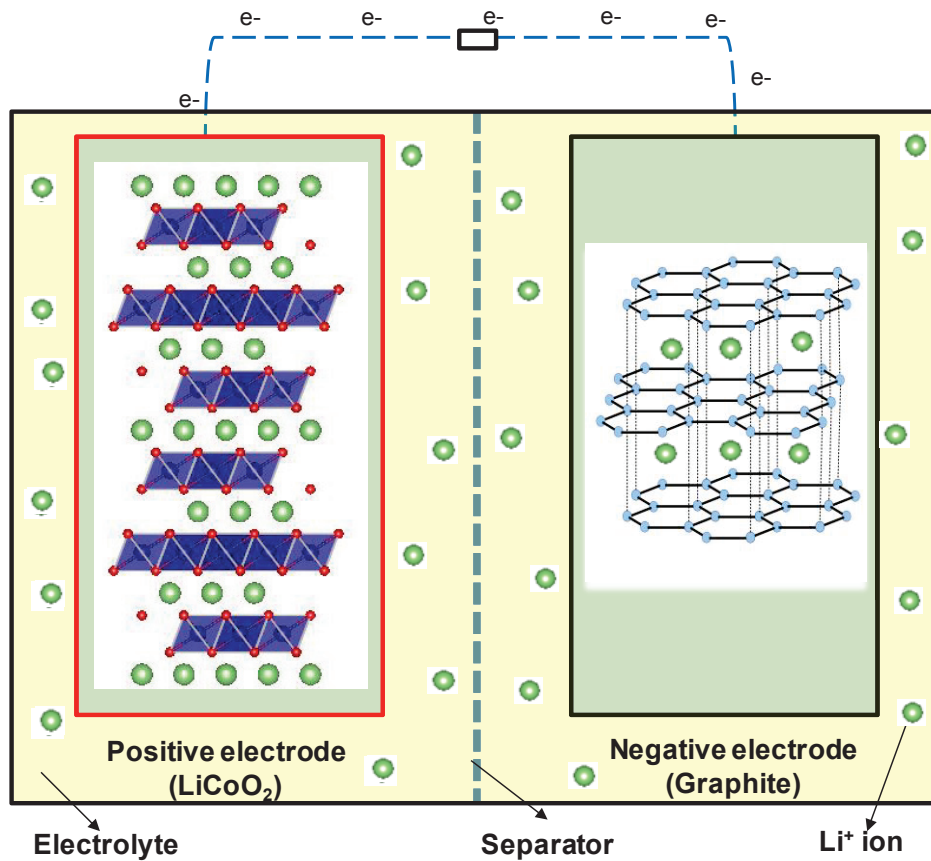
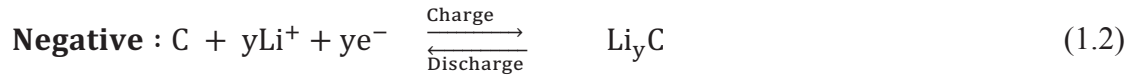
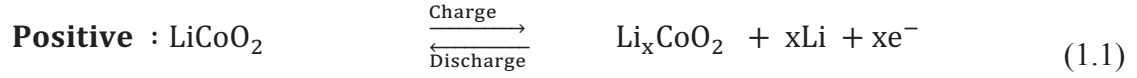


Figure 1.1 Schematic of a Li-ion Cell

Technically, electrode materials such as LiCoO<sub>2</sub> and graphite are called “active materials”, as they directly participate in the electrochemical reactions. In reality, electrodes are made up of active materials and other supporting materials such as binders (*e.g.* polyvinylidene fluoride (PVDF)<sup>6</sup>) and conductive diluents (*e.g.* carbon black<sup>7</sup>). While the binders provide mechanical stability, the conductive diluents enhance electronic conductivity between the active material particles.

During operation, Li<sup>+</sup> ions are inserted (intercalated)<sup>8</sup> in and extracted out (deintercalated) and of the electrode materials along with the corresponding electrons that flow through the external circuit. The intercalation/deintercalation processes occurring in a Li-ion cell are electrochemically-driven guest-host reactions. Li<sup>+</sup> ions act as guests

whereas the active materials act as hosts in a topotactic reaction<sup>9</sup>. The reactions<sup>10</sup> occurring in the electrodes of a LiCoO<sub>2</sub>/graphite Li-ion cell during charge and discharge are:



(Equation (1.1) to (1.3) have been adapted from (Ref. 10))

When a Li-ion cell is charged by applying current, Li<sup>+</sup> ions are deintercalated from the positive electrode along with equal number of electrons resulting from electrochemical oxidation. The released Li<sup>+</sup> ions flow through the electrolyte and intercalate into the negative electrode along with the corresponding electrons arriving through the external circuit. During discharge, a spontaneous reaction occurs, in which the Li<sup>+</sup> ions travel from the negative electrode back to the positive electrode and the electrons flow through the external circuit in the opposite direction. The flow of electrons caused by the spontaneous reaction during discharge is used to transfer stored chemical energy into useful electrical energy.

The equilibrium voltage ( $V$ ) of a Li-ion cell can be thermodynamically deduced by knowing the difference between the chemical potential of lithium in the positive ( $\mu_{Li}^+$ ) and the negative electrodes ( $\mu_{Li}^-$ )<sup>11</sup>. The equilibrium voltage of a Li-ion cell is

$$V = - \frac{\mu_{Li}^+ - \mu_{Li}^-}{F} \quad (1.4)$$

where  $F$  is the Faraday constant. As the Li concentration in electrodes change during charge and discharge, both  $\mu_{Li}^+$  and  $\mu_{Li}^-$  and the resultant  $V$  of a Li-ion cell change. Therefore, the voltage at any state of charge or discharge depends on the extent of the reaction or the corresponding Li concentration.

The maximum available capacity of a Li-ion cell is the amount of charge it could store. However, the practical capacity accounts only for the amount of  $Li^+$  ions that can be reversibly intercalated/deintercalated between the two electrodes. The amount of  $Li^+$  ions that can be practically extracted depends on various factors such as the Li content of the positive electrode, structural stability of the electrode materials and the upper cut-off voltage.

Theoretically, the electrochemical energy ( $E$ ) available from a Li-ion cell can be deduced from its capacity ( $Q$ ) and the voltage ( $V$ ) as shown by:

$$E = \int V dQ \quad (1.5)$$

Figure 1.2 shows a schematic of a voltage ( $V$ ) vs. capacity ( $Q$ ) profile of a Li-ioncell during discharge. The area bounded by the axes and the voltage curve represents the energy obtained from the cell during discharge. At the same time, the total amount of energy available from a given Li-ion cell depends on several factors such as the size of the cell, the proportion of the active materials and charge-discharge conditions.



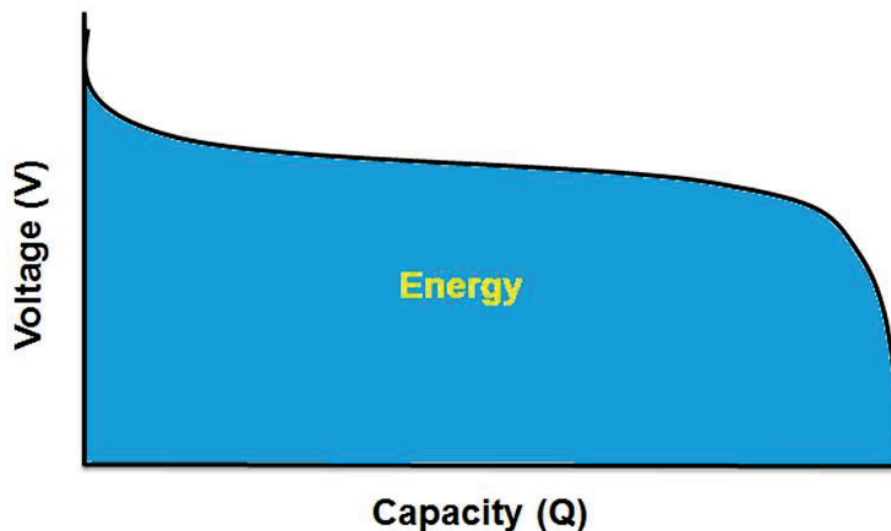


Figure 1.2 Schematic of the voltage-capacity profile of a Li-ion cell during discharge

The research work discussed in this thesis has been exclusively done on positive electrode materials and so only an overview of positive electrode materials is given here and details on negative electrodes<sup>12</sup> or electrolytes<sup>1</sup> can be found elsewhere.

## 1.2 Positive electrode materials

A positive electrode material of a Li-ion cell is a reservoir of  $\text{Li}^+$  ions, which is thermodynamically stable within its structure after synthesis. A good candidate for a positive electrode material is expected to have the following two properties: The material must have a feasible redox center *i.e.*, an easily oxidizing and reducing metal ion such as a transition metal (TM) ion and the material must be structurally stable during intercalation/deintercalation.

Positive electrode materials with high energy density, high power, better safety, low cost and low toxicity are desired for high energy demand applications such as grid-electric storage, plug-in hybrid vehicles and electric vehicles<sup>13,14</sup>. A high energy is

achievable if the positive electrode material has a high potential (around 4 V vs Li/Li<sup>+</sup>) and a high capacity. The nature of the cations and anions of a positive electrode material affects its potential and the capacity. For example, positive electrode materials with polyanionic groups such as LiCoPO<sub>4</sub> have relatively higher potential than that of their corresponding oxides<sup>15</sup>. However, the gain comes at the expense of decreased volumetric capacity due to a decreased crystallographic density caused by their bulkier polyanions. Thus a positive electrode with a fair balance between potential and capacity is desired.

A high capacity is achievable if the structure of a positive electrode material has a high concentration of Li available for reversible intercalation and deintercalation during electrochemical cycling. The theoretical capacity of a positive electrode material is the capacity corresponding to all the Li in the structure. It is normally expressed with respect to its volume (volumetric in mAh/cm<sup>3</sup>) or mass (gravimetric in mAh/g). The equation for determining theoretical gravimetric capacity or specific capacity is

$$\text{Specific Capacity} = \frac{nF}{M} = \frac{n \times 26800 \text{ mAh mol}^{-1}}{M \text{ g mol}^{-1}} \quad (1.6)$$

where  $n$  is the number of Li<sup>+</sup> ions present per formula unit of the material,  $F$  is the Faraday constant and  $M$  is the molar mass of the positive electrode material in g mol<sup>-1</sup>.

Li-ion battery positive electrode materials are broadly classified into three types on the basis of their crystallographic structures: layered lithium transition metal oxides (LLTMO) (*e.g.* LiCoO<sub>2</sub>), spinel-type compounds (*e.g.* lithium manganese oxide (LiMn<sub>2</sub>O<sub>4</sub>)) and lithium polyanionic compounds (*e.g.* lithium iron phosphate (LiFePO<sub>4</sub>)).

The research work in this thesis deals only with LLTMO materials, and therefore, a detailed discussion is given only for LLTMO materials and their derivatives.

### 1.3 Layered lithium transition metal oxides (LLTMO)

The identification of layered  $\text{LiCoO}_2$ <sup>16</sup> by Goodenough's research group became a break-through discovery eventually resulting in the first commercial Li-ion battery by SONY in 1991<sup>17</sup>. Following the success of  $\text{LiCoO}_2$ , LLTMO materials became prominent positive electrode materials for Li-ion batteries.

LLTMO materials adopt the  $\alpha\text{-NaFeO}_2$ <sup>18</sup> structure that can be described using a hexagonal unit cell with  $R\text{-}3m$  space group. Figure 1.3 shows the structure of  $\text{LiCoO}_2$ , which is a representative example of a LLTMO with only one TM ion in a formula unit. Fundamentally, the structure is formed by a face-centred-cubic (FCC) network of oxygen anions. The cations are embedded in the octahedral sites similar to that of a rock-salt structure (*e.g.* NaCl). At the same time, the cations arrange themselves in an orderly fashion in such a way that alternating rows or sheets of octahedral sites are occupied by either  $\text{Li}^+$  or TM ions. Hence the structure is an ordered-rock-salt structure.

The structure of  $\text{Li}[\text{M}]\text{O}_2$  is made up of stacks of  $(\text{MO}_2)_n$  sheets, in which M represents a TM ion. Each  $(\text{MO}_2)$  sheet is formed by edge-sharing  $\text{MO}_6$  octahedra and can be seen as a layer of TM ions sandwiched in between two oxygen layers. Each  $\text{MO}_6$  octahedron is made of six O anions at the corners and a TM ion at the centre. The gaps in between the  $(\text{MO}_2)_n$  sheets are occupied by Li atoms and are referred to as "Li layers".

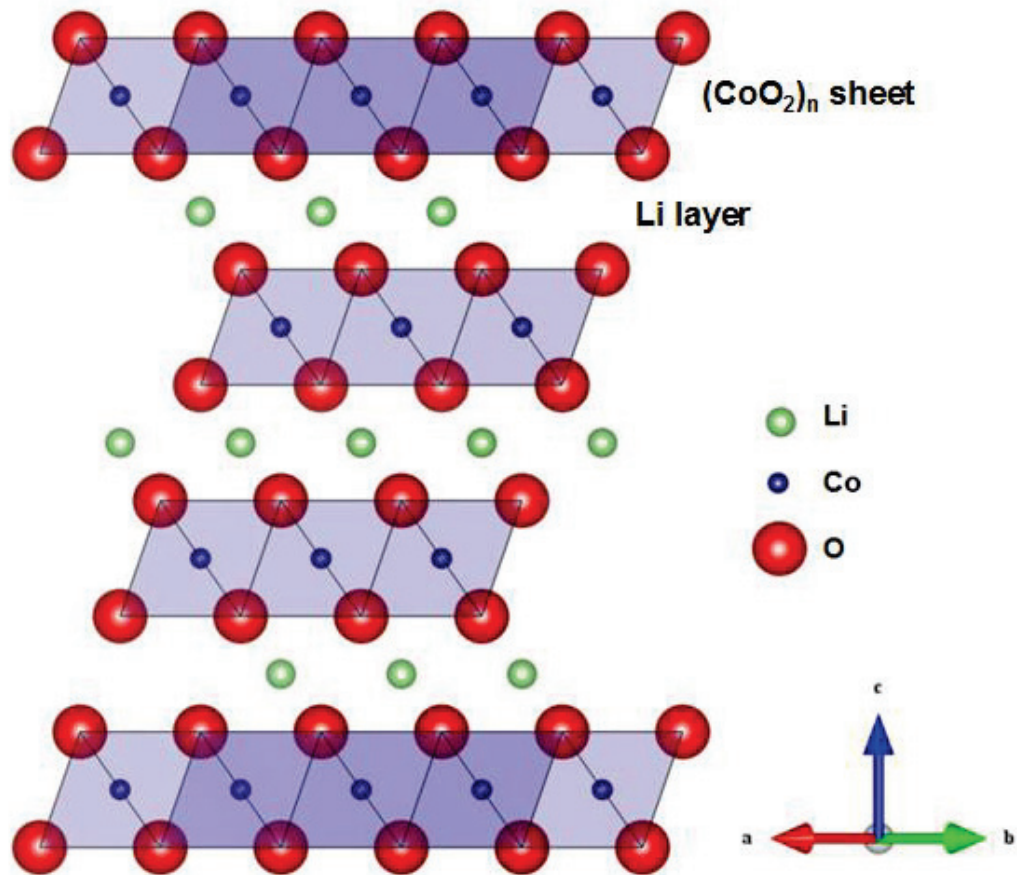


Figure 1.3 Crystal structure of LiCoO<sub>2</sub> projected along [110] plane

The stacking of (MO<sub>2</sub>)<sub>n</sub> sheets changes with the amount of Li and the nature of the M ion in order to minimize the repulsive effect between the (MO<sub>2</sub>)<sub>n</sub> sheets. Instead of octahedral (O) sites, Li atoms can occupy other types of sites such as prismatic (P) or tetrahedral (T) and LLTMO can form different polymorphs of a layered structure. Based on the Li<sup>+</sup> ion occupying sites (P or T or O) and the number of (MO<sub>2</sub>)<sub>n</sub> sheets within a unit cell, Delmas et al. classified the LLTMO materials and proposed a nomenclature<sup>19</sup> as explained in the following example. The LiCoO<sub>2</sub> structure shown in Figure 1.3 is defined as an O3 structure because the Li<sup>+</sup> ions occupy the octahedral (O) sites and there are 3

(MO<sub>2</sub>)<sub>n</sub> sheets before the periodicity repeats. Overall, the structure of LLTMO compounds should satisfy the following set of rules:

- The sequence of layers in the structure should be as follows: TM-O-Li-O-TM-O-Li-O-TM.....;
- The sum of the occupations of the metal atoms in the TM layer must be equal to one or less ;
- The total sum of the products of oxidation states and the corresponding occupancy of the metal atoms in the structure must be equal to four.

### 1.3.1 Li[M]O<sub>2</sub>

LLTMO materials with only one type of TM ion are represented by a general formula Li[M]O<sub>2</sub> where M represents a TM atom. LiCoO<sub>2</sub> is an example of Li[M]O<sub>2</sub> materials. As the difference in the ionic radii between Li<sup>+</sup> ions (0.76 Å) and Co<sup>3+</sup> ions (0.54 Å) is large, the chance of Li and Co exchanging sites (cation mixing) is small. Thus, LiCoO<sub>2</sub> exhibits a structure with ordered pure cationic layers. The theoretical capacity of LiCoO<sub>2</sub> is ~272 mAh/g. The high cost of Co, the toxic nature of Co and the thermal instability of Li<sub>x</sub>CoO<sub>2</sub> with electrolyte at high voltage especially at high temperatures are the main drawbacks of LiCoO<sub>2</sub>.

LiNiO<sub>2</sub> is comparably less toxic and cheaper than LiCoO<sub>2</sub> and so it was initially considered as a possible replacement for LiCoO<sub>2</sub><sup>20</sup>. However, synthesizing a pure layered LiNiO<sub>2</sub> structure is very difficult because of the exchange (cation mixing) between Ni<sup>2+</sup> ions in the TM layer and the Li<sup>+</sup> ions in the Li layer<sup>21</sup>. The cation mixing reduces the Li diffusion coefficient and is detrimental to the cell performance. The thermal instability of

delithiated  $\text{LiNiO}_2$  with electrolyte at temperatures  $> 130^\circ\text{C}$  also prevented the commercialization of  $\text{LiNiO}_2$ <sup>22</sup>.

Layered  $\text{LiMnO}_2$  was found to exhibit structural instability due to a small difference in the ionic radii between  $\text{Mn}^{3+}$  (0.65 Å) in the high spin environment and  $\text{Li}^+$  (0.76 Å). Attempts to synthesize layered  $\text{LiMnO}_2$  resulted in a thermodynamically more stable orthorhombic<sup>23</sup> form of  $\text{LiMnO}_2$ , which exhibits poor electrochemical performance. Metastable layered  $\text{LiMnO}_2$  was successfully synthesized from  $\text{NaMnO}_2$  through an ion-exchange method<sup>24</sup>. However, this O3 layered  $\text{LiMnO}_2$  transforms into spinel  $\text{LiMn}_2\text{O}_4$  upon Li deintercalation. The layered-to-spinel conversion was unstoppable because both lattices are built from the same network of oxygen anions and hence cationic migration to induce the transformation requires only very little energy. Paulsen et al. succeeded in synthesizing an O2 type  $\text{Li}_x\text{MnO}_2$ , which does not have a FCC oxygen lattice and does not convert to spinel<sup>25</sup>. However, this material failed to show improved electrochemical performance.

### 1.3.2 $\text{Li}[\text{M}^{\dagger}_x\text{M}^{\ddagger\dagger}_{1-x}]\text{O}_2$ (binary) and $\text{Li}[\text{M}^{\dagger}_x\text{M}^{\ddagger\dagger}_y\text{M}^{\ddagger\ddagger\dagger}_{1-x-y}]\text{O}_2$ (ternary)

A combination of two or three TM ions in the layered LLTMO structures has been considered in order to overcome the shortcomings of  $\text{Li}[\text{M}]\text{O}_2$  materials with only one TM.  $\text{LiNiO}_2$  forms a solid solution with  $\text{LiCoO}_2$  and so  $\text{LiNi}_x\text{Co}_{1-x}\text{O}_2$  was considered extensively by several researchers, particularly the research group led by Delmas<sup>26</sup>. The substitution of  $\text{Co}^{3+}$  ions in the place of  $\text{Ni}^{3+}$  ions led to decreased cation mixing between the Li and TM layers and caused better electrochemical performance. Moreover, the capacity of  $\text{LiNi}_x\text{Co}_{1-x}\text{O}_2$  is higher than  $\text{LiCoO}_2$  but its capacity fading on repeated cycling make  $\text{LiNi}_x\text{Co}_{1-x}\text{O}_2$  undesirable<sup>22</sup>.

On the other hand,  $\text{Al}^{3+}$  substitution for  $\text{Ni}^{3+}$  resulted in improved thermal stability of the electrodes<sup>27</sup>. It also increased structural stability owing to a stronger Al-O bond vs. Ni-O bond<sup>28,29</sup>. Despite the loss of gravimetric capacity due to the addition of electrochemically inactive  $\text{Al}^{3+}$ , its beneficial properties to the cell performance were attractive. The simultaneous substitution of  $\text{Co}^{3+}$  and  $\text{Al}^{3+}$  for  $\text{Ni}^{3+}$  offered better layered structural stability and improved thermal stability<sup>30</sup>, respectively, leading to the success of lithium nickel cobalt aluminum oxides ( $\text{Li}[\text{Ni}_x\text{Co}_y\text{Al}_{1-x-y}]\text{O}_2$ ), often called NCA materials. The composition  $\text{Li}[\text{Ni}_{0.8}\text{Co}_{0.15}\text{Al}_{0.05}]\text{O}_2$  is one of the most successful NCA materials because of its excellent balance between energy, cost and safety. It exhibits a gravimetric capacity of  $\sim 200$  mAh/g to 4.2 V with excellent thermal stability<sup>31</sup>.

Figure 1.4 shows a pseudo-ternary composition diagram/triangle formed with  $\text{LiCoO}_2$ ,  $\text{LiNiO}_2$  and  $\text{LiMnO}_2$  at the vertices. The ternary system is strictly based on three components: LiCo, LiNi and LiMn and does not take into account O as a component. Hence the ternary system is referred to as “pseudo-ternary” system<sup>32</sup>. The sides of the triangle represent  $\text{Li}[\text{M}^\dagger_x\text{M}^{\ddagger\dagger}_{1-x}]\text{O}_2$  (binary) materials and any point in the interior of the triangle represents a  $\text{Li}[\text{M}^\dagger_x\text{M}^{\ddagger\dagger}_y\text{M}^{\ddagger\ddagger}_{1-x-y}]\text{O}_2$  (ternary) compound. The symbols  $\text{M}^\dagger$ ,  $\text{M}^{\ddagger\dagger}$ , and  $\text{M}^{\ddagger\ddagger}$  in the formula units represent Ni or Mn or Co ions.

The combination of Ni and Mn resulted in the  $\text{Li}[\text{Ni}_x\text{Mn}_{1-x}]\text{O}_2$  solid-solution series and the most-studied composition in this series is  $\text{LiNi}_{0.5}\text{Mn}_{0.5}\text{O}_2$ <sup>33</sup>. Figure 1.4 shows  $\text{LiNi}_{0.5}\text{Mn}_{0.5}\text{O}_2$  as the mid-point of the line joining  $\text{LiNiO}_2$  and  $\text{LiMnO}_2$ . The material  $\text{LiNi}_{0.5}\text{Mn}_{0.5}\text{O}_2$  has been claimed to deliver a capacity of  $\sim 200$  mAh/g with low irreversible capacity and small polarization<sup>33</sup>. However, the difficulty in synthesizing pure material without cation mixing makes  $\text{LiNi}_{0.5}\text{Mn}_{0.5}\text{O}_2$  unattractive<sup>34</sup>. Zhou et al. showed

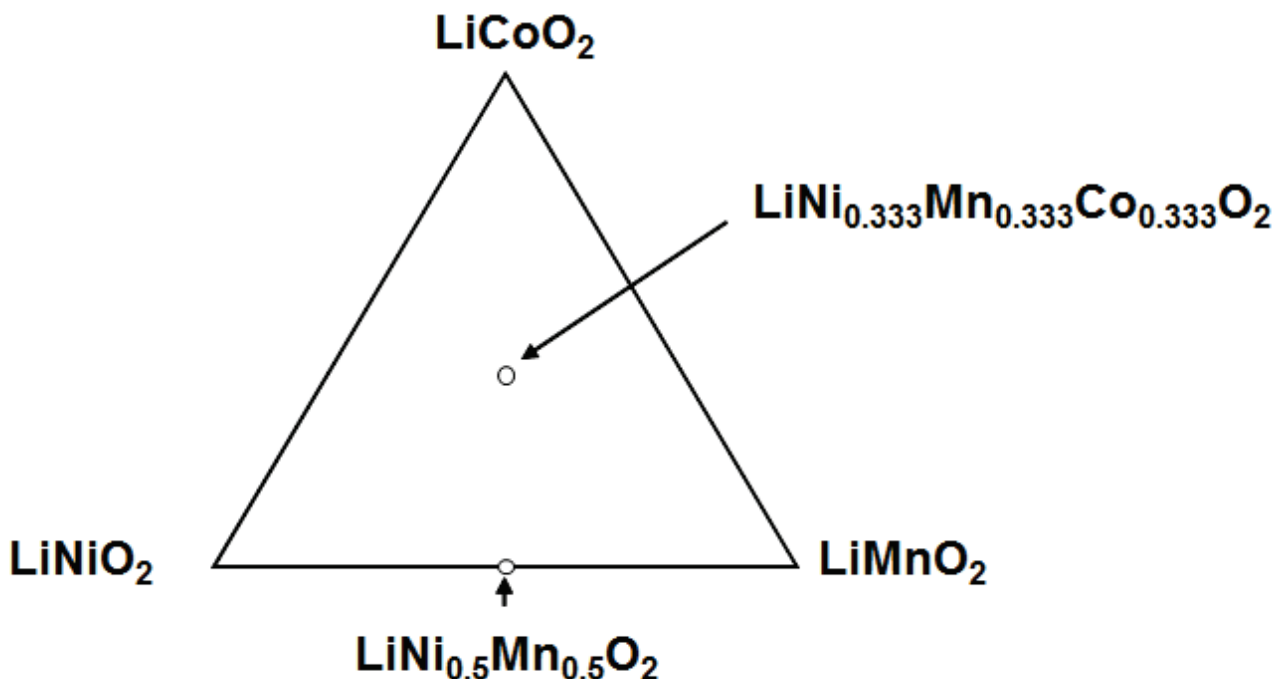


Figure 1.4 Pseudo-ternary composition diagram for LiNiO<sub>2</sub>-LiMnO<sub>2</sub>-LiCoO<sub>2</sub> system

that LiNi<sub>0.666</sub>Mn<sub>0.333</sub>O<sub>2</sub> could deliver a reversible capacity  $\sim 190$  mAh/g<sup>35</sup> but its inferior thermal stability and poor cycle life at elevated temperature was unsatisfactory.

Recently, McCalla et al. mapped the whole Li-Ni-Mn-O pseudo-ternary system and identified different thermodynamically-stable Li-Ni-Mn-O phases under different synthesis conditions<sup>36</sup>. Following that, the electrochemical behavior of a variety of Li-Ni-Mn-O compounds was surveyed by Li et al<sup>37</sup>. They confirmed that the presence of an impure phase such as a rock-salt phase along with a pure layered phase is detrimental for the cell performance.

The research group led by Ohzuku did a systematic research on intercalation materials in the LiCoO<sub>2</sub>-LiNiO<sub>2</sub>-LiMnO<sub>2</sub> pseudo-ternary system using first principles calculations<sup>38</sup>. They proposed that LiCoO<sub>2</sub> is immiscible with LiMnO<sub>2</sub> and does not form a solid solution. By contrast, LiCo<sub>x</sub>Mn<sub>1-x</sub>O<sub>2</sub> has been prepared by some researchers and a



reversible capacity  $\sim 130$  mAh/g was shown but with poor cycle life<sup>39</sup>. Thus the LiCoO<sub>2</sub>-LiMnO<sub>2</sub> combination has received very little attention.

The combination of LiNiO<sub>2</sub>-LiMnO<sub>2</sub>-LiCoO<sub>2</sub> can lead to a group of compounds with varying Ni-Mn-Co compositions to form the solid solution series Li[Ni<sub>x</sub>Mn<sub>y</sub>Co<sub>1-x-y</sub>]O<sub>2</sub> often called as NMC compounds. Among the various members of this series, Li[Ni<sub>1/3</sub>Mn<sub>1/3</sub>Co<sub>1/3</sub>]O<sub>2</sub> has been studied extensively<sup>40</sup> and has been commercialized. In Figure 1.4, the centroid of the equilateral triangle represents the composition Li[Ni<sub>1/3</sub>Mn<sub>1/3</sub>Co<sub>1/3</sub>]O<sub>2</sub>.

In Li[Ni<sub>0.333</sub>Mn<sub>0.333</sub>Co<sub>0.333</sub>]O<sub>2</sub>, Ni in its +2 oxidation state and Co in its +3 state are involved in the electrochemical activity. Mn remains unaffected in the +4 oxidation state during the charge and discharge. Similar to LiCoO<sub>2</sub>, Li[Ni<sub>0.333</sub>Mn<sub>0.333</sub>Co<sub>0.333</sub>]O<sub>2</sub> exhibits an O3 structure<sup>41</sup> and can be defined using the *R-3m* spacegroup. It has been shown to deliver a reversible capacity  $\sim 150$  mAh/g, when cycled between 2.5 to 4.2 V. Li[Ni<sub>0.333</sub>Mn<sub>0.333</sub>Co<sub>0.333</sub>]O<sub>2</sub> exhibits excellent safety characteristics compared to LiCoO<sub>2</sub><sup>30</sup>. Lower cost, comparable capacity and excellent cycling behavior under certain upper cut-off voltages and in particular better safety makes Li[Ni<sub>0.333</sub>Mn<sub>0.333</sub>Co<sub>0.333</sub>]O<sub>2</sub> an attractive positive electrode material. In addition to Li[Ni<sub>0.333</sub>Mn<sub>0.333</sub>Co<sub>0.333</sub>]O<sub>2</sub>, compositions such as LiNi<sub>0.4</sub>Mn<sub>0.4</sub>Co<sub>0.2</sub>O<sub>2</sub>, LiNi<sub>0.5</sub>Mn<sub>0.3</sub>Co<sub>0.2</sub>O<sub>2</sub>, and LiNi<sub>0.8</sub>Mn<sub>0.1</sub>Co<sub>0.1</sub>O<sub>2</sub> have also been studied by many researchers.

### 1.3.3 Layered lithium-rich transition metal oxides (LLRTMO)

Layered lithium-rich transition metal oxides (LLRTMO) are excessively-lithiated compounds that can be theoretically derived from the LLTMO compounds. When Li<sup>+</sup> ions completely fill the Li layer and if excess Li<sup>+</sup> ions occupy the TM layer, LLRTMO

materials result (e.g.  $\text{Li}[\text{Li}_{0.2}\text{Ni}_{0.2}\text{Mn}_{0.6}]\text{O}_2$ ). LLRTMO materials can deliver a reversible specific capacity  $> 250 \text{ mAh/g}^{42}$ .

### 1.3.3.1 $\text{Li}_2\text{MnO}_3$

The compound  $\text{Li}_2\text{MnO}_3$  is an ideal example for a LLRTMO material and could be considered as a model compound to describe the structure of LLRTMO materials. The formula unit of  $\text{Li}_2\text{MnO}_3$  can also be written as  $\text{Li}[\text{Li}_{1/3}\text{Mn}_{2/3}]\text{O}_2$  for conveniently interpreting the structure in the form of  $\text{Li}[\text{M}]\text{O}_2$ . In the formula unit of  $\text{Li}[\text{Li}_{0.333}\text{Mn}_{0.666}]\text{O}_2$  or any other LLRTMO, the ions denoted in the parenthesis represent TM layer cations. As such,  $\frac{1}{4}$  of the  $\text{Li}^+$  ions per formula unit of  $\text{Li}[\text{Li}_{1/3}\text{Mn}_{2/3}]\text{O}_2$  are in the TM layer and the Li/TM ratio is equal to 2 and is always greater than 1 for LLRTMO materials.

Figure 1.5 shows the structure of  $\text{Li}[\text{Li}_{0.333}\text{Mn}_{0.666}]\text{O}_2$  projected along (110) direction.  $\text{Li}[\text{Li}_{0.333}\text{Mn}_{0.666}]\text{O}_2$  as well as other LLRTMO materials adopt the  $\text{O3}$  structure and can be described in a monoclinic system using the  $C2/m$  space group<sup>43</sup>. The  $\text{Mn}^{4+}$  ions and  $\text{Li}^+$  ions order in the TM layers in such a way that each  $\text{Li}^+$  ion is encircled in the plane by 6  $\text{Mn}^{4+}$  ions (honeycomb pattern) and form a superlattice<sup>44,45</sup>. The right panel in Figure 1.5 shows the superlattice ordering between  $\text{Mn}^{4+}$  ions and  $\text{Li}^+$  ions. Compared to LLTMO materials such as  $\text{LiCoO}_2$ , the occurrence of in-plane ordering in  $\text{Li}_2\text{MnO}_3$  and the resultant superlattice formation change the symmetry from  $R-3m$  to  $C2/m$ . A detailed discussion on the superlattice ordering in LLRTMO materials and its implications will be given in Chapter 3.

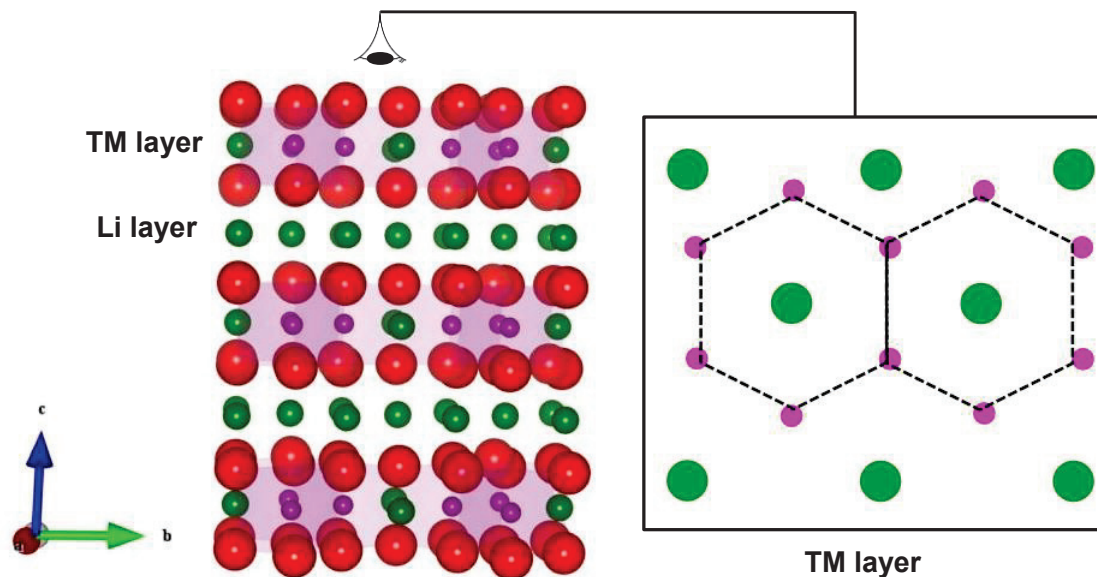


Figure 1.5 Structure of  $\text{Li}_2\text{MnO}_3$  ( $\text{Li}[\text{Li}_{1/3}\text{Mn}_{2/3}]\text{O}_2$ ) projected along (100) (left) direction and the superlattice ordering between  $\text{Mn}^{4+}$  ions and  $\text{Li}^+$  ions from (001) direction (right) (Green and Magenta colored balls represent  $\text{Li}^+$  and  $\text{Mn}^{4+}$  ions)

### 1.3.3.2 Structure of layered lithium-rich transition metal oxides

The crystallographic nature of LLRTMO materials has been under much debate. One set of researchers<sup>46,47</sup>, championed by Thackeray et al., believe that the LLRTMO materials are composite materials made up of domains of layered  $\text{Li}[\text{M}]\text{O}_2$  and  $\text{Li}_2\text{MnO}_3$ . So, they use the notation:  $x\text{Li}_2\text{MnO}_3 \cdot (1-x)\text{Li}[\text{M}]\text{O}_2$ <sup>46</sup> to define the materials in composite formalism. Conversely, a second set of researchers considers LLRTMO materials as layered solid solutions<sup>48,44,49</sup> formed by  $\text{Li}[\text{M}]\text{O}_2$  and  $\text{Li}_2\text{MnO}_3$  materials. Therefore, according to solid-solution nomenclature, certain LLRTMO materials are represented using a formula such as  $\text{Li}[\text{Li}_{1/3-2x/3}\text{Ni}_x\text{Mn}_{2/3-x/3}]\text{O}_2$ . For example, the composition  $\text{Li}_{1.2}\text{Ni}_{0.2}\text{Mn}_{0.6}\text{O}_2$  can be represented as  $\text{Li}[\text{Li}_{0.2}\text{Ni}_{0.2}\text{Mn}_{0.6}]\text{O}_2$  in the solid solution notation or as  $0.6\text{Li}_2\text{MnO}_3 \cdot 0.4\text{Li}[\text{Ni}_{0.5}\text{Mn}_{0.5}]\text{O}_2$  in the composite representation.

Figure 1.6 shows the X-ray diffraction (XRD) pattern of  $\text{Li}[\text{Li}_{0.2}\text{Ni}_{0.2}\text{Mn}_{0.6}]\text{O}_2$ . According to the solid solution perspective, as proved in this thesis, the peaks (indicated using a red box in Figure 1.6) around  $20\text{-}35^\circ$  in the XRD data are caused by superlattice ordering of  $\text{Li}^+$  and  $\text{Mn}^{4+}$  ions<sup>50</sup>. Hence all the peaks can be indexed using  $C2/m$  spacegroup. By contrast, in the composite view, those peaks correspond to nano-domains of a  $\text{Li}_2\text{MnO}_3$  phase embedded within the matrix of layered  $\text{LiMO}_2$  and hence two space groups corresponding to two phases are required to explain the XRD pattern. According to the composite believers, the broad superlattice peaks are caused by nano-domains but solid-solution supporters argue that stacking faults are the underlying reason for the

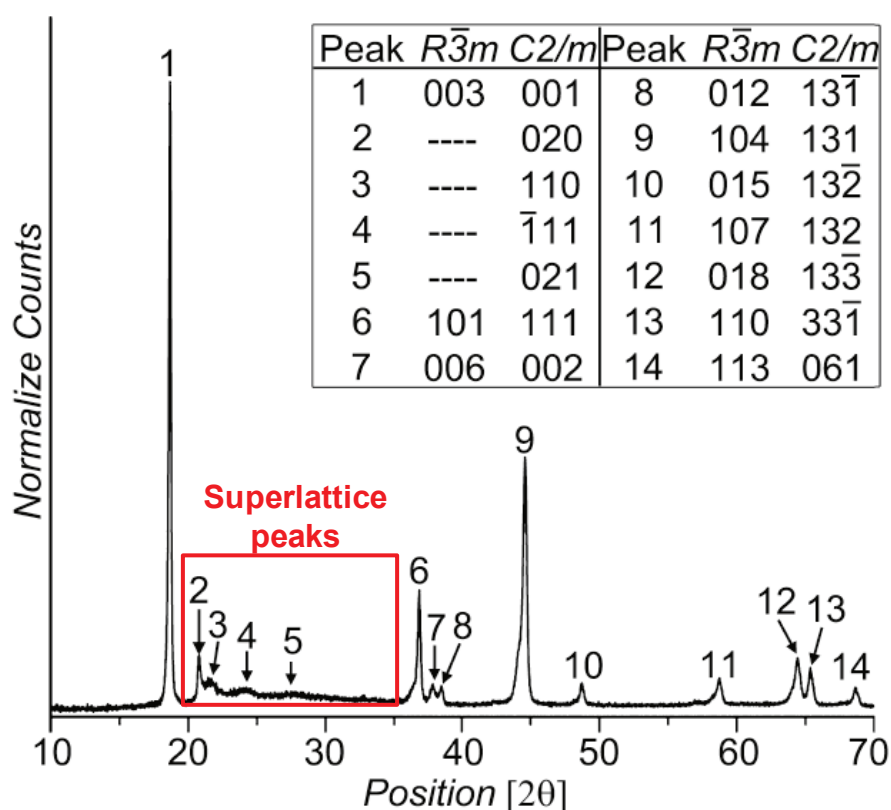


Figure 1.6 XRD pattern of  $\text{Li}[\text{Li}_{0.2}\text{Ni}_{0.2}\text{Mn}_{0.6}]\text{O}_2$ .  
Adapted with permission from (*Chem. Mater.*, 2011, 23 (16), pp 3614–3621)  
Copyright (2011) American Chemical Society

broadness<sup>51</sup>. It will be proved in this thesis that stacking faults can explain the broad superlattice peaks.

Jarvis et al. have studied the atomic structure of  $\text{Li}[\text{Li}_{0.2}\text{Ni}_{0.2}\text{Mn}_{0.6}]\text{O}_2$  and reported that it was a single phase solid solution with  $C2/m$  monoclinic symmetry<sup>44</sup>. Bareno et al. through their TEM study reported that such materials are composed of nano-domains of layered  $\text{LiMO}_2$  and monoclinic  $\text{Li}_2\text{MnO}_3$ <sup>52</sup>. By contrast, another careful TEM study done by Shukla et al on LLRTMO samples proved the solid-solution behavior<sup>49</sup>. The formation of a solid solution between  $\text{Li}_2\text{MnO}_3$  and  $\text{LiMO}_2$ , which have the same close-packed oxygen structure, appears to be more representative and the same consideration is followed in this thesis as well. Results supporting solid-solution<sup>51</sup> behavior of the LLRTMO materials will be discussed in Chapter 3.

### 1.3.3.3 First charge-discharge cycle of layered lithium-rich transition metal oxides

Figure 1.7 shows the charge-discharge profile of a LLRTMO material:  $\text{Li}_{1.200}\text{Mn}_{0.533}\text{Co}_{0.133}\text{Ni}_{0.133}\text{O}_2$ <sup>53</sup>. During first charge (red line), it exhibits a step-wise voltage profile that includes a sloping part (region 1) from OCV to  $\sim 4.5$  V vs  $\text{Li}/\text{Li}^+$ , an irreversible plateau part (region 2) around 4.5 V and a brief sloping part (region 3). By contrast, the first discharge profile and the subsequent charge-discharge profiles are different from the first-charge profile but somewhat similar to that of any non-Li-rich layered material such as  $\text{Li}[\text{Ni}_{0.333}\text{Mn}_{0.333}\text{Co}_{0.333}]\text{O}_2$ .

The sloping part (Region 1) is believed to be caused by the electrochemical oxidation of TM ions<sup>54</sup>. The amount of maximum  $\text{Li}^+$  ions that can be extracted through TM redox is normally equal to the sum of the redox electrons available in the TM ions. In

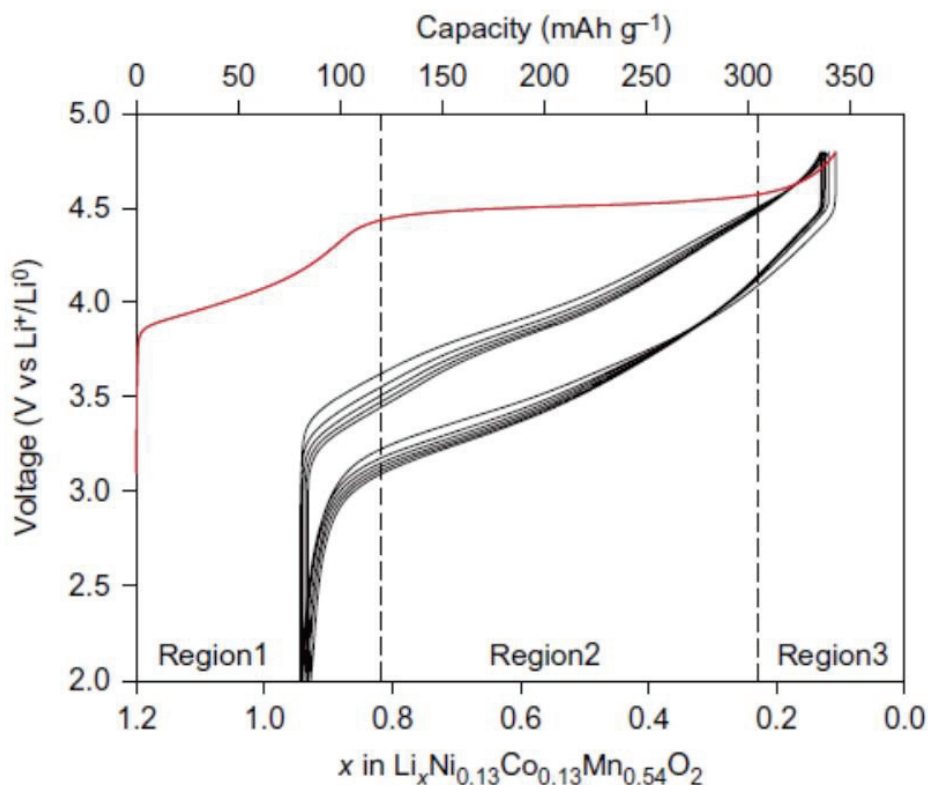


Figure 1.7 Voltage-specific capacity profile of  $\text{Li}_{1.200}\text{Mn}_{0.533}\text{Co}_{0.133}\text{Ni}_{0.133}\text{O}_2$   
 Reprinted with permission from (*Nature Chemistry* **8**, 684-691 (2016))  
 Copyright (2016) Nature Publishing group

LLRTMO materials, the most common oxidation states of Mn, Ni and Co are +4, +2 and +3 respectively<sup>53,55</sup>. In  $\text{Li}_{1.200}\text{Mn}_{0.533}\text{Co}_{0.133}\text{Ni}_{0.133}\text{O}_2$ , Ni can be oxidized from +2 to +4 and Co can be oxidized to +3 to +4 oxidation state. However, Mn, which is in +4 oxidation state, remains as such and cannot be oxidized further in the given structure. So, the TM redox extractable Li and the corresponding TM redox capacity for  $\text{Li}_{1.2}\text{Mn}_{0.53}\text{Co}_{0.13}\text{Ni}_{0.13}\text{O}_2$  is calculated as follows:

$$\begin{aligned} \text{TM redox extractable Li} &= 0.133 \times 2 + 0.133 \times 1 = 0.4 \\ \text{TM redox capacity} &= \frac{0.4 \times 26800 \text{ mAh mol}^{-1}}{85 \text{ g mol}^{-1}} = 126 \text{ mAh g}^{-1} \end{aligned} \quad (1.7)$$

This calculated TM redox capacity ( $126 \text{ mAhg}^{-1}$ ) corresponds to the Region 1 capacity in Figure 1.7. However, LLRTMO materials exhibit a total first charge capacity  $> 300 \text{ mAh/g}^{48}$ . This implies that  $\text{Li}^+$  ions can be extracted from the material beyond the TM redox limitations and the accessibility of this extra capacity makes these LLRTMO materials more attractive.

The irreversible plateau around 4.5 V (Region 2 in Figure 1.7) was found to be associated with an irreversible loss of oxygen<sup>56</sup>. Lu et al., through their *in-situ* XRD studies on  $\text{Li}[\text{Li}_{1/3-2x/3}\text{Ni}_x\text{Mn}_{2/3-x/3}]\text{O}_2$  materials, have proposed the simultaneous release of O and Li along 4.5 V plateau<sup>57</sup>. The release of  $\text{O}_2$  gas from  $\text{Li}[\text{Li}_{0.2}\text{Ni}_{0.2}\text{Mn}_{0.6}]\text{O}_2$  during first charge was later confirmed by Armstrong et al. by using *in-situ* differential electrochemical mass spectrometry (DEMS)<sup>56</sup>. Lu et al. also concluded that the irreversible loss of oxygen resulted in the formation of an oxygen-deficient layered compound at the end of the first charge<sup>57</sup>. The oxygen deficient layered compound reacts with lithium reversibly in the subsequent cycles with the continuous involvement of  $\text{Mn}^{4+}$  to  $\text{Mn}^{3+}$  reduction<sup>58</sup>.

The concomitant oxygen loss with the extraction of Li along the 4.5 V plateau is required in order to maintain the oxidation state balance in the compound. However, a large irreversible capacity loss (IRC) is associated with the irreversible oxygen loss<sup>59,57</sup>. Chapter 4 will discuss one of the several but useful ways to reduce the IRC<sup>60,61</sup> of LLRTMO materials. After the first charge, the subsequent discharge/charge cycles deliver a reversible capacity as large as  $240 \text{ mAh/g}$ . Thus, the intercalation/deintercalation mechanism in the first charge-discharge cycle of LLRTMO materials is unique compared to other layered materials.

Armstrong et al. have done neutron diffraction studies on  $[\text{Li}_{0.2}\text{Ni}_{0.2}\text{Mn}_{0.6}]\text{O}_2$  and proposed that the O loss occurs at the surface and induces the migration of TM ions from the bulk to the surface<sup>56</sup>. Subsequently, Jiang et al. claimed the formation of a second phase during cycling in the high voltage region<sup>62</sup>. Recently, Koga et al. have proposed a similar mechanism for the first-cycle lithium deintercalation/intercalation of  $\text{Li}_{1.200}\text{Mn}_{0.533}\text{Co}_{0.133}\text{Ni}_{0.133}\text{O}_2$ <sup>63</sup>. From detailed XRD and electrochemical analyses, they suggested an evolution of a mixture of two phases (surface and bulk) along the 4.5 V plateau during the first charge<sup>64</sup>. This has been recently confirmed by Li et al., and Luo et al. through *in-situ* XRD studies performed on Mn-rich LLRTMO materials<sup>65</sup>.

Ohzuku et al. reported several possibilities for first-cycle extra capacity and they suggested that the capacity along the 4.5 V plateau might also involve mechanisms such as oxidation of  $\text{Mn}^{4+}$  to  $\text{Mn}^{5+}$  or  $\text{O}^{2-}$  to  $\text{O}^-$ <sup>66</sup>. C. Genevois et al. have demonstrated the occurrence of reversible oxidation of oxygen ( $\text{O}^{2-}$  to  $\text{O}^-$ ) in the bulk and oxygen release at the surface<sup>67</sup>. A recent study by Luo et al. on  $\text{Li}_{1.200}\text{Mn}_{0.533}\text{Co}_{0.133}\text{Ni}_{0.133}\text{O}_2$  claims that  $\text{O}_2^{2-}$  species do not form in 3d-TM-based LLRTMO materials but instead the charge compensation is satisfied by the formation of electron holes on the O ions<sup>53</sup>.

Understanding the oxygen redox behavior of NMC-based LLRTMO materials seems to be quite complicated due to the presence of three redox centers (Ni, Mn and Co) and the associated complex chemistry. Hence, Sathiya et al. have explored 4d-TM-based LLRTMO materials with a single redox center (Ru) such as  $\text{Li}_2\text{Ru}_{1-y}\text{Sn}_y\text{O}_3$  and demonstrated that the involvement of anionic (oxygen) redox activity is the key to the mechanism accounting for the extra capacity of LLRTMO materials<sup>68</sup>. The formation of peroxo-like  $(\text{O}_2)^{n-}$  species as a result of oxygen redox activity was experimentally



evidenced through X-ray photoelectron spectroscopy (XPS) and electron-paramagnetic resonance (EPR) studies<sup>69</sup>. McCalla et al. reported the identification and visualization of O-O dimers resulting from the reversible oxygen redox in  $\text{Li}_2\text{IrO}_3$  through TEM and neutron studies<sup>70</sup>. Recently, Seo et al. explained the structural and chemical origin of the oxygen redox activity in LLRTMO materials on the basis of specific local Li-excess environments around oxygen.

Despite the richness of oxygen-redox chemistry, which could mitigate issues such as progressive voltage fade, 4d-TM-based LLRTMO materials are commercially unpopular due to their increased cost. By contrast, NMC-based LLRTMO materials are cheaper and they could be commercially valuable if their first charge-discharge issues are well understood and resolved. The three major flaws associated with NMC-based LLRTMO materials are: (i) high irreversible capacity loss (IRC) during the first cycle<sup>71</sup>, (ii) progressive voltage fade<sup>72</sup> with cycling and (iii) poor rate capability<sup>73</sup>. Apparently, the high IRC and the voltage fade issues are associated with the reactions occurring during first charge-discharge cycle. The chemistry behind the first charge-discharge properties of the LLRTMO appears to be very significant as it appears to determine the properties of the subsequent cycling performance. Hence the main motivation of this thesis work was to increase the understanding of the first charge-discharge properties of the NMC-based LLRTMO materials.

#### **1.4 Scope of this thesis**

Chapter 2 is devoted to the experimental methods and techniques used in this research. Studying the structural characteristics of some LLRTMO materials is essential to improve their physical and electrochemical properties. Hence the structural

characterization of LLRTMO materials with special emphasis on stacking faults will be discussed in Chapter 3. Chapter 4 will discuss the results of a study of the effect of Li content on the properties of LLRTMO materials and the identification of a new type of LLRTMO materials that exhibit low-IRC. Based on the preliminary results of the low-IRC materials, a search for low-IRC materials in the Li-Ni-Mn-Co pseudo-quaternary system has been done and Chapter 5 will give a summary of that survey. The low-IRC materials were found to contain inherent metal-site vacancies. Chapter 6 will discuss the results of solid-state NMR studies performed on some low-IRC materials that have metal-site vacancies. Chapter 6 also attempts to probe the reasons for the high-IRC behavior in LLRTMO and the correlation with the low-IRC behavior observed in some other LLRTMO. Finally, Chapter 7 will summarize the completed work done for this thesis and suggest some future work that can be continued on the lines of this thesis work.

## Chapter 2 Experimental

This chapter gives a description of the experimental methods and characterization techniques used in this research work. They include materials synthesis, structural characterization and electrochemical characterization. Experimental methods or techniques that are used for any specific investigation will be given in appropriate sections.

### 2.1 Materials synthesis

The synthesis procedures of layered lithium-rich transition metal oxides (LLRTMO), the positive electrode materials of interest, are explained in the following sections. The synthesis of LLRTMO consists of two steps. First, precursors such as transition metal (TM) carbonates (*e.g.*  $\text{Ni}_{0.25}\text{Mn}_{0.75}\text{CO}_3$ ) or hydroxides (*e.g.*  $\text{Ni}_{0.2}\text{Mn}_{0.5}\text{Co}_{0.3}(\text{OH})_2$ ) were synthesized by co-precipitation. Second, the synthesized precursors were mixed with a lithium source such as lithium hydroxide (LiOH) and were converted to LLRTMO through high temperature solid-state synthesis. All the positive electrode materials studied in this work were made from mixed TM carbonate precursors. Hence co-precipitation synthesis of TM carbonates is explained here and the method to prepare TM hydroxides can be found elsewhere<sup>74, 75</sup>.

#### 2.1.1 Co-precipitation synthesis of mixed transition metal carbonates

A variety of Ni-Mn and Ni-Mn-Co carbonates, represented by  $\text{Ni}_x\text{Mn}_y\text{Co}_{1-x-y}\text{CO}_3$ , were synthesized by co-precipitation using a continuously-stirring tank reactor (CSTR). Figure 2.1 shows a schematic of a CSTR. The CSTR has a 2L jacketed glass vessel (reaction chamber) with a metal lid at the top and an overhead stirrer at the center. Hot or

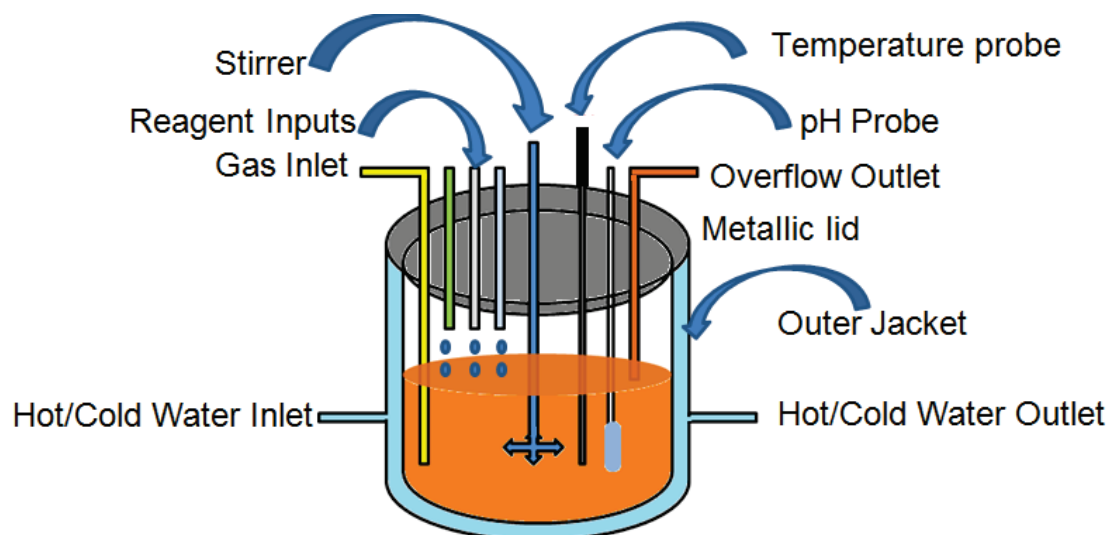


Figure 2.1 Schematic of a continuously-stirring tank reactor

cold water flows in an outer glass jacket continuously to maintain a desired uniform temperature in the reaction chamber. The metal lid at the top of the reaction vessel has several inlets and outlets for reagent addition, product recovery, gas flow and for probes for pH and temperature measurements. The stirrer is attached to a motor, which can rotate the stirrer up to 1000 rpm .

The CSTR is also equipped with sensors for measuring pH, temperature and gas flow. Optimization of reaction conditions such as pH and temperature is necessary to obtain desired particle morphology. For example, Zhou et al.<sup>74</sup> have optimized the conditions to make spherical particles of Ni-Mn hydroxides with high tap density using a CSTR. They found that setting the temperature to 60°C, pH to ~11 and using NH<sub>4</sub>OH as a chelating agent are good conditions for making spherical Ni-Mn mixed hydroxide particles. Using the synthesis conditions reported by Zhou et al., Ni-Mn-Co hydroxide particles having a tap density > 2.0 g/cm<sup>3</sup> were successfully synthesized by Van Bommel et al.<sup>75</sup> Similar reaction conditions except for the concentration of NH<sub>4</sub>OH were used for

the synthesis of  $\text{Ni}_x\text{Mn}_y\text{Co}_{1-x-y}\text{CO}_3$ . Figure 2.2 shows a picture of the CSTR that was used for the co-precipitation synthesis.



Figure 2.2 Continuously-stirring tank reactor

Co-precipitation synthesis of  $\text{Ni}_x\text{Mn}_y\text{Co}_{1-x-y}\text{CO}_3$  involved mixing aqueous solutions of carbonate precipitants (*e.g.* sodium carbonate ( $\text{Na}_2\text{CO}_3$ )) and the TM salts such as mixed TM sulfates (*e.g.*  $\text{Ni}_{0.2}\text{Mn}_{0.5}\text{Co}_{0.3}\text{SO}_4$ ) in a CSTR. The reaction during co-precipitation synthesis of  $\text{Ni}_{0.2}\text{Mn}_{0.5}\text{Co}_{0.3}\text{CO}_3$  is



A 2M aqueous solution of mixed Ni-Mn sulfates was prepared by dissolving appropriate amounts of  $\text{MnSO}_4 \cdot \text{H}_2\text{O}$  (99.0 %, Alfa Aesar),  $\text{NiSO}_4 \cdot 6\text{H}_2\text{O}$  (98.0 %, Alfa Aesar) and  $\text{CoSO}_4 \cdot 7\text{H}_2\text{O}$  (98.0 %, Alfa Aesar) salts in distilled water. In the same way, aqueous solutions of 2M  $\text{Na}_2\text{CO}_3$  (98.0 %, Alfa Aesar) and 0.2 M  $\text{NH}_4\text{OH}$  (28.0 – 30 %, Caledon Laboratory Chemicals) were also prepared. The  $\text{NH}_4\text{OH}$  solution supplied  $\text{NH}_4^+$  ions, which can coordinate TM ions to facilitate the formation of spherical particles at appropriate pH conditions. Van Bommel et al. showed the importance of using ammonia as a coordinating agent to obtain spherical  $\text{Ni}_x\text{Mn}_y\text{Co}_{1-x-y}(\text{OH})_2$ <sup>75</sup>.

In a typical co-precipitation reaction, 0.2 M  $\text{NH}_4\text{OH}$  was used as the initial solution in the reaction vessel. Then solutions of mixed  $\text{Ni}_{0.2}\text{Mn}_{0.5}\text{Co}_{0.3}\text{SO}_4$  and  $\text{Na}_2\text{CO}_3$  were simultaneously fed into the reaction vessel using separate digital peristaltic pumps (Masterflex L/S 07524) at a desired flow rate, usually 0.3 mL/min, for about 20 h. The pH was controlled at 8 by a pH sensor that can trigger the automatic addition of 0.2 M  $\text{H}_2\text{SO}_4$  (95.0-98.0 %, Sigma-Aldrich) or 5M  $\text{NaOH}$  (98.0 % Alfa Aesar) into the reaction vessel as needed. The temperature was maintained as 60°C all through the reaction. After completion of the co-precipitation reaction, the resulting suspension was collected and washed several times with distilled water to remove impurities. Then it was filtered and the resulting wet precipitate was dried in an oven at 100-120°C for about 12 hours. The dried  $\text{Ni}_{0.2}\text{Mn}_{0.5}\text{Co}_{0.3}\text{CO}_3$  powder was recovered and stored for further investigation.

### **2.1.2 Synthesis of layered lithium transition metal oxides**

LLRTMO were synthesized using solid-state methods. The synthesis of  $\text{Li}[\text{Li}_{0.130}\text{Ni}_{0.174}\text{Mn}_{0.435}\text{Co}_{0.261}]\text{O}_2$  from a  $\text{Ni}_{0.2}\text{Mn}_{0.5}\text{Co}_{0.3}\text{CO}_3$  precursor and  $\text{Li}_2\text{CO}_3$  (99.0

%, Sigma-Aldrich) is explained here. The reaction for the formation of 1 mole of  $\text{Li}[\text{Li}_{0.130}\text{Ni}_{0.174}\text{Mn}_{0.435}\text{Co}_{0.261}]\text{O}_2$  is

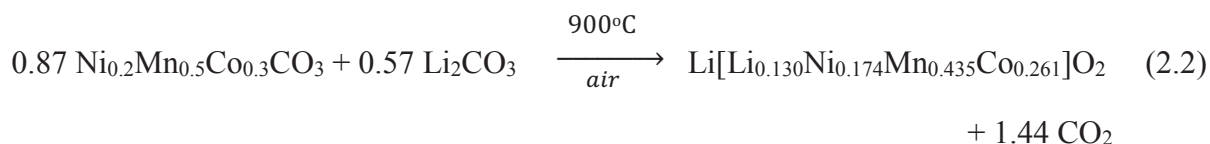


Table 2.1 shows the calculation of stoichiometric amounts (mass) of the  $\text{Ni}_{0.2}\text{Mn}_{0.5}\text{Co}_{0.3}\text{CO}_3$  precursor and  $\text{Li}_2\text{CO}_3$  required for that synthesis. The calculated amounts of  $\text{Ni}_{0.2}\text{Mn}_{0.5}\text{Co}_{0.3}\text{CO}_3$  and  $\text{Li}_2\text{CO}_3$  powders were thoroughly mixed using an agate mortar and pestle. The mixed powders were loaded in an alumina boat and fired in a furnace at  $900^\circ\text{C}$  in air for about 12 h.

Table 2.1 Calculation of stoichiometric amounts of precursors needed for the synthesis of  $\text{Li}[\text{Li}_{0.130}\text{Ni}_{0.174}\text{Mn}_{0.435}\text{Co}_{0.261}]\text{O}_2$

	$\text{Ni}_{0.2}\text{Mn}_{0.5}\text{Co}_{0.3}\text{CO}_3$	$\text{Li}_2\text{CO}_3$	$\text{Li}[\text{Li}_{0.130}\text{Ni}_{0.174}\text{Mn}_{0.435}\text{Co}_{0.261}]\text{O}_2$
Stoichiometric No. of moles	0.87	0.57	1
Molar mass (g/mol)	116.89	73.89	89.31
Stoichiometric Mass (g/mol)	101.64	41.76	89.31
Required mass for 5g product (g)	5.70	2.34	5

Figure 2.3 shows the temperature profile used in the solid-state synthesis of LLRTMO materials. In the heating profile, the calcining mixture was maintained at  $400^\circ\text{C}$  for about 5 hours to facilitate the removal of  $\text{CO}_2$  from the carbonate precursors. Samples of 5 g of LLRTMO material were typically synthesized.

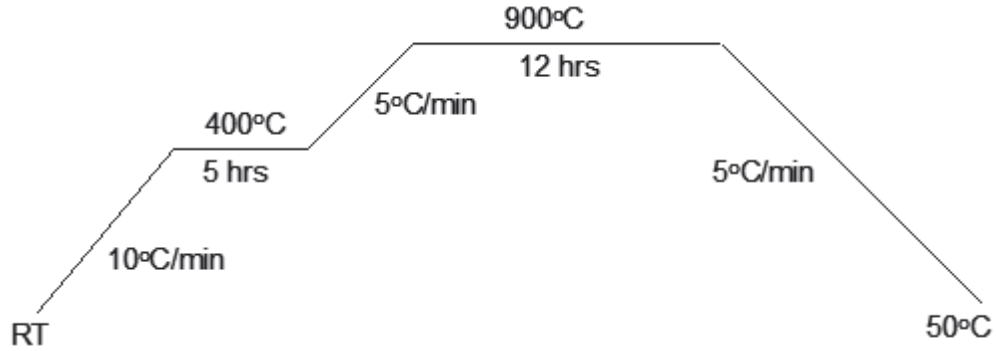


Figure 2.3 Temperature profile for the solid-state synthesis of LLRTMO

## 2.2 Materials characterization

Synthesized materials, both precursors and lithium transition metal oxides, were characterized using a variety of techniques. Characterization techniques used to study structure, morphology, density, surface area and composition will be discussed in the following sections.

### 2.2.1 X-Ray diffraction (XRD)

When X-ray photons interact with electrons, they can undergo elastic scattering (Thompson scattering). When electrons of atoms in a periodic crystal scatter incident X-rays, some of the scattered X-rays undergo constructive interference according to Bragg's law

$$2d\sin\theta = n\lambda \quad (2.3)$$

where  $d$  is a particular spacing between particular planes in the crystal,  $\theta$  is the incident angle of the X-rays with respect to the plane of the sample,  $\lambda$  is the X-ray wavelength and  $n$ , an integer, is the order of the reflection.



A Siemens D5000 diffractometer equipped with a Cu target X-ray tube and a diffracted beam monochromator was used for powder XRD measurements. The diffractometer uses Bragg-Brentano geometry, in which the divergent and the diffracted beams were at a fixed radius from the sample<sup>76</sup>. Figure 2.4 shows a schematic of a Bragg-Brentano diffractometer. It includes an X-ray tube, a sample stage, an X-ray detector and several slits. A high energy electron beam was created in the X-ray tube and was accelerated through 40 keV. The accelerated electrons hit the Cu target to produce Cu-K $\alpha$  ( $\lambda = 1.5418 \text{ \AA}$ ) X-rays. Then the X-rays were directed on the powder sample and diffraction occurred. A diffracted beam monochromator was used to select the wavelength corresponding to Cu-K $\alpha$  radiation and the powder diffraction pattern of the material was collected using a detector. The divergence and anti-scatter slits were both set

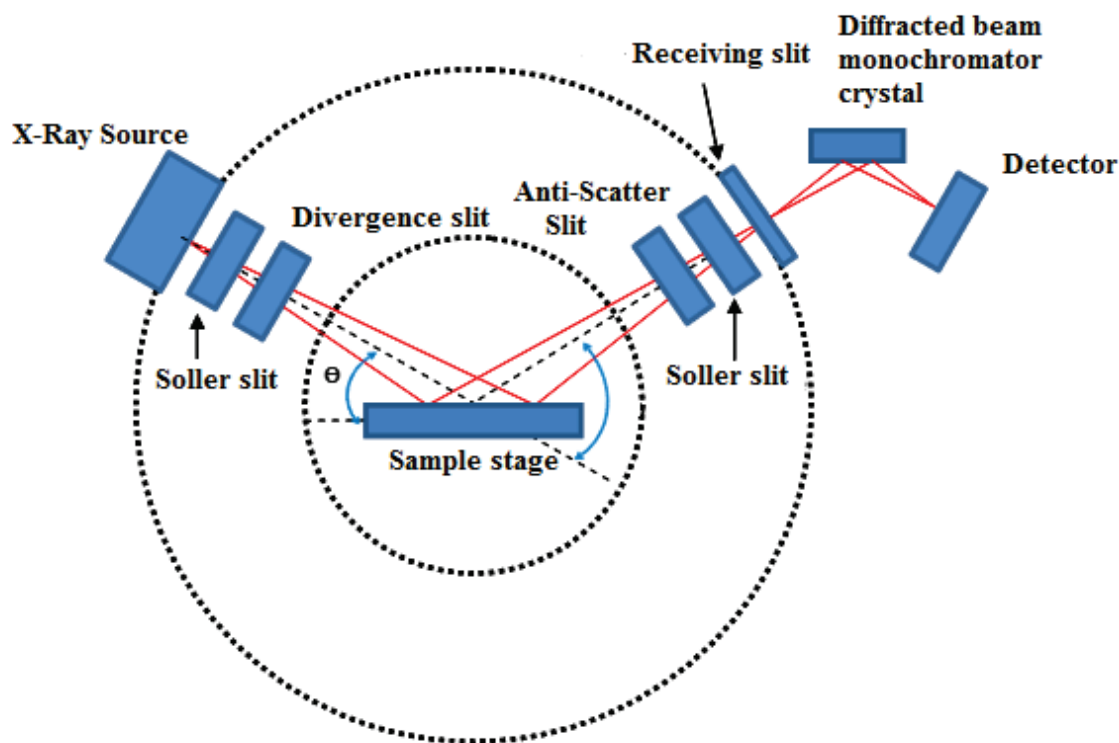


Figure 2.4 Schematic of a Bragg-Brentano diffractometer

to 0.5°, and the receiving slit was 0.2 mm. Data were collected at desired (*e.g.* 0.05°) angular intervals and dwell time (*e.g.* 5 s).

### 2.2.1.1 Rietveld refinement

Rietveld refinement is a data fitting method used in X-ray diffraction pattern analysis. In this method, an X-ray pattern is calculated for a material of interest from its crystal structure data. Then the structural parameters describing the material are adjusted to give the best agreement between the experimental and calculated patterns. The refinement was done on the basis of least square method to minimize the function  $\Delta$ , which is defined as

$$\Delta = \sum_i W_i [y_i(obs) - y_i(cal)]^2 \quad (2.4)$$

where  $W_i$  is the statistical weight,  $y_i(obs)$  is the observed intensity and  $y_i(cal)$  is the calculated intensity.

In the Rietveld refinement routine, a structure is defined with its space group and unit cell parameters. The elemental compositions obtained from inductively coupled plasm-optical emission spectroscopy (ICP-OES) analysis were used to define the stoichiometry of the sample. For  $\text{LiMO}_2$  compounds, the oxygen occupancy was set to be 2.00 per formula unit. The refinement involves adjusting parameters such as lattice parameters, peak shapes, fractional atomic coordinates, site occupancies, and cation exchange levels. The Bragg R factor ( $R_B$ ) is defined as

$$R_B = \frac{\sum |I_k(obs) - I_k(cal)|}{\sum I_k(obs)} \quad (2.5)$$

where  $I_k(obs)$  and  $I_k(cal)$  are the observed and calculated integrated intensity of Bragg peak  $k$  respectively.  $R_B$  is used to measure the ability of the proposed unit cell to describe the calculated pattern. Appendix B gives the details of Rietveld refinement procedure.

### **2.2.2 Scanning electron microscopy (SEM)**

Scanning electron microscopy involves the scanning of the surface of a material with a beam of focussed electrons. As a result of the electron-sample interaction, a variety of signals such as secondary electrons (SE), backscattered electrons (BSE), characteristic X-rays etc., result depending on the electron interaction volume. The SE signal is used to produce SEM images<sup>77</sup>.

A Hitachi (Japan) S-4700 scanning electron microscope was used to study the morphology of the samples. A sample for SEM analysis was prepared by spreading a tiny amount ( $< 1$  mg) of the dry powder onto carbon tape. The carbon tape with sample powder on top was mounted on a metallic stub. Then the stub was introduced into the vacuum chamber of the microscope. Once the stub was positioned properly, an electron beam with an accelerating voltage of 15 to 20 kV was directed on the sample. The beam was then focused to a spot size less than 10 nm and the sample was scanned. The SE signal that was recorded using suitable detectors produced SEM images.

### **2.2.3 Inductively coupled plasma – optical emission spectroscopy (ICP-OES)**

The concentration of a particular metal element in a sample can be measured precisely using ICP-OES. This technique involves the excitation of atoms and ions using an inductively coupled plasma and then measuring the characteristic wavelengths of

electromagnetic radiation that are emitted by the atoms or ions of a particular element. Argon is used to produce the plasma.

A Perkin Elmer Optima 8000 ICP-OES machine located in the Dentistry Department of Dalhousie University was used for the ICP-OES analysis. Standard solutions of known concentrations (0 ppm, 1 ppm and 2 ppm) of elements of interest were prepared from commercial standards (Ultra Scientific Analytical Solutions). Samples (TM carbonates or  $\text{LiMO}_2$  materials) were prepared by dissolving a known amount of material (~ 10 mg) in aqua-regia prepared from HCl (37 %, Sigma-Aldrich) and  $\text{HNO}_3$  (70 %, Sigma-Aldrich). Then the solutions were diluted to 1 ppm solutions using 1 (v/v) % aqueous solution of  $\text{HNO}_3$  solution.

Aqueous solutions of standards and samples were then inserted into a nebulizer to vaporize and convert into a mist. Then the mist was introduced into the Ar plasma, where the atoms or ions of the samples interacted with the plasma and produced characteristic wavelengths. The optical spectrometer measures the characteristic wavelengths of the elements. The intensity of the electromagnetic radiation (light) of a particular element in a sample compared to the intensity from the standard solutions was used to deduce the concentration of an element. The stoichiometry of the materials of interest was calculated from the ICP-OES-derived metal ratios<sup>78</sup>.

#### **2.2.4 Brunauer-Emmett-Teller (BET) surface area analysis**

The BET method for measuring surface area is based on the monolayer physical adsorption of gas molecules on solid surfaces (adsorbent). An inert gas such as nitrogen (adsorbate) is used for the adsorption. Weak van der Waals forces between the adsorbate

gas molecules and the adsorbent surface area cause physical adsorption. This adsorption is usually done at or near the boiling temperature of the adsorbate gas. The area covered by each adsorbed gas molecule is known under specific conditions. The amount of gas adsorbed to form a monolayer on a sample is determined at the specified conditions. Then the number of adsorbed molecules is calculated from the quantity of the gas adsorbed and the area occupied by each gas molecule to get the surface area ( $s$ ) of the sample<sup>79, 80</sup>. The BET adsorption isotherm equation<sup>81</sup> is

$$\frac{\frac{P}{P_0}}{\left[ v_a \left( 1 - \frac{P_0}{P} \right) \right]} = \frac{C - 1}{v_m C} \times \frac{P}{P_0} + \frac{1}{v_m C} \quad (2.6)$$

where  $P$  is the partial vapor pressure of adsorbate gas in equilibrium with the surface at 77.4 K (boiling point of liquid N<sub>2</sub>) in pascals,  $P_0$  is the saturated pressure of adsorbate gas in pascals,  $v_a$  is the volume of gas adsorbed at STP in mL,  $v_m$  is the volume of gas (STP) required to form an adsorbed monolayer on the sample surface in mL and  $C$  is a constant derived from energy of adsorption

A Flowsorb II 2300 (Micromeritics) analyzer was used to measure the surface area of the materials. A solid powdered sample (adsorbent) was pretreated (outgassed) by purging in inert gas or by applying vacuum at high temperature to remove any impure species (normally water) at the surface of the solid. The most favorable condition for monolayer adsorption of N<sub>2</sub> gas from 30 mole % N<sub>2</sub> and 70 % He are established at atmospheric pressure and at the temperature of liquid N<sub>2</sub>. So, the monolayer adsorption was done using a liquid N<sub>2</sub> bath and  $v_m$  was measured. Then the surface area ( $S$ ) can be deduced as follows:

$$S = \frac{v_m N_A A}{V_m} \quad (2.7)$$

where  $N_A$  is the Avogadro number,  $A$  is the area of each adsorbed molecule and  $V_m$  is the molar volume of the gas.

### 2.2.5 Crystallographic density measurement (Pycnometer)

An AccuPyc II 1340 (Micromeritics) gas displacement pycnometer using He gas (ultra high pure 99.999 %) was used to measure the density of the samples. The pycnometer uses the ideal gas law and the gas displacement technique to measure the volume. Figure 2.5 shows a schematic of the pycnometer. The pycnometer consists of two chambers – a sample cell chamber of volume  $V_{cell}$  with a removable lid for holding the sample and an expansion chamber of volume  $V_{exp}$ . They are connected to each other with a valve in between. The sample cell chamber is also connected to a helium tank, for which the pressure is set to approximately 22.00 psig.

Before measuring the density of each set of materials, the pycnometer was calibrated with the given standard (supplied by Precision Ball & Gage Co.), which has a known volume. In a usual density measurement routine, samples were transferred to the pycnometer with minimum exposure to air. First, the mass of the sample was measured by measuring the mass of the empty sample cup and the same cup filled with the sample accurately. After that, the sample cup (with the sample) was placed into the sample cell chamber and it was closed air tight. Then, the sample cell chamber was purged with He 10 times to remove possible moisture. Both purge fill pressure and the cycle fill pressure were set at 19.500 psig.

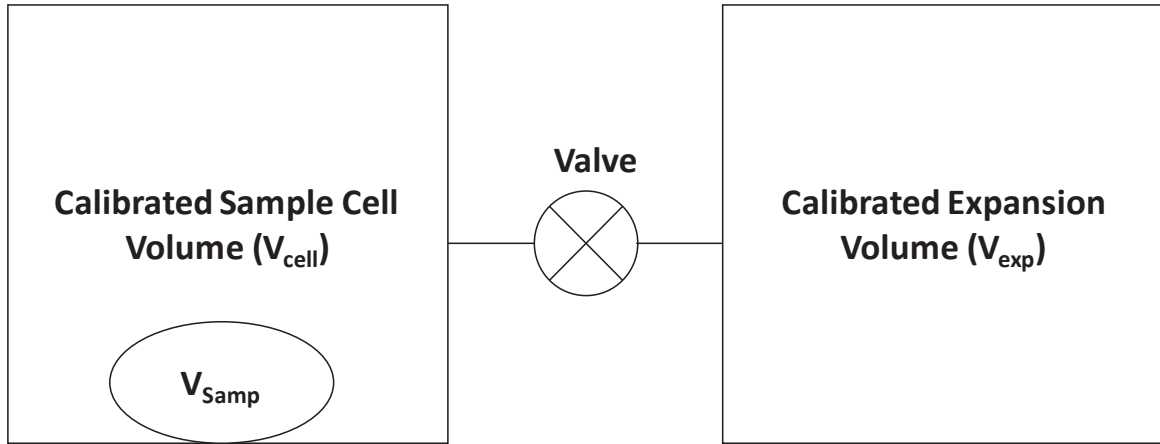


Figure 2.5 Schematic of pycnometer

First, the sample cell chamber with sample and the expansion chamber were at ambient pressure  $P_a$  and at ambient temperature  $T_a$  and the valve between them was closed. Then the sample cell chamber was charged to an elevated pressure  $P_1$  and the ideal gas law applied to the sample cell chamber yields

$$P_1 (V_{cell} - V_{samp}) = n_c RT_a \quad (2.8)$$

where  $n_c$  is the number of moles of gas in the sample cell chamber,  $R$  is the gas constant and  $T_a$  is the ambient temperature. Similarly, the ideal gas law applied to the expansion chamber yields

$$P_a V_{exp} = n_{exp} RT_a \quad (2.9)$$

where  $n_{exp}$  is the number of moles of gas in the expansion volume and  $P_a$  is the ambient pressure. After that, the valve was opened. Now, the pressure fell down to an intermediate pressure  $P_2$  and now the ideal gas law yields

$$P_2 (V_{cell} - V_{samp} + V_{exp}) = n_c RT_a + n_{exp} RT_a \quad (2.10)$$

where  $V_{samp}$  is the volume of the sample. By substituting Equations 2.8 and 2.9 into 2.10 and rearranging, the working equation for the pycnometer can be obtained as shown below:

$$V_{samp} = V_{cell} - \frac{V_{exp}}{\left(\frac{P_1 - P_a}{P_2 - P_a}\right) - 1} \quad (2.11)$$

$V_{cell}$  and  $V_{exp}$  were determined by the calibration procedures as 2.8844 cm<sup>3</sup> and 9.1458 cm<sup>3</sup>, respectively, and the pressures  $P_1$  and  $P_2$  were measured by a gauge pressure transducer. The above procedure to measure  $P_1$  and  $P_2$  was repeated 5 times and the average  $V_{samp}$  was calculated using Equation 2.7. From the average  $V_{samp}$  and the measured mass, the average density of the sample was calculated.

## 2.2.6 Solid-state nuclear magnetic resonance spectroscopy (Solid-state NMR)

Compared to diffraction methods such as XRD, which measures the long-range order, solid-state NMR can be used to study the local structure of positive electrode materials and dynamic processes occurring within the materials. The electronic structure of positive electrode materials has a profound effect on their NMR spectra and so it can be used to discriminate between conductors and insulators or diamagnetic and paramagnetic materials.

Solid-state NMR utilizes the interaction between nuclei of a sample placed in a magnetic field and electromagnetic radiation in the radio frequency (RF) range. When a nucleus having a spin quantum number,  $I$ , of half-integer (*e.g.* <sup>27</sup>Al) or integer (*e.g.* <sup>14</sup>N) is exposed to a strong magnetic field, the energy levels between different spin states are



split into multiplets (Zeeman effect). Transitions between adjacent energy levels can be induced by emission or absorption of photons in the RF range and the frequency of the RF radiation is measured in the NMR experiment. In a solid structure, nuclei exist in different local environments that are shielded by surrounding electrons. Hence different nuclei experience different magnetic fields accordingly, leading to the absorption of photons of different frequencies. So, measuring the change in the energy level separation and the corresponding frequencies with changing local environments is the aim of an NMR experiment. However, the measurement of absolute frequencies is difficult and hence the resonance frequencies are recorded with reference to an external standard compound and corresponding chemical shifts ( $\delta$ ) are reported<sup>82</sup>. When anisotropic shielding affects a nucleus and hence  $\delta$ , the average shift experienced by a nucleus called isotropic shift ( $\delta_{iso}$ ) is chosen as a more meaningful parameter.

A solid-state NMR experiment consists of three basic steps – (A) Preparation, (B) Perturbation (evolution) and (C) Detection. Figure 2.6 shows a schematic of the basic steps of an NMR experiment. In the preparation step, the sample (nuclear spin system) is placed in a magnetic field  $B_0$ . The magnetic moment of each nucleus precesses about the principal axis of the magnetic field. Given a large number of spins (nuclei) respond to the applied magnetic field simultaneously, the average response of the individual spins causes a resultant precession of frequency known as the “Larmor frequency”. A net magnetization ( $M$ ) parallel to  $B_0$  also results from the magnetic moments of all the nuclei.

In the perturbation step, a pulse of plane-polarized (RF) radiation is incident on the sample at the Larmor frequency. As a result, the net magnetization ( $M$ ) gets inclined with respect to the applied magnetic field. For example, a  $\pi/2$  pulse causes  $M$  to be oriented perpendicular to  $B_0$ . In the detection step, the RF irradiation is turned off at the

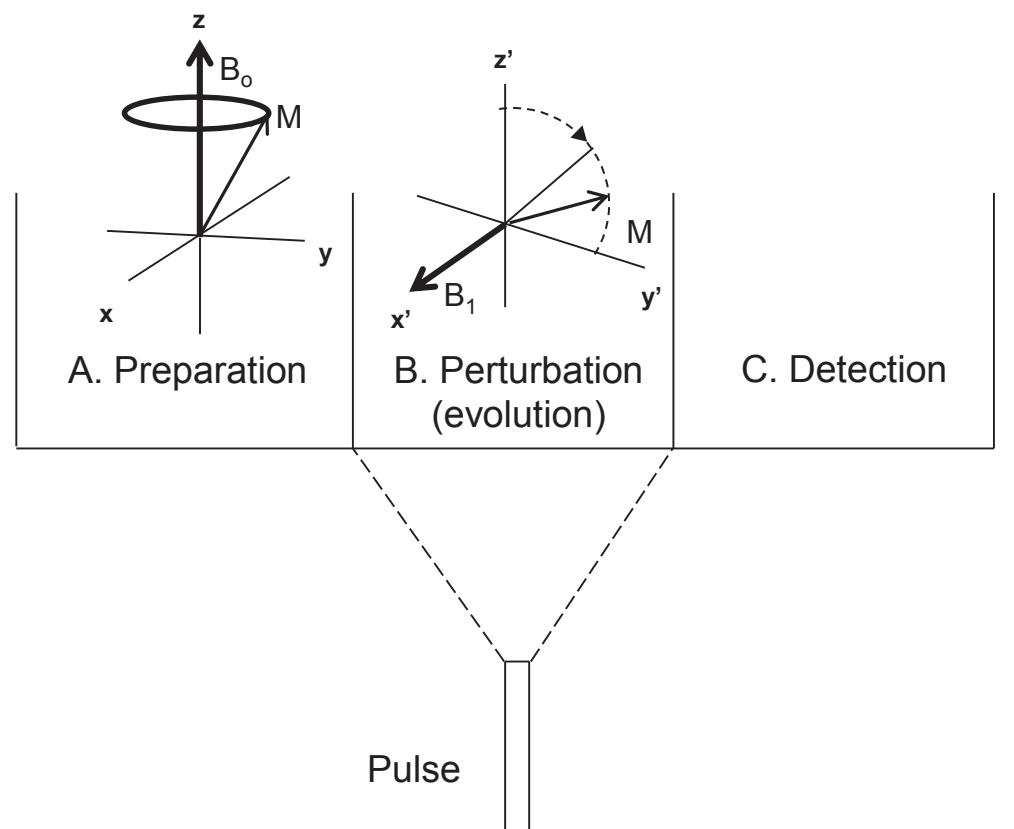


Figure 2.6 Schematic of the three basic steps of a NMR experiment.  
(Adapted from reference 82)

end of the pulse. As a result, the spin system precesses coherently in the transverse plane. The transverse magnetization induces a voltage in the pickup coil and the signal is measured as a function of time and is called the Free Induction Decay (FID). After amplification, the FID is subsequently transformed to the frequency domain via a Fourier transformation (FT) and it results in an NMR spectrum, which is a plot of amplitude as a function of frequency (Figure 2.7).

### 2.2.6.1 Li NMR for LLRTMO materials

Since the  $\text{Li}^+$  ions directly participate in the electrochemical processes involving these materials, lithium nuclei ( $^6\text{Li}$  or  $^7\text{Li}$ ) are used as probe species in LLRTMO

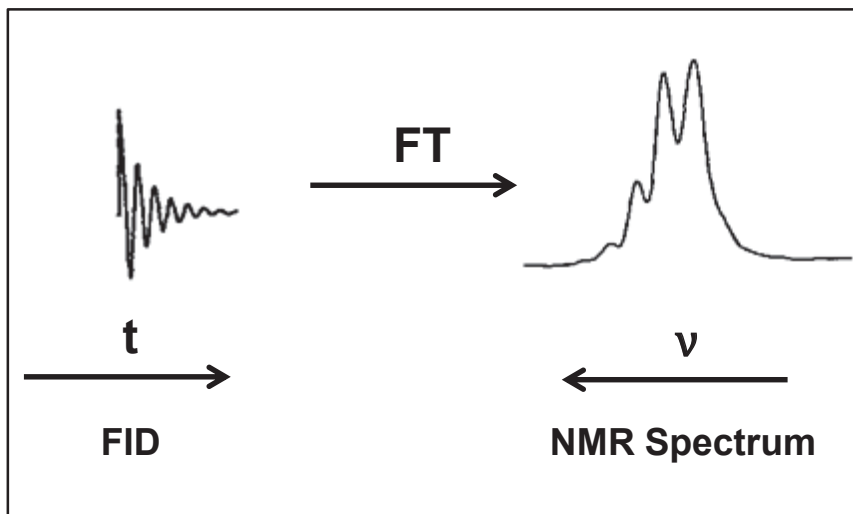


Figure 2.7 Schematic of the conversion of FID into a NMR spectrum  
(Adapted from reference 82)

materials. Figure 2.8 shows the  ${}^6\text{Li}$  NMR spectrographs of a few members of the series  $\text{Li}[\text{Li}_{1/3-2x/3}\text{Ni}_x\text{Mn}_{2/3-x/3}]\text{O}_2$ <sup>83</sup>. Figure 2.8 shows that Li resonances corresponding to Li in the Li layers (500-800 ppm) and Li in the TM layers (1360-1560 ppm) have been clearly resolved. In particular, Figure 2.8 indicates the presence of Li in the TM layer even in the sample  $\text{LiNi}_{0.5}\text{Mn}_{0.5}\text{O}_2$  ( $x = 0$ ) supporting the Li-Ni exchange between the Li and TM layers. Thus solid-state NMR can be used to discriminate the amount of Li between Li and TM layers in LLRTMO materials.

Here,  ${}^7\text{Li}$  NMR experiments were performed on selected LLRTMO materials to quantify and discriminate the amount of Li between Li and TM layers.  ${}^7\text{Li}$  NMR experiments were conducted (by our collaborators) at McMaster University under a 4.7 T applied field using a Bruker DRX console. Samples of interest were shipped to McMaster University. Each spectrum was collected on a milligram size sample undergoing 60 kHz magic-angle spinning using a Bruker 1.3 mm probe in <1 h. Spectra are referenced to 1 M  $\text{LiCl}(\text{aq})$  at 0 ppm, and all experiments used 100 ms recycle delays and  $1.5 \mu\text{s}$   $\pi/2$  pulses. Chapter 6 will discuss the  ${}^7\text{Li}$  NMR results of some LLRTMO materials of interest

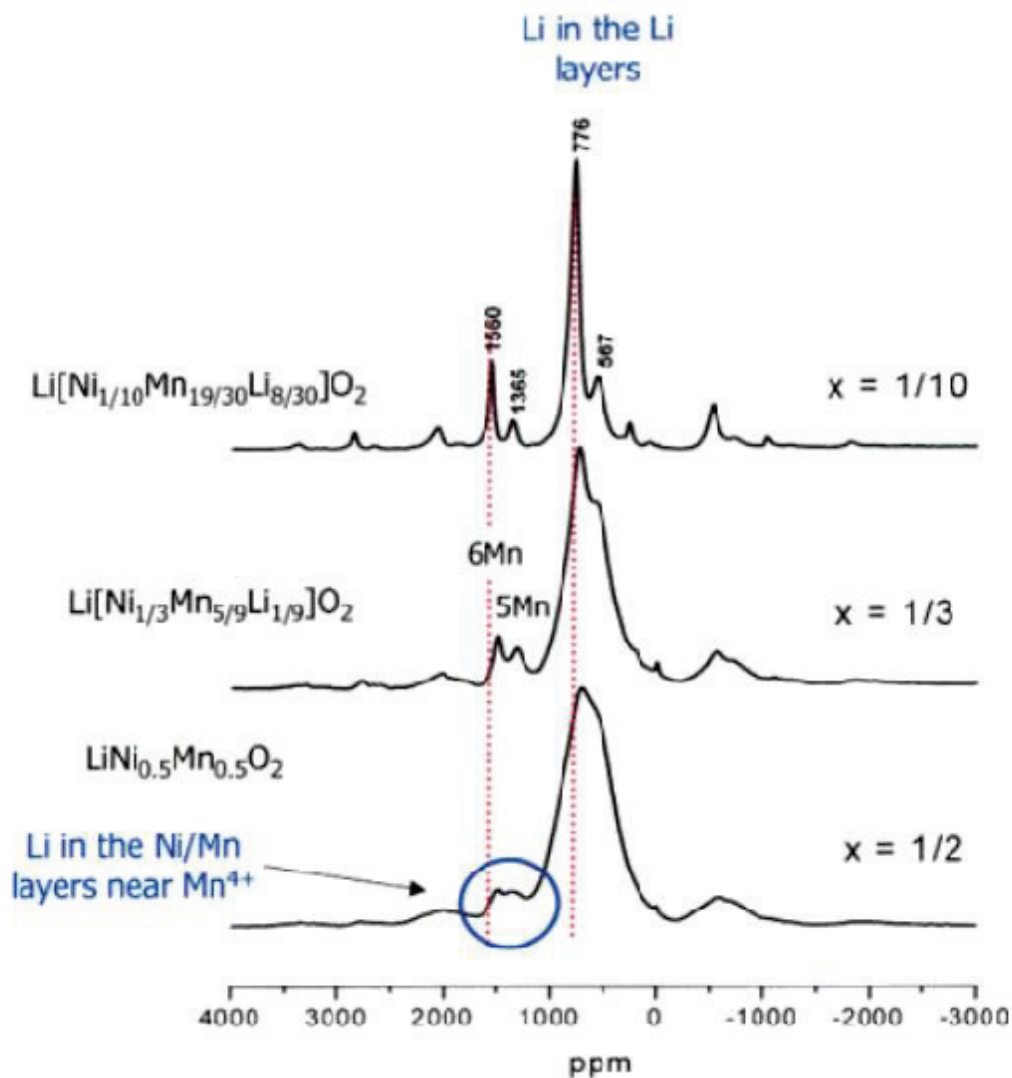


Figure 2.8  ${}^6\text{Li}$  NMR spectrum of LLRTMO materials  
 Adapted with permission from (*Chem. Rev.* **2004**, 104, 4493-4512)  
 Copyright (2004) American Chemical Society

### 2.3 Electrochemical characterization

Electrochemical characterization of a positive electrode material is typically carried out using a coin cell. The steps involved in electrochemical characterization are discussed in the following sections.

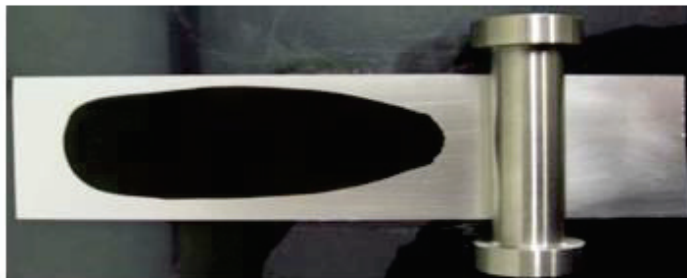


Figure 2.9 Electrode spread making  
(Adapted from reference 84)

### 2.3.1 Preparation of working electrodes

The working electrode was made from the positive electrode material under investigation. The solid powdered material was mixed with known amounts of carbon black (Super C45 from TIMCAL) and polyvinylidene fluoride (PVDF) binder (from ARKEMA). The carbon and the binder were added to the active material to improve the conductivity and mechanical properties of the electrode respectively. The ratio of the active material, carbon and PVDF was 90:5:5 wt %. Then all the ingredients were added to an appropriate amount of an organic solvent (N-methyl pyrrolidone) and mixed in a slurry mixer (Mazerustar) to obtain the electrode slurry.

The slurry of the positive electrode material was spread onto an aluminum foil current collector using a notch-bar (0.006")<sup>84</sup>. Figure 2.9 shows a picture of a positive electrode spread made on aluminum foil with a notch-bar. After drying at least for 3 hours at 120°C to completely remove the solvent, the dried electrode was pressed using a calender. The calendered electrode sheet was punched into several circular disks, which were eventually used as working electrodes in the coin cells.

### 2.3.2 Construction of coin cells

Figure 2.10 shows the parts of a coin cell. Cell assembly was carried out in an argon-filled glovebox. A casing is placed at the bottom with the positive electrode (working electrode). A circular lithium foil serves as the reference and counter electrode. A microporous separator was placed on top of the positive electrode before placing the lithium foil to prevent short circuit. A spacer and a disk spring were placed on top of the lithium foil to prevent short circuit. A gasket and top casing were placed. The arranged stack was crimped and closed using a pressurized argon-controlled crimper. An appropriate amount of electrolyte made of 1 M lithium hexafluorophosphate ( $\text{LiPF}_6$ ) in 1:2 ethylene carbonate (EC)/diethyl carbonate (DEC) from BASF was placed between the positive and negative electrodes.

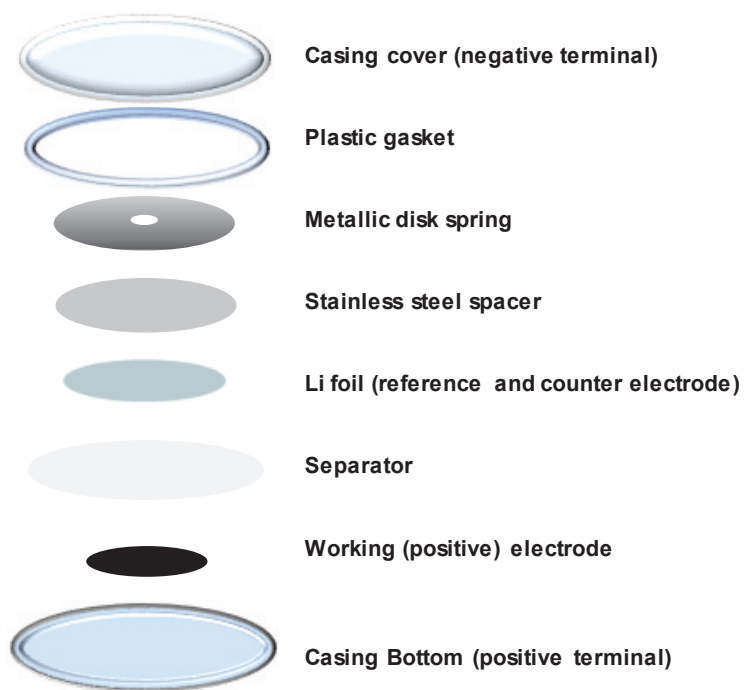


Figure 2.10 Coin-cell assembly

### 2.3.1 Electrochemical testing

The assembled coin cells were connected to chargers (Maccor) operated in constant-current mode. The current applied for the charge/discharge was normally determined on the basis of the mass of the electrode and the desired C-rate, which was usually denoted as  $C/n$ . For example, if the discharge or charge (half cycle) was set to be completed in 20 hours ( $n = 20$ ), then the C-rate is  $C/20$ . By considering the practical specific capacity of the positive electrode material under study, an approximate C-rate current was applied for the charge-discharge cycles. The cycling was within a specified voltage window, usually selected between 2.0 to 4.8 volts. The charge-discharge characteristics of the positive electrode material can be monitored as a function of time or charge passed.

## Chapter 3    **Structural characterization of layered lithium-rich transition metal oxides<sup>A</sup>**

### **3.1 Introduction**

Chapter 1 posed two questions about layered lithium-rich transition metal oxides (LLRTMO). (i) Are LRLTMO materials solid solutions or composites between two layered materials ( $\text{LiMO}_2$  and  $\text{Li}_2\text{MnO}_3$ )? (ii) Are the “broad” peaks between  $20^\circ$  to  $35^\circ$  in their XRD patterns caused by nano-domains of a secondary phase ( $\text{Li}_2\text{MnO}_3$ )? This chapter is devoted to answering those questions through structural analysis of a series of Ni-Mn-based LLRTMO materials.

### **3.2 Superlattice ordering in layered lithium-rich transition metal oxides**

LLRTMO has an O3 structure with A-B-C-A-B-C stacking but the arrangement of the atoms in the TM layer is different from that in other layered materials<sup>85</sup> such as  $\text{LiCoO}_2$ . The presence of  $\text{Li}^+$  ions with large ionic radii ( $0.74 \text{ \AA}$ )<sup>86</sup> and small sized  $\text{Mn}^{4+}$  ions ( $0.54 \text{ \AA}$ )<sup>86</sup> in the TM layer causes an in-plane ordering resulting in a  $\sqrt{3}a \times \sqrt{3}a$  superstructure or superlattice<sup>36</sup>. The superlattice ordering in the TM layer results in superlattice Bragg peaks in the range between  $\sim 20^\circ$  to  $35^\circ$  ( $\text{Cu K}\alpha$ )<sup>85</sup>.

Figure 3.1 shows the superlattice ordering between  $\text{Mn}^{4+}$  and  $\text{Li}^+$  ions in the TM layer of  $\text{Li}_2\text{MnO}_3$ . Weil et al. have characterized and compared the compounds  $\text{Li}(\text{Ni}_{0.425}\text{Mn}_{0.425}\text{Co}_{0.15})\text{O}_2$  and  $\text{Li}_{1.12}(\text{Ni}_{0.425}\text{Mn}_{0.425}\text{Co}_{0.15})_{0.88}\text{O}_2$  using electron diffraction to check for the presence of superlattice ordering<sup>87</sup>. Their work has clearly shown that

---

<sup>A</sup> This chapter was adapted with permission from Shunmugasundaram, R.; Arumugam, R. S.; Dahn, J. R. A Study of Stacking Faults and Superlattice Ordering in Some Li-Rich Layered Transition Metal Oxide Positive Electrode Materials. *J. Electrochem. Soc.* **2016**, *163* (7), A1394–A1400. The author’s contribution to this work included synthesis of materials, XRD measurements, FAULTS fitting and manuscript writing.



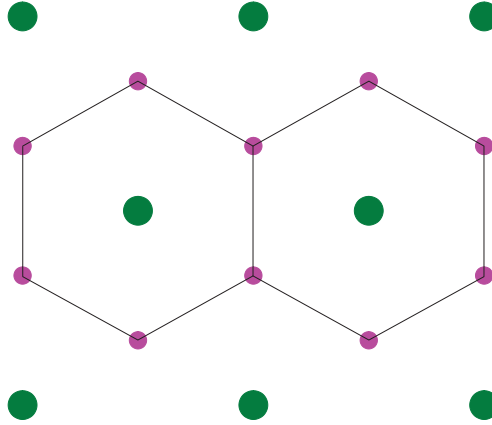


Figure 3.1 Superlattice ordering in the TM layer of  $\text{Li}_2\text{MnO}_3$   
 Adapted with permission from (*J. Electrochem. Soc.* **2016**, *163* (7),  
 A1394–A1400) Copyright (2016)

overlithiation (Li in the TM layer) is required for superlattice reflections. Characterization techniques such as solid-state NMR<sup>88</sup> and EXAFS<sup>89</sup> have also been used to study the superlattice ordering in LLRTMO materials.

### 3.3 Transition metal layer stacking in $\text{Li}_2\text{MnO}_3$

Figure 3.2 shows the structure of  $\text{Li}_2\text{MnO}_3$  in which the boundaries of both the monoclinic ( $C2/m$ ) and hexagonal unit cells ( $R-3m$ ) have been indicated to highlight the correlation between their atomic arrangements. The unit cells have been slightly tilted and the oxygen atoms are not drawn to scale (smaller) for clear visualization. The relations between the monoclinic unit cell and the hexagonal unit cell<sup>83</sup> are

In  $\text{Li}_2\text{MnO}_3$  ( $\text{Li}[\text{Li}_{1/3}\text{Mn}_{2/3}]\text{O}_2$ ), the lattice constants (monoclinic unit cell) are  $a =$

$$(\bar{a} \ \bar{b} \ \bar{c})_{\text{mon.}} = (\bar{a} \ \bar{b} \ \bar{c})_{\text{hex.}} \begin{pmatrix} -2 & 0 & 2/3 \\ -1 & -3 & 1/3 \\ 0 & 0 & 1/3 \end{pmatrix} \quad (3.1)$$

$$(h \ k \ l)_{\text{hex.}} = (h \ k \ l)_{\text{mon.}} \begin{pmatrix} -1/2 & 0 & 1 \\ 1/6 & -1/3 & 0 \\ 0 & 0 & 3 \end{pmatrix} \quad (3.2)$$

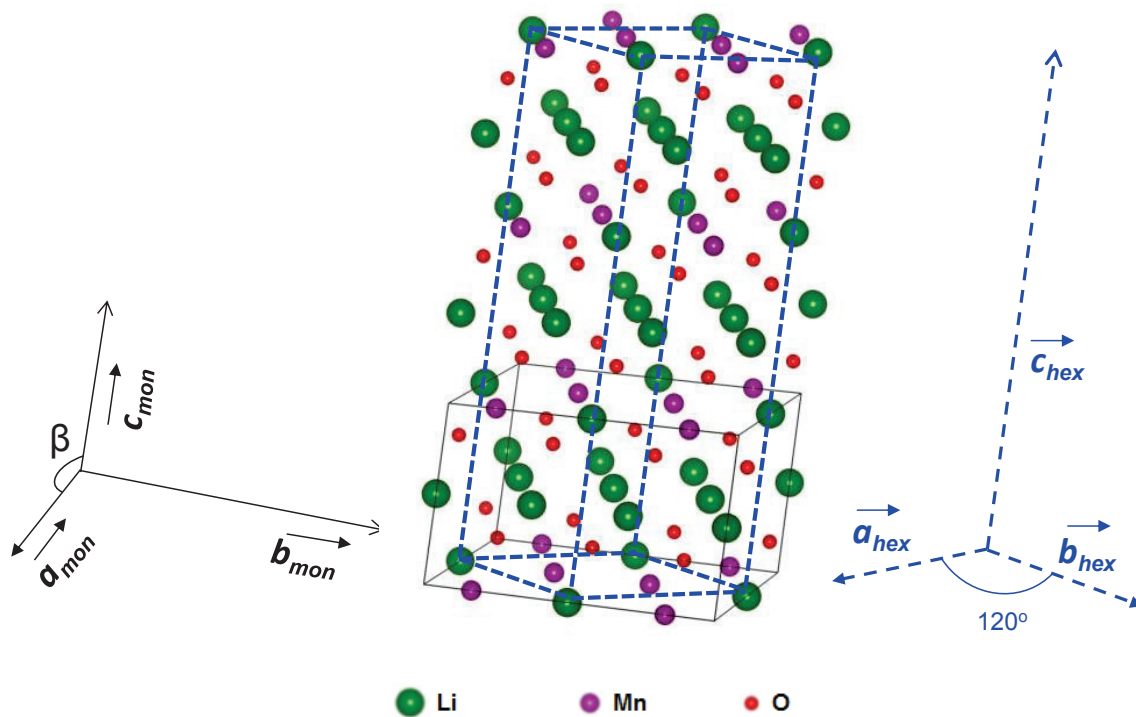


Figure 3.2 Structure of  $\text{Li}_2\text{MnO}_3$   
(Oxygen atoms were not drawn to match their ionic radii)  
Adapted with permission from (*J. Electrochem. Soc.* **2016**, *163* (7), A1394–A1400)  
Copyright (2016)<sup>51</sup>

$4.9292(2) \text{ \AA}$ ,  $b = 8.5315(2)$ ,  $c = 5.0251(1)$  and  $\beta = 109.337(2)^\circ$ .<sup>90</sup>

The top panel of Figure 3.3 shows a triangular lattice plane or layer, labeled as A1, corresponding to the TM layer of  $\text{Li}_2\text{MnO}_3$ . The plane A1 is formed by  $1/3$  Li (green balls) and  $2/3$  Mn atoms (pink balls) and it is easy to identify the ordering in the TM layer. The top panel of Figure 3.3 also shows a 2-D hexagonal unit cell of the layer A1.

Referring to the hexagonal 3-D unit cell of  $\text{Li}_2\text{MnO}_3$  shown in Figure 3.2, the very bottom TM layer is considered to be A1 (the starting layer). Since  $\text{Li}_2\text{MnO}_3$  can be considered as an O3 structure, the TM layer shifts 3 times within one hexagonal 3-D unit

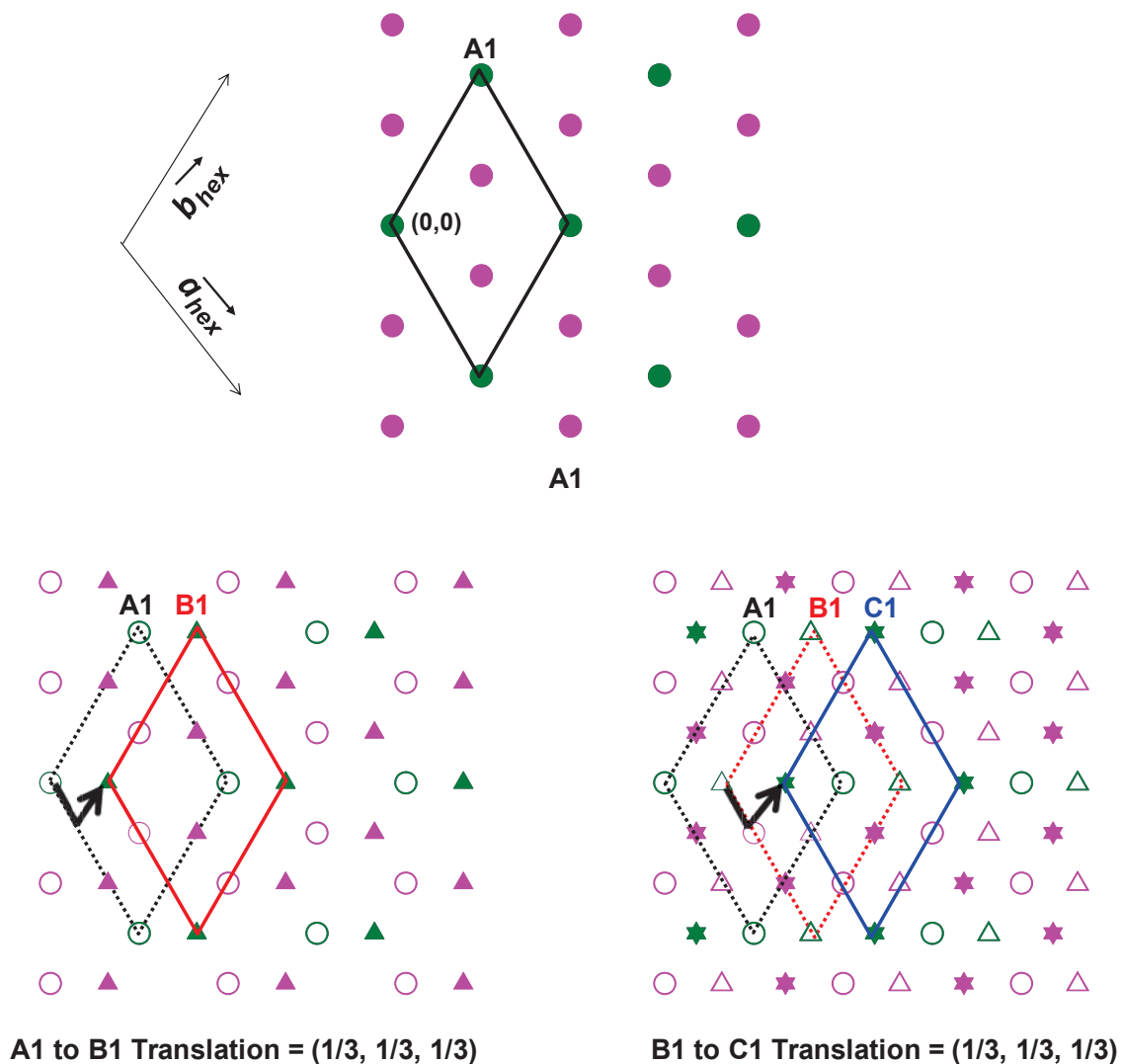


Figure 3.3. TM layers of  $\text{Li}_2\text{MnO}_3$  made up of pink (Mn) and green (Li) balls (A1), triangles (B1) and stars (C1). Top panel: Triangular lattice plane A1, Bottom left panel: A1 to B1 translation. Bottom right panel: B1 to C1 translation. The black, red and the blue hexagonal 2-D unit cells correspond to the A1, B1 and C1 TM layers. Adapted with permission from (*J. Electrochem. Soc.* **2016**, 163 (7), A1394–A1400) Copyright (2016)

cell. With reference to A1, the stacking of the next TM layer follows a  $(1/3, 1/3, 1/3)$  translation in fractional atomic coordinates in accordance with the O3 structure. As a result, the next TM layer, labeled B1, is placed on top of A1. The layer B1 has been constructed from atoms designated by triangles in the bottom panel of Figure 3.3. A

subsequent  $(1/3, 1/3, 1/3)$  translation from B1 results in a TM layer called C1, in which the atoms are designated as stars in the bottom panel of Figure 3.3. The bottom left and right panels of Figure 3.3 show the A1 to B1 and B1 to C1 translations, respectively. The A1 to B1 and B1 to C1 translations can be easily understood by following the 2-D hexagonal unit cells (variants) in the bottom right panel of Figure 3.3. If the TM layer stacking perfectly follows the trend A1-B1-C1-A1-B1-C1..., then there are no stacking faults in the structure.

For convenience of clear understanding, the discussion on stacking order in this chapter considers only A1 as the frame of reference (bottom layer). In addition to the  $(1/3, 1/3, 1/3)$  translation, two other translations are possible:  $(2/3, 0, 1/3)$  and  $(0, 2/3, 1/3)$ , which preserve the O3 stacking but give alternate superlattice arrangements. For

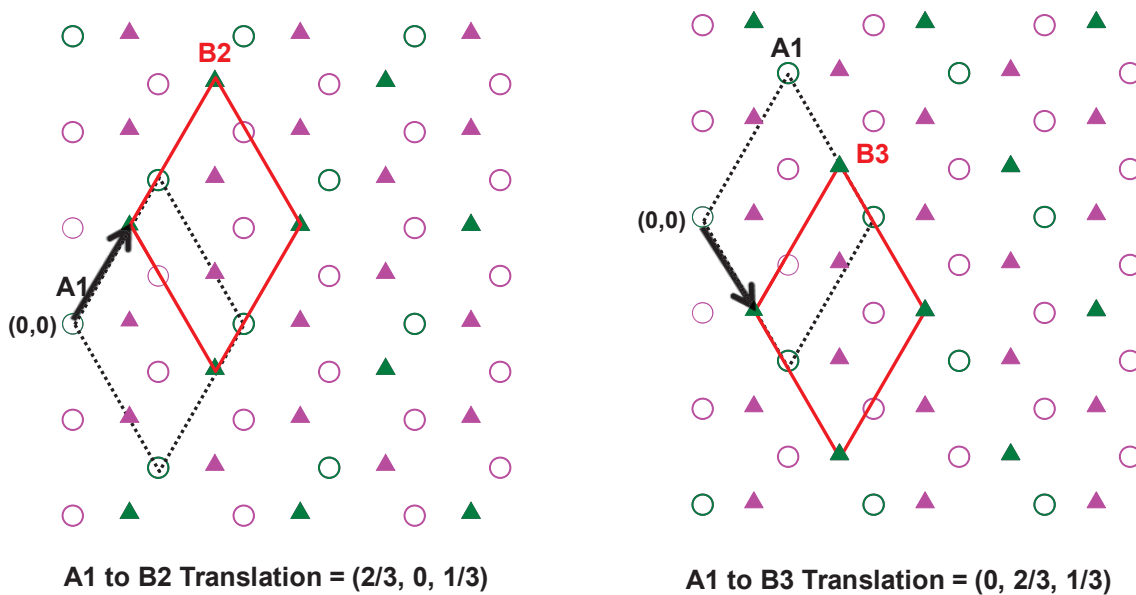


Figure 3.4 TM layers of  $\text{Li}_2\text{MnO}_3$  showing A1 to B2 translation (left panel) and A1 to B3 translation (right panel)

Adapted with permission from (*J. Electrochem. Soc.* **2016**, *163* (7), A1394–A1400)  
Copyright (2016)

example, the next stacking layer above A1 could be B2 or B3. The left panel in Figure 3.4 shows the second possible translation  $(2/3, 0, 1/3)$ , in which A1 is translated to a 2-D hexagonal variant called B2. Similarly, the right panel in Figure 3.4 shows the third possible translation  $(0, 2/3, 1/3)$ , in which A1 is translated to a 2-D hexagonal variant called B3. Thus a total of 3 translations and 9 2-D hexagonal variants, A1, B1, C1, A2, B2, C2, A3, B3 and C3 are involved in the TM layer stacking sequence.

As a general rule, all the translations follow the A-B-C-A sequence. Table 3.1 shows the starting and the resulting 2-D hexagonal variants with respect to the type of translation. For example, the result of  $(2/3, 0, 1/3)$  translation from B2 is C3 but a  $(0, 2/3, 1/3)$  translation from B2 results in C1. It should be noted that the 2-D hexagonal variant, A1 has been treated as the bottom layer of the 3-D unit cell of  $\text{Li}_2\text{MnO}_3$  just for convenience but any 2-D hexagonal variant could be the bottom layer of the structure of  $\text{Li}_2\text{MnO}_3$ .

Table 3.1 Starting and resulting hexagonal variants from possible translations

<b>Translation</b>	<b>Starting 2-D hexagonal variant</b>	<b>Resulting 2-D hexagonal variant</b>
$(1/3, 1/3, 1/3)$	A <sub>n</sub>	B <sub>n</sub>
	B <sub>n</sub>	C <sub>n</sub>
	C <sub>n</sub>	A <sub>n</sub>
$(2/3, 0, 1/3)$	A <sub>n</sub>	B <sub>n+1</sub> or B <sub>n-2</sub> (for n=3)
	B <sub>n</sub>	C <sub>n+1</sub> or C <sub>n-2</sub> (for n=3)
	C <sub>n</sub>	A <sub>n+1</sub> or A <sub>n-2</sub> (for n=3)
	Example B3	C1
$(0, 2/3, 0)$	A <sub>n</sub>	B <sub>n+2</sub> or B <sub>n-1</sub> (for n=2, 3)
	B <sub>n</sub>	C <sub>n+2</sub> or C <sub>n-1</sub> (for n=2, 3)
	C <sub>n</sub>	A <sub>n+2</sub> or A <sub>n-1</sub> (for n=2, 3)
	Example C2	A1

If the stacking sequence follows only one type of translation, then the structure has no stacking faults. Therefore, the stacking order of a structure with no stacking faults could also be B2-C2-A2-B2-C2-A2 using the  $(1/3, 1/3, 1/3)$  translation or B1-C3-A2-B1-C3-A2 using the  $(0, 2/3, 0)$  translation between adjacent layers. A program called FAULTS was used to study the effect of stacking faults on the XRD pattern of LLRTMO materials.

### 3.4 FAULTS

FAULTS is a Fortran90 program to refine both XRD and neutron diffraction patterns of crystal structures with defects such as stacking faults. FAULTS considers the layered arrangements of the structure, which are interconnected through stacking operations occurring with a certain probability. Translation vectors are used to define the planar defects. The average interference wave function scattered from each layer type in a faulted crystal is computed by FAULTS to build a diffraction pattern.

FAULTS calculates or fits the structure based on an algorithm that exploits the recurring pattern of the structure as explained by Treacy et al.<sup>91</sup>. Parameters corresponding to unit cell dimensions, the peak shapes, scale factor and the stacking fault probability were used to calculate the XRD pattern of a structure. For the case of refinement, cell dimensions such as lattice parameters and atomic positions that were borrowed from Rietveld refinement results of the corresponding XRD patterns and arbitrary stacking faults probabilities were used as starting parameters. Once a reasonably good fitting was obtained, the stacking fault probabilities were refined.

Figure 3.5 shows the simulated XRD pattern of  $\text{Li}_2\text{MnO}_3$  obtained from a FAULTS simulation that considers only one type of translation (0 % stacking faults). The

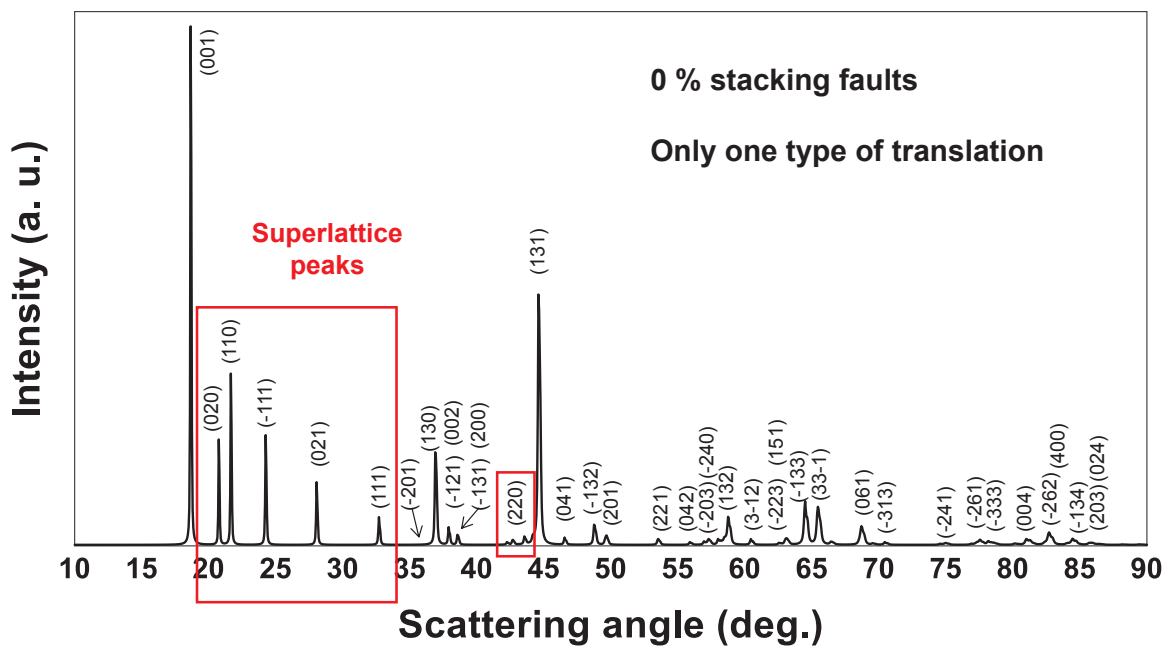


Figure 3.5 FAULTS -Simulated XRD pattern of  $\text{Li}_2\text{MnO}_3$  with 0 % stacking faults. Adapted with permission from (*J. Electrochem. Soc.* **2016**, 163 (7), A1394–A1400) Copyright (2016)

simulation was made using the unit cell parameters of  $\text{Li}_2\text{MnO}_3$  reported by Boulineau et al<sup>90</sup>. All the peaks in the simulated XRD patterns can be indexed using a  $C2/m$  space group. Figure 3.5 shows that the superlattice peaks (indicated by the red boxes) are as sharp as the other peaks.

### 3.5 Stacking faults in $\text{Li}_2\text{MnO}_3$

Stacking disorder of the TM layers along the  $c$  axis causes “stacking faults”. Boulienu et al. have demonstrated the existence of stacking faults in the structure of  $\text{Li}_2\text{MnO}_3$  using high resolution transmission electron microscopy<sup>90</sup>. In their XRD patterns of  $\text{Li}_2\text{MnO}_3$ , the broadening of some selective superlattice peaks was attributed to stacking faults. The extent of superlattice peak broadening increases with increasing probability of stacking faults.

Different stacking sequences of the TM layers along the  $c$  axis in  $\text{Li}_2\text{MnO}_3$  that generate different space groups have been proposed previously. Breger<sup>92</sup> and Meng<sup>85</sup> et al., explained two different ways of stacking: A1-B1-C1 corresponding to  $C2/m$  and A1-B1-C2 corresponding to  $P3_1I2$  space groups. According to Meng et al., the stacking sequences that generate the  $P3_1I2$  space group are due to an abnormality in the  $C2/m$  sequence. Based on these two stacking sequences, they have simulated the XRD patterns of  $\text{Li}_2\text{MnO}_3$  using DiFFaX and found that the  $C2/m$  stacking scheme was better for estimating the stacking fault probabilities. Riou et al. have proposed an A1-B1-C2-A2-B3-C1 stacking sequence to explain the structure of  $\text{Li}_2\text{MnO}_3$  in terms of a  $C2/c$  space group<sup>93</sup>.

The stacking of TM layers with superlattices in real samples of  $\text{Li}_2\text{MnO}_3$  as well as for  $\text{Li}[\text{Li}_{1/3-2x/3}\text{Ni}_x\text{Mn}_{2/3-x/3}]\text{O}_2$  can involve stacking disorder along the  $c$ -axis. In a structure with stacking faults, the TM layer stacking does not follow only one type of translation such as A1-B1-C1.... or A2-B2-C2... or A1-B2-C3-A1-B2-C3...etc., Instead, a disordered stacking sequence occurs, which involves all the three types of translations in various probabilities. For example, a disordered stacking could be A1-B2-C3-A2-B1-C2....or B2-C1-A1-B3-C2.....

The probabilities of all the three translations determine the extent of stacking faults or the stacking fault probability. The TM layers always follow the A-B-C-A-B-C...sequence regardless of the probability of each triangular layer variant and the three translation vectors ensure this. FAULTS simulations were done by including all three translation vectors with appropriate probabilities. Two essential constraints were invoked for the simulations – (i) the sum of the probabilities for all the translations should be one



and (ii) the probabilities of the (2/3, 0, 1/3) and (0, 2/3, 1/3) stacking fault translations were constrained to be equal. For a structure with 100 % stacking faults, the probabilities of all three translations ((1/3, 1/3, 1/3), (2/3, 0, 1/3) and (0, 2/3, 1/3)) must be equal to 1/3. In general, the stacking fault probability,  $s$ , can be calculated from any set of translation probabilities as follows:

where  $P_{11}$  is the probability of the (1/3, 1/3, 1/3) translation. For example, a set of translation probabilities of 0.6, 0.2 and 0.2 for the translation vectors (1/3, 1/3, 1/3), (2/3,

$$\text{stacking fault probability } (s) = (1 - P_{11}) / (2/3) \times 100 \% \quad (3.3)$$

0, 1/3) and (0, 2/3, 1/3) respectively would result in 60 % stacking faults in the structure.

Table 3.2 shows several sets of translation probabilities and the corresponding stacking fault probability,  $s$ .

Table 3.2 Translation vectors that define the translation from one type of TM layer to another, their probabilities and the corresponding stacking fault probabilities

Translation Vectors	Translation probabilities										
	1	0.933	0.866	0.8	0.733	0.667	0.6	0.533	0.467	0.4	0.333
(1/3, 1/3, 1/3)	1	0.933	0.866	0.8	0.733	0.667	0.6	0.533	0.467	0.4	0.333
(2/3, 0, 1/3)	0	0.033	0.067	0.1	0.133	0.167	0.2	0.233	0.267	0.3	0.333
(0, 2/3, 1/3)	0	0.033	0.067	0.1	0.133	0.167	0.2	0.233	0.267	0.3	0.333
<b>Stacking Fault probability (s) (%)</b>	0	10	20	30	40	50	60	70	80	90	100

Figure 3.6 shows the simulated XRD patterns of  $\text{Li}_2\text{MnO}_3$  with varying stacking fault probabilities obtained from FAULTS. As the stacking fault probability increases from 0 % to 100 %, the broadening of the superlattice peaks increases simultaneously. At the same time, the increase in stacking fault probability does not have any effect on the other Bragg peaks. Figure 3.7 shows the simulated XRD patterns of  $\text{Li}_2\text{MnO}_3$  with varying stacking fault probabilities but only in the range between  $20^\circ$  to  $35^\circ$ . The SL peaks of the structure with 0 % stacking faults have a clear 3-D peak signature but they gradually change to a 2-D type peak for the structure with 100% stacking faults. Thus the extent of broadening of the SL peaks should be taken as a direct measure of the

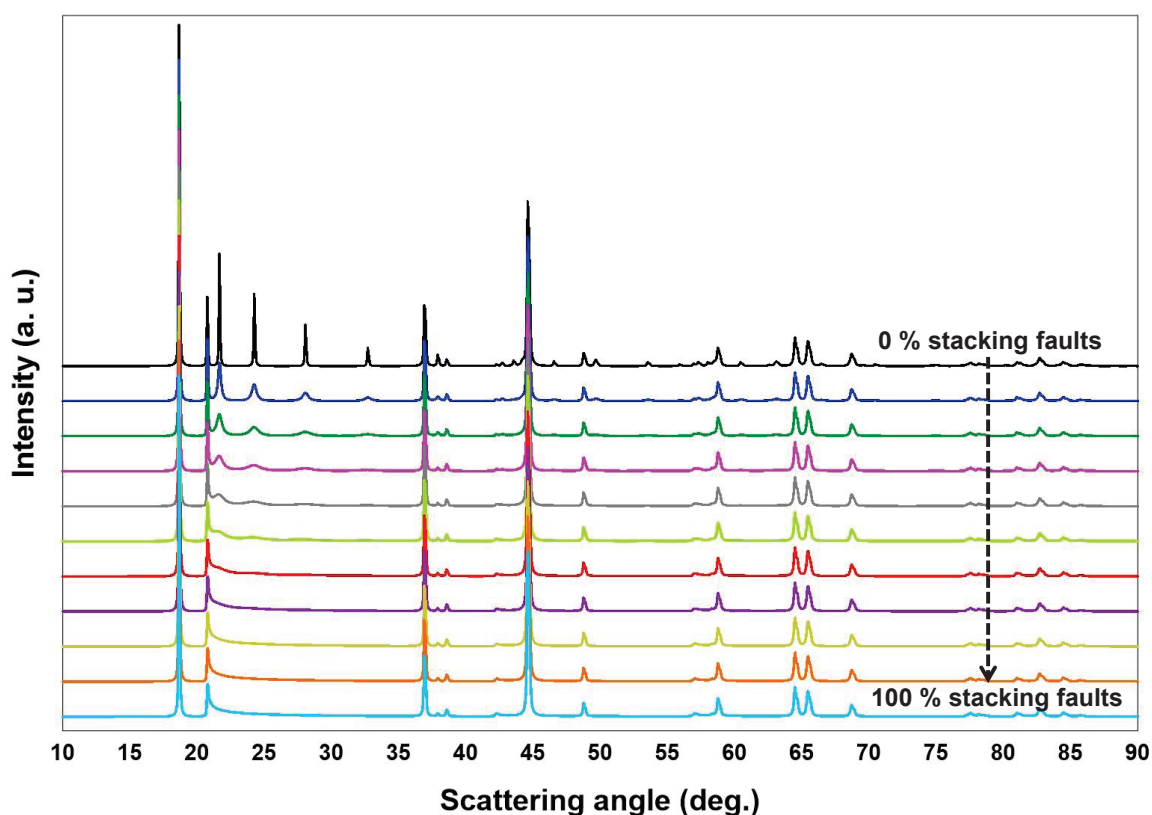


Figure 3.6 FAULTS Simulated XRD patterns of  $\text{Li}_2\text{MnO}_3$  from  $10^\circ$  to  $90^\circ$  with varying stacking fault probabilities

Adapted with permission from (*J. Electrochem. Soc.* **2016**, *163* (7), A1394–A1400)  
Copyright (2016)

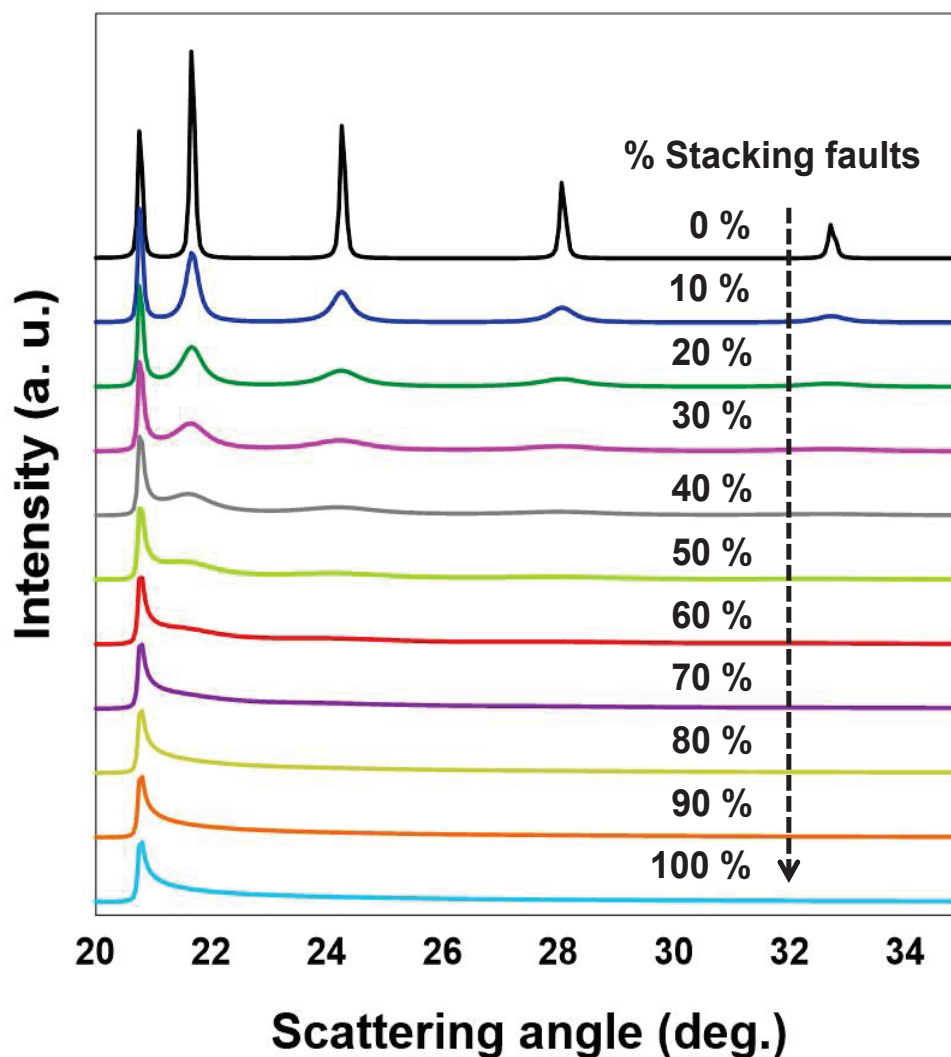


Figure 3.7 Enlarged view of the FAULTS simulated XRD patterns of  $\text{Li}_2\text{MnO}_3$  from  $20^\circ$  to  $34^\circ$  with varying stacking fault probabilities  
Adapted with permission from (*J. Electrochem. Soc.* **2016**, 163 (7), A1394–A1400) Copyright (2016)

probability of stacking faults.

Stacking faults in LLRTMO materials are affected by the synthesis temperature<sup>94</sup>. Several researchers have already reported that  $\text{Li}_2\text{MnO}_3$  synthesized at low temperature (e.g.  $800^\circ\text{C}$ ) has high probability of stacking faults<sup>95</sup>. In particular, Boulineau et al. suggest that synthesizing an ideal  $\text{Li}_2\text{MnO}_3$  with the absence of stacking faults is impossible<sup>96</sup>. The occurrence of stacking faults in two samples of  $\text{Li}_2\text{MnO}_3$  were analyzed

– one made at 1100°C (LM1100) and other at 900°C (LM900). Figure 3.8 shows the XRD patterns of both LM1100 and LM900 and the inset shows the comparison of their superlattice peaks between 20° and 35°. The superlattice peaks of LM1100 are quite sharp but with very slight broadening observed at the bottom of the (020), (110) and (-111) peaks. On the other hand, obvious SL peak broadening due to the occurrence of stacking faults was observed for  $\text{Li}_2\text{MnO}_3$  synthesized at 900°C. However, the shapes of other peaks ( $R\text{-}3m$  reflections) are quite similar for both the samples implying the absence of any other broadening effects.

Boulineau et al. have simulated the XRD pattern of  $\text{Li}_2\text{MnO}_3$  with varying stacking fault probabilities using a program called DiffaX<sup>96</sup>. Lu et al. have also used DiffaX to simulate the XRD patterns of  $\text{Li}_{2/3}[\text{Ni}_{1/3-x}\text{Co}_x\text{Mn}_{2/3}]\text{O}_2$  that contained stacking

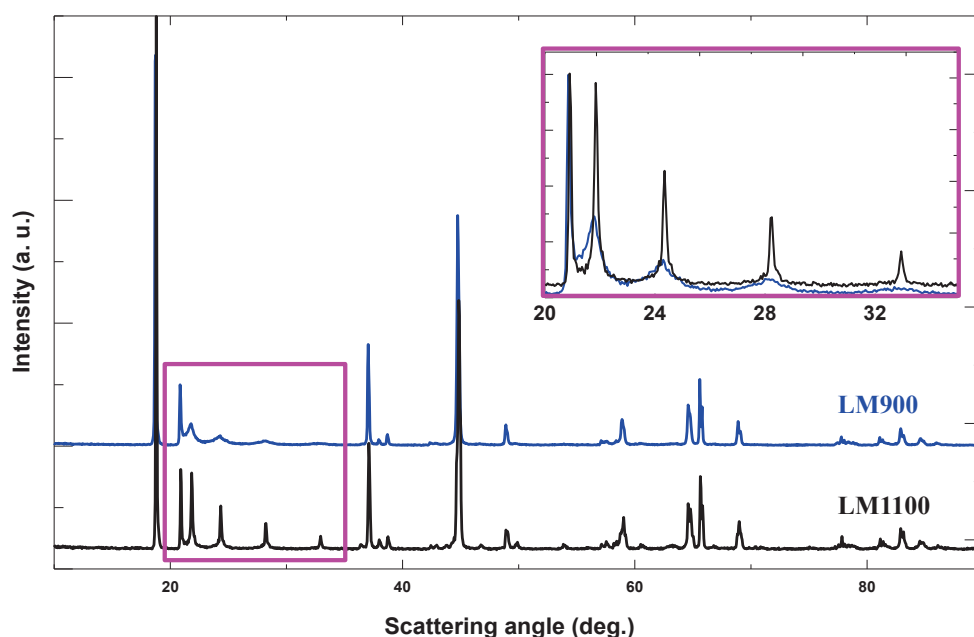


Figure 3.8 XRD patterns of  $\text{Li}_2\text{MnO}_3$  synthesized at 900°C (LM900) and 1100°C (LM1100). Inset: Enlarged view in the range of 20° to 33°. Adapted with permission from (*J. Electrochem. Soc.* **2016**, *163* (7), A1394–A1400) Copyright (2016)

faults<sup>97</sup>. In both those studies, the authors compared simulated XRD patterns to experimental ones but did not do fitting to the experimental patterns. Recently, McCalla et al. have used FAULTS to fit the experimental diffraction pattern of  $\text{Li}_4\text{FeSbO}_6$ <sup>98</sup> to study the stacking faults.

To quantify the stacking fault probability in both the samples explained in Figure 3.8, FAULTS fitting was done on their XRD patterns. Figure 3.9a and Figure 3.9b show the FAULTS fitting results for LM1100 and LM900. The insets show an enlarged view of

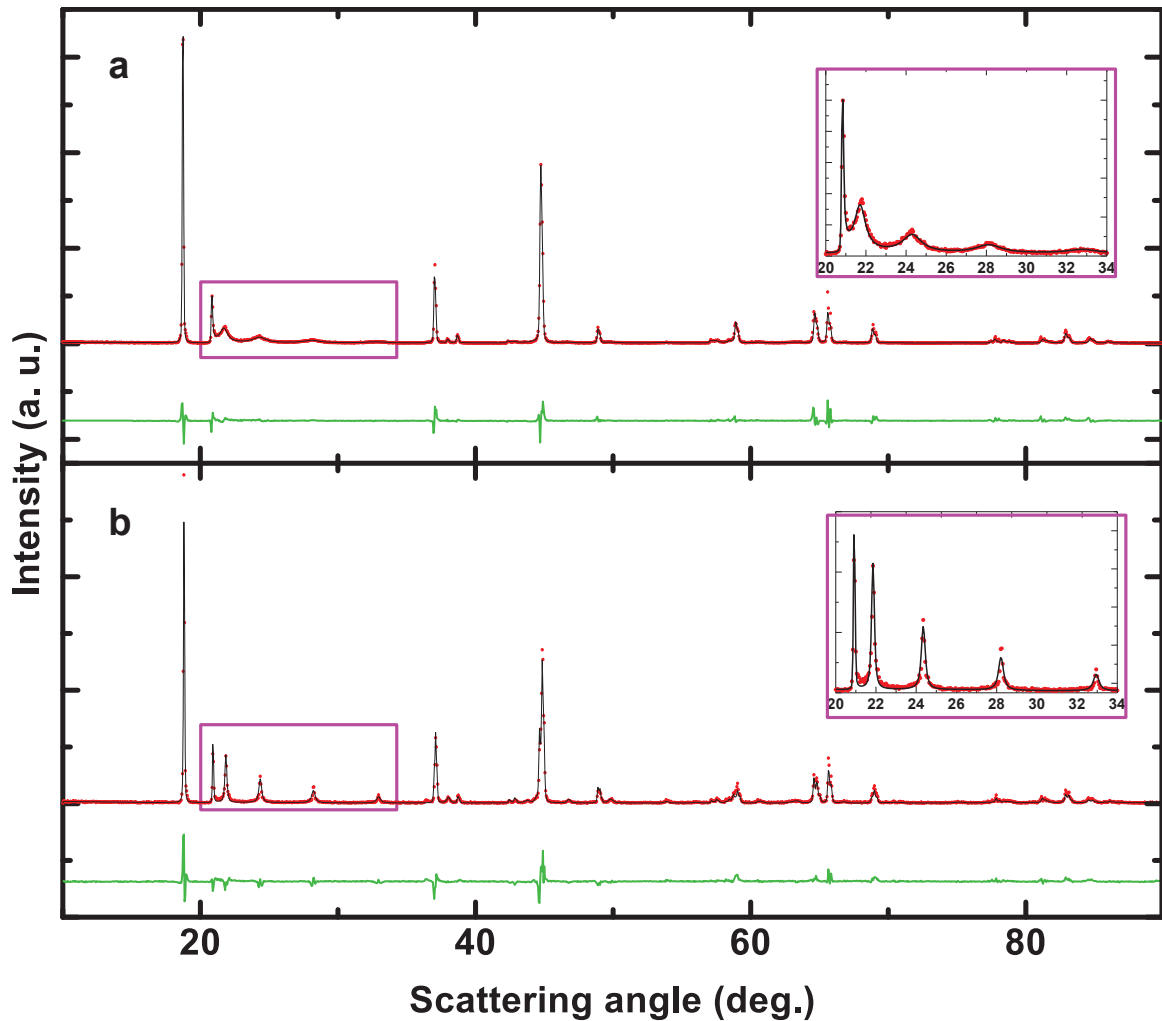


Figure 3.9 Experimental (red points), the calculated (black line) XRD patterns of LM900 (a) and LM1100 (b) obtained from FAULTS refinement and their difference (green line)  
Adapted with permission from (*J. Electrochem. Soc.* **2016**, 163 (7), A1394–A1400)

Copyright (2016)

the superlattice peak region. FAULTS results revealed a 10 % stacking fault probability for LM1100 and a  $\sim 30$  % stacking fault probability for LM900. An increase in the stacking faults for the sample synthesized at low temperature is consistent with the results reported by Breger et al<sup>92,96</sup>. However, they reported only a 2 % stacking fault probability for a sample of  $\text{Li}_2\text{MnO}_3$  synthesized at 1000°C. It may be that simulation, by contrast to fitting, underestimated the probability of stacking faults in their methods.

### 3.6 Superlattice peak positions in $\text{Li}[\text{Li}_{1/3-2x/3}\text{Ni}_x\text{Mn}_{2/3-x/3}]\text{O}_2$

The structural and electrochemical properties of materials from the  $\text{Li}[\text{Li}_{1/3-2x/3}\text{Ni}_x\text{Mn}_{2/3-x/3}]\text{O}_2$  series were first reported by Lu et al<sup>99</sup>. Table 3.2 shows the ICP-OES composition of the studied  $\text{Li}[\text{Li}_{1/3-2x/3}\text{Ni}_x\text{Mn}_{2/3-x/3}]\text{O}_2$  samples.

Table 3.3 ICP-OES compositions for the studied samples in the  $\text{Li}[\text{Li}_{1/3-2x/3}\text{Ni}_x\text{Mn}_{2/3-x/3}]\text{O}_2$  series

Sample ID	ICP-OES composition
	Li : Ni : Mn
LM900	1.332 : 0.000 : 0.677
LNM1	1.302 : 0.054 : 0.654
LNM2	1.213 : 0.217 : 0.593
LNM3	1.043 : 0.471 : 0.506

The Ni content (x) increased from sample LM900 to LMN3, which has a composition close to  $\text{LiNi}_{0.5}\text{Mn}_{0.5}\text{O}_2$ . Figure 3.10 shows the XRD patterns of the studied  $\text{Li}[\text{Li}_{1/3-2x/3}\text{Ni}_x\text{Mn}_{2/3-x/3}]\text{O}_2$  samples. The XRD pattern at the top represents sample LM900 whereas the one at the bottom of the stack represents the sample LMN3. All the diffraction peaks could be indexed using the  $C2/m$  space group including the broad

superlattice peaks between 20° to 30°. The right panel in Figure 3.10 shows an enlarged view of the (001) peaks ( $C2/m$ ) that occur around 18.6°. The (001) peak position shifted from higher to lower angle (black dotted line in **Error! Reference source not found.**) as x (Ni content) increased from LM900 to LNM3 due to an increase in the fraction of larger  $Ni^{2+}$  ions. The (001) peak shift suggests a solid-solution behavior.

This section discusses aspects of the superlattice peaks of the materials in the  $Li[Li_{1/3-2x/3}Ni_xMn_{2/3-x/3}]O_2$  series. Some researchers consider the Ni, Mn and Co containing LLRTMO compounds as solid solutions between layered  $Li[Li_{0.333}Mn_{0.667}]O_2$  (or  $Li_2MnO_3$ ) and layered  $LiMO_2$  structures such as  $Li[Ni_{0.5}Mn_{0.5}]O_2$ <sup>44,48,100,101</sup>. For example, one mole of  $Li[Li_{0.2}Ni_{0.2}Mn_{0.6}]O_2$  is a solid solution formed by 0.6 moles of

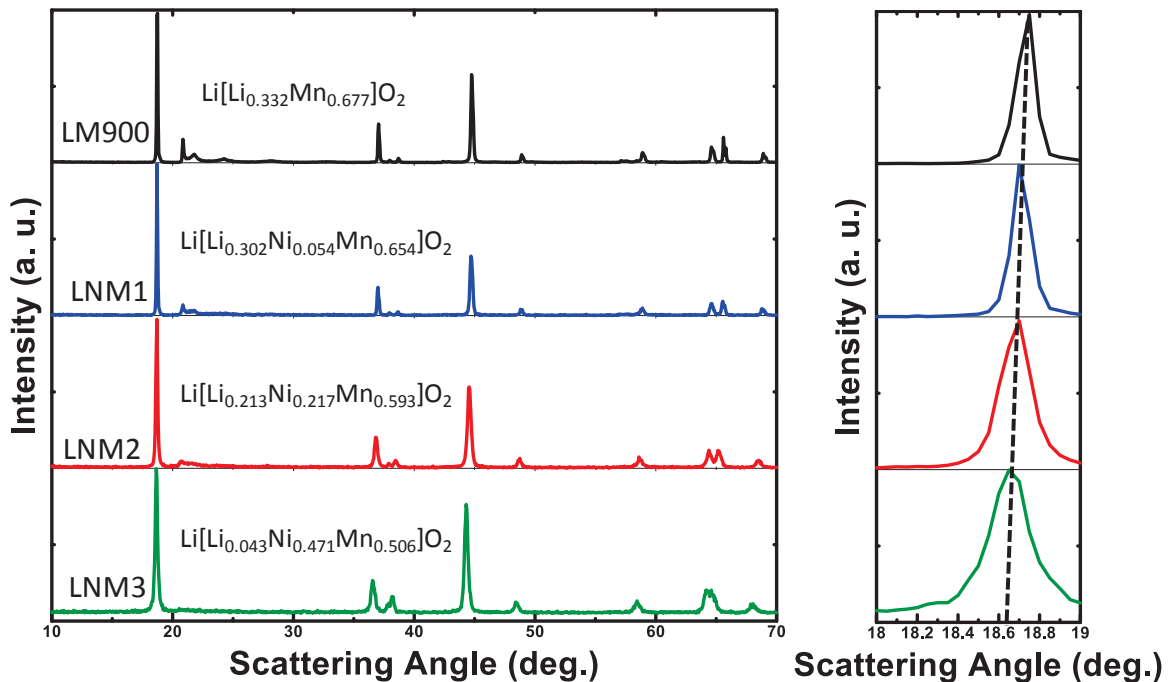


Figure 3.10 XRD of the studied samples in the  $Li[Li_{1/3-2x/3}Ni_xMn_{2/3-x/3}]O_2$  series.

Right panel: Expanded view of (001) peak corresponding to  $C2/m$  spacegroup.

The black dotted line shows the shift in (001) peak

Adapted with permission from (*J. Electrochem. Soc.* **2016**, *163* (7), A1394–A1400)

Copyright (2016)

$\text{Li}[\text{Li}_{0.333}\text{Mn}_{0.667}]\text{O}_2$  and 0.4 moles of  $\text{Li}[\text{Ni}_{0.5}\text{Mn}_{0.5}]\text{O}_2$ . Alternatively, some other researchers consider these materials as composites made up of two separate layered phases. Shukla et al. have recently investigated the microscopic structure of a Ni, Mn and Co containing LLRTMO materials and reported that they are pure solid-solutions<sup>49</sup>.

Figure 3.11 shows the XRD patterns of the studied  $\text{Li}[\text{Li}_{1/3-2x/3}\text{Ni}_x\text{Mn}_{2/3-x/3}]\text{O}_2$  samples in the range of  $20^\circ$  to  $25^\circ$  that show the superlattice peaks. Only the first SL peak

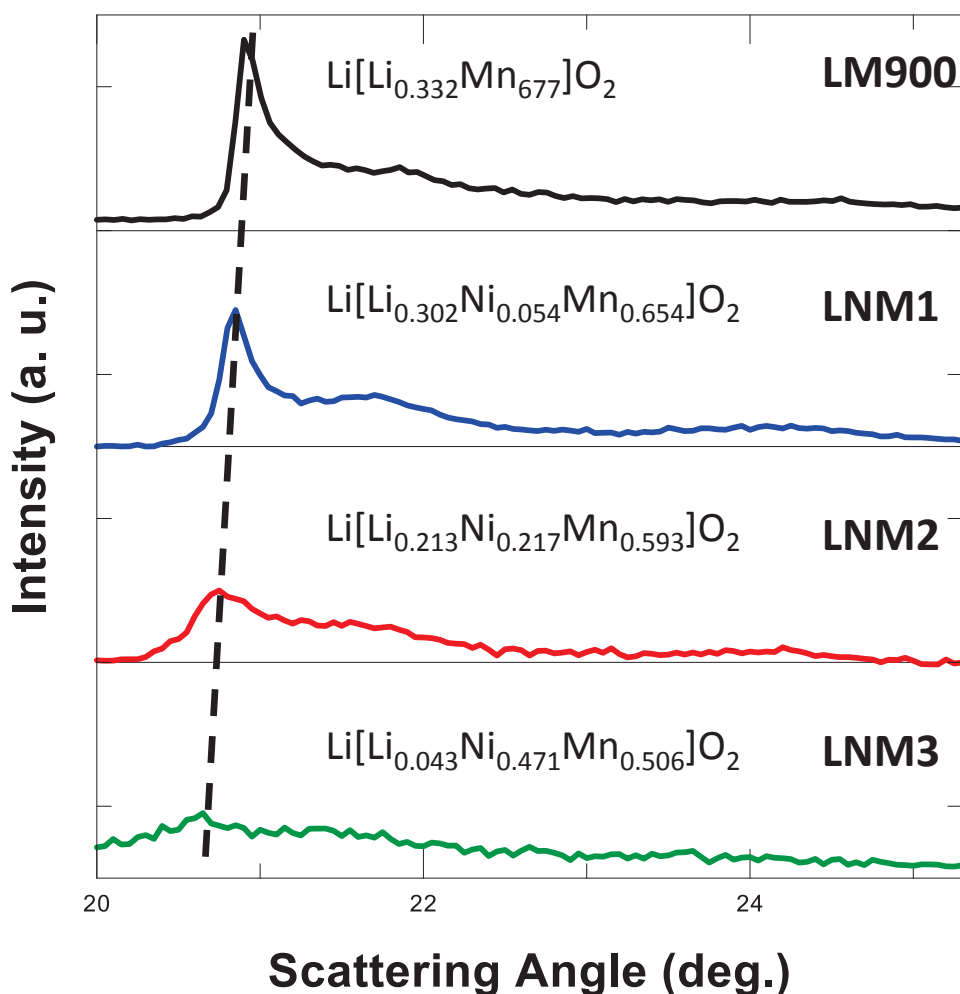


Figure 3.11 XRD patterns showing only the superlattice peaks in the range of  $20^\circ$  to  $25^\circ$  of the studied samples in the  $\text{Li}[\text{Li}_{1/3-2x/3}\text{Ni}_x\text{Mn}_{2/3-x/3}]\text{O}_2$  series. The black dotted line shows the shift in (020) peak corresponding to the  $C2/m$  spacegroup  
Adapted with permission from (*J. Electrochem. Soc.* **2016**, *163* (7), A1394–A1400)  
Copyright (2016)



(020) that belongs to the  $C2/m$  space group and occurs around  $20.5^\circ$  has been considered for peak position analysis. For samples LNM2 and LNM3, the intensities were scaled up slightly for the purpose of clarity. The (020) peak positions of samples LM900 to LNM3 shift from higher to lower scattering angle as the Ni content increases and has been indicated with a dashed line in Figure 3.11. The (020) peak peak shift with increased Ni content for the materials in the  $\text{Li}[\text{Li}_{1/3-2x/3}\text{Ni}_x\text{Mn}_{2/3-x/3}]\text{O}_2$  series also suggests the solid solution behavior as expected from the (001) peak shift belonging to the non-superlattice reflections.

The position of the non-superlattice  $C2/m$  (33-1) peak (corresponds to the  $R-3m$  (110) peak) occurring around  $65^\circ$  and the superlattice  $C2/m$  (020) peak occurring around  $20^\circ$  were compared from samples LM900 to LMN3. Table 3.4 shows the  $2\theta$  positions of  $C2/m$  (020) and the  $C2/m$  (33-1) peaks.

Table 3.4 (020) and (33-1) peak positions ( $C2/m$ ) obtained from the XRD patterns ( $\text{Cu K}\alpha$ ) of the studied samples in the  $\text{Li}[\text{Li}_{1/3-2x/3}\text{Ni}_x\text{Mn}_{2/3-x/3}]\text{O}_2$  series

<b>Sample</b>	<b><math>2\theta</math> (020)</b>	<b><math>2\theta</math> (33-1)</b>
LM900	$20.87^\circ$	$65.62^\circ$
LMN1	$20.85^\circ$	$65.55^\circ$
LMN3	$20.75^\circ$	$65.15^\circ$
LMN5	$20.65^\circ$	$64.73^\circ$

The peak positions ( $2\theta$ ) were converted into  $d$ -spacings using Bragg's law. Figure 3.12 shows a plot of their corresponding  $d$ -spacings. Figure 3.12 shows a linear relationship with an  $R^2$  value equal to 0.998 and a slope of  $\sim 0.4$ . This correlation clearly reiterates that the SL peaks belong to the solid solution between  $\text{Li}_2\text{MnO}_3$  and  $\text{LiMO}_2$  ( $M = \text{Ni, Mn and Co}$ ) and do not originate from any secondary phase. If  $\text{Li}_2\text{MnO}_3$  were a separate phase in the  $\text{Li}[\text{Li}_{1/3-2x/3}\text{Ni}_x\text{Mn}_{2/3-x/3}]\text{O}_2$  series, then peaks corresponding to that phase would not be shifted with an increase in Ni content.

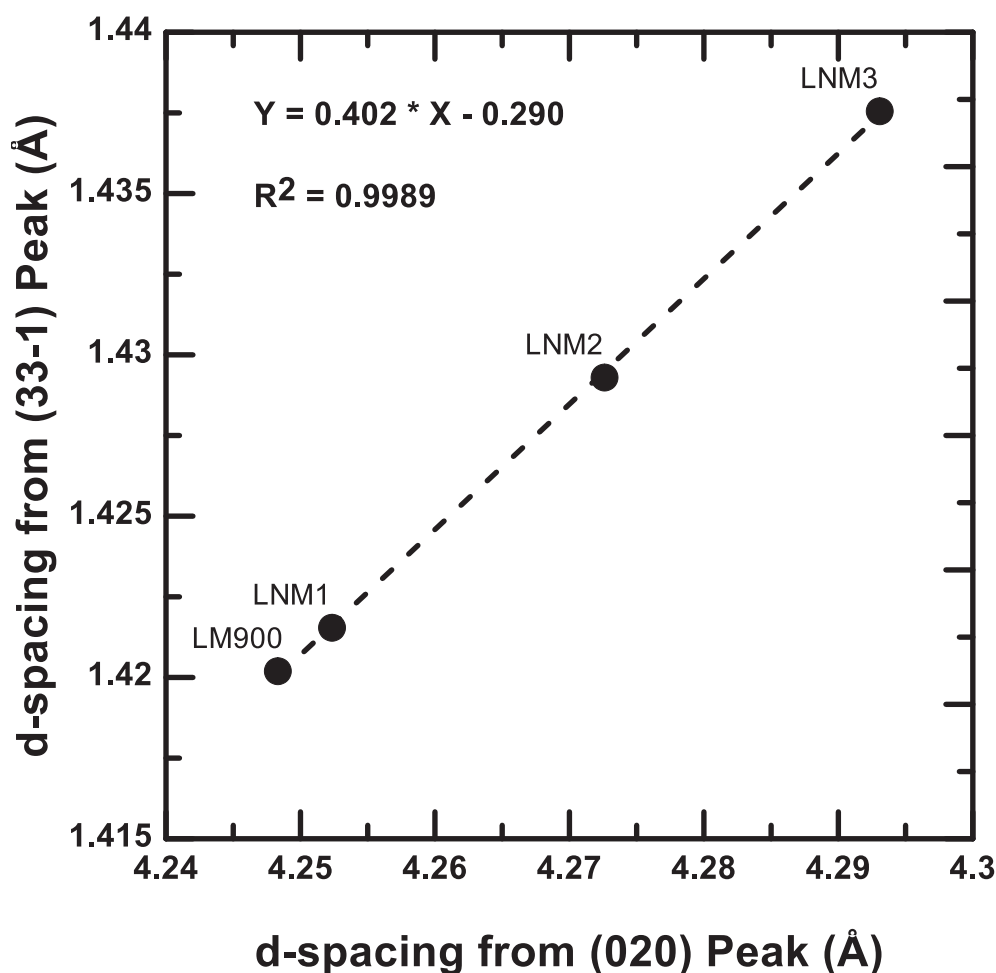


Figure 3.12  $d$ -spacings of  $C2/m$  peaks (33-1) vs. (020) of the studied samples in the  $\text{Li}[\text{Li}_{1/3-2x/3}\text{Ni}_x\text{Mn}_{2/3-x/3}]\text{O}_2$  series.

Adapted with permission from (*J. Electrochem. Soc.* **2016**, 163 (7), A1394–A1400) Copyright (2016)

### 3.7 Superlattice peak broadening in $\text{Li}[\text{Li}_{1/3-2x/3}\text{Ni}_x\text{Mn}_{2/3-x/3}]\text{O}_2$

The cause of superlattice peak broadening in the diffraction patterns of LLRTMO materials has been a subject of debate. Believers in the composite<sup>102</sup> nature of these materials contend that nano-domains of  $\text{Li}_2\text{MnO}_3$  cause the broadened SL peaks<sup>103,104</sup>. On the other hand, believers in the solid solution argue that the SL peak broadening must be attributed to the stacking faults along the  $c$  axis<sup>96,105</sup>.

In the earlier parts of this chapter, the superlattice peak broadening in  $\text{Li}_2\text{MnO}_3$  was attributed to stacking faults. In the same way,  $\text{Li}[\text{Li}_{1/3-2x/3}\text{Ni}_x\text{Mn}_{2/3-x/3}]\text{O}_2$  materials exhibit stacking faults. The probability of stacking faults in  $\text{Li}[\text{Li}_{1/3-2x/3}\text{Ni}_x\text{Mn}_{2/3-x/3}]\text{O}_2$  is comparatively high due to the additional presence of  $\text{Ni}^{2+}$  ions in the TM layers. Boulineau et al. have pointed out that a decrease in the long-range in-plane ordering would lead to sluggish ordered stacking along the  $c$ -axis<sup>90</sup>. It is expected that the 2-D ordering between Li and Mn ions in the TM layers is perturbed by  $\text{Ni}^{2+}$ , which in turn can increase the probability of the stacking disorder along the  $c$  axis. Hence it is very likely to observe superlattice peak broadening in  $\text{Li}[\text{Li}_{1/3-2x/3}\text{Ni}_x\text{Mn}_{2/3-x/3}]\text{O}_2$  materials.

There has been no study using FAULTS to fit the XRD data of  $\text{Li}[\text{Li}_{1/3-2x/3}\text{Ni}_x\text{Mn}_{2/3-x/3}]\text{O}_2$  materials to quantify the stacking fault probability. In this work, the XRD patterns of  $\text{Li}_2\text{MnO}_3$  as well as  $\text{Li}[\text{Li}_{1/3-2x/3}\text{Ni}_x\text{Mn}_{2/3-x/3}]\text{O}_2$  materials have been fit using FAULTS and the results are shared. It would be useful to understand the effect of metal composition on the stacking faults. Here, the effect of  $\text{Ni}^{2+}$  on the superlattice ordering and stacking faults in  $\text{Li}[\text{Li}_{1/3-2x/3}\text{Ni}_x\text{Mn}_{2/3-x/3}]\text{O}_2$  materials was studied and results are reported.

Figure 3.13 shows the FAULTS fitted XRD patterns of samples LM900 to LNM3 from 10° to 70° whereas Figure 3.14 shows only the superlattice region from 20° to 28°.

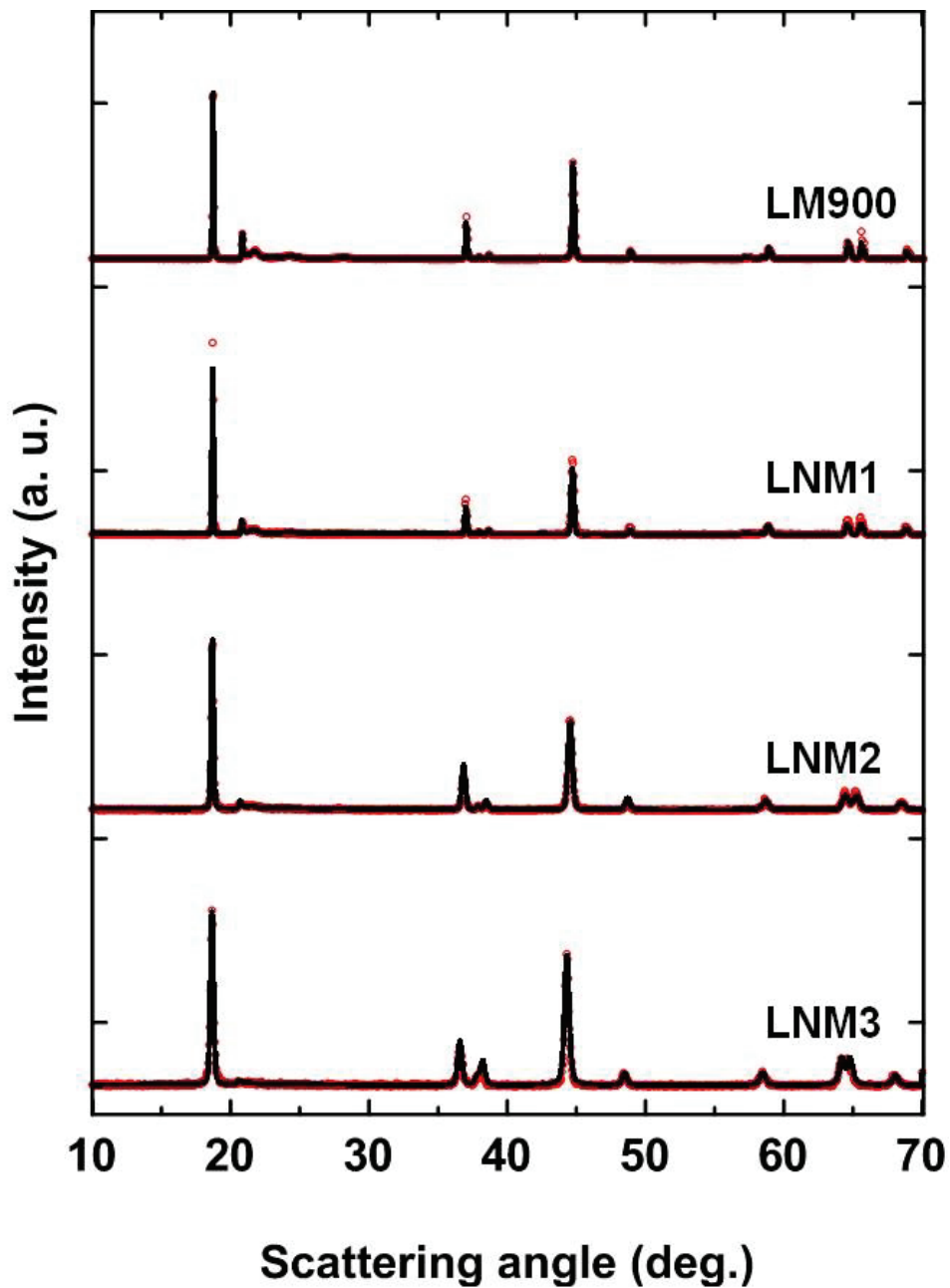


Figure 3.13 Experimental (red points) and the FAULTS fitted (black line) XRD patterns of the studied samples in the  $\text{Li}[\text{Li}_{1/3-2x/3}\text{Ni}_x\text{Mn}_{2/3-x/3}]\text{O}_2$  series. Adapted with permission from (*J. Electrochem. Soc.* **2016**, *163* (7), A1394–A1400) Copyright (2016)

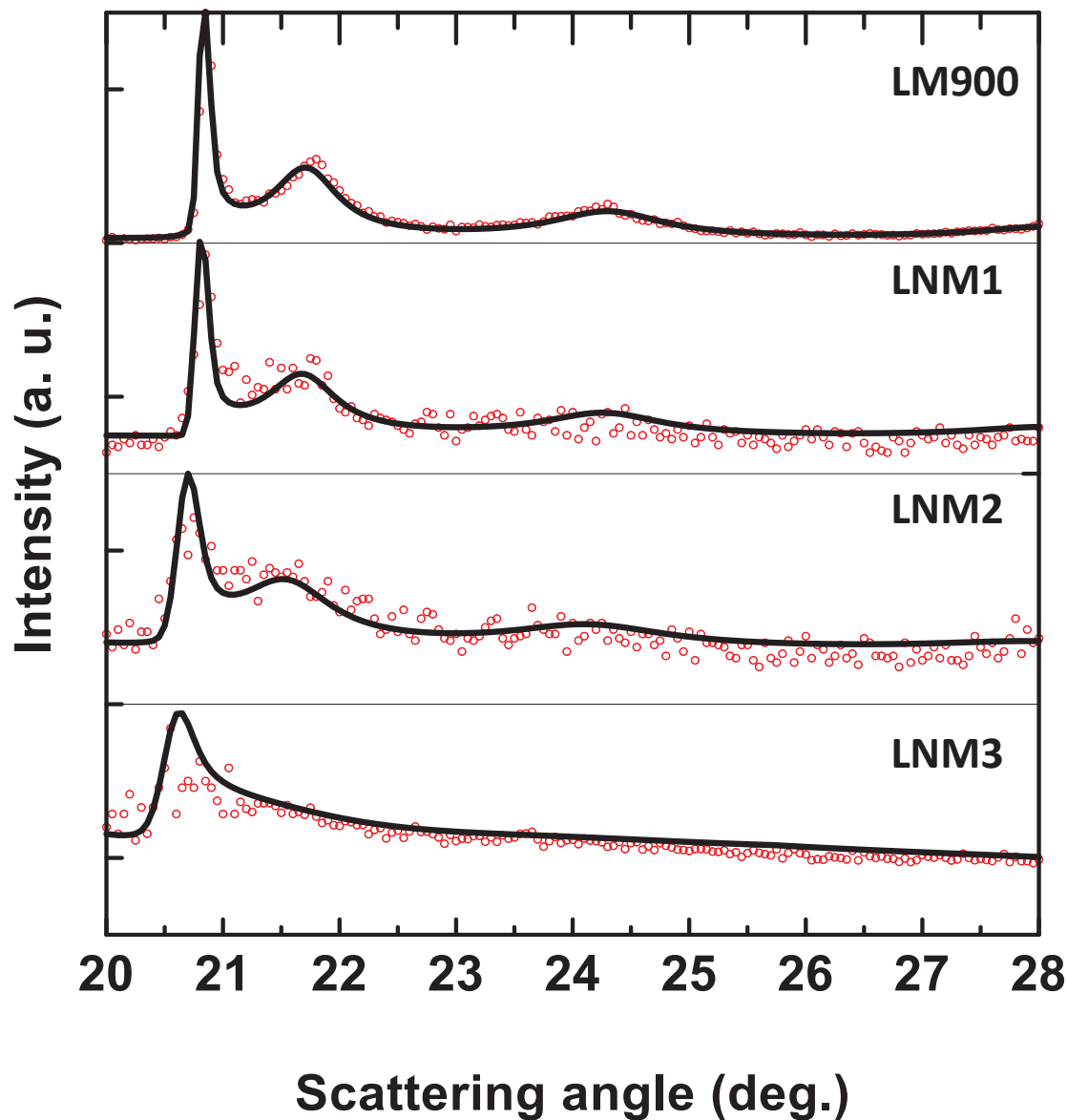


Figure 3.14 Experimental (red points) and the FAULTS fitted (black line) XRD patterns in the superlattice region ( $20^{\circ}$  to  $28^{\circ}$ ) of the studied samples in the  $\text{Li}[\text{Li}_{1/3-2x/3}\text{Ni}_x\text{Mn}_{2/3-x/3}]\text{O}_2$  series. Adapted with permission from (*J. Electrochem. Soc.* **2016**, *163* (7), A1394–A1400) Copyright (2016)

The red points and the black solid lines represent the data points and the calculated patterns, respectively. As the amount of Ni increases, the broadening of the SL peaks increased due to an increase in the stacking fault probability. Figure 3.15 shows the stacking fault probability plotted versus the Ni content. This plot clearly demonstrates how the presence of  $\text{Ni}^{2+}$  ions in the TM layer influences the probability of stacking

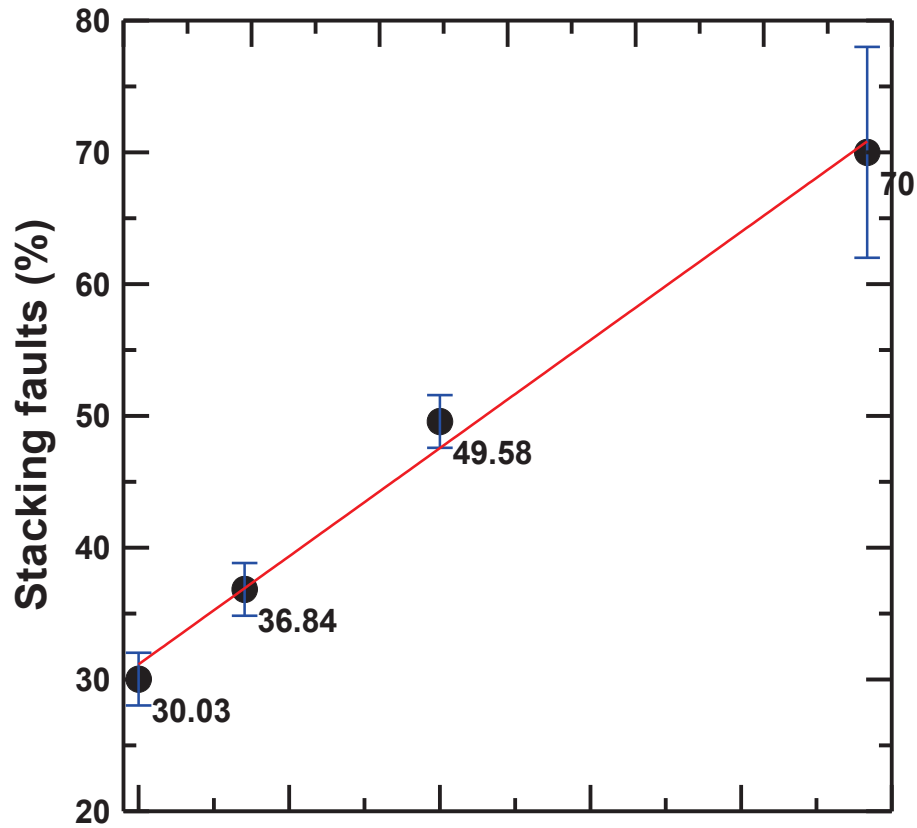


Figure 3.15 Stacking fault probabilities ( $\hat{s}$ ) versus Ni content ( $\hat{x}$ ) of the studied samples in the  $\text{Li}[\text{Li}_{1/3-2x/3}\text{Ni}_x\text{Mn}_{2/3-x/3}]\text{O}_2$  series.

Adapted with permission from (*J. Electrochem. Soc.* **2016**, 163 (7), A1394–A1400) Copyright (2016)

faults. For the sample LNM3, the superlattice peak broadening with change in the stacking faults probability is very subtle due to the very weak superlattice peaks. Hence the uncertainty of the stacking fault probability reported for LNM3 is higher.

### 3.8 Conclusions

The superlattice peak broadening in the XRD patterns of some LLRTMO materials has been examined. First, by using a fitting program called FAULTS, which can take into account the existence of stacking faults, the XRD patterns of  $\text{Li}_2\text{MnO}_3$  were simulated

and fitted. The fitting results revealed that the stacking disorder along the  $c$  axis (stacking faults) is the underlying reason for the superlattice peak broadening. Similarly, the XRD patterns of  $\text{Li}[\text{Li}_{1/3-2x/3}\text{Ni}_x\text{Mn}_{2/3-x/3}]\text{O}_2$  materials were also examined. The superlattice peak positions of  $\text{Li}[\text{Li}_{1/3-2x/3}\text{Ni}_x\text{Mn}_{2/3-x/3}]\text{O}_2$  materials changed monotonically with Ni content, as did the main peaks, demonstrating that the superlattice peaks originate from solid solutions and are not caused by any separate phase such as  $\text{Li}_2\text{MnO}_3$  in a composite.

FAULTS results on  $\text{Li}[\text{Li}_{1/3-2x/3}\text{Ni}_x\text{Mn}_{2/3-x/3}]\text{O}_2$  materials showed that stacking fault probability increased with Ni content. Hence, it is believed that presence of aliovalent ions such as  $\text{Ni}^{2+}$  in the TM layer can perturb the stacking order along the  $c$ -axis and thus the broadening of the superlattice peaks of  $\text{Li}[\text{Li}_{1/3-2x/3}\text{Ni}_x\text{Mn}_{2/3-x/3}]\text{O}_2$  materials. It is expected that the presence of  $\text{Co}^{3+}$  ions in the TM layer can also induce the stacking faults in the same way as  $\text{Ni}^{2+}$  ions.

## Chapter 4 Effect of lithium content on the first-cycle irreversible capacity loss of layered lithium-rich transition metal oxides<sup>B</sup>

### 4.1 Introduction

Layered Li-rich transition metal oxide (LLRTMO) materials suffer from high irreversible capacity (IRC). For example,  $\text{Li}[\text{Li}_{0.2}\text{Ni}_{0.2}\text{Mn}_{0.6}]\text{O}_2$  and  $\text{Li}[\text{Li}_{0.200}\text{Mn}_{0.533}\text{Ni}_{0.133}\text{Co}_{0.133}]\text{O}_2$  exhibit IRCs of about 70 mAh/g (~20 %) <sup>106</sup> and 75 mAh/g (~17 %) <sup>64</sup>, respectively. Understanding the effect of metal composition on the first-cycle behavior of LLRTMO is essential to find ways for lowering the IRC. This chapter explores how IRC can be reduced by adjusting the Li content of a LLRTMO material.

IRC in positive electrode materials is a measure of the proportion of  $\text{Li}^+$  ions that is unable to reintercalate back into the host structure during the first discharge at reasonable rates <sup>107</sup>. Researchers generally believe that a large IRC in LLRTMO materials is associated with the irreversible oxygen loss occurring around 4.5 V during the first charge <sup>48,59</sup>. Hence, there have been several attempts to reduce the oxygen release during the first charge. One general approach to suppress the oxygen release is partially delithiating the pristine material using chemical methods and thereby limiting the total amount of Li extraction while traversing along the 4.5 V plateau. Chemical delithiation of pristine LLRTMO materials has been attempted using acid leaching but caused structural instability associated with a  $\text{H}^+/\text{Li}^+$  exchange reaction <sup>108</sup>. A similar approach to acid leaching is chemical treatment of the pristine LLRTMO materials using reagents such as

---

<sup>B</sup> Portions of this Chapter were adapted with permission from Shunmugasundaram, R.; Arumugam, R. S.; Dahn, J. R. High Capacity Li-Rich Positive Electrode Materials with Reduced First-Cycle Irreversible Capacity loss. *Chem. Mater.*, **2015**, 27 (3), 757–767. The author's contribution to this work included synthesis of materials, XRD measurements and electrochemical characterization.



$\text{Na}_2\text{S}_2\text{O}_8$ <sup>109</sup>. The observed low-IRC behavior was claimed to be caused by the formation of a spinel phase on the surface of the active material. Blending LLRTMO materials with different materials such as  $\text{V}_2\text{O}_5$ <sup>110</sup> or  $\text{LiV}_3\text{O}_8$ <sup>111</sup>, which can intercalate lithium near 3.5 V, reduces IRC but at the expense of lower energy density. Surface coating<sup>112</sup> methods have been shown to reduce the IRC in an unknown manner and at the apparent expense of overall specific capacity. All the above strategies use post-synthesis chemical treatments of the pristine materials. Such methods not only require harsh chemical conditions but also incur extra processing costs. By contrast, this study focuses on making new LLRTMO materials with a synthesis procedure that can be scaled-up.

A recent report from the Tarascon group showed reduced IRC (only 10 to 12 %) in  $\text{Li}_2\text{Ru}_{0.5}\text{Sn}_{0.5}\text{O}_3$  or  $\text{Li}_{1.333}\text{Ru}_{0.333}\text{Sn}_{0.333}\text{O}_2$ <sup>68</sup>. They claim that the Sn atoms make the M-O bonding “more flexible” and essentially minimize the oxygen release, hence reducing IRC. Alternatively, interlayer cation mixing may have been prevented or hindered by using a larger ion ( $\text{Sn}^{4+}$ ) in the place of the 3d metals. However, such materials with expensive 4d-TM ions will have no commercial value.

In this work, the impact of Li content on the IRC of LLRTMO materials made from a  $\text{Ni(II)}_{0.167}\text{Mn(II)}_{0.5}\text{Co(II)}_{0.333}\text{CO}_3$  (sample A) precursor and  $\text{Li}_2\text{CO}_3$  was systematically studied. First, a stoichiometric LLRTMO material (sample A1) from precursor A was made as per the calculation explained in Table 2.2 (See Chapter 2). Apart from that, “Li-deficient” LLRTMO materials (A2 and A3) were also made by adding less  $\text{Li}_2\text{CO}_3$  than that required for stoichiometric balance. A systematic comparison of the properties of these materials, that were characterized using X-ray

diffraction, elemental analysis, He pycnometry, and electrochemical methods, will be the subject of this chapter.

## 4.2 First charge-discharge cycle

Table 4.1 shows the nominal (target) compositions of the samples A1, A2 and A3. The Li/TM ratio was reduced gradually from A1 to A2 and to A3. This particular change in the Li/TM ratio between the samples has a profound effect on the electrochemical behaviour, especially on the IRC of the materials.

Table 4.1 Nominal compositions of the precursors and the LLRTMO samples A1 to A3

<b>Nominal Precursor Composition</b>	<b>Nominal Composition of the sample</b>	<b>Expected specific capacity if all Li removed (mAh/g)</b>
$\text{Ni}_{0.166}\text{Mn}_{0.5}\text{Co}_{0.333}$ (A)	$\text{Li}_{1.143}\text{Ni}_{0.143}\text{Mn}_{0.429}\text{Co}_{0.285}\text{O}_2$ (A1)	345
$\text{Ni}_{0.166}\text{Mn}_{0.5}\text{Co}_{0.333}$ (A)	$\text{Li}_{1.067}\text{Ni}_{0.156}\text{Mn}_{0.467}\text{Co}_{0.311}\text{O}_2$ (A2)	309
$\text{Ni}_{0.166}\text{Mn}_{0.5}\text{Co}_{0.333}$ (A)	$\text{Li}_{1.050}\text{Ni}_{0.159}\text{Mn}_{0.475}\text{Co}_{0.316}\text{O}_2$ (A3)	301

Figure 4.1 shows the first cycle voltage - specific capacity profiles ranging between 2 V and 4.8 V for LLRTMO samples A1, A2 and A3. As explained in section 1.3.3.3, the sloping region between the OCV and  $\sim 4.5$  V corresponds to the oxidation of TM ions ( $\text{Ni}^{2+}$  to  $\text{Ni}^{4+}$  and  $\text{Co}^{3+}$  to  $\text{Co}^{4+}$ ). The plateau region starting from  $\sim 4.5$  V is caused by oxygen release, oxygen oxidation or a combination of both. The total charge specific capacity obtained from the first charge (indicated by vertical lines) decreases

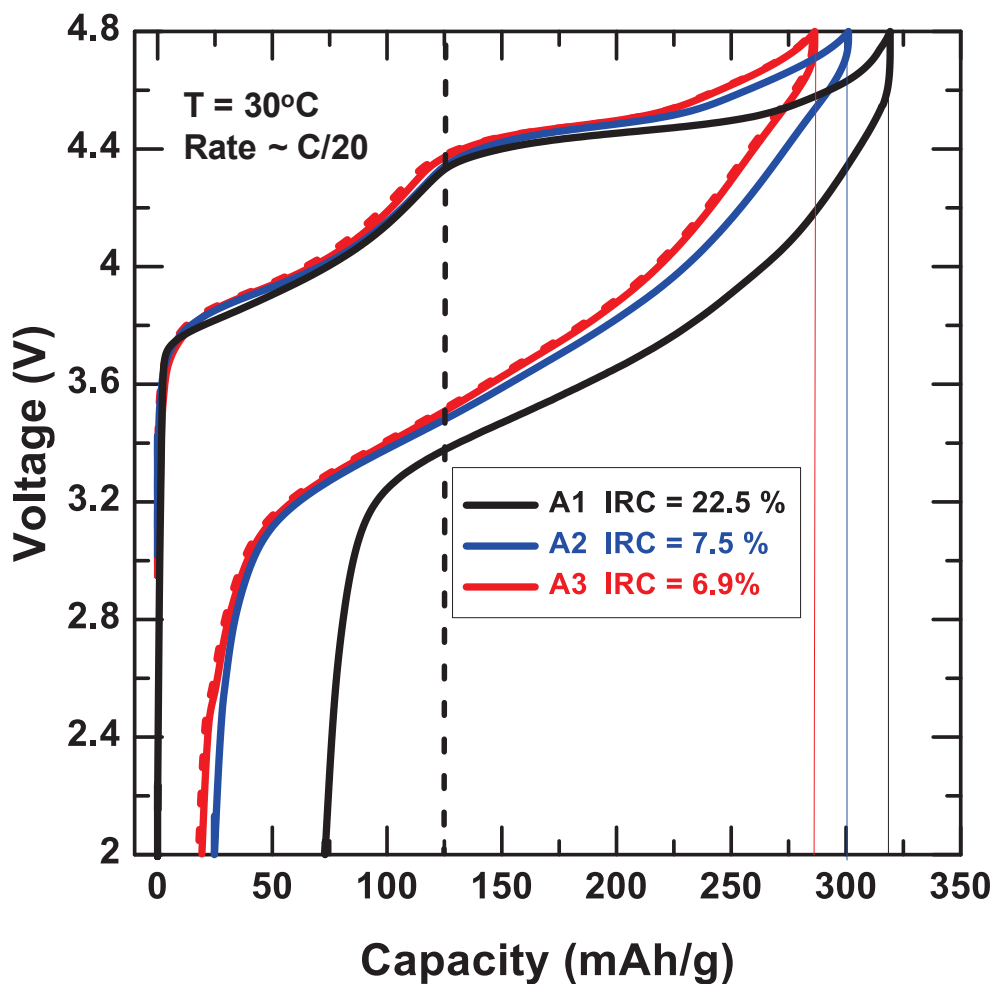


Figure 4.1 First-cycle voltage vs specific capacity profiles of samples: A1, A2 and A3.

The dotted lines represent their respective sister cells.

Adapted with permission from (*Chem. Mater.*, **2015**, 27 (3), 757–767)

Copyright (2015) American Chemical Society

from sample A1 to A2 to A3 in accordance with their total Li content. By contrast, the first discharge specific capacity increases from sample A1 (247 mAh/g) < A2 (272 mAh/g) and A3 (266 mAh/g). The IRC also drops from A1 to A2 to A3. The % IRC is given in the legend of Figure 4.1 Sample A1, which has a stoichiometrically balanced amount of Li, has an IRC greater than 20%, as expected for a typical LLRTMO material such as  $\text{Li}[\text{Li}_{0.2}\text{Ni}_{0.2}\text{Mn}_{0.6}]\text{O}_2$ <sup>71</sup>. Surprisingly and beneficially, the Li-deficient members (e.g. A2 and A3) show IRCs as low as 6.5 %.

Figure 4.1 shows that the sloping region capacity (indicated by a dotted vertical line) of all the samples is very close implying the total capacity obtained as a result of TM redox is almost the same. However, sample A1 exhibits the largest plateau-region capacity whereas the A3 has the smallest. A lower Li content in the pristine structure, for A2 and A3, may cause a relatively smaller amount of oxygen release or oxygen oxidation during the  $\sim 4.5$  V plateau. In any event, adjusting the Li/M ratio dramatically affects the IRC.

Figure 4.2 shows the measured (black dotted line) and calculated (red line) XRD patterns of samples A1, A2 and A3. The difference between the calculated and the measured patterns is shown using a green line below the XRD patterns. The calculated patterns were deduced from the Rietveld method with appropriate crystallographic

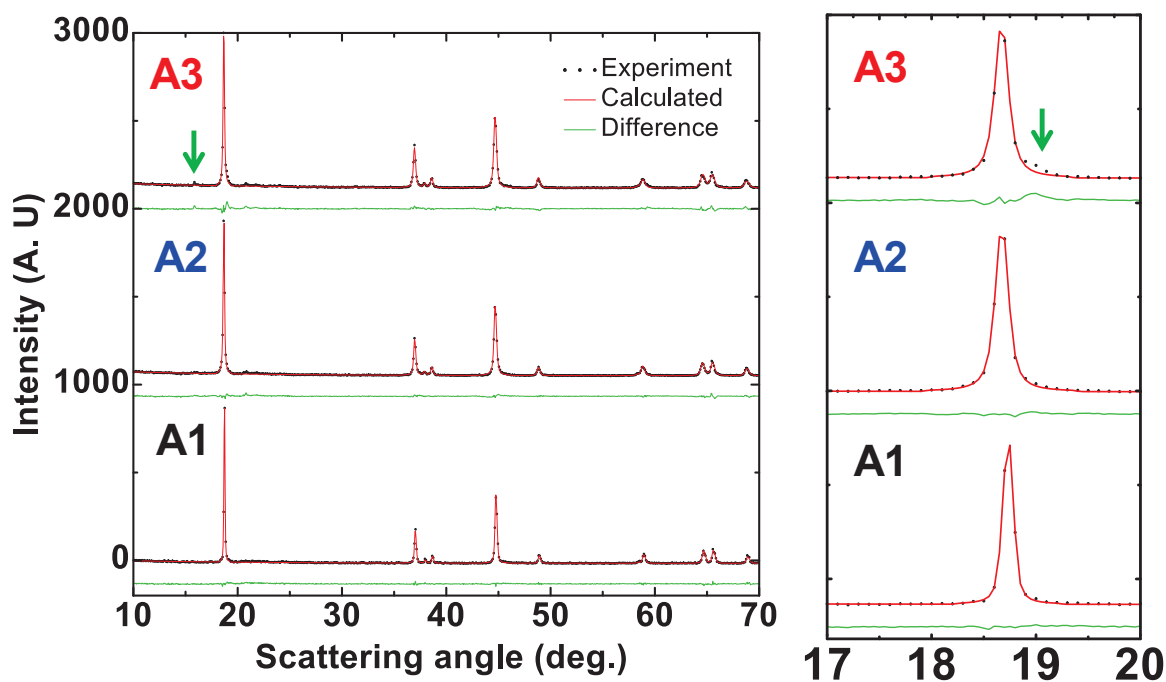


Figure 4.2 Left Panel: X-ray diffraction patterns of samples A1, A2 and A3. Right panel: Enlarged view between  $17^\circ$  and  $20^\circ$  showing the (003) peak corresponding to  $R\text{-}3m$  spacegroup.

Adapted with permission from (*Chem. Mater.*, **2015**, 27 (3), 757–767)  
Copyright (2015) American Chemical Society

Table 4.2 Structural parameters obtained from Rietveld refinement of the XRD patterns of samples A1, A2 and A3

Sample	$a$ (Å)	$c$ (Å)	$z(\text{O})$	n Ni in Li sites	$R_B$
A1	2.8452(8)	14.213(4)	0.259(3)	0.006(3)	2.58
A2	2.8476(6)	14.235(2)	0.258(4)	0.013(6)	2.75
A3	2.8483(3)	14.243(1)	0.254(7)	0.027(2)	4.14

parameters. Table 4.2 shows the structural parameters that include  $a$  and  $c$ , obtained from the Rietveld refinement. Sample A1 is a pure single-phase layered material with O3 structure, analogous to  $\alpha$ -NaFeO<sub>2</sub>. The Rietveld refinements have been made using the space group  $R\bar{3}m$  but their weak superstructure peaks between 20° to 30° were not considered. Table 4.2 shows that very little cation mixing occurred in any of the samples.

The XRD patterns in Figure 4.2 suggest that samples A1 and A2 are predominantly single phase. However, sample A3 has two impurity peaks indicated by arrows in its XRD pattern in Figure 4.2. First, there is a very low intensity peak at ~15.8° which may correspond to orthorhombic LiMnO<sub>2</sub> that could have emerged during the synthesis. The JCDPS database shows that orthorhombic LiMnO<sub>2</sub> has a strong Bragg peak at ~15.8°<sup>13</sup>. However, the presence of such a tiny amount of orthorhombic LiMnO<sub>2</sub> is not expected to cause the low-IRC behavior. Second, there is a hump at 18.7° (clearly shown in the right panel in Figure 4.2) in the XRD pattern of A3. This may be an evidence of nano-domains of an adjoining spinel phase. The spinel structure can accommodate Li<sup>+</sup> ions into its 16c sites during discharge provided the lower cut-off potential is below 2.8 V so it could be

the reason for the low-IRC behavior<sup>114</sup>. Hence experiments were conducted to ascertain the presence of spinel phase and its possible contribution to the low-IRC behavior.

### 4.3 Effect of spinel impurity

To check whether the XRD experiments could detect small amounts of spinel admixture, nano-sized spinel  $\text{LiNi}_{0.5}\text{Mn}_{1.5}\text{O}_4$  (sample S) was synthesized at low temperature. Figure 4.3 shows scanning electron micrograph images of the nano-sized  $\text{LiNi}_{0.5}\text{Mn}_{1.5}\text{O}_4$  indicating that the primary particles were about 100 nm in size. The nano-

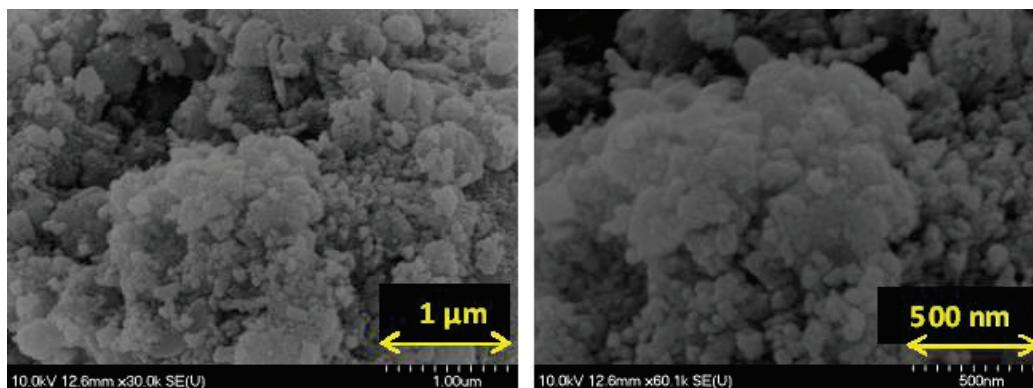


Figure 4.3. SEM images of sample S (nano-sized  $\text{LiNi}_{0.5}\text{Mn}_{1.5}\text{O}_4$ )  
Adapted with permission from (*Chem. Mater.*, **2015**, 27 (3), 757–767)  
Copyright (2015) American Chemical Society

sized spinel was physically mixed with sample A1 in two different weight proportions (5 and 10 wt %) and XRD patterns were measured. Figure 4.4 shows the XRD patterns of admixtures 95 wt % A1 + 5 wt % of spinel and 90 wt % A1 + 10 wt % of spinel. For comparison, the XRD patterns of the sample A1 and the nano-sized spinel (S) are also presented in Figure 4.4. The evolution of a new Bragg peak at  $36.4^\circ$  (shown using green arrows in Figure 4.4) is a clear marker for the presence of the nano-sized spinel phase. With the increase in the fraction of the spinel phase from 5% to 10%, the peak intensity

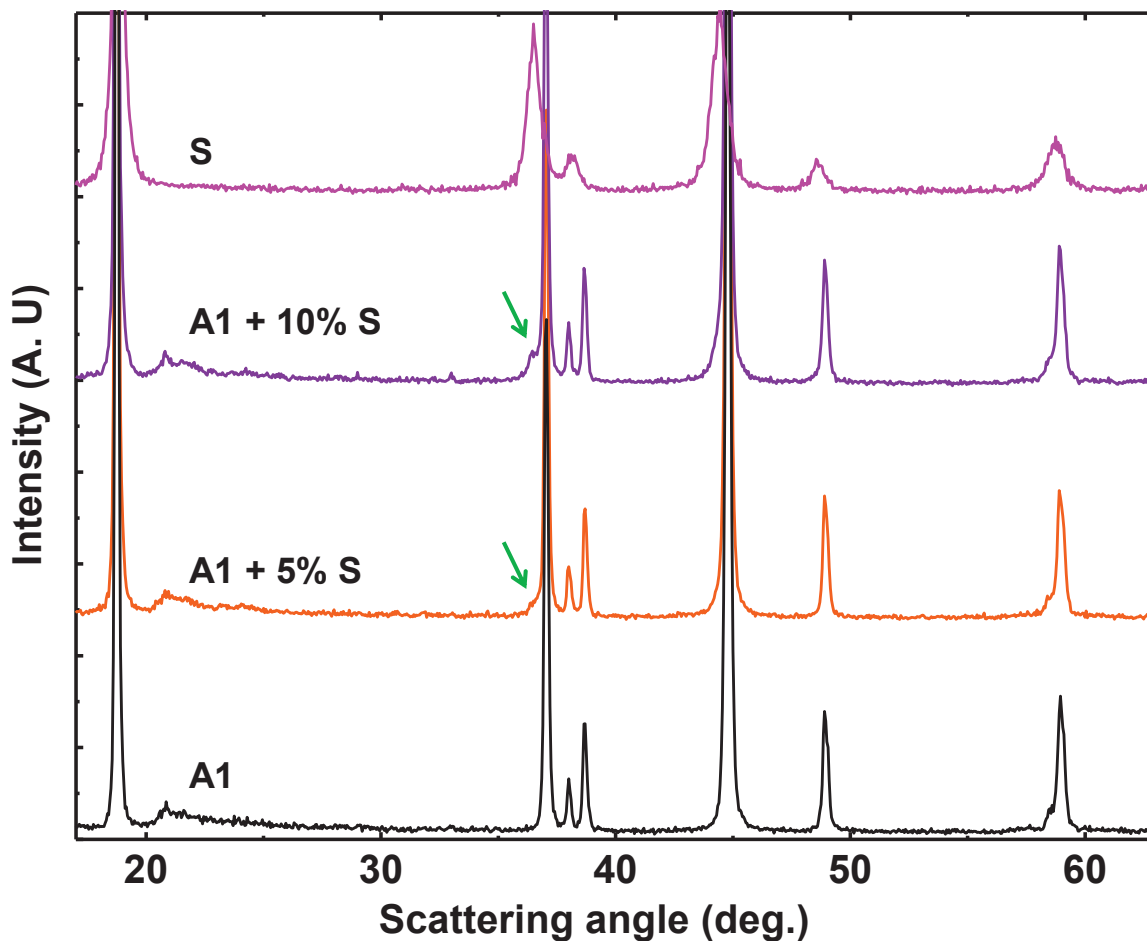


Figure 4.4 X-ray diffraction patterns of samples A1, A1 + 5% Spinel, A1 + 10% Spinel and pure Spinel

“S” refers to nano-sized spinel  $\text{LiNi}_{0.5}\text{Mn}_{1.5}\text{O}_4$ . Green arrows indicate the presence of spinel “S”

Adapted with permission from (*Chem. Mater.*, **2015**, 27 (3), 757–767) Copyright (2015) American Chemical Society

grows proportionally. Thus the XRD patterns can detect the presence of nano-sized spinel.

Figure 4.5 shows the XRD patterns in the range of scattering angles from  $35^\circ$  to  $39^\circ$  for samples A1, A2 and A3 along with the spinel admixtures containing the intentionally added nano-sized spinel. The XRD patterns of A2 and A3 did not show any peaks corresponding to the spinel phase. However, the (101) peaks at ( $\sim 37^\circ$ ) of samples

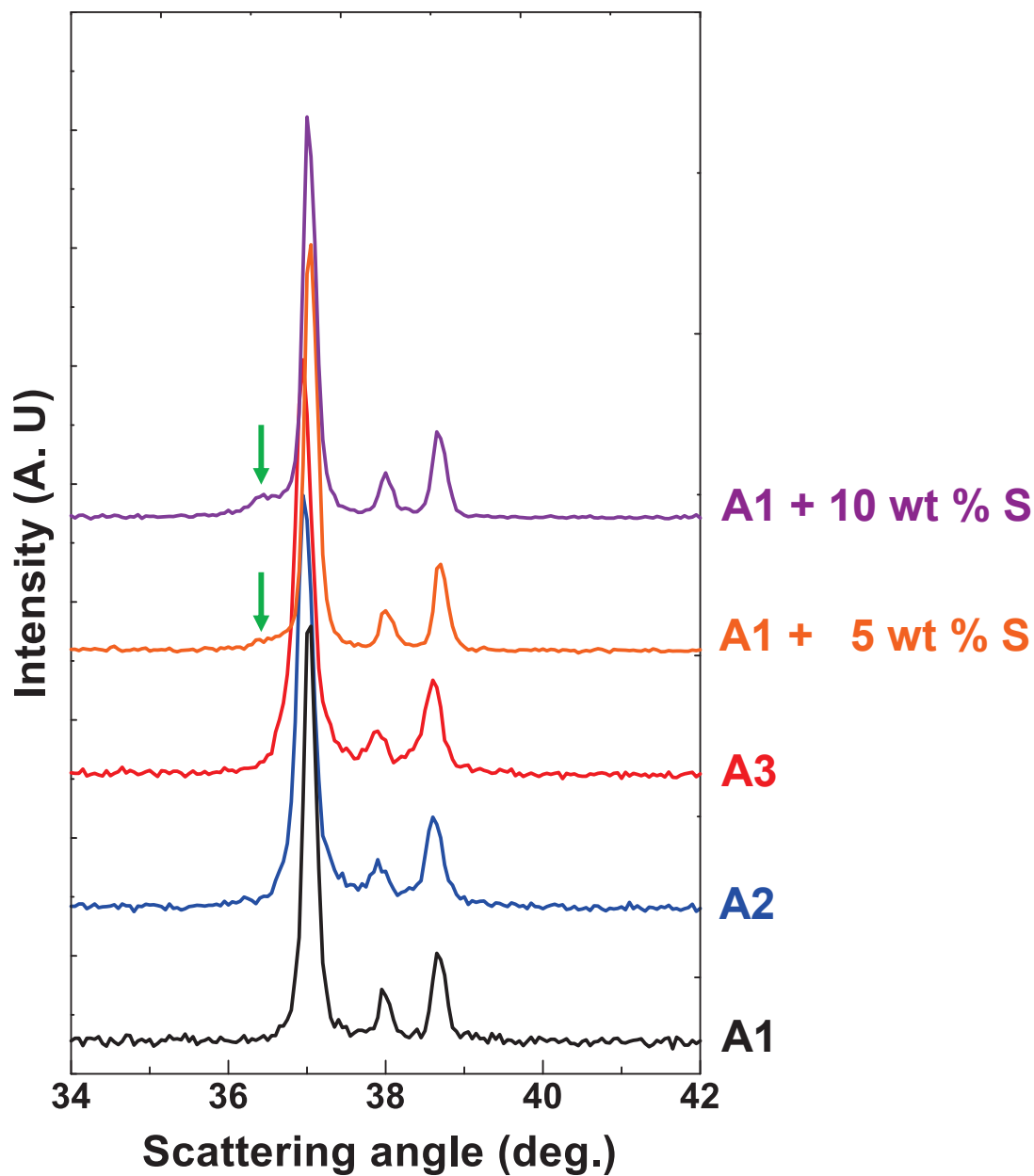


Figure 4.5 X-ray diffraction patterns in the range of  $35^{\circ}$  to  $39^{\circ}$  for A1, A2, A3, A1 + 5% Spinel, A1 + 10% Spinel.

“S” refers to nano-sized  $\text{LiNi}_{0.5}\text{Mn}_{1.5}\text{O}_4$ . Green arrows indicate the presence of spinel “S” Adapted with permission from (*Chem. Mater.*, **2015**, 27 (3), 757–767) Copyright (2015) American Chemical Society

A2 and A3 were broader than that of A1 and may have been caused by an overlapping peak from the spinel phase. Hence the samples were characterized electrochemically to probe for the presence of the spinel phase.



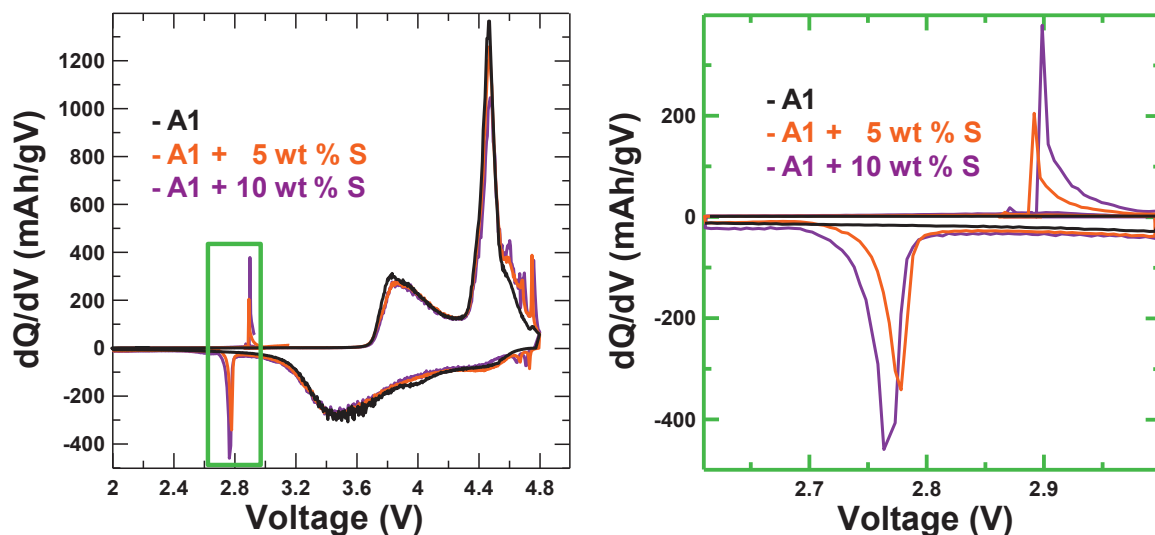


Figure 4.6 Left panel:  $dQ/dV$  versus  $V$  for samples A1, A1 + 5% Spinel and A1 + 10% Spinel in the voltage range between 2 and 4.8 V. Right panel: The green bordered portion between 2.6 and 3 V has been enlarged and is shown separately for clarity Adapted with permission from (*Chem. Mater.*, **2015**, 27 (3), 757–767). Copyright (2015) American Chemical Society

Coin cells were made from the electrodes of samples A1, 95 wt % A1 + 5 wt % of spinel and 90 wt % A1 + 10 wt % of spinel were measured and electrochemically cycled from 2 V to 4.8 V and Figure 4.6 shows their  $dQ/dV$  versus  $V$  plots. The right panel shows an enlarged portion of the  $dQ/dV$  vs  $V$  plot in the voltage range from 2.6 V to 3 V. The oxidation peaks around 2.9 V and the concomitant reduction peaks around 2.75 V were caused by the spinel  $\text{LiNi}_{0.5}\text{Mn}_{1.5}\text{O}_4$ . The  $dQ/dV$  peaks grow with the fraction of the spinel phase just as the growth of the  $36.4^\circ$  peak in the XRD patterns in Figure 4.4. Thus electrochemical characterization proves to be quite powerful to identify any spinel phase even in tiny amounts.

Figure 4.7 shows  $dQ/dV$  vs  $V$  for samples A1, A2, and A3 along with A1 + 5% spinel and A1 + 10% spinel admixtures. Figure 4.7 shows no evidence of spinel  $\text{LiNi}_{0.5}\text{Mn}_{1.5}\text{O}_4$  in samples A2 and A3. However, Figure 4.7 reveals an extra pair of redox

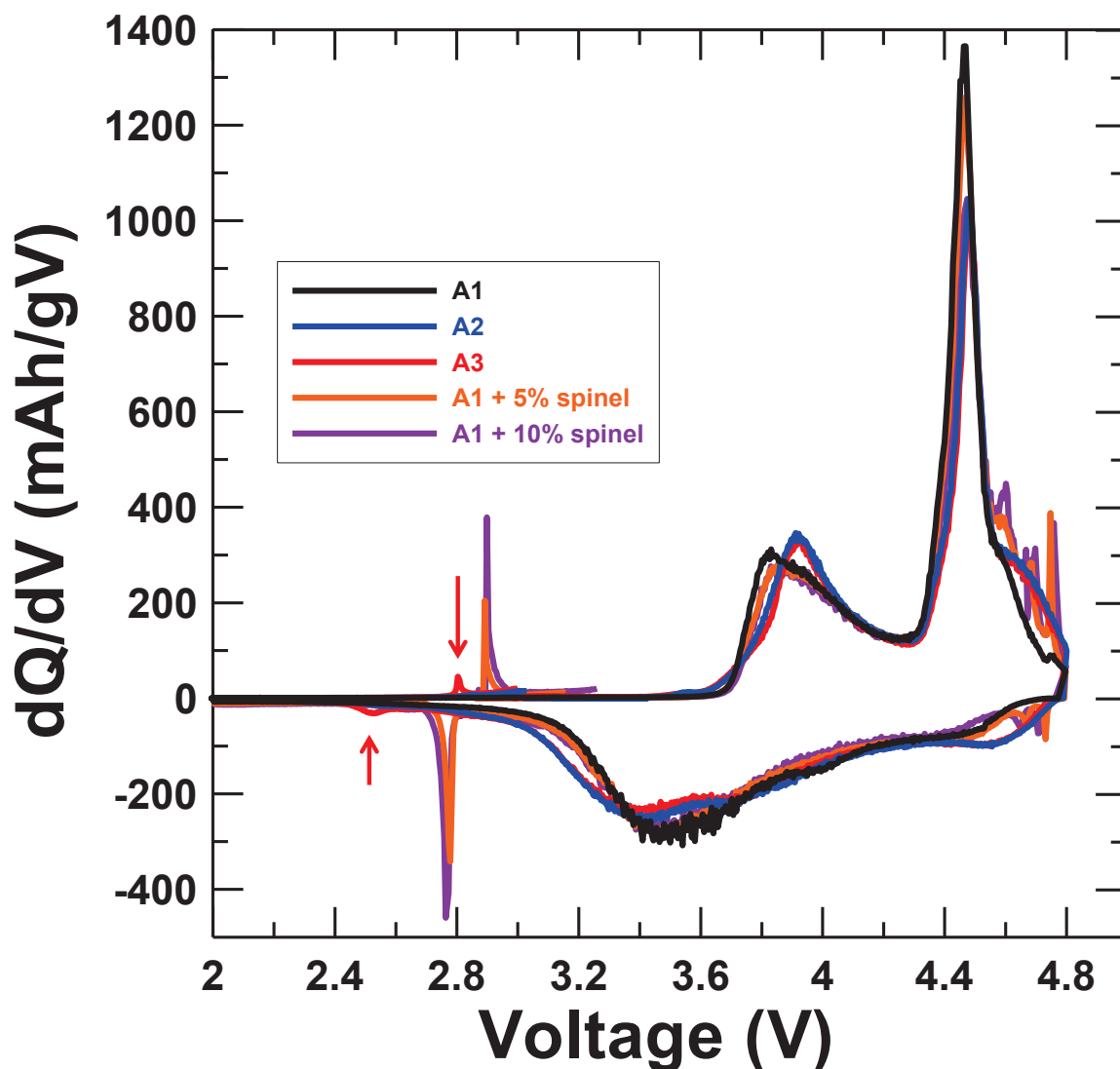


Figure 4.7 dQ/dV versus V for samples A1, A2, A3, A1 + 5% Spinel and A1 + 10% Spinel. Red arrows indicate the presence of an impure phase in A3. Adapted with permission from (*Chem. Mater.*, **2015**, 27 (3), 757–767). Copyright (2015) American Chemical Society

peaks in sample A3, which can be distinguished from the peaks corresponding to the  $\text{LiNi}_{0.5}\text{Mn}_{1.5}\text{O}_4$  spinel phase (S) that appeared between 2.4 V and 2.9 V. Those two peaks, both during charge and discharge are indicated using red arrows in Figure 4.7. If a feature representing a particular crystallographic phase can be identified in dQ/dV versus V, then there should be a corresponding signature in the XRD pattern as well. Hence the XRD patterns of the samples, particularly sample A3, were re-examined carefully.

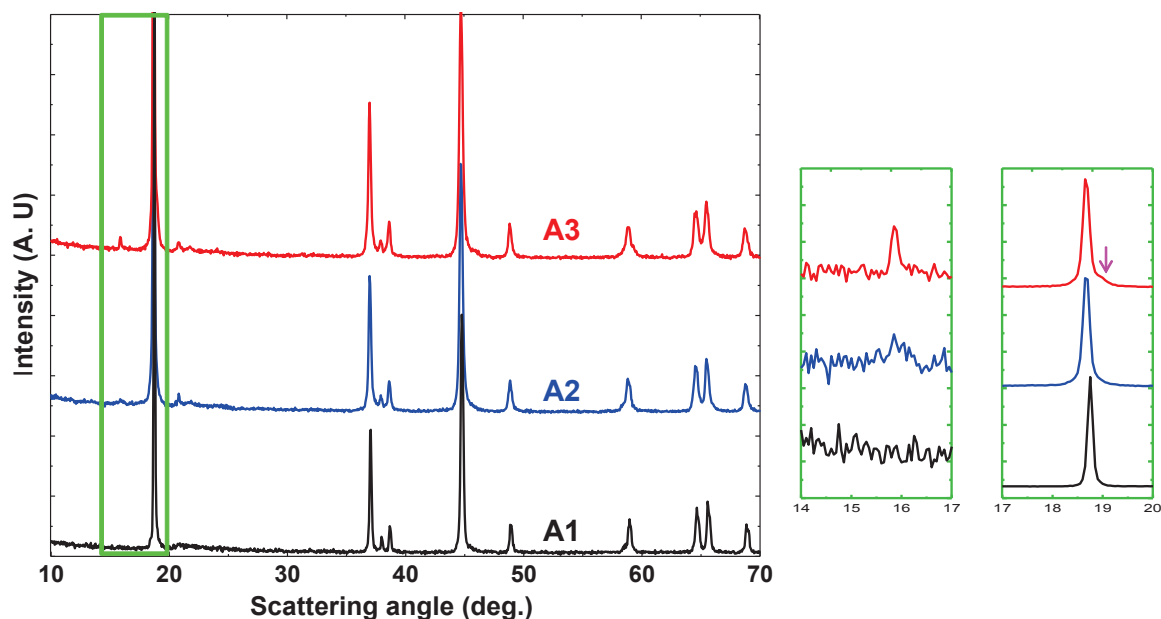


Figure 4.8 Left panel: X-ray diffraction patterns of samples A1, A2 and A3. Bottom panel: Right panels: The green bordered portion between  $14^{\circ}$  and  $17^{\circ}$  and  $17^{\circ}$  and  $20^{\circ}$  has been enlarged and is shown separately for clarity.

Adapted with permission from (*Chem. Mater.*, **2015**, 27 (3), 757–767). Copyright (2015) American Chemical Society

Figure 4.8 shows the XRD patterns of samples A1, A2 and A3 over the complete range between  $10^{\circ}$  to  $90^{\circ}$  and an expanded view of the patterns between  $14^{\circ}$  to  $17^{\circ}$  and  $17^{\circ}$  to  $20^{\circ}$  is given separately in the right panels. The extra pair of redox peaks in dQ/dV vs. V especially for sample A3 may correlate to either the appearance of an XRD peak at  $15.7^{\circ}$  or to the hump at  $18.7^{\circ}$ . The enlarged portion in the right panel between  $14^{\circ}$  to  $17^{\circ}$  shows that the  $15.7^{\circ}$  XRD peak can be seen in sample A2 as well whereas the panel between  $17^{\circ}$  to  $20^{\circ}$  shows that the hump at the  $18.7^{\circ}$  is absent in sample A2. The electrochemical characterization of the composite layered-spinel in Ref. 26 shows a pair of redox peaks closer to the one observed here that corresponds to  $\text{LiNi}_{0.425}\text{Co}_{0.075}\text{Mn}_{1.5}\text{O}_4$ . The redox peaks for orthorhombic  $\text{LiMnO}_2$  are at a higher voltage<sup>24</sup>. Hence, the hump at  $18.7^{\circ}$  is most likely due to a spinel phase, whose composition remains unknown here.

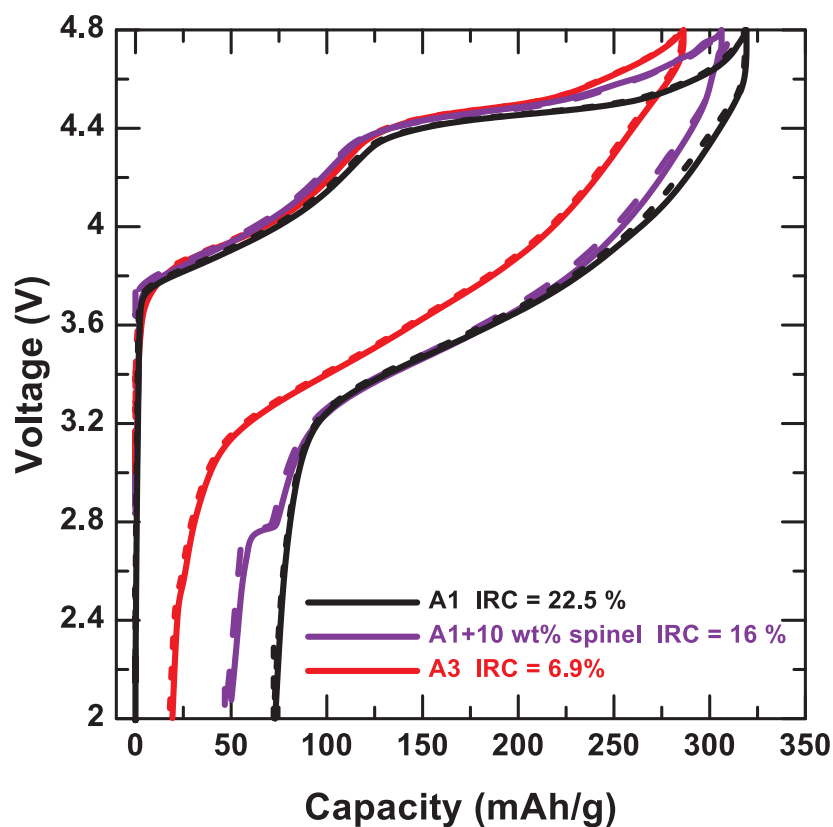


Figure 4.9 First. cycle voltage - specific capacity profiles of samples, A1, A1+10 wt. % spinel and A3

Figure 4.9 shows the first cycle voltage - specific capacity profiles of samples, A1, A1+10 wt. % spinel and A3. The sample A1+10 wt. % spinel exhibited an IRC of 16 %. The reduced IRC was clearly caused by the 10 wt % spinel phase only when discharged below 2.8 V. However, even after the addition of 10 wt. % spinel, the IRC was not as small as sample A3 (6.5 %). A spinel-layered composite reported by Lee et al. had 18 % IRC even with 25 mol % of spinel. It should be noted that the extra discharge capacity observed below 2.8 V in A3 is very small and cannot be responsible for such small IRC. In other words, if the lower cut-off voltage was set to 2.8 V, for example, low-IRC would still be observed. Thus the possibility of nano-domains of impurity phases for the cause of small IRC observed in samples A2 and A3 can be ruled out. Instead the low-IRC appears

to be inherent to LLRTMO layered materials of such compositions. It is quite difficult to determine the composition of the impurities because their proportions are very low. Instead of trying to identify the composition of the impurities, steps were taken to eliminate the impurities from sample A3 and to check if the reduced IRC is in any way associated to the presence of the impurity phases.

#### 4.4 Synthesis by quenching

Based on suggestions in the work of McCalla et al.<sup>115</sup>, a sample (A3Q) with composition exactly same as that of A3 was synthesized using the same precursor (A) but was quenched from 900°C to room temperature instead of cooling slowly. Figure 4.10

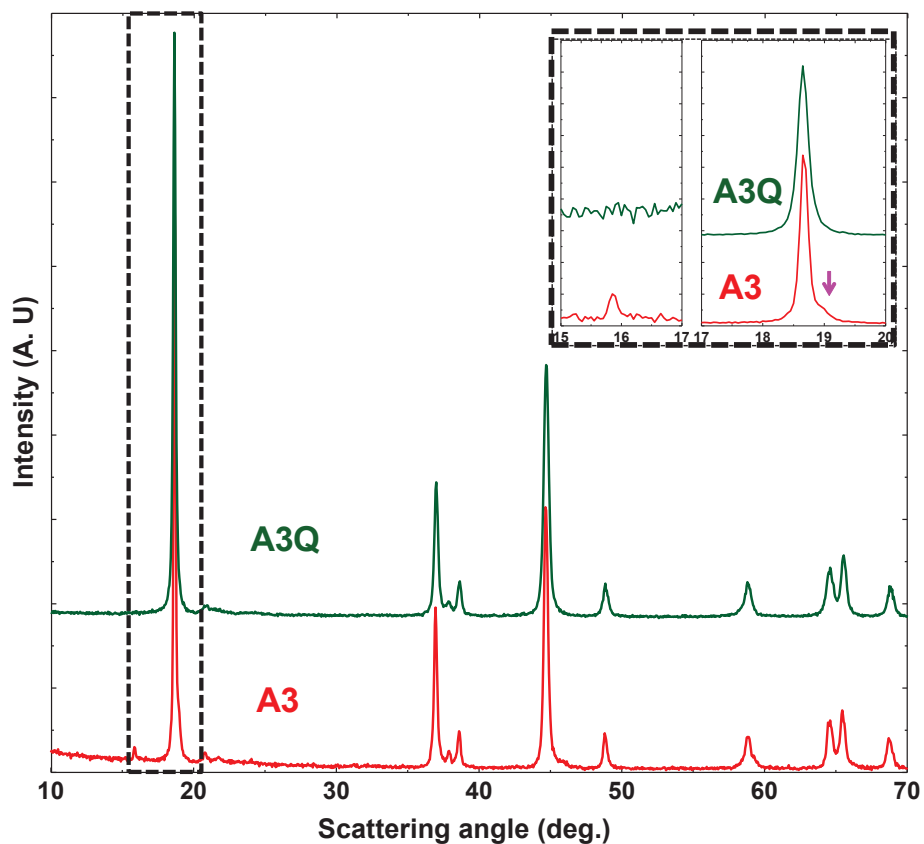


Figure 4.10 XRD patterns of A3 and A3Q (Quenched)  
Adapted with permission from (*Chem. Mater.*, **2015**, 27 (3), 757–767). Copyright (2015) American Chemical Society

shows the XRD patterns of samples A3 and A3Q. The inset shows an enlarged view of pattern between  $14^\circ$  and  $20^\circ$  to check for the presence of impurities. The quenching strategy resulted in a single phase material and eliminated the impurities completely. The XRD patterns of A3 and A3Q are otherwise identical, as expected, with the absence of the impurity peak at  $15.7^\circ$  and the hump at  $18.7^\circ$  as well. Sample A3Q was also tested electrochemically and the first cycle data were extracted.

Figure 4.11 shows the first cycle V vs Q profile of samples A3 and A3Q. The voltage profile of sample A3Q replicates that of sample A3. The IRC measured for sample A3Q (6.9 %) is very close to that of sample A3 (6.5 %). This unambiguously shows that the reduction in IRC is not an effect of an impurity phase including any spinel

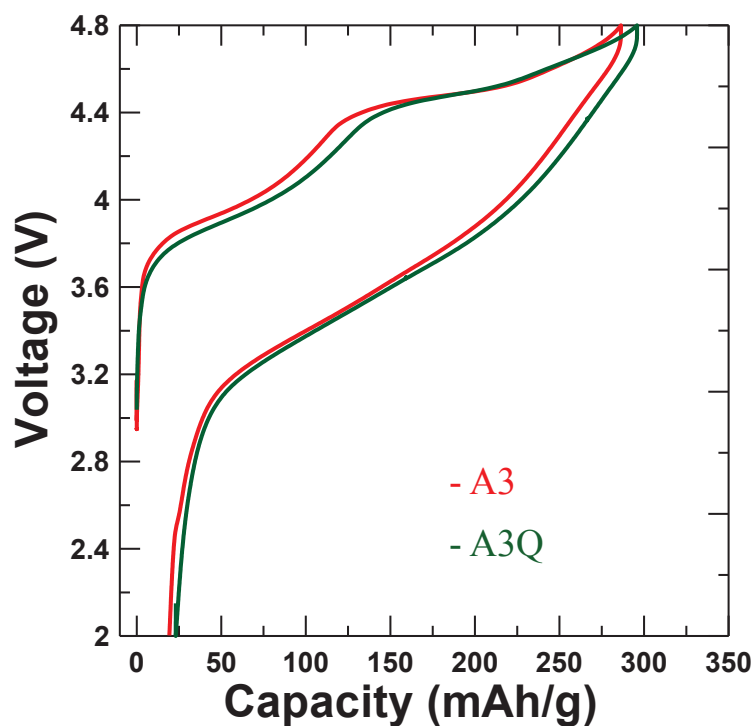


Figure 4.11 First cycle voltage-capacity profile of samples A3 and A3Q.

Adapted with permission from (*Chem. Mater.*, **2015**, 27 (3), 757–767). Copyright (2015) American Chemical Society

phase in sample A3.

Figure 4.12 shows the comparison of the  $dQ/dV$  vs  $V$  plots of samples A3 and A3Q and the bottom panel in Figure 4.12 shows an enlarged view between 2.2 to 3 V. As

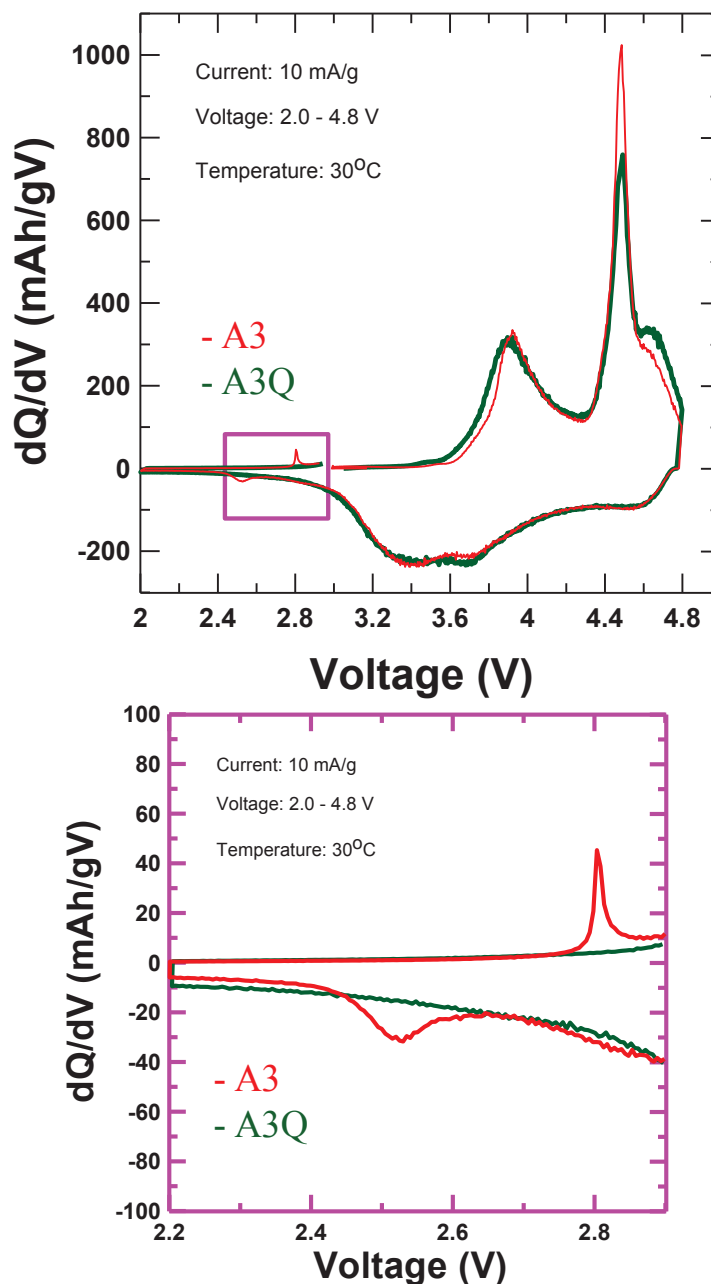


Figure 4.12 Top panel:  $dQ/dV$  versus  $V$  for samples A3 and A3Q (prepared by quenching). Bottom panel: The pink bordered portion between 2.2 and 3 V has been enlarged and is shown separately for clarity. Adapted with permission from (*Chem. Mater.*, **2015**, 27 (3), 757–767). Copyright (2015) American Chemical Society

expected, the dQ/dV profiles of samples A3 and A3Q are very similar, but the pair of redox peaks corresponding to the extra phase(s) in sample A3 does not appear in sample A3Q implying the disappearance of the impurity after quenching.

#### 4.5 Effect of surface area

What can be responsible for the small IRC in samples A2, A3 and A3Q? First of all, the effect of surface area on IRC was analyzed. Table 4.3 shows the measured specific surface area (SSA) of the samples A1, A2, A3 and A3Q. The surface area increased as the Li content decreased which is consistent with the literature<sup>116</sup>. The SSA of samples A3 and A3Q are almost equal implying that quenching did not alter the SSA. Figure 4.13 shows SEM images of the samples A1, A2 and A3. Compared to that of sample A1, the particle sizes are smaller for samples A2 and A3 and hence the higher SSAs for samples A2 and A3 are not unanticipated.

To see if high surface area caused the reduced IRC, sample A1 was ground using a mortar and pestle (for about 1h) until its SSA matched that of sample A3Q. Figure 4.13

Table 4.3 BET surface area of the samples A1, A2, A3, A3Q and GA1

Sample	Specific surface area (m <sup>2</sup> /g)
A1	1.09 ± 0.11
A2	4.09 ± 0.72
A3	4.60 ± 0.43
A3Q	4.60 ± 0.21
GA1	5.02 ± 0.07



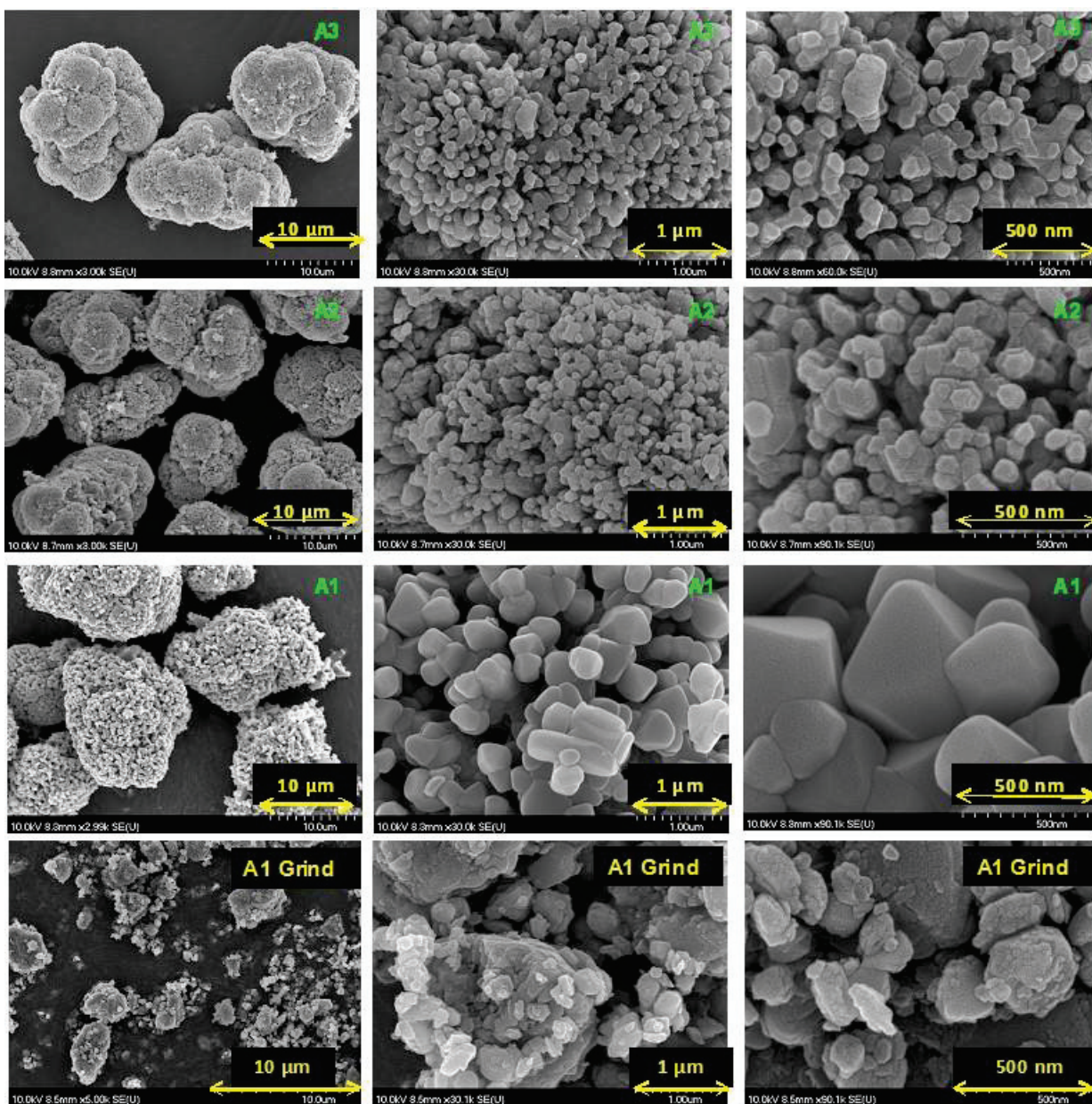


Figure 4.13 Scanning electron micrograph images of samples A1, A2, A3 and GA1 (ground sample)

Adapted with permission from (*Chem. Mater.*, **2015**, 27 (3), 757–767). Copyright (2015) American Chemical Society

shows the SEM images (bottom) of the ground sample (GA1). GA1 had a higher surface area than A1 (See Table 4.3). The first cycle IRC of GA1 was measured in the same way as done before grinding. Figure 4.14 shows the comparison of the first cycle behavior of samples A1 and GA1 and indicates that the ground sample showed the same IRC (22.5

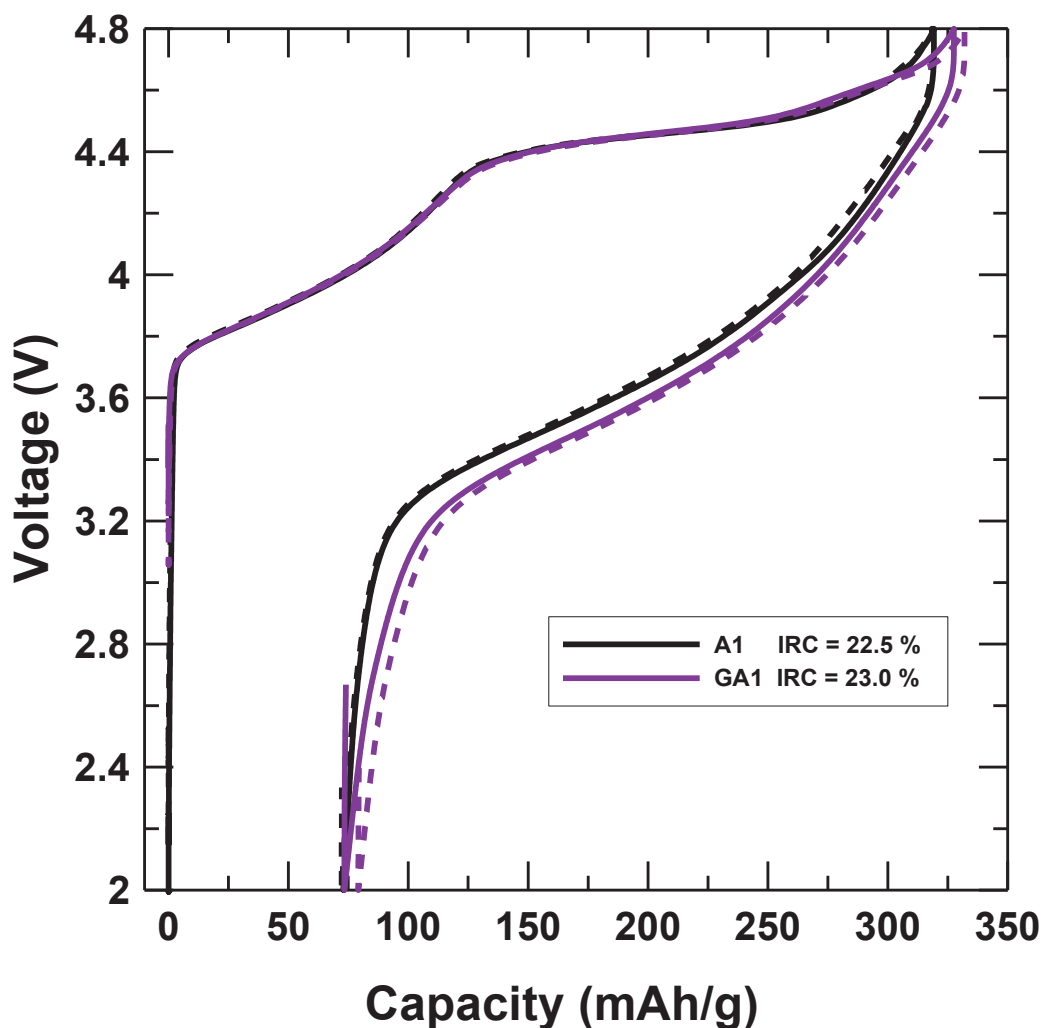


Figure 4.14 First-cycle charge-discharge voltage profiles of samples A1 and GA1 (ground sample)  
 Adapted with permission from (*Chem. Mater.*, **2015**, 27 (3), 757–767).  
 Copyright (2015) American Chemical Society

%) as the pristine one. This experiment suggests that the low-IRC behaviour has little dependence on the specific surface area at least in the compositions studied here. Recently, Verde et al. have reported that carbonate-derived Li-rich material had better first-cycle coulombic efficiency (IRC) than hydroxide or sol-gel counterparts and that might be the case in the current study<sup>117</sup>. However, all of our samples were prepared using the same methods to explore the impact of Li content on IRC.

## 4.6 ICP results

A careful analysis using ICP-OES was made to determine the true chemical compositions of the samples. Table 4.4 shows the results of the ICP-OES analysis in comparison with the target composition. The ICP-OES compositions (Li:Ni:Mn:Co) were very close to the target compositions. The total occupancy of the metal sites versus the oxygen sites is perfectly balanced in the  $\text{LiMO}_2$  structural motif. However, the total charge balance between cations and anions is not equal in samples A2 and A3 assuming  $\text{Li}^+$ ,  $\text{Ni}^{2+}$ ,  $\text{Mn}^{4+}$ ,  $\text{Co}^{3+}$  and  $\text{O}^{2-}$  <sup>118, 119, 55</sup>, because the Li/TM has been reduced from A1 to A2 to A3. For samples A2, A3 and A3Q, when the Li, Ni, Mn and Co ions are assumed to be in the +1, +2, +4 and +3 oxidation states, respectively, the total cationic charge is larger than 4. At the same time, XRD proves that they are predominantly single phase

Table 4.4 Sample, target composition, number of moles of lithium required to get a formula unit of target material, number of moles of lithium originally added including extra 5 wt % for compensating Li loss to get a formula unit of target composition, composition observed from chemical analysis (ICP-OES)

Sample	Target Composition	No. of moles of Li required to get a formula unit of target composition	No. of moles of Li originally added including extra 5 wt % for Li loss	ICP-OES Li : Ni : Mn : Co = 1+p' : a : b : c	Total charge of cations in a formula unit
A1	$\text{Li}_{1.143}\text{Ni}_{0.143}\text{Mn}_{0.429}\text{Co}_{0.285}\text{O}_2$	1.143	1.200	1.126:0.147:0.429:0.298	4.030
A2	$\text{Li}_{1.067}\text{Ni}_{0.156}\text{Mn}_{0.467}\text{Co}_{0.311}\text{O}_2$	1.067	1.120	1.049:0.161:0.466:0.325	4.207
A3	$\text{Li}_{1.05}\text{Ni}_{0.159}\text{Mn}_{0.475}\text{Co}_{0.316}\text{O}_2$	1.05	1.103	1.013:0.167:0.484:0.336	4.290
A3Q	$\text{Li}_{1.05}\text{Ni}_{0.159}\text{Mn}_{0.475}\text{Co}_{0.316}\text{O}_2$	1.05	1.103	1.017:0.166:0.482:0.335	4.283

layered  $\text{LiMO}_2$  type materials. These above two observations imply that there must be an excess of oxygen, leading to metal-site vacancies, or the presence of either  $\text{Co}^{2+}$  or  $\text{Mn}^{3+}$  ions in the material.

It is very unlikely to have Co or Mn in the +2 or +3 oxidation states, respectively, because they are not stable oxidation states in the studied materials<sup>118, 119, 55</sup>. Moreover, in that case, the redox capacity during charge would have been higher than the observed values for samples A2, A3 and A3Q. Figure 4.15 shows the results of a calculation of first

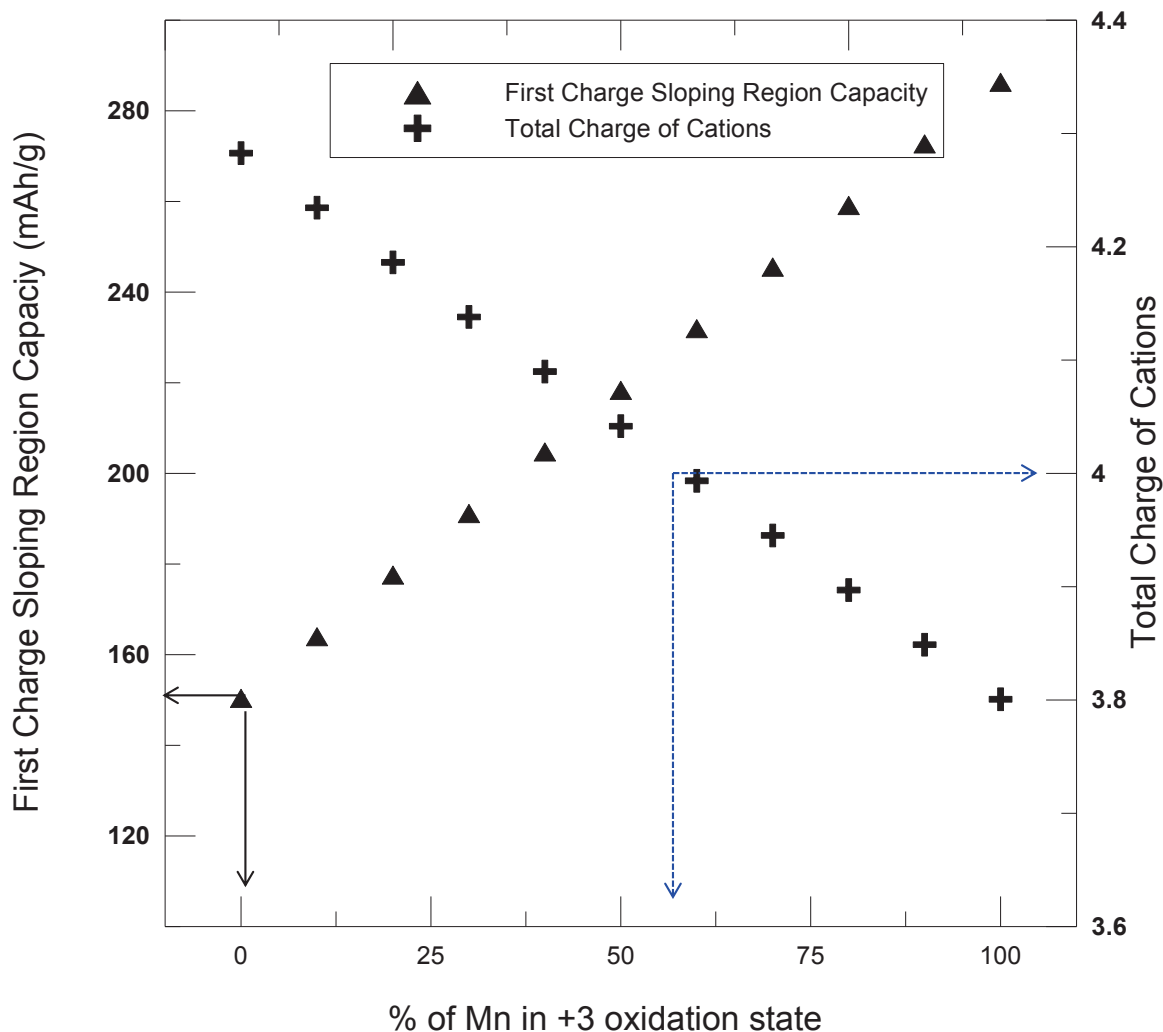


Figure 4.15 Plot of first charge sloping region capacity vs % Mn in +3 oxidation state and total charge of the cations vs % Mn in +3 oxidation state for A3Q  
Adapted with permission from (*Chem. Mater.*, **2015**, 27 (3), 757–767). Copyright (2015) American Chemical Society

charge redox capacity (due to TM oxidation) and the total cationic charge both plotted against the amount of the assumed  $\text{Mn}^{3+}$  for the A3Q sample. The first charge redox capacity calculation assumes the oxidation of  $\text{Ni}^{2+}$  to  $\text{Ni}^{4+}$ ,  $\text{Mn}^{3+}$  (if any) to  $\text{Mn}^{4+}$  and  $\text{Co}^{3+}$  to  $\text{Co}^{3.6+}$ <sup>120</sup>. The calculated redox region capacity for sample A3Q is  $\sim 150$  mAh/g, assuming no  $\text{Mn}^{3+}$  and agrees well with that observed (145 mAh/g). Figure 4.15 shows that approximately 50% of Mn should be in the +3 oxidation state in order to have a total cationic charge equal to 4 in  $\text{LiMO}_2$  having cation ratios corresponding to sample A3Q. According to Figure 4.15, having 50% of Mn in the +3 oxidation state would have resulted in a first charge redox capacity equal to at least 200 mAh/g, which is not the case here.

The only way to explain the observed results is if metal-site vacancies exist. Transition metal vacancies have been shown by McCalla et al. to exist at some layered oxides when the amount of Li used in synthesis is smaller than normally used to balance the cation and anion charges<sup>115</sup>, so their occurrence here is not unanticipated. The possibility for the presence of metal-site vacancies is now explored.

#### 4.7 Predicting metal-site vacancies

The metal atom ratios Li:Ni:Mn:Co from ICP-OES listed in Table 4.4 were taken to accurately describe each sample. The ratios are represented by the variables  $p'$ ,  $a$ ,  $b$ , and  $c$ , respectively. The values  $p'$ ,  $a$ ,  $b$ , and  $c$  in Table 4.4 have been scaled so that their sum is exactly 2.0. After heating, it is assumed that the final compound is  $\text{Li}_p\text{Ni}_x\text{Mn}_y\text{Co}_z\text{O}_2$ , where:

$$p + q + x + y + z = 2 \quad (4.1)$$

$$p + 2x + 4y + 3z = 4 \quad (4.2)$$

Equations (4.1) and (4.2) result from a filling of all metal sites by Li, Ni, Mn, Co or vacancies (Eqn. 1) and from charge balance, assuming  $\text{Li}^+$ ,  $\text{Ni}^{2+}$ ,  $\text{Mn}^{4+}$  and  $\text{Co}^{3+}$  (Eqn. 2), respectively. The metal atom ratios as determined by ICP-OES must match those in  $\text{Li}_{p-q}\text{Ni}_x\text{Mn}_y\text{Co}_z\text{O}_2$ , leading to the equations:

$$x = a(2 - q)/2 \quad (4.3)$$

$$y = b(2 - q)/2 \quad (4.4)$$

$$z = c(2 - q)/2 \quad (4.5)$$

$$p = p'(2 - q)/2 \quad (4.6)$$

Equations (4.3) – (4.6) can be used to solve for  $q$ , the vacancy content of the resulting layered material. One obtains:

$$q = 2 - 8/A, \quad (4.7)$$

$$\text{where } A = p' + 2a + 4b + 3c$$

When the calculated value of  $q \leq 0$ , it is believed that there are no metal-site vacancies in the structure. However, instead, it is believed that a small amount of Ni is in the 3+ oxidation state.  $\text{Ni}^{3+}$  and metal-site vacancies are not expected to exist at the same time in these materials.

#### 4.8 Density measurements

Table 4.5 shows the calculated metal-site vacancy content based on the ICP-OES compositions and the oxidation state rules ( $\text{Ni} = 2+$ ,  $\text{Mn} = 4+$  and  $\text{Co} = 3+$ ) as well as the



Table 4.5 Sample, calculated vacancies based on ICP-OES compositions and oxidation state rules, composition of formula units with calculated vacancies, calculated densities based on ICP-OES compositions and calculated vacancy content, densities determined from He-Pycnometer, calculated densities based on ICP-OES compositions and measured lattice parameters assuming no vacancies

<b>Sample</b>	<b>Calculated metal-site vacancy content based on ICP-OES results</b>	<b>Composition of a formula unit with calculated metal-site vacancy</b>	<b>Calculated density based on ICP-OES composition, calculated metal-site vacancy content and measured lattice parameters from XRD ( g/cm<sup>3</sup> )</b>	<b>Measured density from Helium Pycnometer (g/cm<sup>3</sup> )</b>	<b>Calculated density based on ICP-OES compositions and measured lattice parameters from XRD assuming no vacancies (g/cm<sup>3</sup> )</b>
A1	0.015(2)	Li <sub>1.118</sub> □ <sub>0.015</sub> Ni <sub>0.146</sub> Mn <sub>0.426</sub> Co <sub>0.296</sub> O <sub>2</sub>	4.46 ± 0.03	4.453 ± 0.005	4.48 ± 0.03
A2	0.098(7)	Li <sub>0.998</sub> □ <sub>0.098</sub> Ni <sub>0.153</sub> Mn <sub>0.443</sub> Co <sub>0.309</sub> O <sub>2</sub>	4.51 ± 0.03	4.531 ± 0.008	4.66 ± 0.03
A3	0.135(12)	Li <sub>0.945</sub> □ <sub>0.135</sub> Ni <sub>0.156</sub> Mn <sub>0.451</sub> Co <sub>0.313</sub> O <sub>2</sub>	4.53 ± 0.03	4.601 ± 0.018	4.74 ± 0.04
A3Q	0.132(11)	Li <sub>0.950</sub> □ <sub>0.132</sub> Ni <sub>0.155</sub> Mn <sub>0.450</sub> Co <sub>0.313</sub> O <sub>2</sub>	4.54 ± 0.03	4.603 ± 0.003	4.75 ± 0.04
Commercial LiCoO <sub>2</sub>	-		-	5.057 ± 0.008	5.073

\* Lattice parameters obtained from Ref. <sup>120</sup> to calculate the density

composition of the formula units with the calculated vacancy contents. In Table 4.5, 'q' represents the calculated metal-site vacancy content based on the above calculation. Table 4.5 also shows true density measurements obtained using a helium pycnometer. The densities were calculated from the XRD results assuming the vacancy content based on Equation 4.7 and also based on zero vacancies. The results from both calculations are also listed in the Table 4.5. In the latter case, Mn ions were assumed to be a mixture of  $\text{Mn}^{3+}$  and  $\text{Mn}^{4+}$  ions so that the total positive charge adds up to 4 in a formula unit.

The calculated densities for the case assuming metal-site vacancies agree well with the measured densities. The results in Table 4.5 suggest that very few, if any, Mn ions are  $\text{Mn}^{3+}$  in samples A2, A3 and A3Q. In order to show that the pycnometer measurements are reliable, the density of commercial  $\text{LiCoO}_2$  (obtained from E-one Moli Energy) was measured. Table 4.5 also shows the measured density of  $\text{LiCoO}_2$  and it is very close to the crystallographic density calculated from the  $\text{LiCoO}_2$  lattice constants<sup>121</sup>. Therefore, samples A2, A3 and A3Q contain metal-site vacancies and it is believed that these vacancies are responsible for the low-IRC in these materials.

The presence of the vacancies may help facilitate any needed atom motion to enable low-IRC. However, one must realize that these would normally be thought of as "Li-rich" materials because the lithium to transition metal ratio is still greater than 1. This suggests the origin of the high IRC in sample A1 is the presence of Li atoms in the TM layer and the lack of vacancies to enable needed atom motions to allow re-intercalation of all the lithium.



## 4.9 Constant current charge-discharge

Figure 4.16 shows the first cycle profiles of samples A1, A2, A3 and A3Q charged to the same delithiation limit to check the effect of delithiation level on the IRC. All the samples were charged with the same current density for the same duration (25 h) in such a way that all of them have the same length (capacity) along the 4.5 V plateau. Figure 4.16 shows that A1 exhibits higher IRC whereas A2, A3 and A3Q show low IRC. Therefore, the decreased IRC found in samples A2, A3 or A3Q is not caused by the fact that they have smaller first-charge capacity (See Figure 4.1) on the 4.5 V plateau. Instead, it is believed that metal-site vacancies give extra room for the reintercalation of extra Li into the host structure.

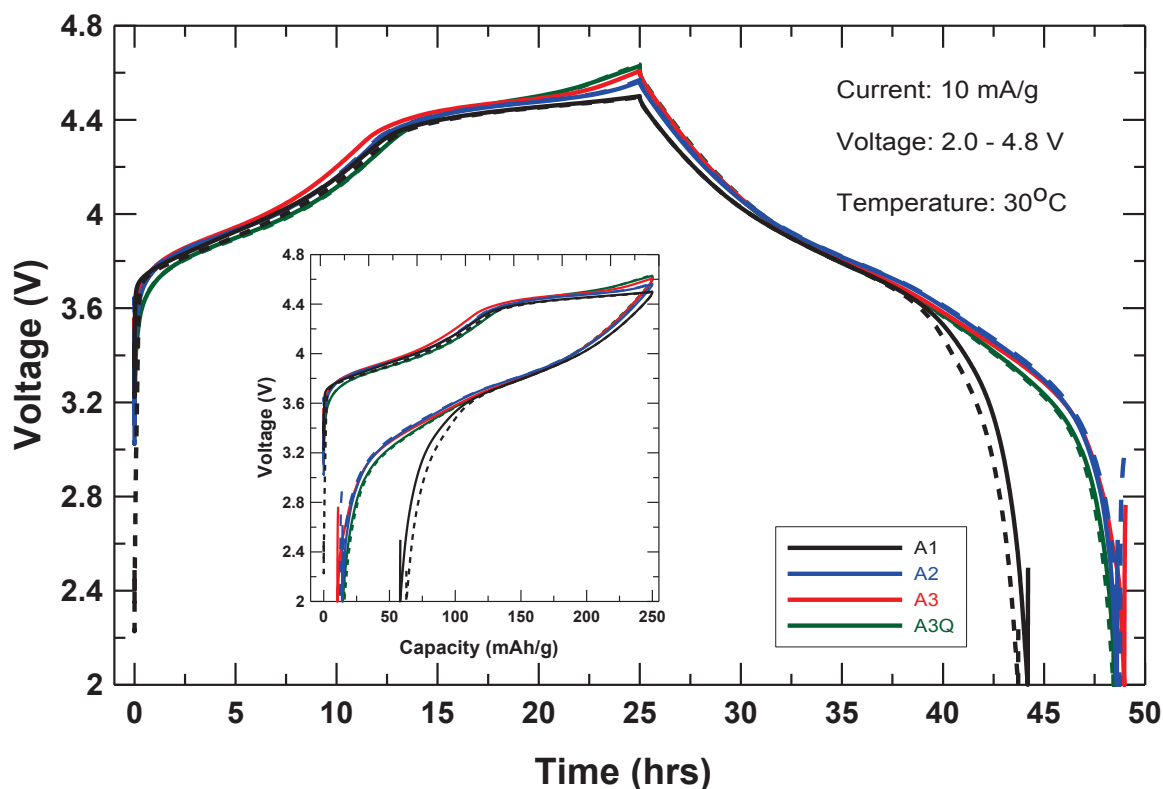


Figure 4.16 First-cycle charge-discharge voltage profiles of A1, A2, A3 and A3Q during constant time (25 h) first charge protocol.

Adapted with permission from (*Chem. Mater.*, **2015**, 27 (3), 757–767). Copyright (2015) American Chemical Society

#### 4.10 Conclusions

Layered positive electrode materials with slightly different lithium to transition metal ratio were synthesized from the same precursor and electrochemically characterized with a focus on the first cycle behaviour, especially the IRC. Surprisingly and beneficially, the samples having lower lithium to transition metal ratio exhibited IRC as small as 6.5 % of the first charge capacity. Few impurities (secondary phases) were found in the low-IRC materials but quenching resulted in pure phase materials. Analyzing  $dQ/dV$  vs.  $V$  plots confirmed that the secondary phases were removed by quenching and that quenching did not affect the low-IRC. Careful studies showed that the low-IRC behavior did not originate from any impurity phases including nano-domains of spinel. Therefore, the small IRC of these samples was inherent to their composition and structure.

The metal compositions from ICP-OES results and the oxidation state versus atomic occupancy rules suggested that the compounds exhibiting low-IRC contain metal-site vacancies. This was further supported by true density measurements using a helium pycnometer. The metal-site vacancies may provide avenues for enhanced atomic diffusion during and after the oxygen loss process which may contribute to the small irreversible capacity.

## Chapter 5 Search for low-irreversible capacity layered lithium-rich transition metal oxides in the Li-Ni-Mn-Co-O pseudo-quaternary system<sup>3</sup>

### 5.1 Introduction

The identification of low-irreversible capacity (IRC) materials (labelled as A2, A3 and A3Q) that were discussed in Chapter 4 fueled the idea of searching for similar materials in the Li-Ni-Mn-Co-O pseudo-quaternary system. The low-IRC samples A2 and A3Q were found to be single-phase layered materials with inherent metal-site vacancies that were synthesized from  $\text{Ni}_{0.166}\text{Mn}_{0.5}\text{Co}_{0.333}\text{CO}_3$  (labelled as A) In order to know whether other Ni-Mn-Co compositions could yield low-IRC materials synthesis and characterization of such materials from precursors of different Ni-Mn-Co compositions were explored and their results are discussed in this chapter.

Figure 5.1 shows a pseudo-ternary composition diagram of Ni, Mn and Co, in which every point represents the composition of a  $\text{Ni}_x\text{Mn}_y\text{Co}_{1-x-y}\text{CO}_3$  precursor (e.g.  $\text{Ni}_{0.4}\text{Mn}_{0.2}\text{Co}_{0.4}\text{CO}_3$ ). The three vertices of the triangle in Figure 5.1 represent  $\text{MnCO}_3$ ,  $\text{NiCO}_3$  and  $\text{CoCO}_3$ . The given pseudo-ternary composition diagram is also applicable for hydroxide precursors. LLRTMO materials can be made from such precursors by heating with an appropriate lithium source such as  $\text{Li}_2\text{CO}_3$ . The stoichiometric amount of Li required to make a layered LLRTMO, without vacancies, from any  $\text{Ni}_x\text{Mn}_y\text{Co}_{1-x-y}\text{CO}_3$  precursor can be calculated assuming that the total metal occupancy and total metal charge must be 2 and 4, respectively, in a  $\text{LiMO}_2$  formula unit. In Figure 5.1, the number (in blue) displayed above each point is the calculated number of moles of Li ( $u$ ) required

---

<sup>3</sup> This chapter was adapted with permission from Shunmugasundaram, R.; Arumugam, R. S.; Dahn, J. R. A Search for Low-Irreversible Capacity and High-Reversible Capacity Positive Electrode Materials in the Li-Ni-Mn-Co Pseudoquaternary System. *Chem. Mater.*, **2016**, 28 (1), 55–66. The author's contribution to this work included synthesis of materials, XRD measurements and electrochemical characterization.

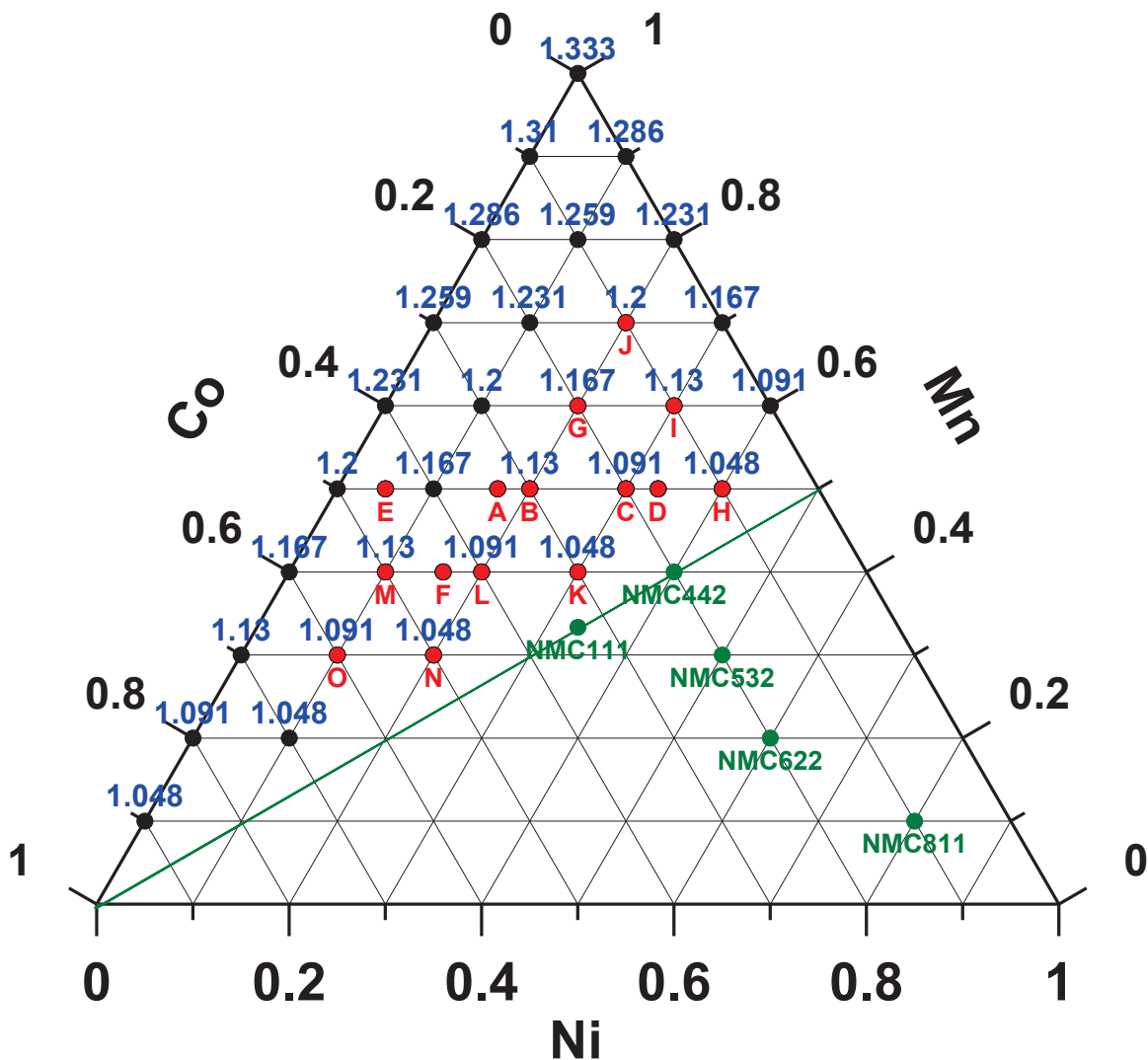


Figure 5.1 Ni-Mn-Co ternary diagram with every point representing  $\text{Ni}_x\text{Mn}_y\text{Co}_{1-x-y}$  precursor composition (e.g.  $\text{Ni}_{0.4}\text{Mn}_{0.2}\text{Co}_{0.4}\text{CO}_3$ ) Black and red points (samples studied here) represent precursor compositions that can be used to make Li-excess materials. Adapted with permission from (*Chem. Mater.*, 2016, 28 (1), 55–66). Copyright (2016) American Chemical Society

to be mixed with  $(2-u)$  moles of  $\text{Ni}_x\text{Mn}_y\text{Co}_{1-x-y}\text{CO}_3$  precursor to make one mole of stoichiometrically balanced single-phase  $\text{Li}_u\text{M}_{2-u}\text{O}_2$  type material. For example, the number of moles of Li ( $u$ ) required to make one mole of  $\text{Li}[\text{Li}_{0.166}\text{Ni}_{0.083}\text{Mn}_{0.417}\text{Co}_{0.333}]\text{O}_2$  from 0.833 moles of  $\text{Ni}_{0.1}\text{Mn}_{0.5}\text{Co}_{0.4}\text{CO}_3$  precursor is 1.167. The calculation has been

done assuming Ni, Mn and Co adopt the +2, +4 and +3 oxidation states, respectively, in a  $\text{Li}_u\text{M}_{2-u}\text{O}_2$  formula unit.

In Figure 5.1, the line drawn between Co to  $\text{Ni}_{0.5}\text{Mn}_{0.5}$  divides the ternary diagram into two regions based on the Li/TM ratio in the anticipated  $\text{LiMO}_2$  type compounds. LLRTMO without vacancies and subject to the oxidation state rules,  $\text{Mn}^{4+}$ ,  $\text{Co}^{3+}$ ,  $\text{Ni}^{2+}$  or  $\text{Ni}^{3+}$  and  $\text{Li}^{1+}$ , must have more lithium atoms than transition metal atoms when synthesized from precursors lying above the line. This triangular area bounded by Co,  $\text{Ni}_{0.5}\text{Mn}_{0.5}$  and Mn in Figure 5.1 is called the “Li-rich region” as the LLRTMO synthesized from the precursors of this region have  $\text{Li/TM} > 1$ . Any  $\text{LiMO}_2$  compound synthesized on (e.g.  $\text{LiNi}_{0.4}\text{Mn}_{0.4}\text{Co}_{0.2}\text{O}_2$  (NMC 442)) or below (e.g.  $\text{LiNi}_{0.8}\text{Mn}_{0.1}\text{Co}_{0.1}\text{O}_2$  (NMC 811)) the line joining Co to  $\text{Ni}_{0.5}\text{Mn}_{0.5}$  represents a  $\text{LiNi}_x\text{Mn}_y\text{Co}_{1-x-y}\text{O}_2$  (NMC) material for which the Li/TM can be 1. The red points (labelled from A to O) within the Li-rich region in Figure 5.1 are the Ni-Mn-Co precursor compositions that have been studied in this work.

The Li/TM ratio and the synthesis conditions are crucial in the synthesis of pure layered  $\text{LiMO}_2$  type material. If a  $\text{Li}_u\text{M}_{2-u}\text{O}_2$  material is synthesized with less Li than required for stoichiometric charge balance under an excess oxygen atmosphere (synthesis in a furnace under air), the co-existence of a spinel phase ( $\text{LiM}_2\text{O}_4$ ) along with the layered phase is normally expected. The layered-spinel coexistence regions in the Li-Ni-Mn-O pseudoternary and the Li-Ni-Mn-Co-O pseudoquaternary systems have been mapped by McCalla et al.<sup>36</sup> and Brown et al.<sup>122</sup> respectively. Lee et al. showed the formation of layered-spinel composite by reducing the Li/TM ratio from that of the stoichiometric

requirement<sup>131</sup>. However, the evolution of a spinel phase did not occur when the Li/TM ratio was reduced slightly to make A2 from precursor A.

McCalla et al. also showed, in a separate report<sup>115</sup>, the existence of single-phase layered materials such as  $\text{Li}[\square_{1/6}\text{Ni}_{1/6}\text{Mn}_{2/3}]\text{O}_2$ , which contain metal-site vacancies. In this case, quenching after calcining was required to synthesize single-phase  $\text{Li}[\square_{1/6}\text{Ni}_{1/6}\text{Mn}_{2/3}]\text{O}_2$ . Attempts to synthesize  $\text{Li}[\square_{1/6}\text{Ni}_{1/6}\text{Mn}_{2/3}]\text{O}_2$ , with slow cooling resulted in a layered-spinel composite. Compared to  $\text{Li}[\square_{1/6}\text{Ni}_{1/6}\text{Mn}_{2/3}]\text{O}_2$ , which did not show low-IRC behavior, the low-IRC material A2 had metal-site vacancies, also contained Co and was synthesized with slow cooling. It appears that the presence of Co is important for observing low-IRC and also favors the formation of a single layered phase during slow cooling. This raises a question about the contribution of the overall metal composition, especially Co, to promote low-IRC behavior and to promote the formation of pure layered single phases under Li deficient conditions. Hence the focus of this chapter is to evaluate the combined effect of Li-deficiency and overall metal composition on the structural and electrochemical properties of materials in the Li-Ni-Mn-Co-O system.

A search for low-IRC materials (IRC < 10%) in the Li-Ni-Mn-Co-O pseudo-quaternary system was made by synthesizing  $\text{LiMO}_2$  type materials with less Li than required for a stoichiometric balance. For example, less than 1.166 moles of Li has been mixed with 0.833 moles of  $\text{Ni}_{0.1}\text{Mn}_{0.5}\text{Co}_{0.4}\text{CO}_3$  precursor to make a low-IRC material. In this work, a total of 15 selected  $\text{Ni}_x\text{Mn}_y\text{Co}_{1-x-y}\text{CO}_3$  precursors (red circles in Figure 5.1) were made and their lithiated oxides were studied. As such, each precursor composition (e.g. B) forms a series of lithiated materials (see Table 5.1), in which the first member

(*e.g.* A1, B1) is stoichiometrically balanced whereas the rest of the samples (*e.g.* A2, B2,) in each series are Li-deficient but their Li/TM ratio is not necessarily less than 1.

Table 5.1 shows the nominal composition of the precursors, the number of moles of Li ( $u$ ) to be mixed with  $2-u$  moles of precursor required to make one mole of stoichiometric  $\text{Li}_u\text{M}_{2-u}\text{O}_2$ , the observed number of moles of lithium (from ICP-OES) per mole of total metals in the synthesized  $\text{LiMO}_2$  composition ( $v$ ) and their relative difference  $[(u-v)/u \times 100]$  which is called the “lithium deficiency” here. Table 5.1 also lists the first charge capacity, the first discharge capacity, the observed IRC and indicates whether the sample was single phase or not. Table 5.1 shows that IRC decreases, in general, as the Li deficiency increases. The identification of low-IRC materials from a variety of Ni-Mn-Co compositions in the Li-rich region of the Ni-Mn-Co ternary system (Figure 5.1) suggested that low-IRC behavior is not just confined to one particular Ni-Mn-Co composition.

Table 5.1 Sample, nominal precursor composition, calculated [Li] to make one mole of the corresponding stoichiometric  $\text{LiMO}_2$ , observed [Li] in one mole of synthesized  $\text{LiMO}_2$  derived from ICP-OES, % Li deficiency, first charge specific capacity, first discharge specific capacity, % IRC relative to the first charge specific capacity and layered single phase purity of the sample.

(Table 5.1 continues on the next two pages)

Sample	ICP-OES Precursor Composition (Ni:Mn:Co)	Calculated [Li] to make one mole of the $\text{Li}_u\text{M}_{2-u}\text{O}_2$ ( $u$ )	ICP-OES [Li] in one mole of the synthesized compound ( $v$ )	Li deficiency = $[(u-v)/u]$ (%)	First charge capacity (mAh/g)	First discharge capacity (mAh/g)	Observed IRC (% first cycle charge capacity)	Pure layered single phase? (based on XRD)
A1	0.169:0.491:0.341	1.161	1.126	3.02	319	247	22.5± 0.5	Yes

Sample	ICP-OES Precursor Composition (Ni:Mn:Co)	Calculated [Li] to make one mole of the $\text{Li}_u\text{M}_{2-u}\text{O}_2$ ( $u$ )	ICP-OES [Li] in one mole of the synthesized compound ( $v$ )	Li deficiency = $[(u-v)/u]$ (%)	First charge capacity (mAh/g)	First discharge capacity (mAh/g)	Observed IRC (% first cycle charge capacity)	Pure layered single phase? (based on XRD)
A2	0.169:0.491:0.341	1.161	1.049	9.63	295	272	7.7± 0.5	Yes
A3	0.169:0.491:0.341	1.161	1.014	12.70	285	266	6.5± 0.5	No
B1	0.199:0.495:0.306	1.148	1.156	-0.61	315	246	22± 0.5	Yes
B2	0.199:0.495:0.306	1.148	1.054	8.21	295	267	9.5± 0.5	Yes
B3	0.199:0.495:0.306	1.148	1.046	8.93	280	259	7.5± 0.5	Yes
C1	0.301:0.497:0.202	1.098	1.079	1.76	295	228	22.7± 0.5	Yes
C2	0.301:0.497:0.202	1.098	1.082	1.44	283	228	19.5± 0.5	Yes
C3	0.301:0.497:0.202	1.098	1.058	3.71	275	235	14.5± 0.5	Yes
C4	0.301:0.497:0.202	1.098	1.021	6.99	265	237	10.7± 0.5	Yes
C5	0.301:0.497:0.202	1.098	1.008	8.17	257	232	9.8± 0.5	No
D1	0.333:0.498:0.169	1.082	1.076	0.55	276	208	24.5± 0.5	Yes
D2	0.333:0.498:0.169	1.082	1.072	0.97	274	212	22.4± 0.5	Yes
D3	0.333:0.498:0.169	1.082	1.065	1.59	273	218	20.3± 0.5	Yes
D4	0.333:0.498:0.169	1.082	1.016	6.10	270	249	7.6± 0.5	Yes
D5	0.333:0.498:0.169	1.082	1.003	7.30	258	240	6.9± 0.5	No
E1	0.051:0.494:0.456	1.221	1.155	5.39	327	206	37.0± 0.5	Yes
E2	0.051:0.494:0.456	1.221	1.103	9.66	317	241	23.9± 0.5	No
F1	0.164:0.390:0.446	1.113	1.053	5.35	300	233	22.5± 0.5	Yes
F2	0.164:0.390:0.446	1.113	1.008	9.47	274	233	15.0± 0.5	Yes
F3	0.164:0.390:0.446	1.113	0.994	10.74	268	233	13.2± 0.5	Yes



Sample	ICP-OES Precursor Composition (Ni:Mn:Co)	Calculated [Li] to make one mole of the $\text{Li}_u\text{M}_{2-u}\text{O}_2$ ( $u$ )	ICP-OES [Li] in one mole of the synthesized compound ( $v$ )	Li deficiency = $[(u-v)/u]$ (%)	First charge capacity (mAh/g)	First discharge capacity (mAh/g)	Observed IRC (% first cycle charge capacity)	Pure layered single phase? (based on XRD)
G1	0.191:0.603:0.207	1.206	1.178	2.40	332	281	15.5± 0.5	Yes
G2	0.191:0.603:0.207	1.206	1.075	10.87	285	257	10.1± 0.5	No
H1	0.382:0.515:0.103	1.066	1.050	1.58	279	235	15.7± 0.5	Yes
H2	0.382:0.515:0.103	1.066	0.966	9.41	256	243	5.0± 0.5	No
H3	0.382:0.515:0.103	1.066	0.943	11.55	240	233	3.0± 0.5	No
I1	0.264:0.603:0.103	1.155	1.151	0.38	314	240	23.5± 0.5	Yes
I2	0.264:0.603:0.103	1.155	1.050	9.17	279	259	7.3± 0.5	No
J1	0.197:0.702:0.101	1.252	1.192	4.78	311	218	30.0± 0.5	Yes
J2	0.197:0.702:0.101	1.252	1.090	13.01	299	258	13.8± 0.5	No
K1	0.298:0.395:0.307	1.048	1.029	1.86	290	220	24.0± 0.5	Yes
K2	0.298:0.395:0.307	1.048	0.926	11.63	243	218	10.4± 0.5	Yes
L1	0.199:0.394:0.406	1.097	1.088	0.91	308	231	25.0± 0.5	Yes
L2	0.199:0.394:0.406	1.097	0.982	10.49	263	241	8.5± 0.5	Yes
M1	0.101:0.389:0.510	1.144	1.121	2.01	320	218	32.0± 0.5	Yes
M2	0.101:0.389:0.510	1.144	1.016	11.16	274	246	10.1± 0.5	No
N1	0.202:0.289:0.509	1.044	1.014	2.87	280	207	26.2± 0.5	Yes
N2	0.202:0.289:0.509	1.044	0.926	11.28	242	222	8.2± 0.5	Yes
O1	0.101:0.291:0.609	1.095	1.073	1.97	308	213	30.9± 0.5	Yes
O2	0.101:0.291:0.609	1.095	0.973	11.19	252	233	7.6± 0.5	No

Figure 5.2 shows scanning electron micrograph (SEM) images of some selective precursors A, C, H, J, L and O, which have different Ni:Mn:Co ratios. Although the same reaction conditions (pH, temperature, ammonia concentration, solution feed rates, stirring) were maintained during the synthesis of these precursors, their morphology varied somewhat, which could be attributed to their varying Ni:Mn:Co compositions. Van Bommel et al. showed how the pH and ammonia concentration affected the solubility of  $\text{TM}[\text{NH}_3]_n$  ions and the importance of optimizing these conditions for different Ni:Mn:Co ratios to get spherical particles of the same size<sup>123</sup>. However, Figure 5.2 and Table 5.1 show that morphology changes in the precursors had a minimal impact in reducing the IRC. Therefore it is believed that the variations in precursor morphology do not

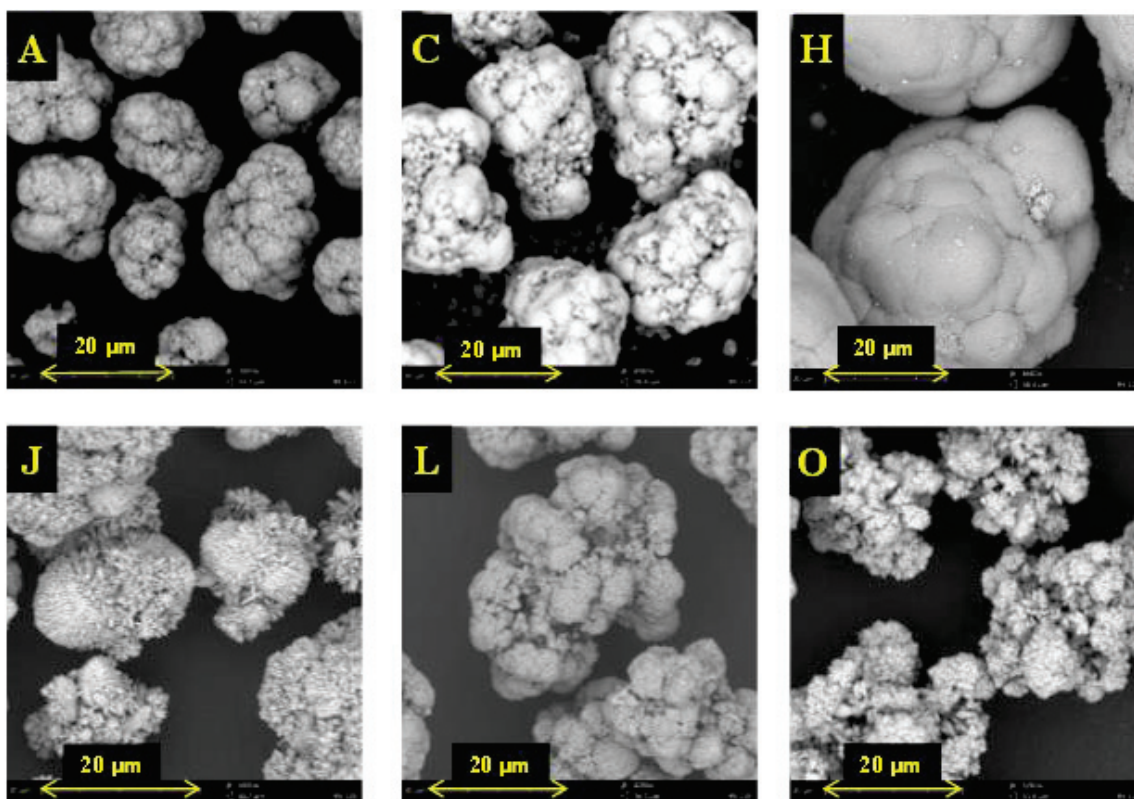


Figure 5.2 Scanning electron micrograph images of selected precursors A, C, H, J, L and O  
Adapted with permission from (*Chem. Mater.*, 2016, 28 (1), 55–66). Copyright (2016)  
American Chemical Society

significantly impact the values of IRC in this work.

## 5.2 Single phase low-irreversible capacity materials

Table 5.1 shows that Li-deficient materials were either single-phase layered materials (*e.g.* C4) or layered-spinel composites (*e.g.* C5) depending on the degree of Li deficiency and the overall metal composition. The single-phase low-IRC materials were found to be solid solutions between  $\text{Li}_2\text{MnO}_3$  and  $\text{LiMO}_2$ <sup>124,44,125</sup> containing “metal-site vacancies”<sup>115</sup>. The existence of vacancies will be addressed in the next paragraph. Figure 5.3 shows the XRD patterns of a few single phase low-IRC materials in the angular range

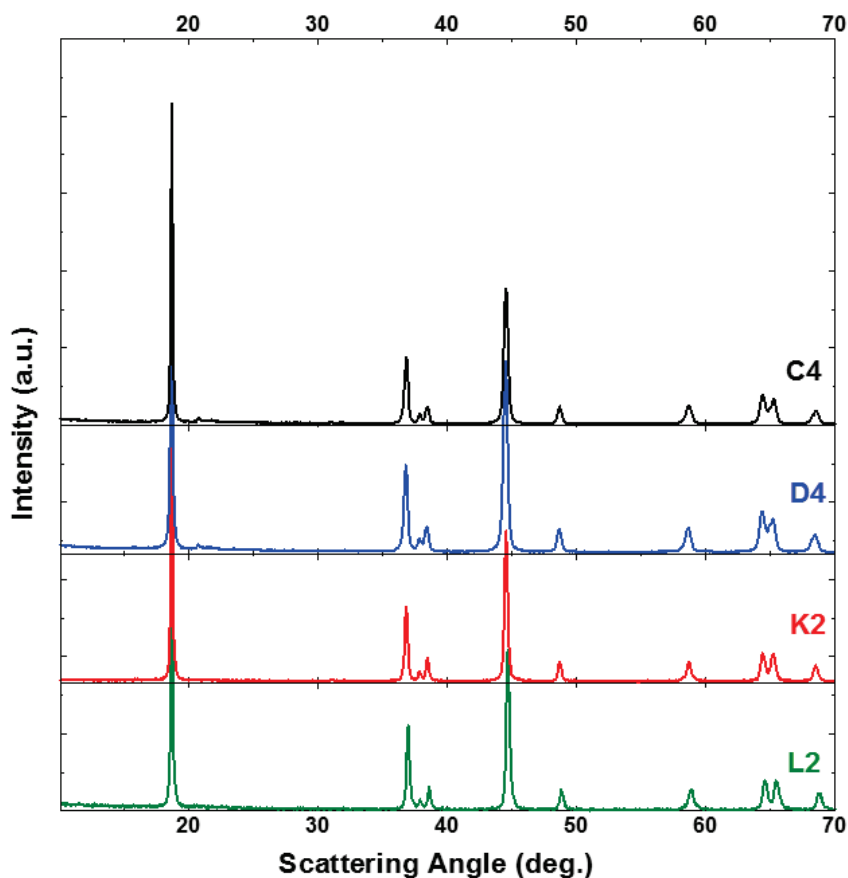


Figure 5.3 XRD patterns of few single phase low-IRC materials (samples C4, D4, K2 and L2) between 20° to 70° Adapted with permission from (*Chem. Mater.*, **2016**, 28 (1), 55–66). Copyright (2016) American Chemical Society

of 10° to 70°. They are all layered O3 structures (similar to  $\alpha$ -NaFeO<sub>2</sub>), which can be defined in the  $R\bar{3}m$  space group. The set of superstructure peaks between 20° and 30° are due to the ordering ( $C2/m$ ) of Li or vacancies with Ni, Mn and Co to form the  $\sqrt{3}a_{hex} \times \sqrt{3}a_{hex}$  superlattice in the TM layer. Superlattice formation does not necessarily require Li in the TM layer as was shown by McCalla et al. for the case of  $\text{Li}[\square_{1/6}\text{Ni}_{1/6}\text{Mn}_{2/3}]\text{O}_2$ <sup>115</sup>, where vacancies order with TM atoms to form a superlattice. Table 5.2 shows the XRD Rietveld refinement results of single-phase samples of two selected series (D and K) including the lattice parameters. In every series, the lattice parameters increase as the Li deficiency increases, which is expected based on an increase in the TM/Li ratio. Appendix C shows the XRD patterns of all the samples (A1 to O2) and Appendix D shows a table of lattice constants of all the samples (A1 to O1) obtained from the Rietveld refinement.

Table 5.2 Rietveld refinement results of samples from D and K series

Sample	$a$ (Å)	$c$ (Å)	$z(\text{O})$	n Ni in Li sites	Calculated metal-site vacancy content	$R_B$
D1	2.8613(4)	14.243(8)	0.258(3)	0.035(8)	0.000(2)	2.02
D2	2.8635(1)	14.258(4)	0.257(9)	0.032(3)	0.003(1)	1.66
D3	2.8644(3)	14.263(7)	0.257(7)	0.049(5)	0.012(3)	2.01
D4	2.8653(3)	14.276(3)	0.252(7)	0.063(3)	0.063(6)	4.05
K1	2.8549(6)	14.225(2)	0.259(1)	0.015(1)	0.014(2)	2.07
K2	2.8592(2)	14.242(7)	0.256(2)	0.033(8)	0.119(13)	2.40

The total cationic charge of the single phase low-IRC materials calculated from the as-obtained ICP-OES composition (Li:Ni:Mn:Co) was above 4 when the oxidation states of the cations are  $\text{Li}^+$ ,  $\text{Ni}^{2+}$ ,  $\text{Co}^{3+}$  and  $\text{Mn}^{4+}$ . Hence the formula unit of any single-phase low-IRC compound would have excess oxygen ( $> 2$ ). However, the total oxygen content in a formula unit can be adjusted to 2 by introducing metal-site vacancies. The amount of metal-site vacancies required in each composition was calculated based on the amount of excess cationic charge. That is, the ICP-OES composition formula unit was renormalized for a total oxygen content equal to 2 to get the formula unit with metal-site vacancies. For example, the formula unit of sample L2:  $\text{Li}_{0.982}\text{Ni}_{0.203}\text{Mn}_{0.402}\text{Co}_{0.413}\text{O}_{2.117}$  has been renormalized to  $\text{Li}_{0.928}\square_{0.111}\text{Ni}_{0.192}\text{Mn}_{0.380}\text{Co}_{0.390}\text{O}_2$ , which includes metal-site vacancies. Table 5.3 shows the metal atom ratios observed from ICP-OES analysis, the calculated vacancy content per mole of synthesized compound and the formula unit with metal-site vacancies of the single-phase low-IRC materials.

The existence of metal-site vacancies can be verified by comparing measured and calculated densities. The densities of the samples were measured using a helium pycnometer, and they were calculated from the lattice parameters (XRD) and chemical compositions that include metal-site vacancies. Table 5.3 shows the experimentally measured densities (pycnometer) and the calculated densities. For comparison purposes, the densities of the materials were also calculated for corresponding  $\text{LiMO}_2$  units in which the ICP-OES based metal composition was substituted for a LiM unit with no vacancies. In the latter case, some TM ions must exist in lower oxidation states than normal in order to compensate for the total anionic charge of 4. For example, the zero

Table 5.3 Sample ID, ICP-OES metal ratio, calculated no. of moles of vacancies in one mole of synthesized LiMO<sub>2</sub>, calculated formula unit with metal-site vacancies, layered single phase purity, measured density from a He pycnometer, calculated density assuming metal-site vacancies and calculated density assuming no vacancies of single-phase low-IRC materials

Sample	ICP-OES metal ratio Li : Ni : Mn : Co	Calculated no. of moles of vacancies (q)	Formula unit with calculated metal-site vacancies Li <sub>p</sub> □ <sub>q</sub> Ni <sub>x</sub> Mn <sub>y</sub> Co <sub>z</sub> O <sub>2</sub>	Measured density from He Pycnometer (g/cm <sup>3</sup> )	Calculated density assuming No vacancies (g/cm <sup>3</sup> )	Calculated density assuming No vacancy (g/cm <sup>3</sup> )
A2	1.049:0.161:0.466:0.325	0.098	Li <sub>0.998</sub> □ <sub>0.098</sub> Ni <sub>0.153</sub> Mn <sub>0.443</sub> Co <sub>0.309</sub> O <sub>2</sub>	4.530 ± 0.008	4.50 ± 0.03	4.65 ± 0.03
B2	1.054:0.187:0.470:0.289	0.084	Li <sub>1.01</sub> □ <sub>0.084</sub> Ni <sub>0.179</sub> Mn <sub>0.450</sub> Co <sub>0.277</sub> O <sub>2</sub>	4.511 ± 0.017	4.50 ± 0.03	4.62 ± 0.03
B3	1.046:0.190:0.472:0.292	0.091	Li <sub>0.998</sub> □ <sub>0.091</sub> Ni <sub>0.181</sub> Mn <sub>0.451</sub> Co <sub>0.279</sub> O <sub>2</sub>	4.531 ± 0.025	4.51 ± 0.03	4.64 ± 0.03
C2	1.082:0.275:0.455:0.187	0.008	Li <sub>1.078</sub> □ <sub>0.008</sub> Ni <sub>0.274</sub> Mn <sub>0.454</sub> Co <sub>0.186</sub> O <sub>2</sub>	4.491 ± 0.010	4.50 ± 0.03	4.52 ± 0.03
C3	1.057:0.282:0.468:0.193	0.035	Li <sub>1.038</sub> □ <sub>0.035</sub> Ni <sub>0.277</sub> Mn <sub>0.46</sub> Co <sub>0.19</sub> O <sub>2</sub>	4.535 ± 0.011	4.52 ± 0.03	4.57 ± 0.03
C4	1.021:0.294:0.486:0.198	0.072	Li <sub>0.985</sub> □ <sub>0.071</sub> Ni <sub>0.284</sub> Mn <sub>0.469</sub> Co <sub>0.191</sub> O <sub>2</sub>	4.531 ± 0.021	4.55 ± 0.03	4.66 ± 0.03
D2	1.072:0.312:0.460:0.157	0.003	Li <sub>1.07</sub> □ <sub>0.003</sub> Ni <sub>0.311</sub> Mn <sub>0.459</sub> Co <sub>0.157</sub> O <sub>2</sub>	4.522 ± 0.030	4.54 ± 0.03	4.54 ± 0.03
D3	1.065:0.311:0.465:0.158	0.012	Li <sub>1.059</sub> □ <sub>0.01</sub> Ni <sub>0.309</sub> Mn <sub>0.463</sub> Co <sub>0.157</sub> O <sub>2</sub>	4.541 ± 0.020	4.53 ± 0.03	4.55 ± 0.03
D4	1.016:0.328:0.489:0.167	0.063	Li <sub>0.984</sub> □ <sub>0.062</sub> Ni <sub>0.318</sub> Mn <sub>0.474</sub> Co <sub>0.162</sub> O <sub>2</sub>	4.542 ± 0.016	4.57 ± 0.04	4.66 ± 0.03
E2	1.103:0.046:0.440:0.411	0.090	Li <sub>1.053</sub> □ <sub>0.09</sub> Ni <sub>0.044</sub> Mn <sub>0.42</sub> Co <sub>0.393</sub> O <sub>2</sub>	4.428 ± 0.008	4.45 ± 0.03	4.58 ± 0.03
F2	1.008:0.163:0.387:0.443	0.099	Li <sub>0.957</sub> □ <sub>0.1</sub> Ni <sub>0.155</sub> Mn <sub>0.368</sub> Co <sub>0.421</sub> O <sub>2</sub>	4.610 ± 0.007	4.64 ± 0.03	4.79 ± 0.03
F3	0.993:0.162:0.394:0.450	0.116	Li <sub>0.936</sub> □ <sub>0.115</sub> Ni <sub>0.153</sub> Mn <sub>0.371</sub> Co <sub>0.424</sub> O <sub>2</sub>	4.595 ± 0.013	4.64 ± 0.03	4.82 ± 0.03
K2	0.926:0.320:0.424:0.330	0.119	Li <sub>0.871</sub> □ <sub>0.119</sub> Ni <sub>0.301</sub> Mn <sub>0.399</sub> Co <sub>0.31</sub> O <sub>2</sub>	4.705 ± 0.013	4.72 ± 0.03	4.91 ± 0.03
L2	0.982:0.203:0.402:0.413	0.111	Li <sub>0.928</sub> □ <sub>0.111</sub> Ni <sub>0.192</sub> Mn <sub>0.38</sub> Co <sub>0.39</sub> O <sub>2</sub>	4.670 ± 0.012	4.66 ± 0.03	4.83 ± 0.03
M2	1.016:0.099:0.383:0.502	0.118	Li <sub>0.956</sub> □ <sub>0.119</sub> Ni <sub>0.093</sub> Mn <sub>0.36</sub> Co <sub>0.472</sub> O <sub>2</sub>	4.595 ± 0.011	4.62 ± 0.04	4.80 ± 0.03
N2	0.926:0.217:0.310:0.547	0.114	Li <sub>0.873</sub> □ <sub>0.114</sub> Ni <sub>0.205</sub> Mn <sub>0.292</sub> Co <sub>0.516</sub> O <sub>2</sub>	4.834 ± 0.005	4.83 ± 0.04	5.02 ± 0.03
O2	0.973:0.103: 0.300:0.625	0.118	Li <sub>0.915</sub> □ <sub>0.119</sub> Ni <sub>0.097</sub> Mn <sub>0.282</sub> Co <sub>0.588</sub> O <sub>2</sub>	4.733 ± 0.006	4.77 ± 0.04	4.96 ± 0.04

metal-site vacancy counterpart of  $\text{Li}_{1.01}\square_{0.084}\text{Ni}_{0.179}\text{Mn}_{0.450}\text{Co}_{0.277}\text{O}_2$  (sample B2) is  $\text{Li}_{1.054}\text{Ni}_{0.187}\text{Mn}_{0.470}\text{Co}_{0.289}\text{O}_2$ , where the total cationic charge is 4.1749 and hence some Mn ions must be in the +3 oxidation state to balance the total anionic charge of 4.

Figure 5.4 shows a comparison of the measured densities to the calculated densities. In Figure 5.4, the densities calculated assuming metal-site vacancies are shown

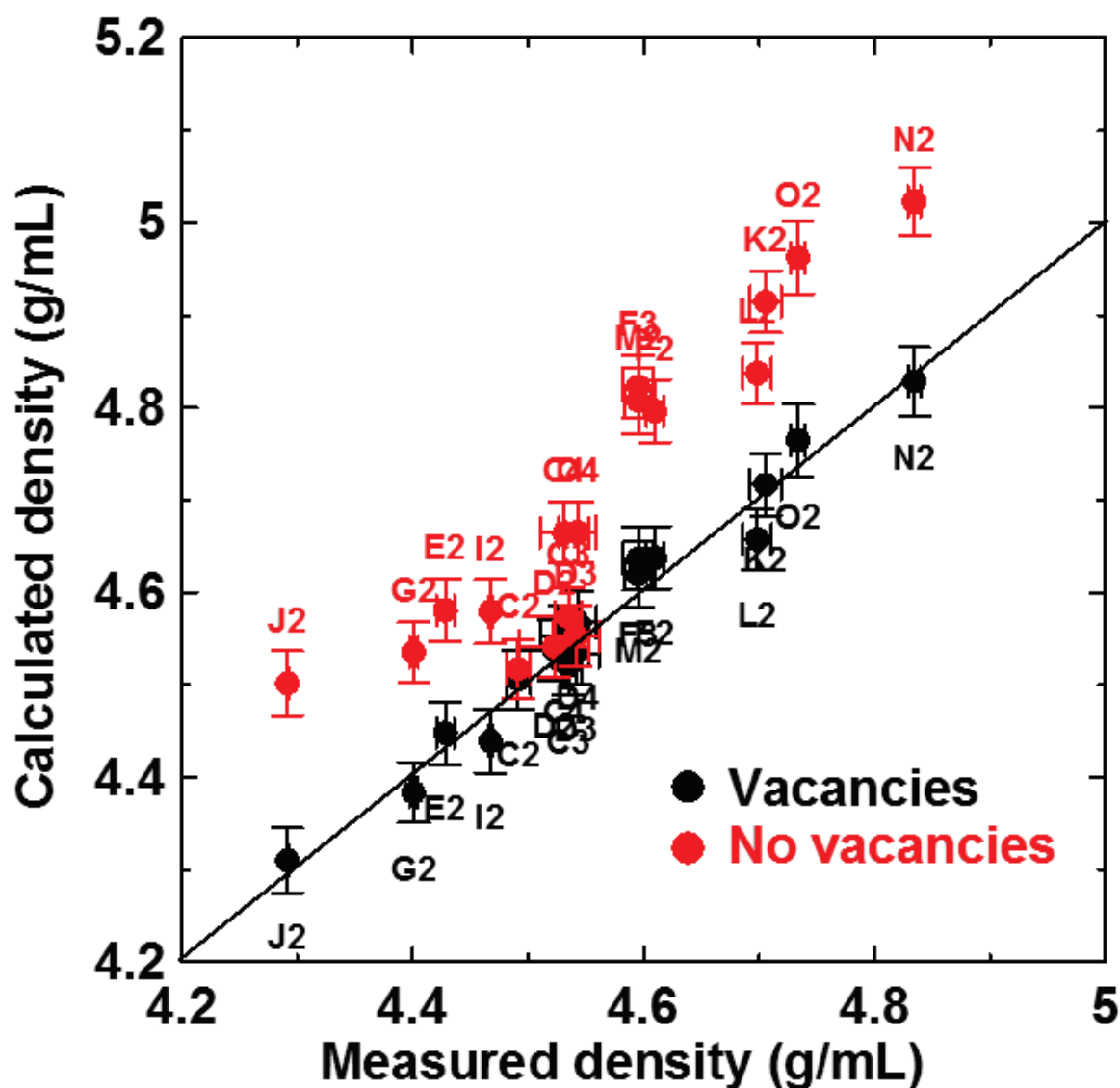


Figure 5.4 Calculated densities assuming metal-site vacancies (black) and no vacancies (red) vs measured densities (using a He-pycnometer)  
Adapted with permission from (*Chem. Mater.*, 2016, 28 (1), 55–66). Copyright (2016) American Chemical Society

as black circles and the densities assuming no vacancies are shown as red circles. The measured densities and the calculated densities assuming metal-site vacancies agree very well (black circles) resulting in data with a slope of 1.00 and an intercept of zero in Figure 5.4. By contrast, the measured densities do not agree well with densities calculated assuming no metal-site vacancies (red circles) except for a few points where, it turns out, the vacancy content is very small. The close agreement between the measured densities and the densities calculated assuming metal-site vacancies strongly suggests the presence of vacancies in the pristine single-phase materials. Moreover, simultaneous metal-site vacancies and oxygen vacancies would result in even lower density and this possibility was discarded. The possibility of having just oxygen vacancies was also discarded because the synthesis of materials under an oxygen-rich environment would not favor oxygen vacancies. By contrast, the synthesis conditions for introducing oxygen vacancies must require some special chemical treatment. For example, Qiu et al. showed the introduction of oxygen vacancies in the surface of LLRTMO materials by treating the pristine materials with  $\text{CO}_2$  to form carbonate ( $-\text{CO}_3$ ) groups.<sup>126</sup>

The calculated compositions with metal-site vacancies have the same the metal atom ratios as obtained from the ICP-OES results. Hence the mass difference between the formula units of the two structures (with and without vacancies) should be the weighted average of cation atomic mass multiplied by the vacancy content. This means the density difference should be approximately proportional to the vacancy content, neglecting small variations in unit cell size because all compositions have approximately a 1:1 Li:TM ratio. Figure 5.5 shows a plot of the difference between the measured density (pycnometer) and the calculated densities that assume no vacancies versus the vacancy



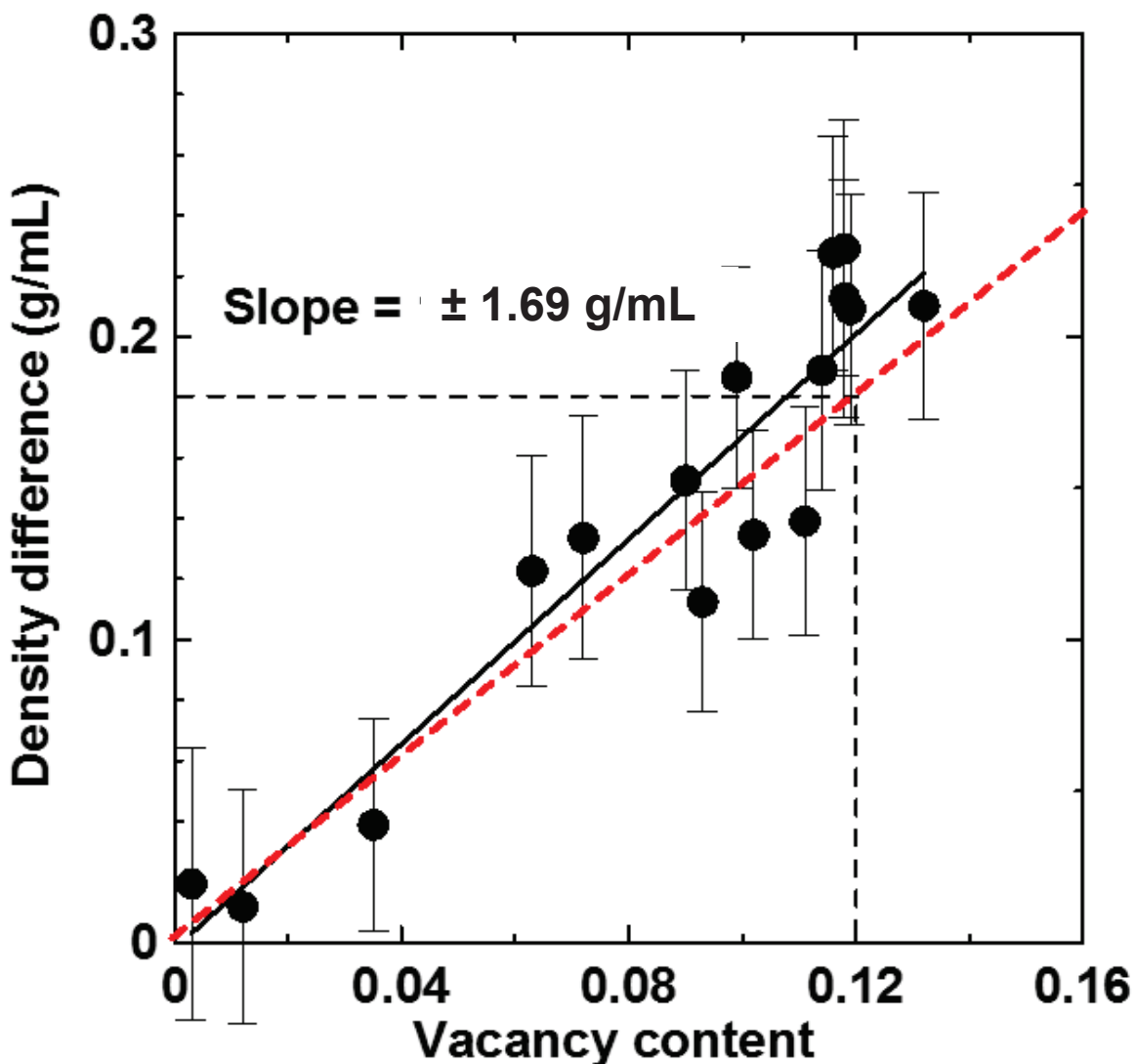


Figure 5.5 Density difference between the calculated (no vacancy case) and the measured densities (from He pycnometer) vs the calculated metal-site vacancy content  
Adapted with permission from (*Chem. Mater.*, **2016**, 28 (1), 55–66). Copyright (2016) American Chemical Society

content. Figure 5.5 shows that the expected linearity is observed. If the vacant sites had been occupied by equal amounts of Li and TM (*i.e.* a 1:1 ratio), then the slope of the plot is expected to be very close to 1.5 g/mL shown by the red line in Figure 5.5. The measured slope of a best fit line through the data is equal to  $\pm 1.69$  g/mL and is shown as a black line in Figure 5.5. The measured slope agrees quite well with the “back of the envelope” estimate.

Figure 5.6 shows a representative set (samples C4, D4, K2 and L2) of first cycle charge-discharge voltage profiles (voltage vs. specific capacity) of cells with electrodes of several single-phase low-IRC materials in the range between 4.8 and 2.0 V. Most of the samples display two distinct regions on their first charge profile: (a) a sloping region corresponding to the oxidation of TM ions and (b) a  $\sim 4.5$  V plateau region corresponding to the electrochemical reactions dictated by oxygen anions (oxygen release<sup>56</sup> or oxygen

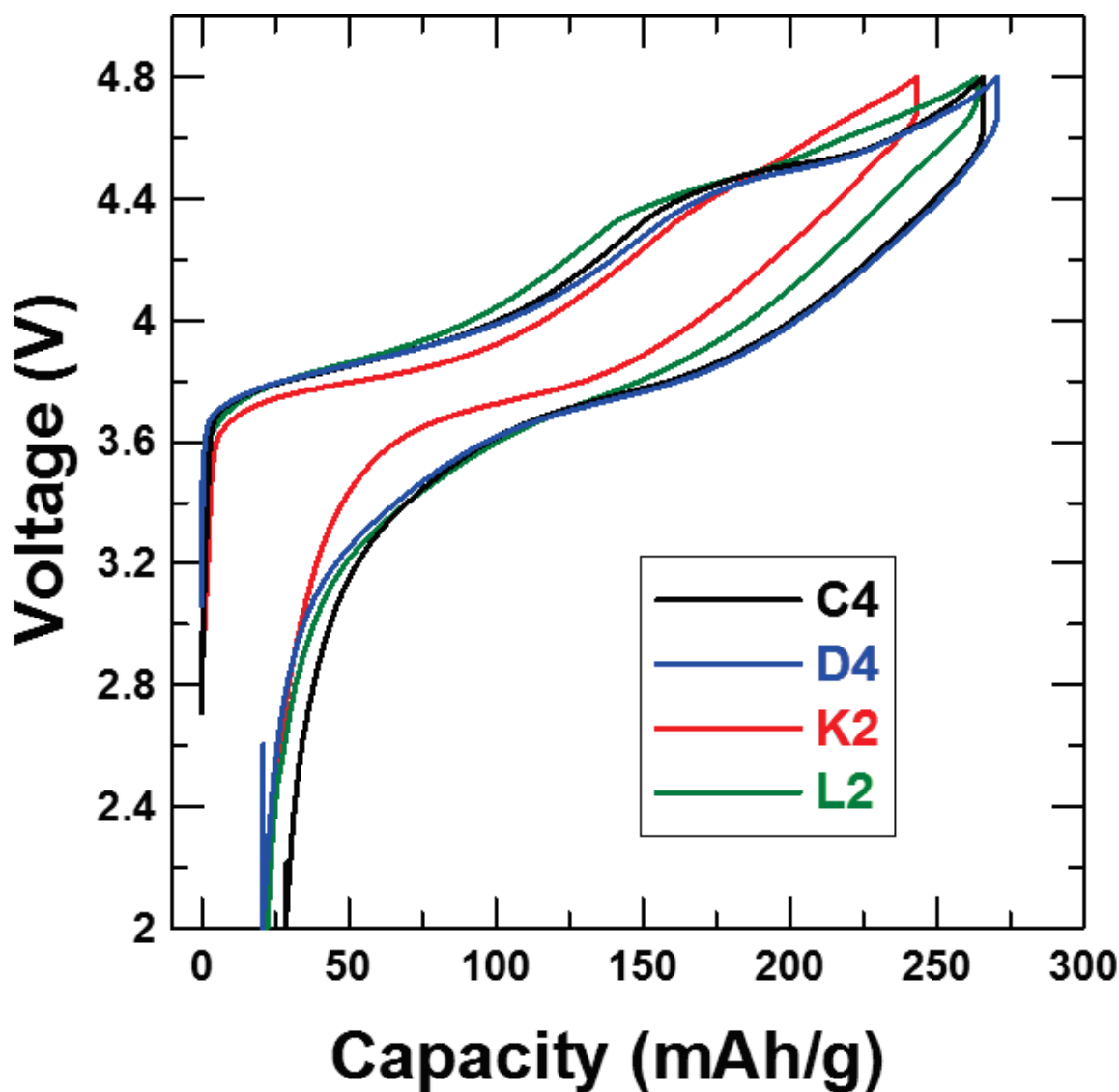


Figure 5.6 First cycle charge-discharge voltage vs specific capacity profiles of few single phase low-IRC materials represented in Figure 5.3

Adapted with permission from (*Chem. Mater.*, 2016, 28 (1), 55–66). Copyright (2016) American Chemical Society

oxidation<sup>68</sup>) similar to other reported Li-excess materials. The observed first charge specific capacities of all the samples were between 240 and 270 mAh/g. The charge capacity increases with increasing Li content whereas the sloping region (redox) capacity increases with an increasing proportion of TM redox ions. Table 5.1 shows the first charge and discharge capacities of the single-phase materials. The first cycle charge-discharge voltage profiles of all the samples studied are given in Appendix E.

Figure 5.7 shows the first cycle differential capacity versus potential profiles of the cells described by Figure 5.6. Every sample exhibits an oxidation peak at  $\sim 3.8$  V corresponding to Ni ( $\text{Ni}^{2+}$  to  $\text{Ni}^{4+}$ ) and Co ( $\text{Co}^{3+}$  to  $\text{Co}^{4+}$ ) oxidation. The oxidation peak around 4.5 V corresponds to the oxygen release or oxygen oxidation or a combination of both. Figure 5.7 also shows the difference in the shape of the 4.5 V oxidation peaks between the samples. The intensity of the peaks varies with the involvement of the oxygen anions in the electrochemical reaction, which in turn depends on the available redox TM ions. For example, sample K2 has almost no oxygen-based redox peak implying that nearly all the Li ions were extracted with the aid of redox TM ions similar to traditional layered materials<sup>40</sup>. Sample K2 has a Li/TM ratio less than 1 and hence it is not a Li-rich material. Hence samples such as K2 are traditional layered materials **but** notably contain metal-site vacancies.

While the focus of this study is finding high capacity low-IRC materials, discovering materials such as K2 is a bonus as they represent another category of positive electrode materials. The single phase low-IRC materials with metal-site vacancies can be categorized into two types. The first (*e.g.* K2) are similar to traditional layered materials, such as  $\text{LiNi}_{0.333}\text{Mn}_{0.333}\text{Co}_{0.333}\text{O}_2$ , but with metal-site vacancies. The second type of

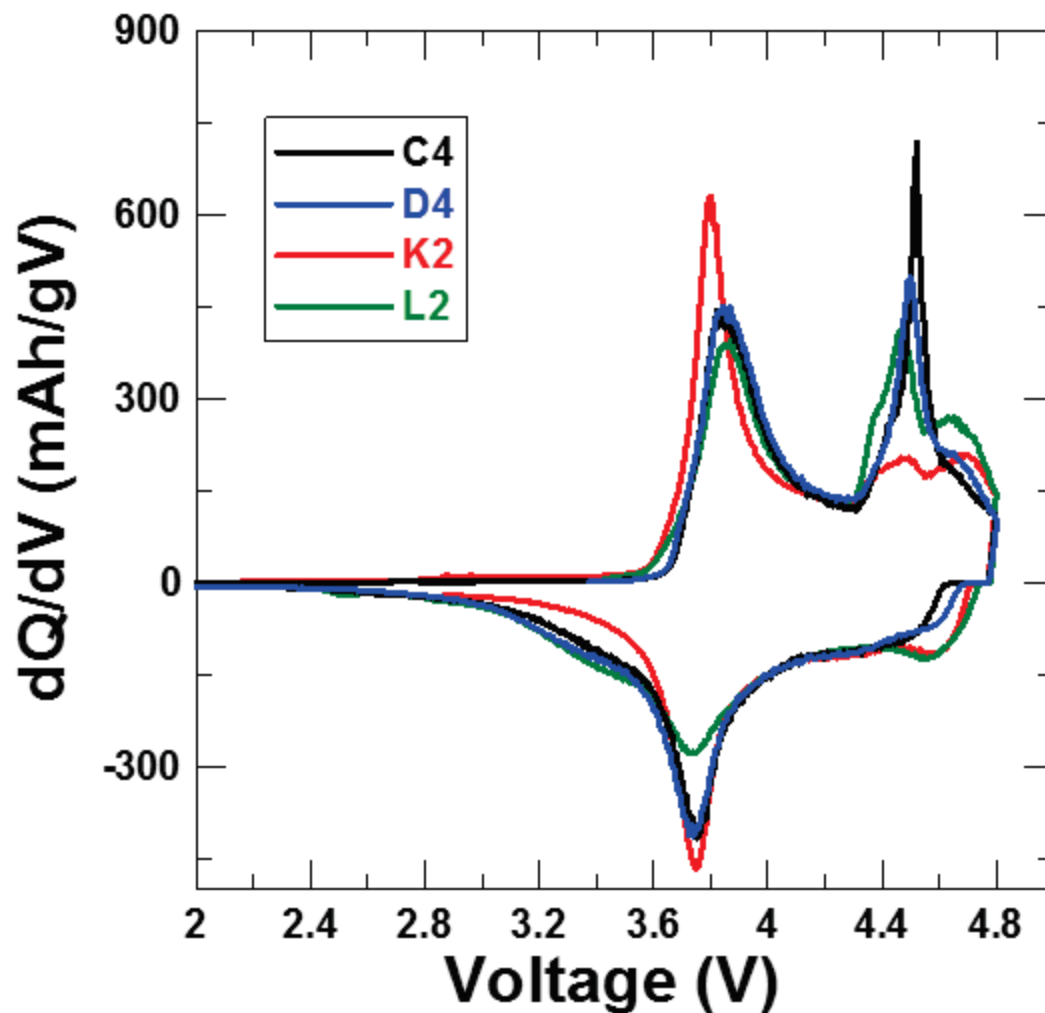


Figure 5.7 First cycle charge-discharge differential capacity profiles of few single phase low-IRC materials represented in Figure 5.3  
Adapted with permission from (*Chem. Mater.*, **2016**, 28 (1), 55–66). Copyright (2016) American Chemical Society

materials have  $\text{Li/TM} > 1$  (e.g. B2), contain metal-site vacancies and exhibit high capacity with oxygen-based redox activity such as is observed in a typical LLRTMO material. Figure 5.7 shows that other single phase low-IRC materials exhibit the oxygen-based redox reaction. The redox capability of the TM ions, which primarily depends on the overall composition, and the initial lithium content affects the extent of reversible Li deintercalation and intercalation as will be discussed after the next section on two-phase materials.

### 5.3 Two-phase low- irreversible capacity materials

Some low-IRC materials were found to contain impurities such as a spinel phase. Li-deficient materials in the H and E series, which were predominantly Ni-rich, exhibited two-phase behavior. Figure 5.8 shows the XRD patterns of series H materials in the angular range between  $10^{\circ}$  to  $70^{\circ}$ . Figure 5.8 shows that the Li-deficient members

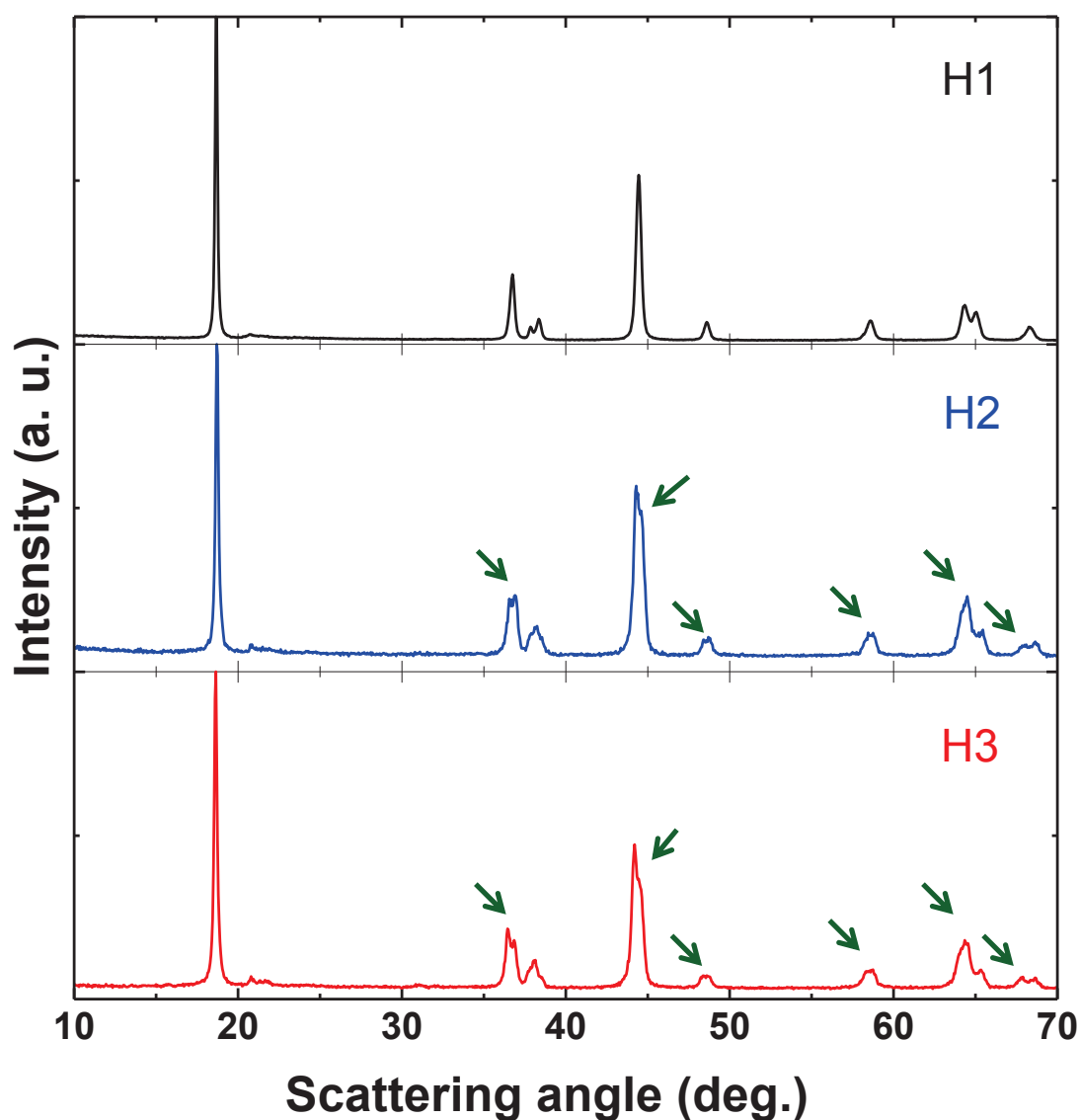


Figure 5.8 XRD patterns of samples H1, H2 and H3. Green arrows indicate the secondary spinel phase

Adapted with permission from (*Chem. Mater.*, 2016, 28 (1), 55–66). Copyright (2016) American Chemical Society

(samples H2 and H3) are two-phase composites with a spinel component. The green arrows in the XRD patterns of the samples H2 and H3 (Figure 5.8) indicate the Bragg peaks corresponding to the spinel phase.

Figure 5.9 shows the first cycle charge-discharge profiles of the H series, in which the low-IRC counterparts are layered-spinel composites. Their first cycle electrochemical behavior is similar to that of high capacity layered-spinel composites reported elsewhere<sup>127</sup>. Sample H3 exhibits an IRC as low as 3%, the lowest IRC ever reported for

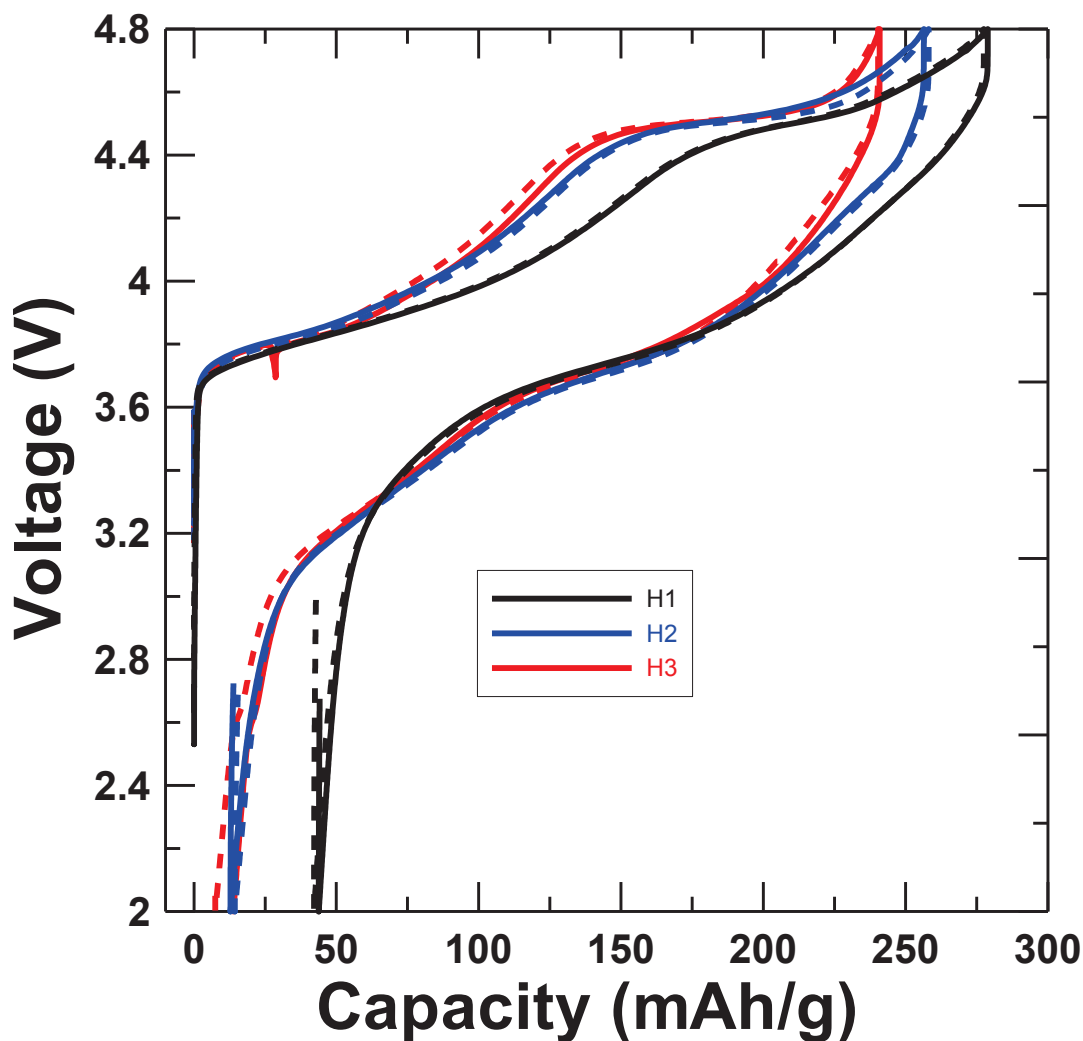


Figure 5.9 First cycle charge-discharge voltage vs specific capacity profiles of H series. H1 and H2 are two-phase low-IRC materials.

Adapted with permission from (*Chem. Mater.*, **2016**, 28 (1), 55–66). Copyright (2016) American Chemical Society

such composite materials. The reduced IRC in spinel-layered composites may be attributed to the combined effect of spinel and layered components – the ability of the spinel component to intercalate Li into its, initially empty, 16c sites and the presence of metal-site vacancies in the layered component. The vacancy content of two-phase materials were calculated as if they were pure layered  $\text{LiMO}_2$  materials even though the additional phase may contribute to the reduced IRC behavior.

The key condition for realizing low-IRC in single-phase  $\text{LiMO}_2$  type materials is sufficient Li deficiency. By comparing the electrochemical behavior of all the low-IRC materials discussed in this paper, correlations between materials that show low-IRC can be observed. Figure 5.10a shows the correlation between the IRC and the vacancy content. The black and red circles or diamonds in Figure 5.10 represent the single phase and two phase materials respectively. As the number of metal-site vacancies increases, the IRC is reduced. Figure 5.10b shows the first discharge capacity of the materials studied. Some of the low-IRC materials exhibit relatively high capacity.

IRC is determined by the ability or inability of the Li ions to intercalate back into the host structure after the first charge<sup>107</sup>. For conventional Li-excess materials  $\text{Li}[\text{Li}_u\text{M}_{1-u}]\text{O}_2$ , the relative number of transition metal atoms versus oxygen atoms increases after the irreversible oxygen loss leading to structures such as  $\text{M}_{1-u}\text{O}_{2-j}$  (j is the amount of irreversible oxygen loss during first charge) at the end of the first charge. Therefore reaccommodating all the deintercalated Li may not be possible after the first charge and a large irreversible capacity results. By contrast, the low-IRC materials reported here have metal-site vacancies in the pristine state and can compensate for the irreversible oxygen loss.

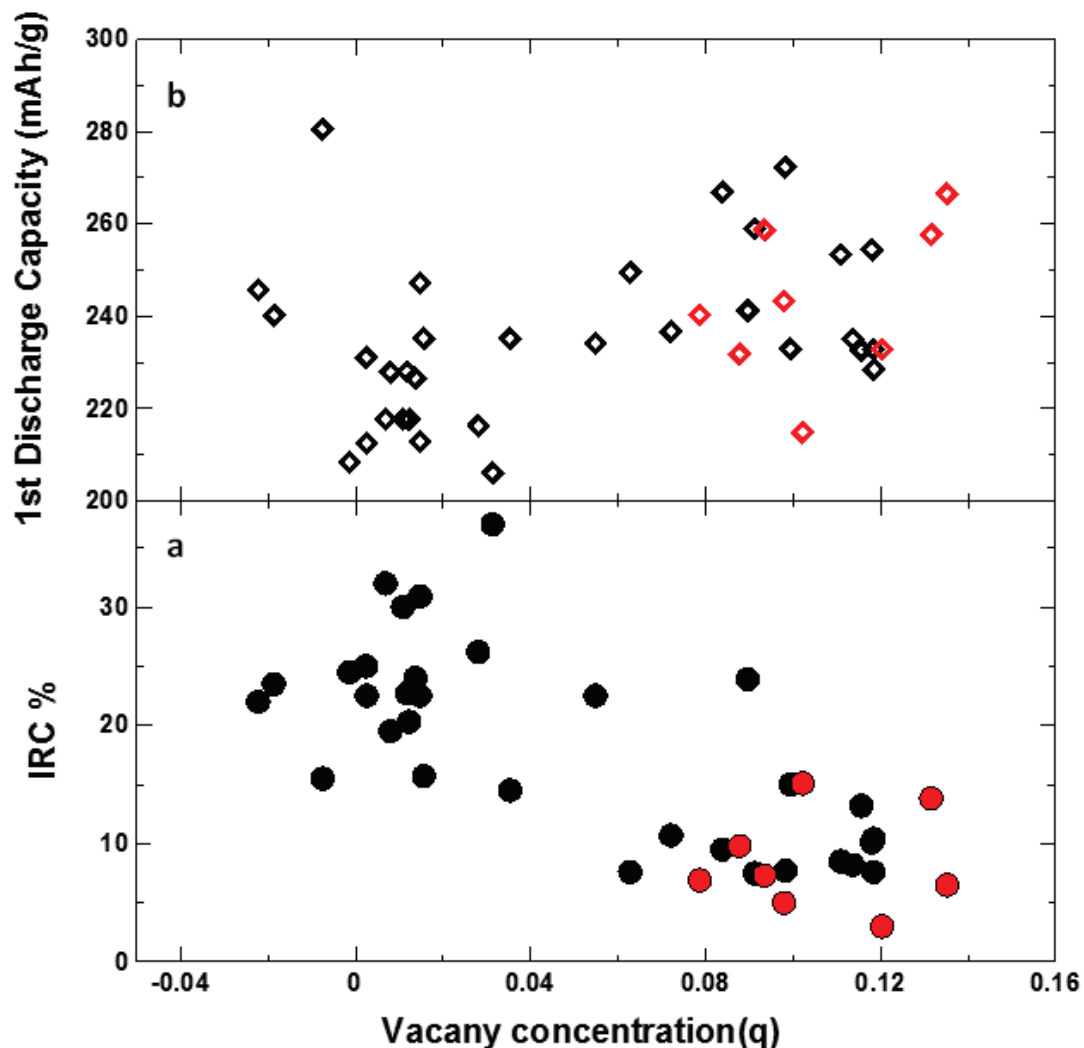


Figure 5.10 (a) Irreversible capacity vs. vacancy content and (b) first discharge capacity vs. vacancy content showing single phase (black circles or diamonds) and two phase (red circles or diamonds) samples.

Adapted with permission from (*Chem. Mater.*, **2016**, 28 (1), 55–66). Copyright (2016) American Chemical Society

Figure 5.11 summarizes the data presented in this chapter. Figure 5.11a shows the irreversible capacity plotted versus the “Li excess” in the materials. The Li excess is the difference of the total lithium content from 1.00. If the Li excess is greater than 0.00, then there are certainly Li atoms in the transition metal layer and the irreversible capacity increases. If the Li excess is less than 0.00, then there are vacancies in the Li layer, as



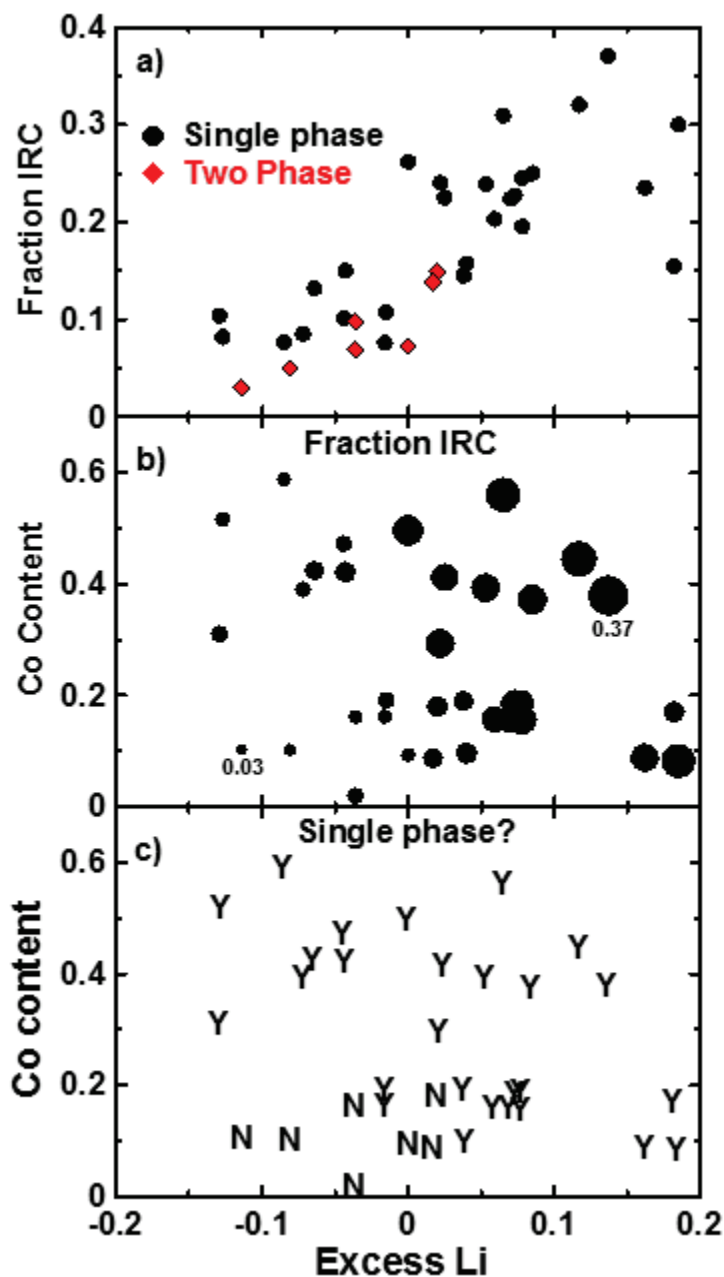


Figure 5.11 (a) Fraction IRC vs. Li excess showing single (black points) and two phase (red points) samples, (b) Co content vs. Li excess (fraction of IRC represented as size of the data points) and (c) Co content vs. Li excess showing whether a sample is single phase (Y) or not (N). Adapted with permission from (*Chem. Mater.*, **2016**, 28 (1), 55–66). Copyright (2016) American Chemical Society

well as possible vacancies in the TM layer and the IRC decreases. Figure 5.11a separates the results according to whether samples are single phase (black symbols) or two phase

(red symbols). The appearance of the spinel phase when the lithium excess is less than 0.00 is not unexpected. However, it is important to understand the compositions that are single phase and also have large negative values of lithium excess (*i.e.* lithium deficiency).

Figure 5.11b and 11c show the variation of the fraction of IRC and the phase purity respectively versus the lithium excess and the Co content in a formula unit. Li-deficient materials (Li excess less than 0.00) with higher Co content can tolerate a higher content of vacancies and remain in a single layered phase. By contrast, Ni-rich materials readily form a co-existing spinel phase when they have the same degree of Li deficiency. For example, the Li and vacancy content of samples A2 ( $\text{Li}_{0.998}\square_{0.098}\text{Ni}_{0.153}\text{Mn}_{0.443}\text{Co}_{0.309}\text{O}_2$ ) and I2 ( $\text{Li}_{1.00}\square_{0.094}\text{Ni}_{0.266}\text{Mn}_{0.547}\text{Co}_{0.093}\text{O}_2$ ) are the same but A2 (Co content is 0.309) is single phase while I2 (Co content is 0.093) is two phase. The reason an increased Co content favors a single layered phase material containing metal-site vacancies may be understood as follows. Co hinders the interlayer mixing of Li and Ni ions between Li and TM layers in  $\text{LiMO}_2$  materials<sup>128,129</sup>. Increased Ni in the Li layer may promote spinel phase formation. Rietveld refinements of the XRD patterns given in Table 5.2 shows that, in the case of Ni-rich samples, the probability of finding Ni in the Li layer is higher. Spinel formation when the Li/TM ratio is low may be a consequence of increased Ni in the Li layer which can be suppressed by addition of Co. Thus a material with an appropriate amount of Li, Co, Ni, Mn and metal-site vacancies can be prepared as a single layered phase even when cooled slowly.

## 5.4 Conclusion

A search for low-IRC ( $\sim 10\%$  or lower) materials was performed in the Li-Ni-Mn-Co-O pseudo-quatarnary system by synthesizing materials with a variety of Li, Ni, Mn, and Co compositions. Low-IRC materials ( $\sim 10\%$  or less) can be synthesized at most Ni-Mn-Co combinations by forcing sufficient Li deficiency. The as-prepared materials were characterized structurally using XRD. Most of the low-IRC materials were single-phase layered, contained metal-site vacancies and exhibited an O3 type structure. If the Li deficiency was increased beyond a certain limit, depending on the Ni:Mn:Co ratios in the material, a spinel phase appeared in the samples and the materials which contained a spinel phase component generally had low-IRC. In general, materials with high cobalt content appeared to tolerate more Li deficiency in the layered single phase and delayed the appearance of spinel. Among the single phase low-IRC materials, some can be regarded as traditional layered materials without a 4.5 V oxygen loss plateau, but containing metal-site vacancies (*e.g.* sample K2). Other single phase low-IRC materials with metal-site vacancies have a 4.5 V oxygen loss plateau that appears in typical LLRTMO materials.

## Chapter 6 Understanding irreversible capacity behavior in layered lithium-rich transition metal oxides<sup>4</sup>

### 6.1 Introduction

Chapter 6 discusses the low-irreversible capacity (IRC) behavior observed in some layered lithium-rich transition metal oxides (LLRTMO) that were identified (Chapter 4) and surveyed (Chapter 5) in the Li-Ni-Mn-Co pseudo-quaternary system. Density measurements suggested the presence of metal-site vacancies in the pristine LLRTMO. Locating the metal-site vacancies in the Li and/or TM layer is essential to understand the low-IRC behavior. <sup>7</sup>Li NMR spectroscopy was used to investigate the local environments and to measure the distribution of Li atoms in the Li and TM layers. The first part of Chapter 6 describes <sup>7</sup>Li NMR studies on some low-IRC materials. Chapter 6 also presents studies that explore the cause of high IRC in LLRTMO materials with no vacancies. The final part of Chapter 6 discusses the correlation between the metal composition, TM ion migration during the first charge and the low-IRC behavior.

### 6.2 <sup>7</sup>Li NMR studies on layered lithium-rich transition metal oxides

Solid-state Li NMR spectra of LLRTMO materials are dominated by Fermi contact interactions with any paramagnetic metals that are bonded to the same oxygen atom as a given Li<sup>130</sup>. The amount of unpaired-electron-spin density that is shared to the Li site across the intervening oxygen bonds by a particular metal atom is relatively consistent as

---

<sup>4</sup> Portions of this Chapter were adapted with permission from Shunmugasundaram, R.; Arumugam, R. S.; Harris, K. J.; Goward, G. R.; Dahn, J. R. A Search for Low-Irreversible Capacity and High-Reversible Capacity Positive Electrode Materials in the Li-Ni-Mn-Co Pseudoquaternary System. *Chem. Mater.*, **2016**, 28 (1), 55–66. The author's contribution to this work included synthesis of materials, XRD measurements, electrochemical characterization and manuscript preparation. Dr. Kris Harris from McMaster University did the NMR experiments and data analyses.

the stoichiometry is changed, making at least partial assignment of the spectra straightforward<sup>130</sup>. Figure 6.1 shows the  ${}^7\text{Li}$  NMR spectrum of  $\text{Li}_2\text{MnO}_3$  ( $\text{Li}[\text{Li}_{1/3}\text{Mn}_{2/3}]\text{O}_2$ ), which has Li atoms in both TM and Li layers. Peaks corresponding to Li in the TM layer are shifted strongly to high frequency with respect to those in the Li layer. The  ${}^7\text{Li}$  NMR spectrum of  $\text{Li}_2\text{MnO}_3$  ( $\text{Li}[\text{Li}_{1/3}\text{Mn}_{2/3}]\text{O}_2$ ) has two distinct peaks: one peak at  $\sim 1420$  ppm caused by Li in the TM layer fully surrounded by Mn and another peak at  $\sim 700$  ppm caused by Li in the Li layer<sup>130</sup>.

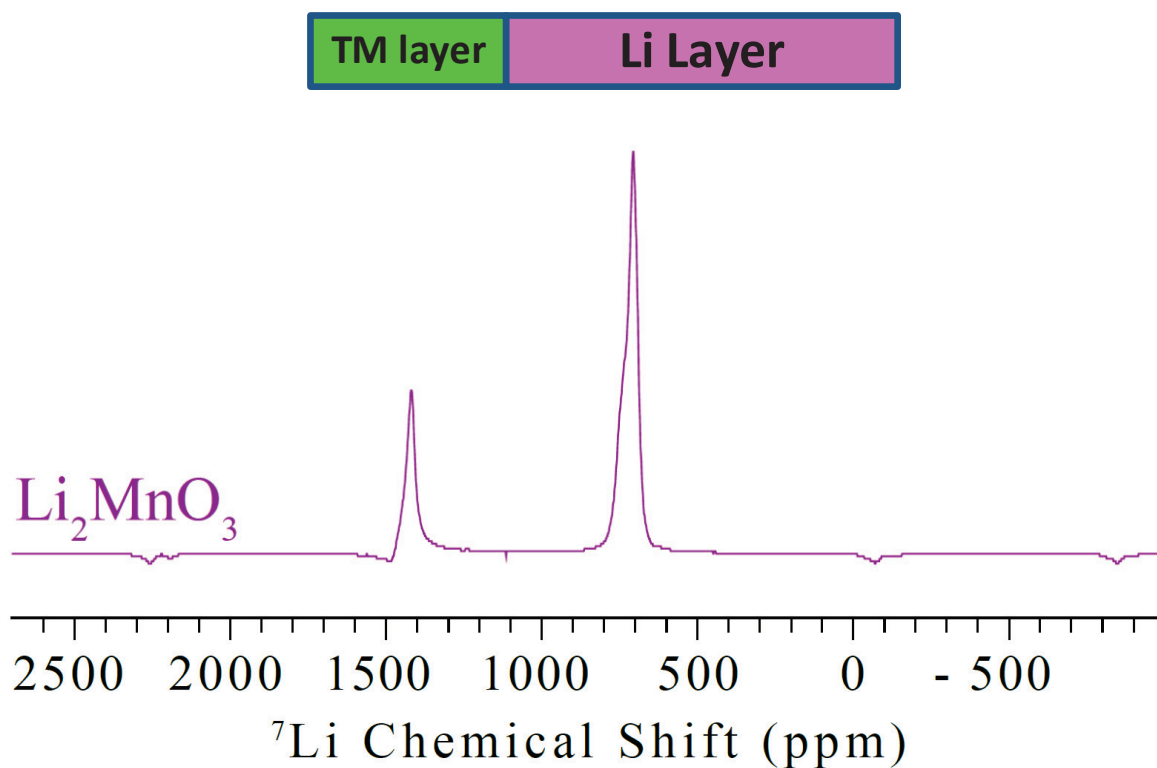


Figure 6.1  ${}^7\text{Li}$  NMR spectrograph of  $\text{Li}_2\text{MnO}_3$ .  
The green and blue regions indicate the limits of TM layer and Li layer regions respectively

Figure 6.2 (left panel) shows the  $^7\text{Li}$  NMR spectra from 2000 to -1000 ppm collected for some selected LLRTMO samples. The right panels in Figure 6.2 from ~ 1500 ppm to ~ 1200 ppm and from ~ 1000 ppm to ~ -500 ppm represent Li in TM layer

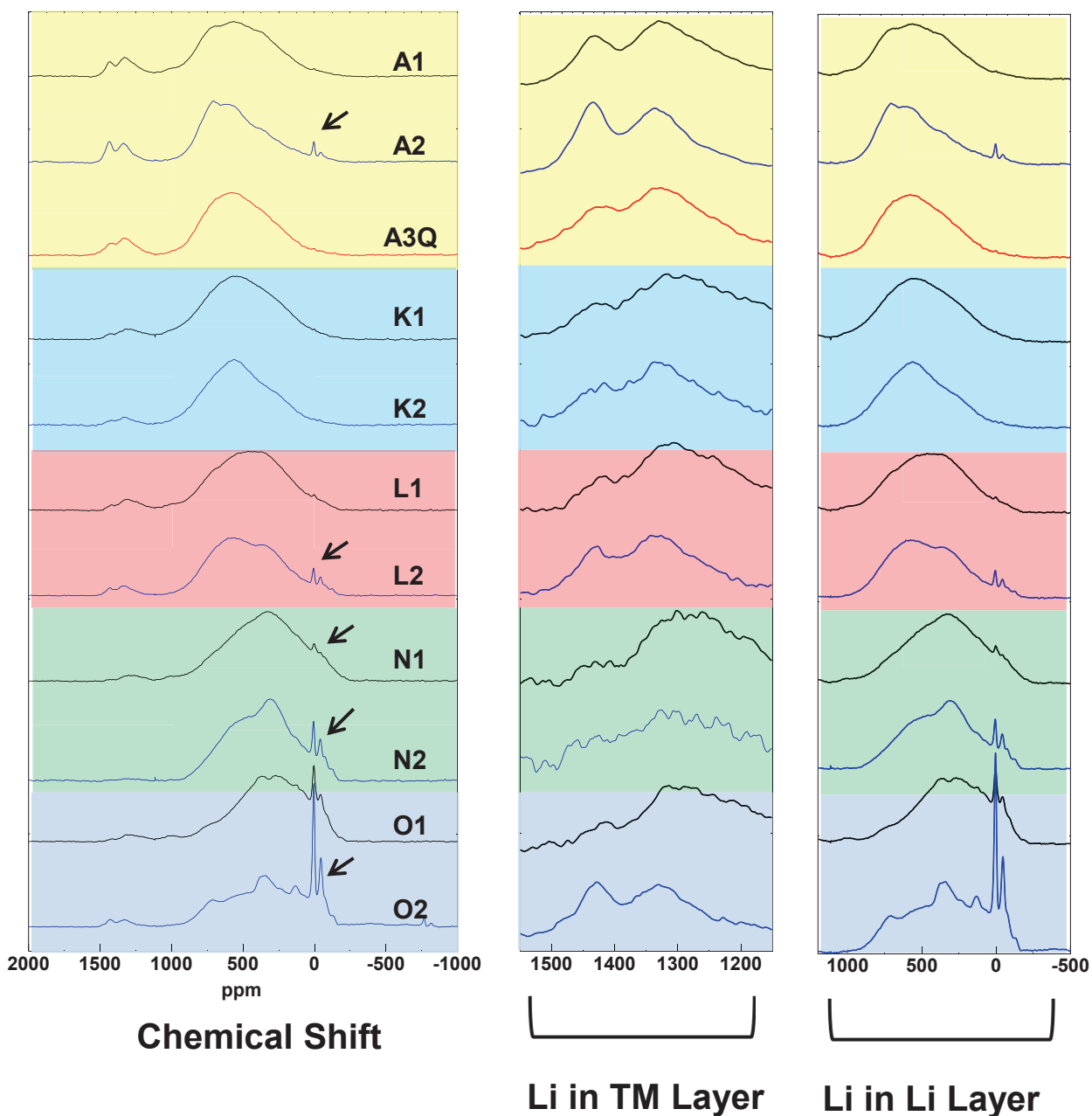


Figure 6.2  $^7\text{Li}$  NMR spectrographs of A1, A2, A3Q, K1, K2, L1, L2, N1, N2, O1 and O2 (refer Table 6.1)

The right panels from 1500 ppm to 1100 ppm and from 1000 ppm to -500 ppm show the peaks corresponding to TM layer Li and Li layer respectively

Adapted with permission from (*Chem. Mater.*, 2016, 28 (1), 55–66). Copyright (2016) American Chemical Society

and the Li layer respectively. The peaks indicated by black arrows in Figure 6.2 represent spinning side bands. The  $^7\text{Li}$  NMR spectra of the studied samples follow the same pattern as that of  $\text{Li}_2\text{MnO}_3$  differing only in that each region of the spectrum is broadened by the larger array of local metal clusters. Similar features have been reported for a wide range of stoichiometries<sup>130</sup> using the more time-consuming  $^6\text{Li}$  NMR spectroscopy, and appear as expected here when the much more rapid  $^7\text{Li}$  magic-angle spinning method<sup>131</sup> is employed.

The simple two-peak structure of the  $^7\text{Li}$  NMR spectra allows facile estimation of the ratio of Li atoms in the TM layer to those in the Li layer. Table 6.1 shows  $^7\text{Li}$  NMR-derived Li occupations of the LLRTMO materials, from spectra shown in Figure 6.2. Given a formula with metal-site vacancies (refer Table 5.3) such as  $\text{Li}_p\text{Ni}_x\text{Mn}_y\text{Co}_z\text{O}_2$ , there are  $1-(x+y+z)$  sites in the TM layer and  $1-p$  sites in the Li layer that can be occupied by metal-site vacancies. The NMR spectrum yields the percentage of Li atoms in each layer, and these may be compared to the number of available sites to estimate the location of the vacancies. For example, A2 has a formula unit of  $\text{Li}_{0.998}\text{Ni}_{0.153}\text{Mn}_{0.443}\text{Co}_{0.309}\text{O}_2$ , which has  $1-(x+y+z) = 0.095$  sites in the TM layer that may be occupied by either Li atoms or vacancies. The NMR spectrum shows that 9.9% of the 0.998 Li atoms in the formula unit, *i.e.*, 0.099 Li atoms, are inside the TM layer (see Table 6.1). As a result the formula unit of A2 can be written as  $\text{Li}_{0.899}\text{Ni}_{0.003}[\text{Li}_{0.099}\text{Ni}_{0.150}\text{Mn}_{0.443}\text{Co}_{0.309}]\text{O}_2$ , where all the metal-site vacancies are found to reside in the Li layer.

Table 6.1 shows that similar behaviour was observed in all of the vacancy-containing samples and none showed evidence of vacancies in the TM layer. In all

Table 6.1 Combined  $^7\text{Li}$  NMR- and ICP-OES derived Li populations of selected LLRTMO materials

Sample	NMR <sup>a</sup> % of Li in Li Layer	NMR <sup>a</sup> % of Li in TM Layer	NMR- ICP <sup>b</sup> [Li] in Li Layer per Formula Unit	NMR- ICP <sup>b</sup> [Li] in TM Layer per Formula Unit	Formula Unit (NMR-ICP)
$\text{Li}_2\text{MnO}_3$	74.5	25.5	0.997(3)	0.336(1)	$\text{Li}_{0.997}[\text{Li}_{0.336}\text{Mn}_{0.664}]\text{O}_2$
A1	90.4	9.6	1.010(3)	0.107(1)	$\text{Li}[\text{Li}_{0.118}\text{Ni}_{0.146}\text{Mn}_{0.426}\text{Co}_{0.296}]\text{O}_2$
A2	90.1	9.9	0.899(3)	0.099(2)	$\text{Li}_{0.899}\square_{0.098}\text{Ni}_{0.003}[\text{Li}_{0.099}\text{Ni}_{0.150}\text{Mn}_{0.443}\text{Co}_{0.309}]\text{O}_2$
A3Q	90.3	9.7	0.858(3)	0.092(1)	$\text{Li}_{0.858}\square_{0.132}\text{Ni}_{0.010}[\text{Li}_{0.092}\text{Ni}_{0.145}\text{Mn}_{0.450}\text{Co}_{0.313}]\text{O}_2$
D1	89.9	10.1	0.968(3)	0.109(2)	$\text{Li}_{0.968}\text{Ni}_{0.032}[\text{Li}_{0.109}\text{Ni}_{0.277}\text{Mn}_{0.459}\text{Co}_{0.157}]\text{O}_2$
D4	92.0	8.0	0.905(3)	0.079(1)	$\text{Li}_{0.905}\square_{0.063}\text{Ni}_{0.032}[\text{Li}_{0.079}\text{Ni}_{0.286}\text{Mn}_{0.474}\text{Co}_{0.162}]\text{O}_2$
K1	92.3	7.7	0.942(3)	0.079(1)	$\text{Li}_{0.942}\square_{0.014}\text{Ni}_{0.044}[\text{Li}_{0.079}\text{Ni}_{0.250}\text{Mn}_{0.378}\text{Co}_{0.293}]\text{O}_2$
K2	96.5	3.5	0.841(3)	0.030(1)	$\text{Li}_{0.841}\square_{0.118}\text{Ni}_{0.041}[\text{Li}_{0.030}\text{Ni}_{0.261}\text{Mn}_{0.399}\text{Co}_{0.310}]\text{O}_2$
L1	93.3	6.7	1.013(3)	0.073(1)	$\text{Li}[\text{Li}_{0.086}\square_{0.002}\text{Ni}_{0.180}\text{Mn}_{0.359}\text{Co}_{0.372}]\text{O}_2$
L2	94.4	5.6	0.875(3)	0.052(1)	$\text{Li}_{0.875}\square_{0.111}\text{Ni}_{0.015}[\text{Li}_{0.052}\text{Ni}_{0.177}\text{Mn}_{0.379}\text{Co}_{0.390}]\text{O}_2$
N1	96.3	3.7	0.963(3)	0.037(1)	$\text{Li}_{0.963}\square_{0.028}\text{Ni}_{0.009}[\text{Li}_{0.037}\text{Ni}_{0.187}\text{Mn}_{0.280}\text{Co}_{0.496}]\text{O}_2$
N2	98.7	1.3	0.862(3)	0.011(1)	$\text{Li}_{0.862}\square_{0.114}\text{Ni}_{0.024}[\text{Li}_{0.011}\text{Ni}_{0.180}\text{Mn}_{0.292}\text{Co}_{0.516}]\text{O}_2$
O1	95.7	4.3	1.019(3)	0.046(1)	$\text{Li}[\text{Li}_{0.065}\square_{0.015}\text{Ni}_{0.092}\text{Mn}_{0.268}\text{Co}_{0.560}]\text{O}_2$
O2	96.6	3.4	0.884(3)	0.031(1)	$\text{Li}_{0.884}\square_{0.116}[\text{Li}_{0.031}\square_{0.003}\text{Ni}_{0.097}\text{Mn}_{0.282}\text{Co}_{0.588}]\text{O}_2$

<sup>a</sup> Obtained from integrated intensities from the  $^7\text{Li}$  NMR spectra shown in Figure 6.2 measuring the percentage of Li observed in the shift region for the TM or Li layers in these structures.

<sup>b</sup> Separation of the ICP-OES-measured Li atoms per  $\text{LiMO}_2$  formula unit (Table 5.3), into those in the Li layer and those in the TM layer, using the NMR-measured percentages shown in the first two columns

samples, the measured values from NMR and ICP-OES of the Li populations within the TM layer are approximately equal to the calculated number of sites available for Li atoms or vacancies. In some cases, slightly more Li atoms than the sites available are



incorporated, likely because of some TM ions (presumably due to Ni to Li exchange) in the Li layer, and small errors in the measurements.

The NMR results suggest that the metal-site vacancies, which could be located on any cation site, predominantly occupy the sites in the Li layer. The density of the low-IRC material is independent of the location (Li layer or TM layer) of the vacancies. Hence, the assignment of vacancies in the Li layer (*e.g.* A2) does not mean they were simply substituted for Li atoms in the Li layer of a stoichiometrically balanced compound (*e.g.* A1). Instead, incorporation of metal-site vacancies in the Li layer is accompanied by a change in metal composition in the TM layer to satisfy the total metal occupancy of 2 and the total charge balance of 4 in a formula unit.

Jiang et al. have carried out  $^6\text{Li}$  MAS spectra studies on Li-excess materials by recovering active materials after the first cycle and showed that only a reduced amount of Li could be reinserted back into the TM layers, contributing to irreversible capacity<sup>62</sup>. As a consequence, reintercalation of extra Li during the first discharge could fill or partially fill the metal-site vacancies in the Li layer and contribute to reduced irreversible capacity. In order to understand how metal-site vacancies help to reduce the IRC, it is essential to investigate the reasons for the high IRC in LLRMTO materials with no vacancies and that is the subject of the following discussion.

### **6.3 Effect of metal composition**

LLRTMO samples with a variety of chemical compositions were studied in Chapter 5. The results suggested that the IRC of LLRTMO materials with no metal-site vacancies ranged from 16 % (*e.g.* H1) up to 37 % (*e.g.* E1) when charged and discharged between

4.8 V and 2.0 V at a relatively low rate (e.g. C/20). High IRC in LLRTMO materials has mainly been attributed to the irreversible oxygen release during first charge, which depends on the total TM redox limit and hence the overall metal composition. Li et al.<sup>65</sup> showed that variations in the particle morphology can affect the irreversible oxygen loss (and hence the IRC) and that the IRC can be changed by modifying the particle size and morphology. In order to see how morphology affects the low-IRC behavior, two samples (A2† and A2††) with the same composition as A2 but with different morphologies were synthesized. The precursors of samples A2† and A2†† were synthesized using the same conditions as that of the sample A2 (2M mixed TM sulfate solution, pH = 8, T = 60°C and stirring rate of = 1000 rpm) except for the following changes: a 1M mixed TM sulfate solution and Na<sub>2</sub>CO<sub>3</sub> were used for the synthesis of A2† and a stirring rate of 800 rpm (but with a 2M mixed TM sulfate and Na<sub>2</sub>CO<sub>3</sub> solution) was used for making A2††.

Figure 6.3 shows that the XRD patterns of the samples A2, A2† and A2†† (10° to 70°) are very close to each other implying that their structures are nearly identical. The Bragg peak positions of A2, A2† and A2†† did not show any deviation. The right panel in Figure 6.3 shows an enlarged view of the (003) peak corresponding to the spacegroup *R-3m*. The scattering angles of (003) peaks of samples A2, A2† and A2†† were nearly the same. Table 6.2 shows the metal composition measured from ICP-OES, lattice parameters (*a* and *c*) and the % Ni in the Li layer of the samples A2, A2† and A2††. All the structural parameters were virtually the same. Table 6.2 shows the specific surface area measured using the BET method and the density obtained from the pycnometer for samples A2, A2† and A2††. While the densities of the samples were quite similar, their specific surface areas were not equal. Due to the change in the particle size and morphology (see Figure 6.4), the change in the specific surface area was not unexpected.

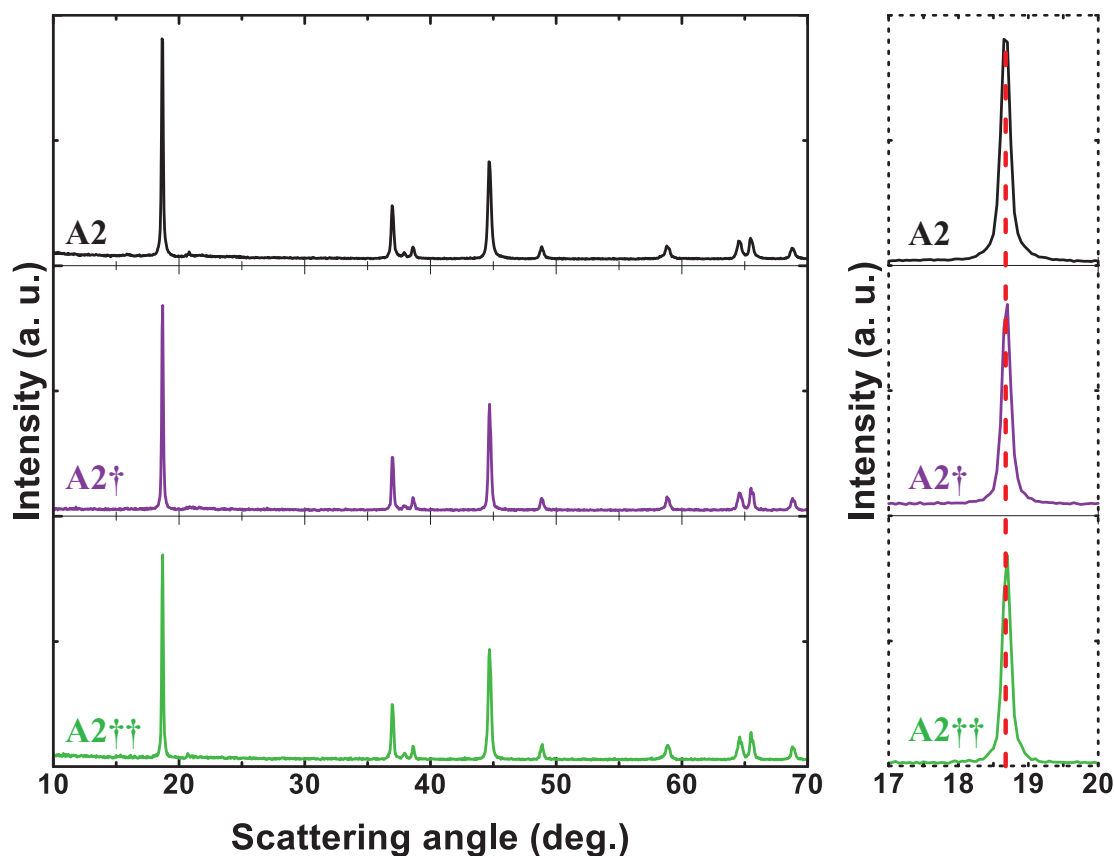


Figure 6.3 XRD patterns of samples A2, A2<sup>†</sup> and A2<sup>††</sup> between 10° to 70°  
 Right panel: Enlarged view of (003) peak corresponding to *R-3m* spacegroup

Table 6.2 ICP-OES metal composition, structural parameters, surface area and density of samples A2, A2<sup>†</sup> and A2<sup>††</sup>

Sample	ICP-OES metal composition (Li:Ni:Mn:Co)	<i>a</i>	<i>c</i>	% Ni in the Li layer	BET specific surface area (m <sup>2</sup> /g)	Density from Pycnometer (g/cm <sup>3</sup> )
A2	1.049:0.161:0.466:0.325	2.847(1)	14.23(5)	1.6(2) %	4.09 ± 0.72	4.531 ± 0.008
A2 <sup>†</sup>	1.062:0.157:0.461:0.313	2.847(2)	14.22(5)	2.0(5) %	4.93 ± 0.57	4.519 ± 0.003
A2 <sup>††</sup>	1.058:0.163:0.473:0.315	2.84(3)	14.22(6)	1.8(3) %	2.26 ± 0.36	4.527 ± 0.006

Figure 6.4 shows the SEM images of samples A2, A2<sup>†</sup> and A2<sup>††</sup> with their respective IRC values indicated below each panel. The IRC changed only slightly even with changes in the primary particle morphology or size suggesting a superficial effect of particle surface on the IRC in materials of this composition. Hence the effect of particle morphology on low-IRC behavior is ignored in the forthcoming discussion.

The chemical composition of the compounds determines the IRC more fundamentally due to the oxidation limits of TM ions during first charge. Arunkumar et al. studied a few sets of solid solution series:  $(1-z)\text{Li}[\text{Li}_{1/3}\text{Mn}_{2/3}]\text{O}_2 \cdot (z)\text{Li}[\text{Mn}_{0.5-y}\text{Ni}_{0.5-y}\text{Co}_{2y}]\text{O}_2$  and  $(1-z)\text{Li}[\text{Li}_{1/3}\text{Mn}_{2/3}]\text{O}_2 \cdot (z)\text{Li}[\text{Ni}_{1-y}\text{Co}_y]\text{O}_2$ , with a number of y and z values and attempted to understand the factors that affect the irreversible oxygen release<sup>54</sup>. They

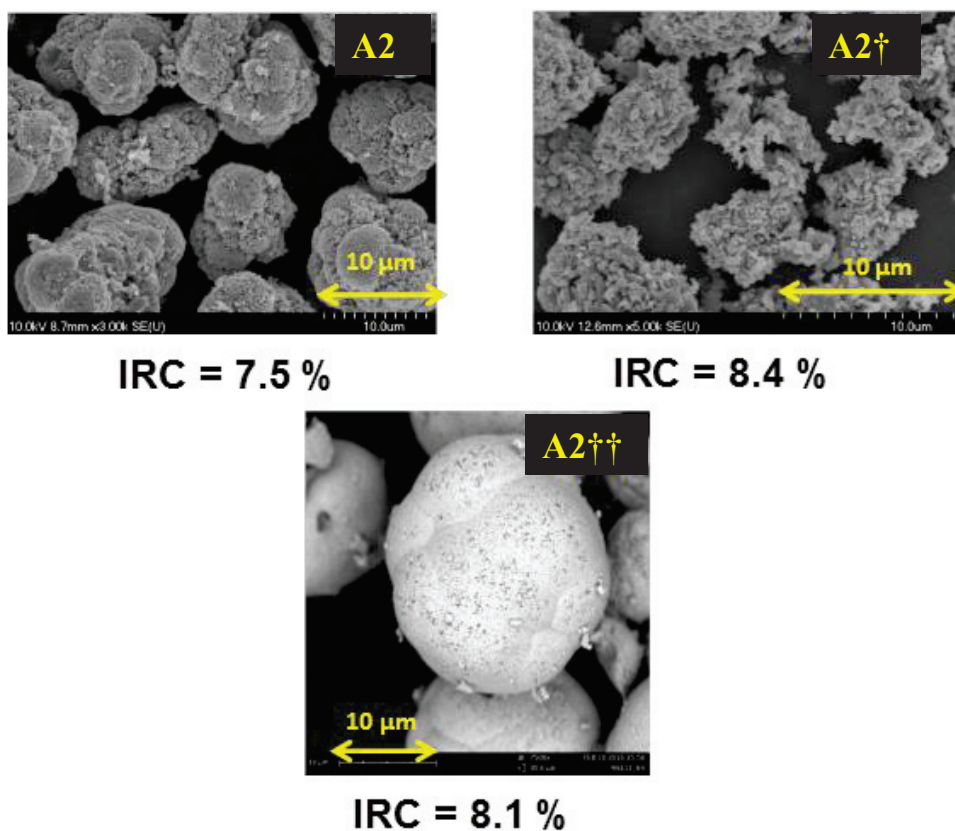


Figure 6.4 SEM images of samples A2, A2<sup>†</sup> and A2<sup>††</sup>

concluded that the amount of Li in the TM layer is a strong determinant of the extent of irreversible oxygen loss. However, they were not able to find an unified trend for IRC versus the amount of irreversible oxygen loss. This raises a question whether the irreversible oxygen loss alone that can account for all the observed IRC. In this section, the first-cycle voltage-specific capacity profiles of some selected LLRTMO materials with no metal-site vacancies are revisited to learn more about the origin of the IRC.

Table 6.3 lists some selected LLRTMO materials and their chemical compositions derived from ICP-OES. The selected LLRTMO samples in the order E1, A1, B1, C1, D1 and H1 form a solid-solution series with increasing Ni/Co ratio. Table 6.3 shows that the precursors of the selected samples have same Mn content but the Li and Mn content vary in their lithated oxides (middle column) with changing Ni/Co ratio. As per the oxidation state rules ( $\text{Ni}^{2+}$ ,  $\text{Mn}^{4+}$  and  $\text{Co}^{3+}$ ), the Li contents decrease from E1 to H1.

Table 6.3 ICP-OES formula unit and the precursor compositions of samples E1, A1, B1, C1, D1 and H1

<b>Sample</b>	<b>Formula unit derived from ICP-OES</b>	<b>Precursor composition</b>
E1	$\text{Li}[\text{Li}_{0.155}\text{Ni}_{0.043}\text{Mn}_{0.417}\text{Co}_{0.385}]\text{O}_2$	$\text{Ni}_{0.05}\text{Mn}_{0.5}\text{Co}_{0.45}\text{Co}_3$
A1	$\text{Li}[\text{Li}_{0.126}\text{Ni}_{0.147}\text{Mn}_{0.429}\text{Co}_{0.298}]\text{O}_2$	$\text{Ni}_{0.167}\text{Mn}_{0.5}\text{Co}_{0.333}\text{Co}_3$
B1	$\text{Li}[\text{Li}_{0.155}\text{Ni}_{0.163}\text{Mn}_{0.430}\text{Co}_{0.251}]\text{O}_2$	$\text{Ni}_{0.2}\text{Mn}_{0.5}\text{Co}_{0.3}\text{Co}_3$
C1	$\text{Li}[\text{Li}_{0.079}\text{Ni}_{0.277}\text{Mn}_{0.458}\text{Co}_{0.186}]\text{O}_2$	$\text{Ni}_{0.3}\text{Mn}_{0.5}\text{Co}_{0.2}\text{Co}_3$
D1	$\text{Li}[\text{Li}_{0.076}\text{Ni}_{0.309}\text{Mn}_{0.458}\text{Co}_{0.156}]\text{O}_2$	$\text{Ni}_{0.33}\text{Mn}_{0.5}\text{Co}_{0.167}\text{Co}_3$
H1	$\text{Li}[\text{Li}_{0.049}\text{Ni}_{0.362}\text{Mn}_{0.492}\text{Co}_{0.097}]\text{O}_2$	$\text{Ni}_{0.4}\text{Mn}_{0.5}\text{Co}_{0.1}\text{Co}_3$

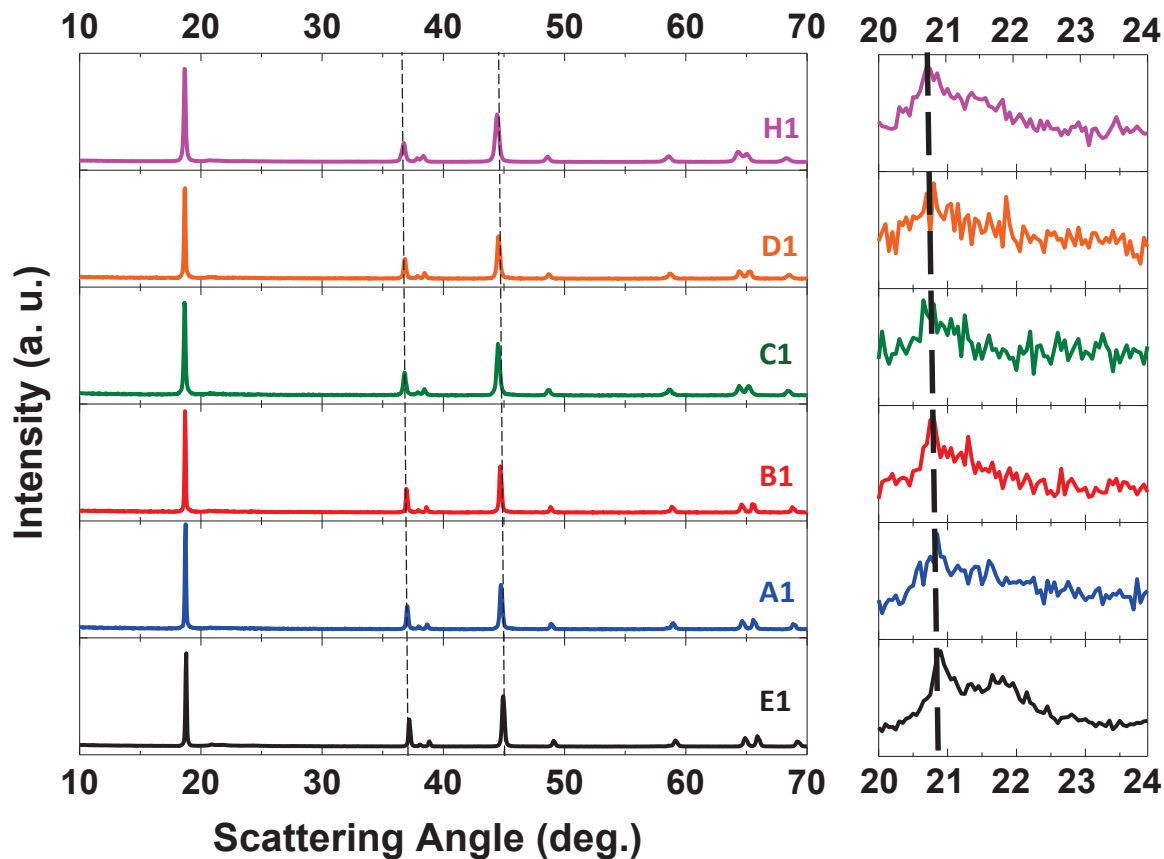


Figure 6.5 XRD patterns of samples E1, A1, B1, C1, D1 and H1 between  $10^\circ$  and  $70^\circ$   
 Right panel: Enlarged view of the superlattice peaks between  $20^\circ$  and  $24^\circ$

Figure 6.5 shows a stack of the XRD patterns of the samples from E1 to H1. The main peaks, which can be described with  $R-3m$  spacegroup ( $\alpha$ - $\text{NaFeO}_2$  structure), in the XRD patterns shift towards lower angles from sample E1 to H1 implying the substitution of larger  $\text{Ni}^{2+}$  ions for smaller  $\text{Co}^{3+}$  ions. The right panel of Figure 6.5 shows an enlarged view of the superlattice peaks between  $20^\circ$  and  $24^\circ$ . The superlattice peaks also shift in the same manner as the main peaks implying solid solution behavior (previously explained in Chapter 3).

The structure of the LLRTMO materials E1, A1, B1, C1, D1 and H1 should be ideally described with the  $C2/m$  spacegroup in the monoclinic setting but just for

convenience, the lattice parameters are reported in terms of hexagonal setting. Figure 6.6 shows a plot of lattice parameter ( $a$  and  $c$ ) variation with the amount of Co. As expected, a decrease in the lattice parameters was observed with the substitution of Co for Ni (see Table 6.3).

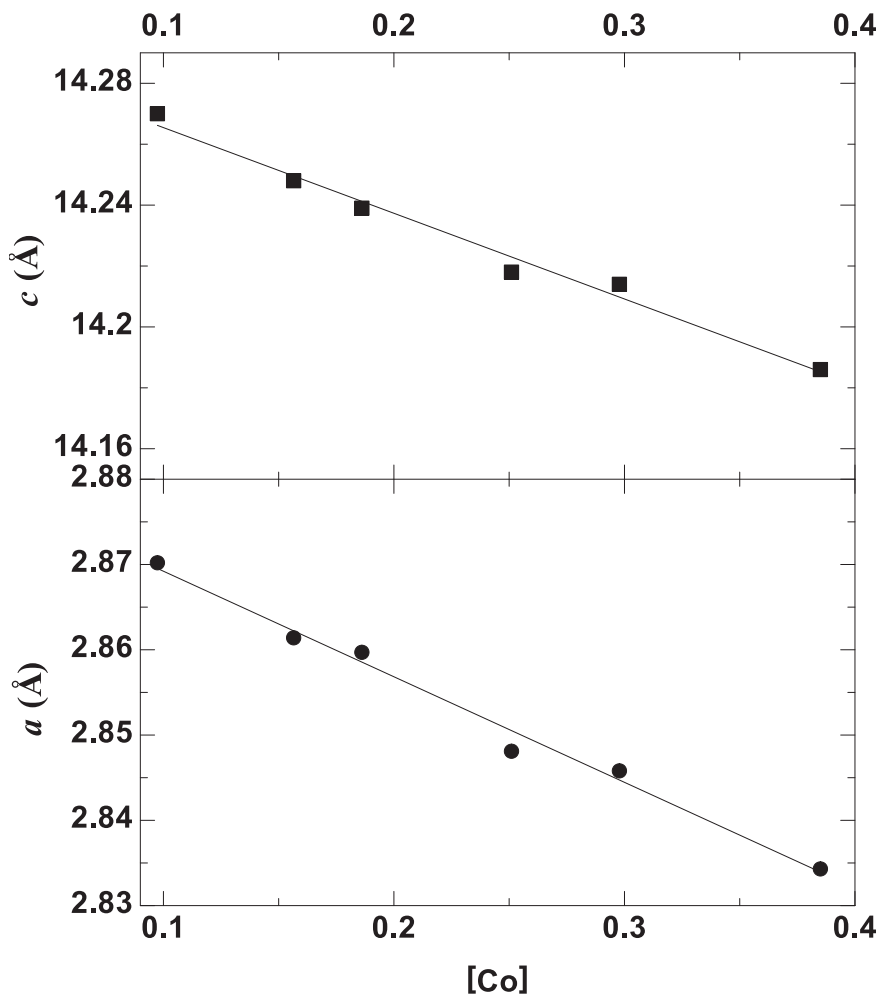


Figure 6.6 Lattice parameters  $a$  and  $c$  vs. the amount of Co for samples E1, A1, B1, C1, D1 and H1

Figure 6.7 shows the first cycle voltage-specific capacity profiles of the samples E1, A1, B1, C1, D1 and H1 between 2.0 V and 4.8 V vs Li/Li<sup>+</sup>. As discussed previously in Chapter 1 (refer to Figure 1.7), the first charge profile can be divided into two regions – a sloping region corresponding to the TM redox processes and the plateau region

corresponding to oxygen release or oxygen redox. In Figure 6.7, the sloping region and the plateau region limits have been indicated using a thick line and a dashed-line,

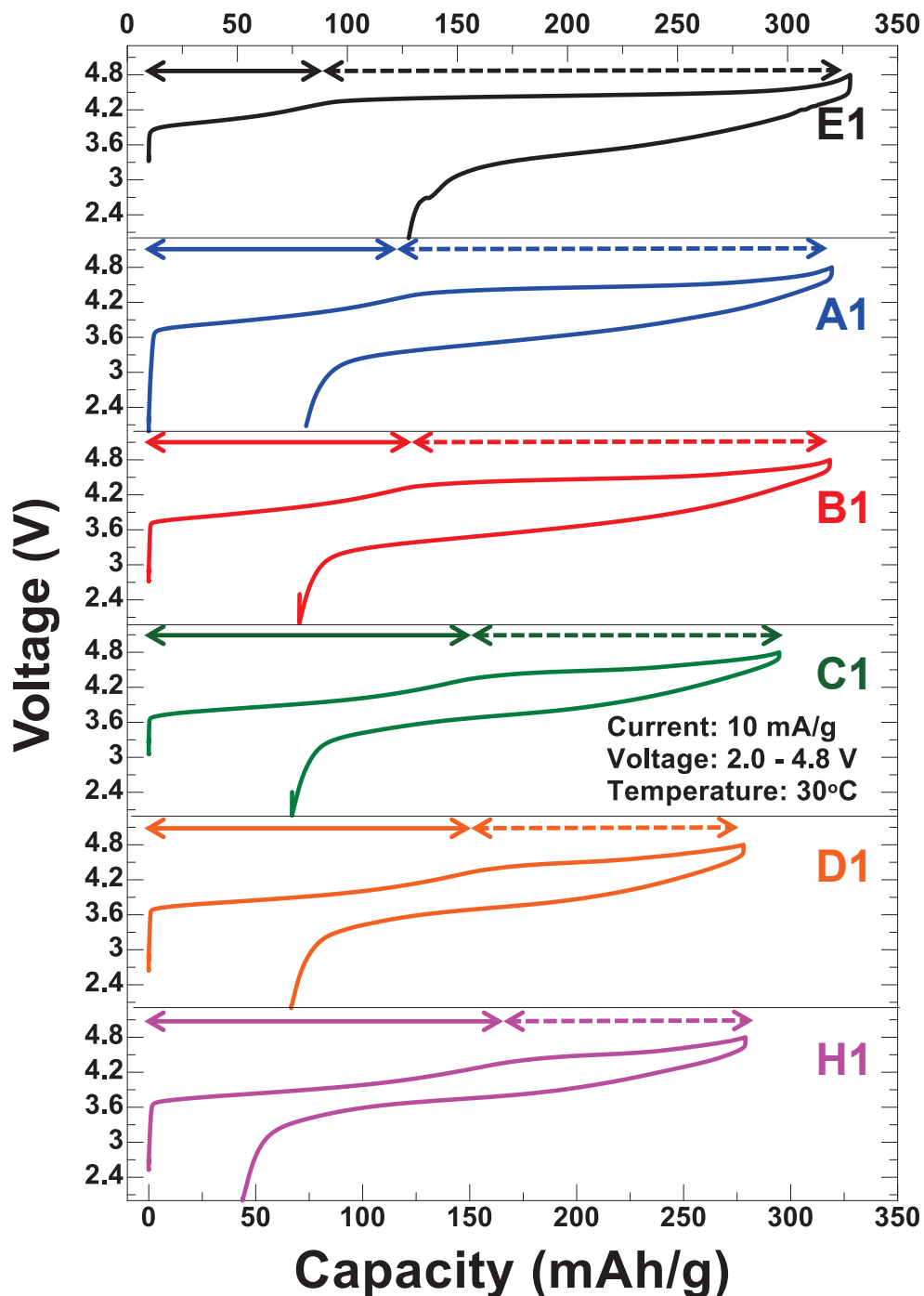


Figure 6.7 First cycle voltage-capacity profiles of samples E1, A1, B1, C1, D1 and H1 between 2.0 V and 4.8 V.

The transition metal redox limits (solid lines) and the oxygen-activity (oxygen release and/or oxygen redox) (dashed lines) limits are shown in each panel



respectively, in each panel.

Table 6.4 shows the total first charge capacity, the sloping region (TM redox) capacity, the plateau capacity and the IRC of the samples from E1, A1, B1, C1, D1 and H1. The first charge capacities were consistent with their respective total Li content. As the sloping region capacity increases, the plateau capacity decreases from sample E1, A1, B1, C1, D1 and H1. As the Ni/Co ratio increases from sample E1, A1, B1, C1, D1 and H1, more Ni is involved in the redox region and thus gives rise the increase in the sloping region capacity.

Table 6.4 Sloping region, plateau region and the total capacities observed during the first charge of samples E1, A1, B1, C1, D1 and H1 (refer Figure 6.7 )

Sample	Total Li (ICP-OES)	Total calculated capacity (mAh/g)	Total observed capacity (mAh/g)	Sloping region capacity (mAh/g)	Plateau capacity (mAh/g)	Discharge capacity (mAh/g)	IRC %
E1	1.155	351	327	90	237	206	37.00
A1	1.126	337	319	125	194	247	22.50
B1	1.155	351	315	130	185	246	22.00
C1	1.079	314	295	155	140	228	22.70
D1	1.076	313	280	160	120	211	24.50
H1	1.051	301	278	170	108	234	15.70

Figure 6.8 shows the  $dQ/dV$  vs  $V$  plots of samples E1, A1, B1, C1, D1 and H1. The oxidation peaks between 3.6 V and 4.2 V are caused by the oxidation of  $Ni^{2+}$  and  $Co^{3+}$  ions. For sample E1, which has a tiny amount of  $Ni^{2+}$ , the oxidation peak that is centered at  $\sim 4.0$  V predominantly corresponds to the oxidation of  $Co^{3+}$ . The oxidation peaks of

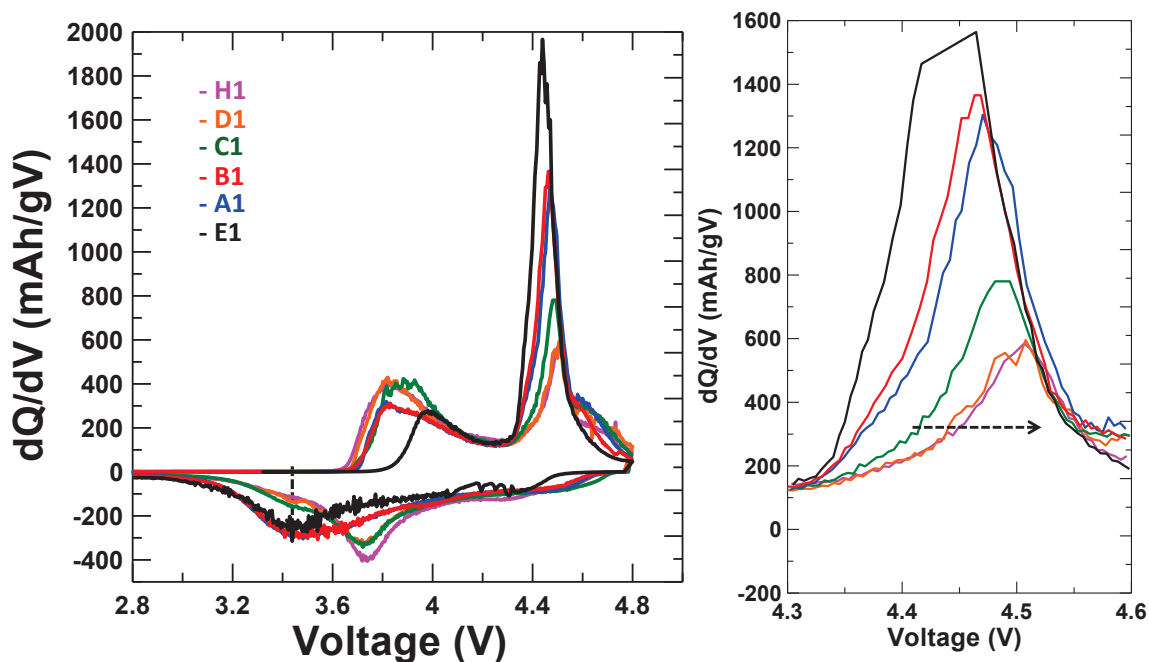


Figure 6.8 Differential voltage-capacity profiles during the first cycle of samples E1, A1, B1, C1, D1 and H1.

Right Panel: Enlarged view of the oxygen-release peaks between 4.3 V and 4.6 V

samples from E1, A1, B1, C1, D1 and H1 progressively shift towards lower voltage indicating the increased participation of  $\text{Ni}^{2+}$  oxidation. The peaks that are centered around 4.5 V in the charge profile correspond to the oxygen release or oxygen redox. The right panel of Figure 6.8 shows an enlarged view of the oxygen release peaks of samples E1, A1, B1, C1, D1 and H1. The centers of the oxygen release (and/or oxygen redox) peaks shift to high voltage from sample E1 to H1 implying a delay in the oxygen release or oxygen redox for samples with increased Ni/Co and TM redox.

Figure 6.9 shows a plot of IRC against plateau capacity of the samples E1, A1, B1, C1, D1 and H1. As the Ni/Co ratio increases from sample E1, A1, B1, C1, D1 and H1, which causes more TM redox capacity, the plateau capacity decreases. Sample E1, which has the lowest Ni/Co ratio, exhibits the highest plateau capacity (~ 72 %) and IRC (37 %) and sample H1, which has the highest Ni/Co ratio exhibits the lowest plateau capacity (~

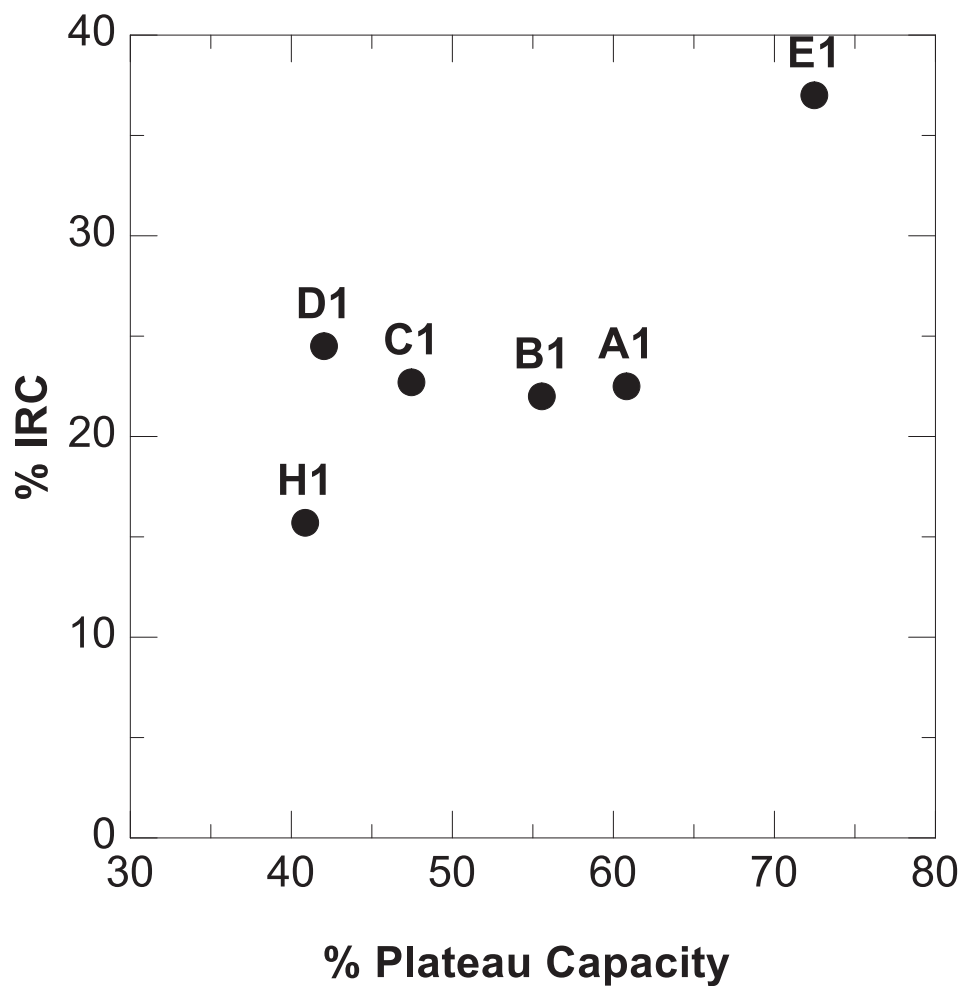


Figure 6.9 Irreversible capacity vs. 4.5 V plateau capacity of samples E1, A1, B1, C1, D1 and H1

40 %) and IRC (15.7 %). It appears that the IRC increases with increase in plateau capacity (due to irreversible oxygen release) but they were not correlated linearly. This suggests that oxygen release may not be the only factor for high IRC observed in LLRTMO materials. Arunkumar et al. reported that the compound  $\text{Li}[\text{Li}_{0.08}\text{Ni}_{0.55}\text{Mn}_{0.37}]\text{O}_2$  showed no obvious plateau during first charge but exhibited an IRC of 17 %<sup>138</sup>. For this compound, according to the stoichiometry, the first charge capacity can be explained by Ni redox. So, both a delay in the oxygen release (sample H1) and/or the absence of oxygen release<sup>137</sup> in Ni-rich LLRTMO compounds did not

reduce the IRC below a certain level. So, there must be another factor that contributes to the IRC. In Ni-rich samples, Ni ions are very likely to migrate to the Li sites and stabilize there and impede the re-entry of the Li ions during the first discharge step. So, the next section will explore the effect of migration of TM ions as another possible reason for high IRC.

#### **6.4 Effect of TM migration**

The effect of TM migration into the TM layer on the progressive voltage fade in LLRTMO materials has been studied by Sathya et al.<sup>132</sup> They reported that the trapping or stabilization of smaller TM ions such as  $Ti^{4+}$  in the tetrahedral sites in the Li layer induced spinel-like phases and caused voltage fade. However, larger TM ions such as  $Sn^{4+}$  did not cause such a voltage fade. Their studies suggest that mitigation of TM ions migration to the Li layer could also reduce IRC.

In order to study the effect of TM migration on IRC clearly, a Fe containing LLRTMO compound ( $Li[Li_{0.143}Fe_{0.286}Mn_{0.286}Co_{0.286}]O_2$ ), labelled as Fe-A1, with almost same amount of Li and same theoretical TM redox capacity as to that of sample A1, was synthesized and its properties were characterized. The reason for the selection of Fe is that it has been known to migrate easily to the Li layer<sup>133</sup>. A carbonate precursor of composition  $Fe_{0.333}Mn_{0.333}Co_{0.333}CO_3$  was synthesized through co-precipitation under the same conditions as explained in section 2.1.1. A required amount of  $Li_2CO_3$  was added to  $Fe_{0.333}Mn_{0.333}Co_{0.333}CO_3$  and fired at  $900^\circ C$  to obtain sample Fe-A1.

Figure 6.10 shows the experimental and calculated (Rietveld refinement) XRD pattern of the sample Fe-A1. The black and the red lines represent the experimental and

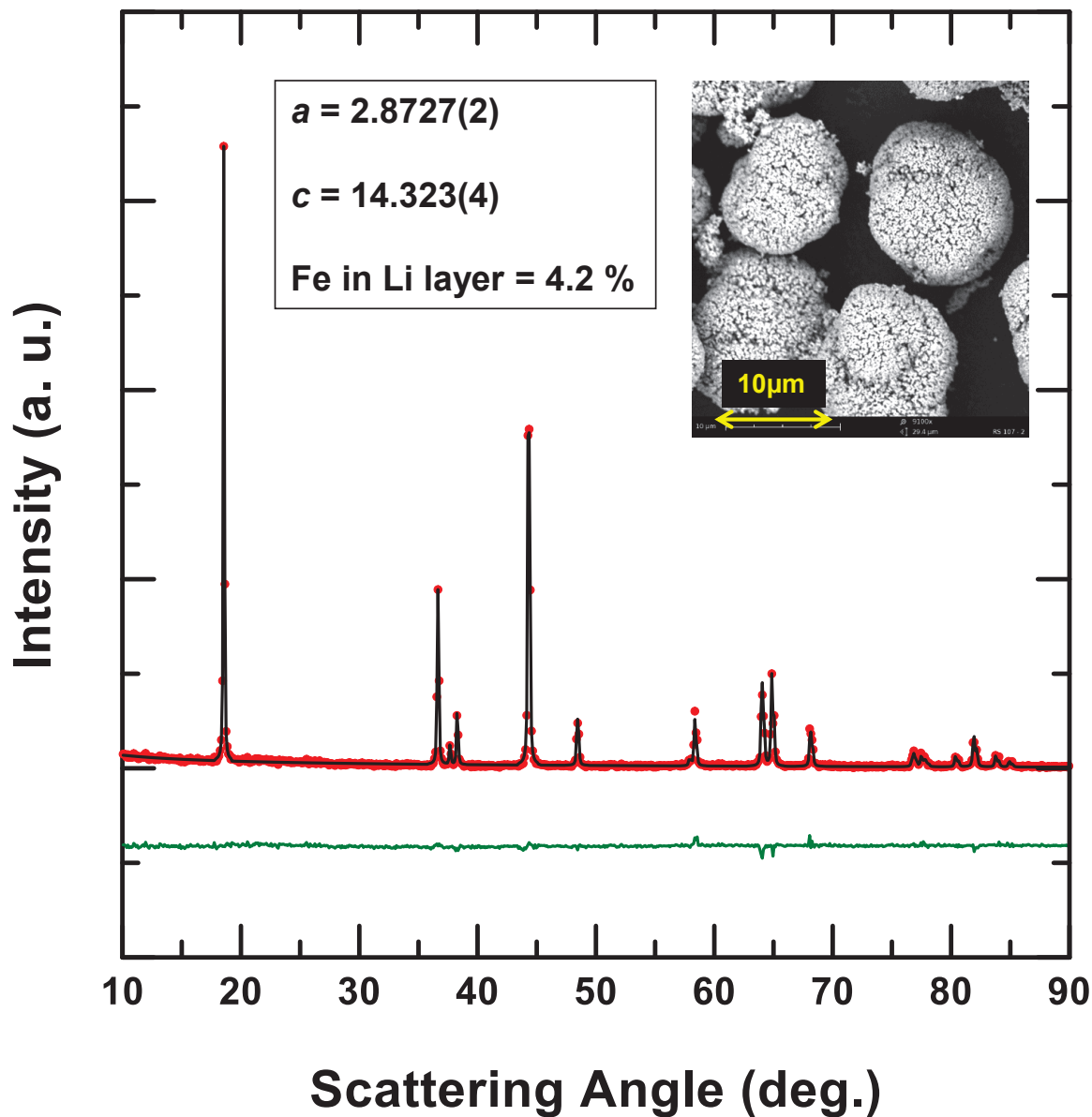


Figure 6.10 XRD pattern of sample Fe-A1

Black – experimental, red - calculated and green - difference from Rietveld refinement. Inset: structural parameters obtained from the Rietveld refinement (top left) and the SEM image of Fe-A1 (top right)

the calculated patterns respectively and the green line is the difference between them. The inset at the top left of Figure 6.10 shows the structural parameters of sample Fe-A1 that were obtained from Rietveld refinement of the XRD pattern. The inset at the top right of Figure 6.10 shows the SEM image of Fe-A1. The particles were nearly spherical and the particle size is comparable to that of the sample A1 (see Figure 5.2).

Table 6.5 compares a few properties of samples A1 and Fe-A1. The specific surface area of Fe-A1 was slightly smaller than that of A1. Similar to A1, the measured density of Fe-A1 was very close to its calculated density implying the absence of metal-site vacancies. Hence it is assumed that factors such as particle size, specific surface area and density do not affect the comparison of first-cycle electrochemical properties between A1 and Fe-A1.

Table 6.5 Comparison of properties of A1 and Fe-A1

Sample	A1	Fe-A1
ICP-OES metal composition	1.126:0.147:0.429:0.298 (Li:Ni:Mn:Co)	1.132:0.284:0.295:0.288 (Li:Fe:Mn:Co)
Calculated specific capacity	336 mAh/g	342 mAh/g
Calculated redox capacity	177 mAh/g	173 mAh/g
% Redox capacity	52.7 %	50.5 %
BET surface area (m <sup>2</sup> )	1.09 ± 0.11	0.85 ± 0.13
Calculated density	4.46 ± 0.03	4.52 ± 0.03
Density from pycnometer	4.453 ± 0.005	4.531 ± 0.005

Figure 6.11 shows the first-cycle voltage-specific capacity profile of samples A1 (black line) and Fe-A1 (red line). The observed first charge capacity of Fe-A1 was 282 mAh/g, which is consistent with the work by Tabuchi et al<sup>141</sup>. They showed that all the Fe<sup>3+</sup> could not be oxidized to Fe<sup>4+</sup>. Figure 6.11 shows a plateau at ~ 4.0 V in the voltage profile of Fe-A1 most likely corresponding to the oxidation of Fe<sup>3+</sup> to Fe<sup>4+</sup><sup>141</sup> and Co<sup>3+</sup> to Co<sup>4+</sup>. The proportion of plateau capacity of Fe-A1 (~ 37 %) is lower than that of sample A1 (~ 61 %). However, sample Fe-A1 exhibited an IRC of ~ 48 % compared to 22 % IRC

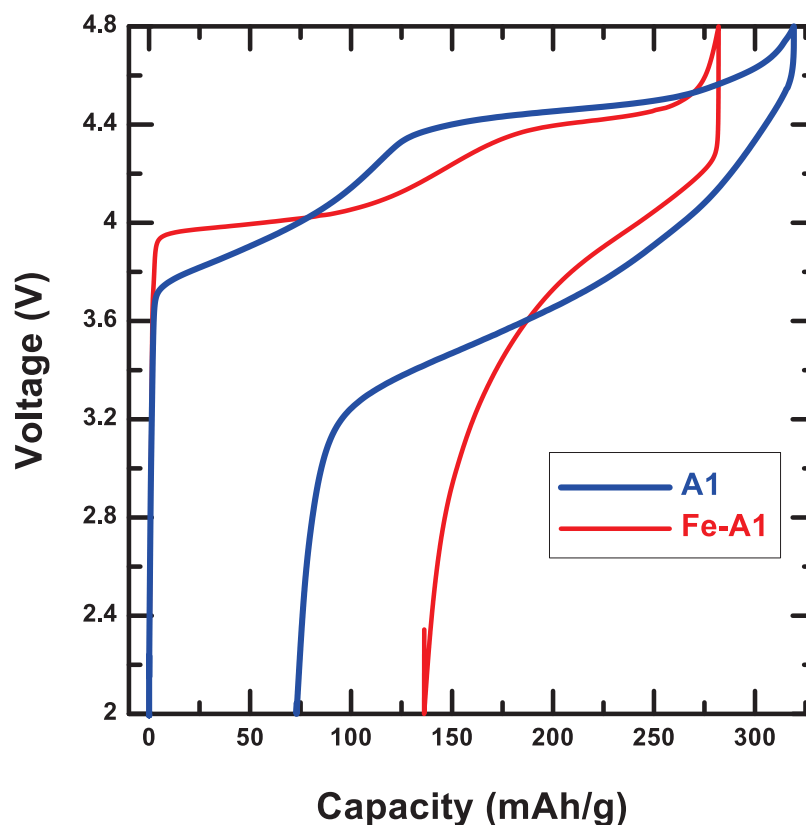


Figure 6.11 First cycle voltage-specific capacity profiles of samples A1 (blue) and Fe-A1 (red) between 4.8 V and 2.0 V

observed in sample A1. Figure 6.11 confirms that the extent of plateau capacity during first charge is not directly proportional to the IRC. This is consistent with the fraction of TM ions in the Li layer in the pristine material obtained from Rietveld refinement, which showed the pristine Fe-A1 had a larger (see the inset in Figure 6.10) fraction of  $\text{Fe}^{3+}$  ions in the Li layer than the  $\text{Ni}^{2+}$  ions in the pristine A1 (see Table 4.2). So, the most likely other factor that affects IRC is TM migration during the first charge.

In order to see how the migration of TM ions during the first charge affects the IRC, a step-wise charge-discharge experiment was conducted. The samples A1, Fe-A1 and A2 were charged to the upper cut-off step-voltages (4.0 V, 4.4 V, 4.6 V and 4.8V) and then discharged to 2.0 V each time. Figure 6.12 shows the voltage-capacity profiles

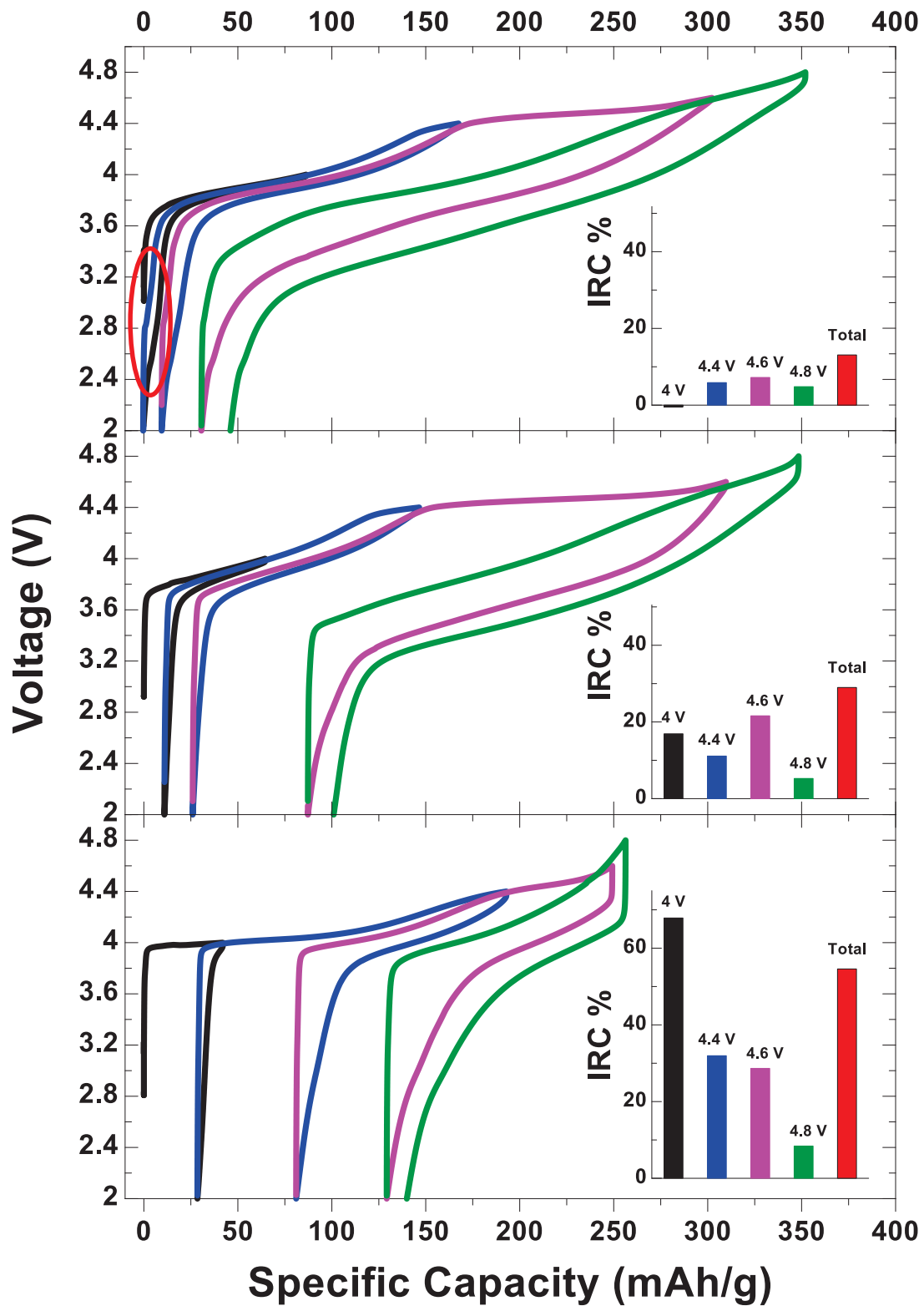


Figure 6.12 Voltage-specific capacity profiles obtained from step-wise charge-discharge cycles between 2.0 V and upper cut-off voltages 4.0 V (black), 4.4 V (blue), 4.6 V (pink) and 4.8 V (green). Inset: % IRC observed in each step (upper-cut-off voltage) cycle and the total % IRC as indicated.



of samples A1, A2 and Fe-A1 obtained from the step-wise charge-discharge experiments. The inset in each panel of Figure 6.12 shows the IRC observed after the charge-discharge step. The IRC after the 4.0 V step cycle for the sample Fe-A1 is very high (~ 68 %) implying that the Li<sup>+</sup> ions are unable to reenter the host structure just after charging up to 4.0 V. This was consistent with the results obtained by McLaren et al.<sup>134</sup>, who showed a very large irreversible capacity in LiFe<sub>0.2</sub>Co<sub>0.8</sub>O<sub>2</sub>. They found that 50 % Fe ions became disordered after the first charge. It strongly suggests that Fe ion migration into the TM layer could prevent the reentry of Li. There may be a possibility that the deintercalation of Li from the TM layer could have occurred first and caused the huge IRC, which needs further investigation.

On the other hand, sample A1 exhibited an IRC of 17 % after the 4.0 V step cycle implying that TM migration even after 4.0 V charge is significant. By contrast to that of the samples Fe-A1 and A1, the IRC exhibited by sample A2 (-0.5 %) was very low when charged to 4.0 V. However, the discharge profile of sample A2 exhibited a small curvature (indicated with a red oval in Figure 6.12). It is speculated that most likely the low voltage curvature in A2 corresponds to a tiny amount of impurity similar to that found in sample A3 (see Figure 4.7) or a spinel phase. At the same time, it should be noted that the impurity in A3 was removed by quenching and A3 exhibited low-IRC behavior even after that, which is applicable to A2 as well. So, the negative values of IRC for sample A2 suggest that the metal-site vacancies could be used for accommodating the Li ions during discharge and that TM ions migration is negligible after the 4.0 V charge.

The results of the above experiments suggest that both oxygen release and TM ions migration during first charge causes high IRC in the LLRTMO materials. The predominance of one effect over the other depends on the chemical composition of the positive electrode material. For the Co-rich LLRTMO samples with no vacancies (*e.g.* A1, B1), it is speculated that oxygen release predominates due to decreased TM redox and causes permanent oxygen loss (mainly at the surface) and concomitant Li loss leading to high IRC. For the Ni-rich (*e.g.* H1) or Fe-rich LLRTMO samples with no vacancies, it is speculated that TM ion migration predominates and impedes the re-entry of Li during first discharge and causes high IRC. For the LLRTMO materials with metal-site vacancies, it is speculated that metal-site vacancies facilitate the accommodation of extra Li ions during first discharge compensating for the high IRC factors (oxygen release and TM ion migration) and caused reduced IRC.

## **6.5 Conclusion**

Solid-state  $^7\text{Li}$  NMR experiments were performed on some LLRTMO materials that included some low-IRC materials. The  $^7\text{Li}$  NMR results were used to measure the amount of Li in the Li layer and in the TM layer, which in turn was used to estimate the distribution of metal-site vacancies between the two layers. The results of the  $^7\text{Li}$  NMR studies suggested that the metal-site vacancies were predominantly located the Li layer of the single-phase low-IRC materials. To probe the underlying reason for the high IRC in LLRTMO materials, properties of a solid-solution series comprised of six LLRTMO materials with no vacancies were revisited. Analyzing the first charge-discharge cycles of those LLRTMO materials showed that irreversible oxygen release might not be the only reason for the high IRC. To test if TM migration during the first charge could contribute

to the IRC, a Fe-containing LLRTMO compound was synthesized and its properties were compared to the sample A1. The Fe-containing material had a very high IRC compared to that of the sample A1 suggesting the view that TM migration could cause high IRC. Further, the results of step-wise charge-discharge experiments with different upper cut-off voltages suggested that TM migration could cause high IRC and that metal-site vacancies facilitated the reentry of extra Li ions during the first discharge.

## Chapter 7 Conclusions and suggested future work

### 7.1 Conclusions

Layered Li-rich transition metal oxides (LLRTMO) are one of the potential candidate positive electrode materials for high-energy Li-ion batteries because they can deliver very high specific capacity ( $> 250$  mAh/g). From an academic point of view, LLRTMO materials have been the subject of several thesis works in recent years. Table 7.1 shows a few examples of recent thesis works from various universities around the world showing that LLRTMO materials have received extensive research.

Table 7.1 Examples of recent thesis works done in LLRTMO materials

Year	Thesis title	University	Ref
2010	Li-rich transition metal oxides as positive electrode materials in Li-ion batteries	Dalhousie University	135
2012	Structural factors affecting the Li transport in Li-excess layered cathode materials	University of Florida	136
2013	Study of Li-rich lamellar oxides as positive electrode materials for Li-ion batteries	University of Science and Technology Bordeaux	137
2014	Electrochemical properties and ion-extraction mechanisms of Li-rich layered oxides and spinel oxides	University of Texas, Austin	138
2015	High energy density cathode active materials for Li-ion batteries	Northeastern University	139

LLRTMO materials have several drawbacks such as a very high first cycle irreversible capacity and progressive voltage fade, which prevent their usefulness in commercial Li-ion batteries. Hence there have been intense efforts to understand the

properties of LLRTMO materials and to solve the problems associated with them. This doctoral thesis is one of the several attempts to understanding the properties of the LLRTMO materials and find solutions to the aforementioned problems. This thesis investigated both structural and electrochemical properties of Li-Ni-Mn-Co based LLRTMO materials, especially the first cycle charge-discharge profile.

### 7.1.1 Structural characterization (Chapter 3)

Chapter 3 used X-ray diffraction to study certain structural properties of LLRTMO. In the structure of LLRTMO materials, the presence of  $\text{Li}^+$  ions with large ionic radii (0.74 Å) and small sized  $\text{Mn}^{4+}$  ions (0.54 Å) in the TM layer causes in-plane ordering resulting in the formation of a superstructure or superlattice. Due to the superlattice ordering, the diffraction patterns of LLRTMO materials exhibit special peaks called as “superlattice peaks”.  $\text{Li}_2\text{MnO}_3$  can be used as a model material to study the superlattice ordering in LLRTMO.

In LLRTMO materials, including  $\text{Li}_2\text{MnO}_3$ , the stacking of TM layers along the  $c$ -axis theoretically follows an order between adjacent layers dictated by translation vectors. If a structure has no faults in the stacking order, then it is said to be a structure with zero stacking faults. In reality, LLRTMO structures have stacking disorder caused by various factors such as synthesis conditions and presence of aliovalent ions in the TM layer and as a result, superlattice peaks become broader.

The XRD patterns of  $\text{Li}_2\text{MnO}_3$  with varying amounts of stacking faults were simulated using a program called FAULTS, which can take into account the existence of stacking fault probability.  $\text{Li}_2\text{MnO}_3$  with different amounts of stacking faults were

synthesized at different temperatures (900°C and 1100°C) and their XRD patterns were fitted with FAULTS. The FAULTS results determined the amount of stacking faults in the two samples and supported the view that increased synthesis temperature tend to lowers the stacking disorder.

Similar to  $\text{Li}_2\text{MnO}_3$ , the XRD patterns of  $\text{Li}[\text{Li}_{1/3-2x/3}\text{Ni}_x\text{Mn}_{2/3-x/3}]\text{O}_2$  materials were also examined. The superlattice peak positions in the XRD patterns of  $\text{Li}[\text{Li}_{1/3-2x/3}\text{Ni}_x\text{Mn}_{2/3-x/3}]\text{O}_2$  materials changed monotonically with Ni content, as did the main Bragg peaks, demonstrating that the superlattice peaks originate from solid solutions and are not caused by any separate phase such as  $\text{Li}_2\text{MnO}_3$  in a composite. FAULTS results on  $\text{Li}[\text{Li}_{1/3-2x/3}\text{Ni}_x\text{Mn}_{2/3-x/3}]\text{O}_2$  materials revealed that the stacking fault probability increased with Ni content. The presence of aliovalent ions ( $\text{Ni}^{2+}$ ) in the TM layer perturbed the stacking order along the  $c$ -axis and thus caused the broadening of the superlattice peaks of  $\text{Li}[\text{Li}_{1/3-2x/3}\text{Ni}_x\text{Mn}_{2/3-x/3}]\text{O}_2$  materials.

### **7.1.2 Effect of lithium content (Chapter 4)**

The Li content of LLRTMO materials affects their first-cycle characteristics especially the length of the 4.5 V plateau. Excess Li in LLRTMO materials generally causes an increase in specific capacity. By contrast, removing Li electrochemically beyond a certain limit, especially from the TM layer, causes irreversible oxygen loss from the host structure and hence a high irreversible capacity loss (IRC).

To reduce the first cycle IRC, three different LLRTMO materials with varying Li/TM ratio were synthesized from the same precursor. One of them was synthesized with appropriate amount of Li based on the stoichiometric calculation. All the three samples

were electrochemically characterized with a focus on the first cycle behaviour. Surprisingly and beneficially, the samples having lower Li/TM ratio exhibited IRC as small as 6.5 % of the first charge capacity. Few impurities were found in one of the two low-IRC materials but quenching resulted in pure phase materials. Analyzing dQ/dV vs. V plots confirmed that the impurities were removed after quenching and that quenching did not affect the low-IRC behavior.

Careful XRD and dQ/dV studies showed that the low-IRC behavior did not originate from any impurity phases including nano-domains of spinel. Therefore, the small IRC of these samples was found to be inherent to their composition and structure. The metal compositions from ICP-OES results and the oxidation states versus atomic occupancy rules suggested that the compounds exhibiting low-IRC had metal-site vacancies. This was further supported by true densities obtained from a helium pycnometer. It is speculated that the metal-site vacancies may provide avenues for enhanced atomic diffusion during and after the oxygen loss process which may contribute to the small IRC.

### **7.1.3 Effect of transition metal composition (Chapter 5)**

A search for low-IRC behavior in other LLRTMO materials with different metal composition is the subject of Chapter 5. The search for low-IRC (~ 10 % or lower) materials was performed in the Li-Ni-Mn-Co-O pseudo-quaternary system by synthesizing materials with a variety of Li, Ni, Mn, and Co compositions. The first-cycle electrochemical results showed that low-IRC materials (~ 10 % or less) can be synthesized at most Ni-Mn-Co combinations by forcing sufficient Li deficiency.

The structures of the materials were characterized using XRD, which showed that several low-IRC materials were single-phase layered containing metal-site vacancies and exhibited an O3 structure. If the Li deficiency was increased beyond a certain limit, depending on the Ni:Mn:Co ratios in the material, a spinel phase appeared in the samples and the materials which contained a spinel phase component generally had low-IRC. Compared to the Ni-rich materials, materials with high Co content appeared to tolerate more Li deficiency (metal-site vacancies) in the layered single phase and delayed the appearance of spinel. Among the single phase low-IRC materials, some can be regarded as traditional layered materials because they did not exhibit the 4.5 V plateau but they had metal-site vacancies (*e.g.* sample K2). Other single phase low-IRC materials with metal-site vacancies exhibited the 4.5 V plateau, which usually appears in typical LLRTMO materials.

#### **7.1.4 Understanding the irreversible capacity loss in layered lithium-rich transition metal oxides (Chapter 6)**

From Chapters 4 and 5, several single-phase LLRTMO materials with metal-site vacancies but varying Li:Ni:Mn:Co ratios were identified. In order to find the location of metal-site vacancies, solid-state  $^7\text{Li}$  NMR experiments were performed on some selected low-IRC materials (*e.g.* A2, D4) and their corresponding low-IRC counterparts (A1, D1). The  $^7\text{Li}$  NMR results were used to measure the amount of Li in the Li layer and in the TM layer, which in turn was used to estimate the distribution of metal-site vacancies between the two layers. The results of the  $^7\text{Li}$  NMR studies suggested that the metal-site vacancies predominantly occupied the Li layer in the single-phase low-IRC materials.



To probe the cause for the high IRC in LLRTMO materials, properties of a solid-solution series comprised of six LLRTMO materials with increasing Ni/Co ratio but with no vacancies were examined. The first charge-discharge cycles, especially the 4.5 V plateaus, of those LLRTMO materials revealed that a higher Ni content caused increased TM redox capacity. However, the comparison of IRC with respect to Ni/Co ratio suggested that irreversible oxygen release may not be the only reason for the high IRC. It is speculated that TM migration during the first charge in Ni-rich materials could contribute to the IRC.

A Fe-containing LLRTMO compound (Fe-A1) with same theoretical TM redox capacity as sample A1 was synthesized and its properties were compared to sample A1. Rietveld refinement of the XRD pattern of the compound Fe-A1 showed a relatively large fraction of Fe ions in the Li layer. The compound Fe-A1 had a very high IRC compared to that of the sample A1 supporting the view that TM ions in the Li layer (after TM migration) could cause high IRC.

A step-wise charge-discharge experiment with different upper cut-off voltages were performed with samples A1, A2 and Fe-A1 and their IRCs were measured. The IRC of the Fe-A1 was very high even for the upper cut-off voltage of 4.0 V. By contrast, the sample containing metal-site vacancies (A2) showed a very low-IRC even after charging up to 4.8 V. Hence, it is speculated that TM migration could cause high IRC and that metal-site vacancies facilitated the reentry of extra Li ions during the first charge.

### **7.1.5 Low-IRC behavior in core-shell positive electrode materials**

One of the main impacts of this thesis work is the utilization of low-IRC materials in the core-shell positive electrode materials. Li et al. have shown the usefulness of the low-IRC materials in core-shell materials<sup>140</sup>. Designing positive electrode materials in the form of core-shell is being pursued as a novel strategy to simultaneously harvest two different beneficial properties. For example, a Ni-rich material is used as core to get high specific capacity but Ni in the particle surface can undergo unwanted reactions with electrolytes at high voltage and affects the battery life time. Hence the Ni-rich core should be protected with materials of other metal composition such as a Mn-rich material. In the core-shell materials studied by Li et al., low-IRC materials were used as shell materials and the resulting core-shell materials exhibited a relatively lower IRC. Thus low-IRC materials have possible application in the design of core-shell type positive electrode materials.

## **7.2 Suggested future work**

### **7.2.1 Presence of Mn<sup>3+</sup> in the low-irreversible capacity samples**

The presence of metal-site vacancies in Li-deficient (low-IRC) materials was identified and investigated in chapters 4 and 5. The stoichiometry of the formula unit of those Li-deficient materials was derived from ICP-OES metal ratio (see. Section 4.7) . To accommodate the metal-site vacancies in a formula unit of LiMO<sub>2</sub>, the oxidation states of Ni, Mn and Co were assumed to be +2, +4 and +3 respectively. One possible counter-argument against the presence of metal-site vacancies (or excess oxygen) would be the presence of Mn<sup>3+</sup> ions substituting for some of the Mn<sup>4+</sup> ions in the synthesized samples.

Hence, X-ray absorption near edge structure (XANES) experiments probing the oxidation states of Mn in low-IRC materials are important to perform. Required oxidation state standards for  $\text{Mn}^{3+}$  (e.g.  $o\text{-LiMn}^{3+}\text{O}_2$ ) and  $\text{Mn}^{4+}$  (e.g.  $\text{Li}_2\text{Mn}^{4+}\text{O}_3$ ) ions should be used for comparison.

### 7.2.2 Effect of the nature of precursor on the low-irreversible capacity behavior

Verde et al.<sup>117</sup> studied the first cycle properties of a set of LLRTMO materials with the same stoichiometry ( $\text{Li}[\text{Li}_{0.166}\text{Ni}_{0.25}\text{Mn}_{0.583}]\text{O}_2$ ) but synthesized by three different routes – sol-gel method, hydroxide co-precipitation and carbonate co-precipitation. They

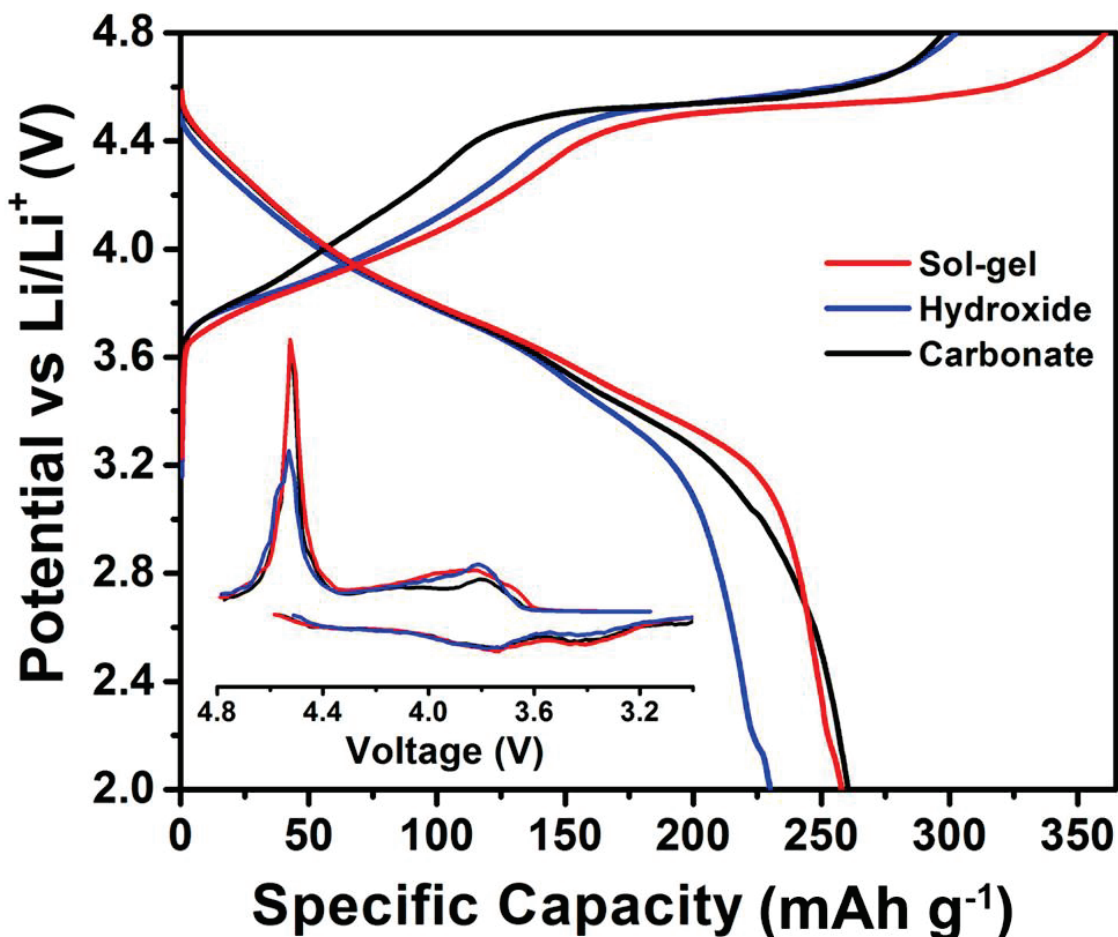


Figure 7.1 First cycle charge-discharge profiles of  $\text{Li}[\text{Li}_{0.166}\text{Ni}_{0.25}\text{Mn}_{0.583}]\text{O}_2$  synthesized from sol-gel method, hydroxide co-precipitation and carbonate co-precipitation. Reprinted with permission from (*ACS Appl. Mater. Interfaces*, 2014, 6 (21), pp 18868–18877) Copyright (2014) American Chemical Society

showed that the IRC values of LLRTMO materials derived from carbonate precursors were smaller than those of materials from hydroxides. Figure 7.1 shows the first charge-discharge profiles of those LLRTMO materials. According to Verde et al., the relatively homogeneous nature of LLRTMO particles from carbonate co-precipitation resulted in better electrochemical performance. So, a similar type of comparison of the properties of low-IRC materials that are derived from sol-gel method, carbonate and hydroxide co-precipitations might be an interesting study.

### **7.2.3 Long-term electrochemical properties of low-irreversible capacity materials**

Figure 7.2 shows the cycling properties (capacity retention and average voltage) of low-IRC materials A2 and B2 compared with their stoichiometric counterparts A1 and B1 respectively. In both cases, the capacity retention of low-IRC materials was neither superior nor inferior to that of its stoichiometric counterparts. However, the average voltage of low-IRC materials was somewhat better than their stoichiometric counterparts. In any case, a study to improve the long-term electrochemical properties of low-IRC materials is necessary. Metal-site vacancies in a LLRTMO material offer extra discharge capacity during the first-cycle by providing extra room during the first discharge. However, the effect of metal-site vacancies on the electrochemical properties such as coulombic efficiency is not known in detail. Hence this study should also investigate the effect of metal-site vacancies on life-time related properties such as coulombic efficiency.

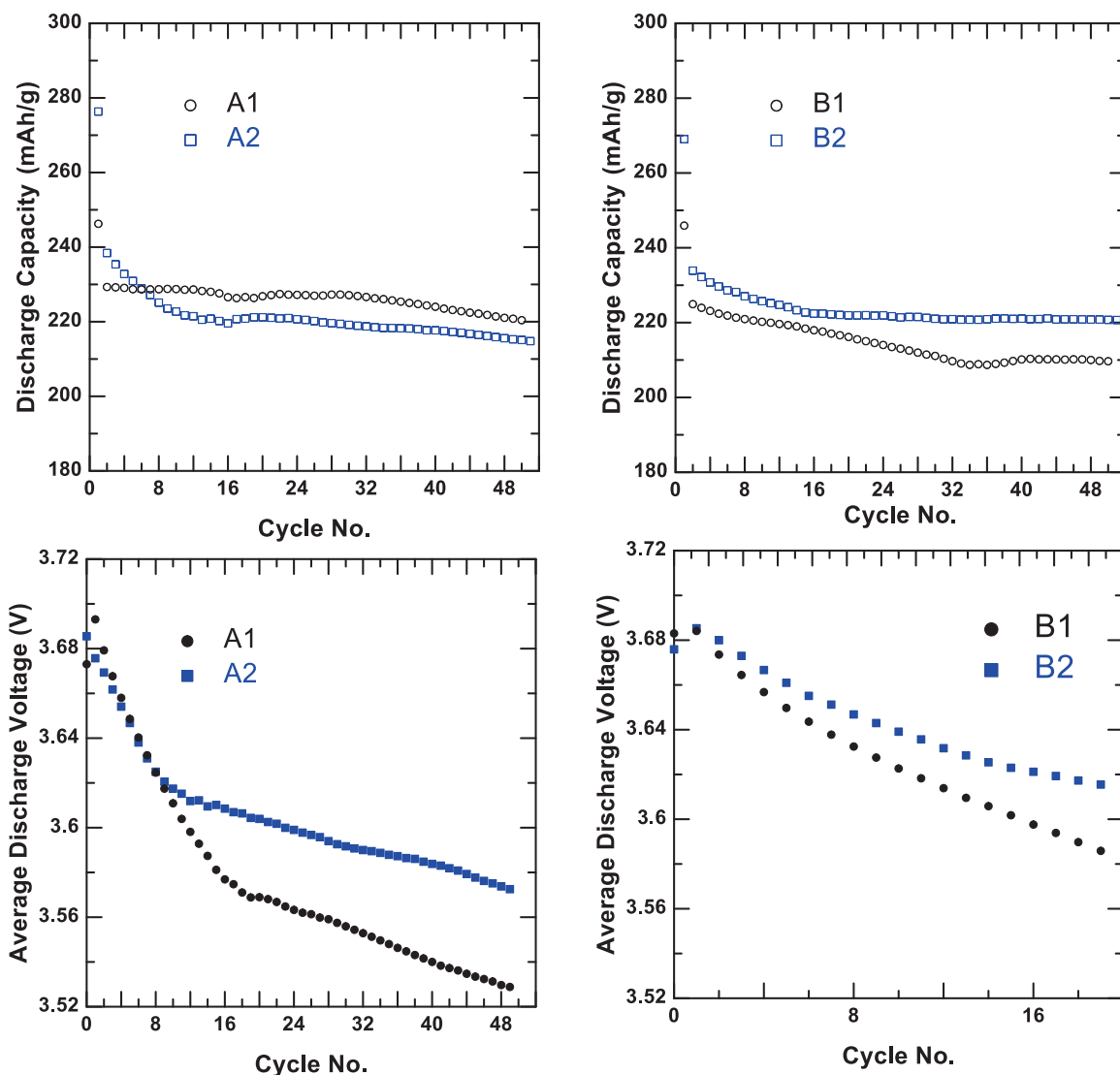


Figure 7.2 Top panels: Discharge specific capacity vs cycle number and bottom panels: Average discharge voltage vs. cycle number of samples A1, A2, B1 and B2

#### 7.2.4 FAULTS and Neutron diffraction in LLRTMO with metal-site vacancies

Chapter 3 discussed the effect of metal composition on the stacking fault probability in  $\text{Li}[\text{Li}_{1/3-2x/3}\text{Ni}_x\text{Mn}_{2/3-x/3}]\text{O}_2$  solid solution series. It was showed that aliovalent ions, such as,  $\text{Ni}^{2+}$  in the transition metal layers disturbed the superlattice ordering between  $\text{Li}^+$  and  $\text{Mn}^{4+}$  ions and hence the stacking order along the  $c$  axis leading

to stacking faults. Chapters 4 and 5 showed the existence of many Li-Ni-Mn-Co containing LLRTMO materials with metal-site vacancies. So, it would be interesting to study the impact of metal-site vacancies on the stacking fault probability using FAULTS.

$^7\text{Li}$  NMR results from Chapter 6 suggested that metal-site vacancies prefer to reside in the Li layer of the single phase low-IRC materials with metal-site vacancies. At the same time, it is not known whether  $\text{Ni}^{2+}$  ions can exchange sites with metal-site vacancies in the same way as Li ions do. The possible exchange between metal-site vacancies and  $\text{Ni}^{2+}$  ions could also impact the stacking order and hence the superlattice broadening. So, careful neutron diffraction studies would be useful to probe the nature of the superlattice ordering with respect to metal-site vacancies. Once the composition of the TM layers is known precisely, FAULTS can be used to fit the superlattice peak broadening in LLRTMO materials with metal-site vacancies. As an extension, *in-situ* and *ex-situ* neutron diffraction studies at different cut-off voltages during the first cycle in combination with FAULTS analysis will give clues about the TM ion dynamics during the first cycle profile.

### **7.2.5 Origin of metal-site vacancies in Li-Ni-Mn-O vs Li-Ni-Mn-Co-O systems**

McCalla et al.<sup>115</sup> showed the presence of metal-site vacancies in some Li-Ni-Mn-O based LLRTMO materials. Those materials were synthesized through quenching but synthesizing the same material under slow-cooling method caused phase separation into layered and spinel components. Figure 7.3 shows the XRD pattern of the Li-deficient material synthesized through quenching by McCalla et al. By contrast, Li-deficiency incurred on some Co-rich materials can accommodate metal-site vacancies even under slow-cooling synthesis<sup>61</sup>. It is known that Ni ions exchange sites with Li in the Li layer

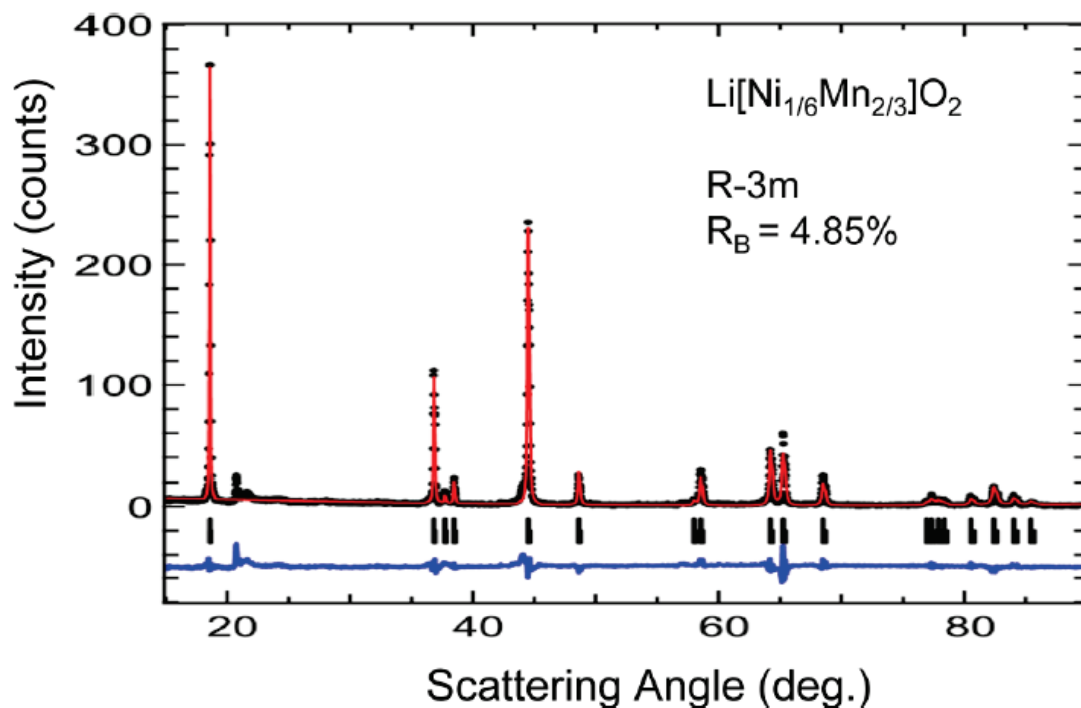


Figure 7.3 XRD pattern of the compound  $\text{Li}[\text{Ni}_{1/6}\text{Mn}_{2/3}]\text{O}_2$  (observed – black, calculated – red and difference – blue). Reprinted with permission from (*Chem. Mater.*, **2013**, 25 (13), pp 2716–2721) (Ref.141) Copyright (2013) American Chemical Society

and Co ions have the tendency to prevent that<sup>141</sup>. So, it may be that the exchanged Ni ions in the Li layer would activate the formation of a spinel phase as soon as Li deficiency is attained. So, a study correlating the cation exchange level, metal composition, amount of vacancies and the phase separation tendency would be an interesting future work. This study would also be useful to understand the origin and onset of the layered-to-spinel conversion occurring in LLRTMO materials during the first cycle.

Figure 7.4 shows the voltage-specific capacity profiles corresponding to several cycles of the material  $\text{Li}[\text{Ni}_{1/6}\text{Mn}_{2/3}]\text{O}_2$ .  $\text{Li}[\text{Ni}_{1/6}\text{Mn}_{2/3}]\text{O}_2$  exhibited an IRC of 16 % even in the presence of metal-site vacancies. McCalla et al.<sup>115</sup> reported that the metal-site vacancies in the compound of  $\text{Li}[\text{Ni}_{1/6}\text{Mn}_{2/3}]\text{O}_2$  reside in the TM layer causing superlattice ordering. So, it is speculated that the vacancies in the TM layer may not be useful in re-

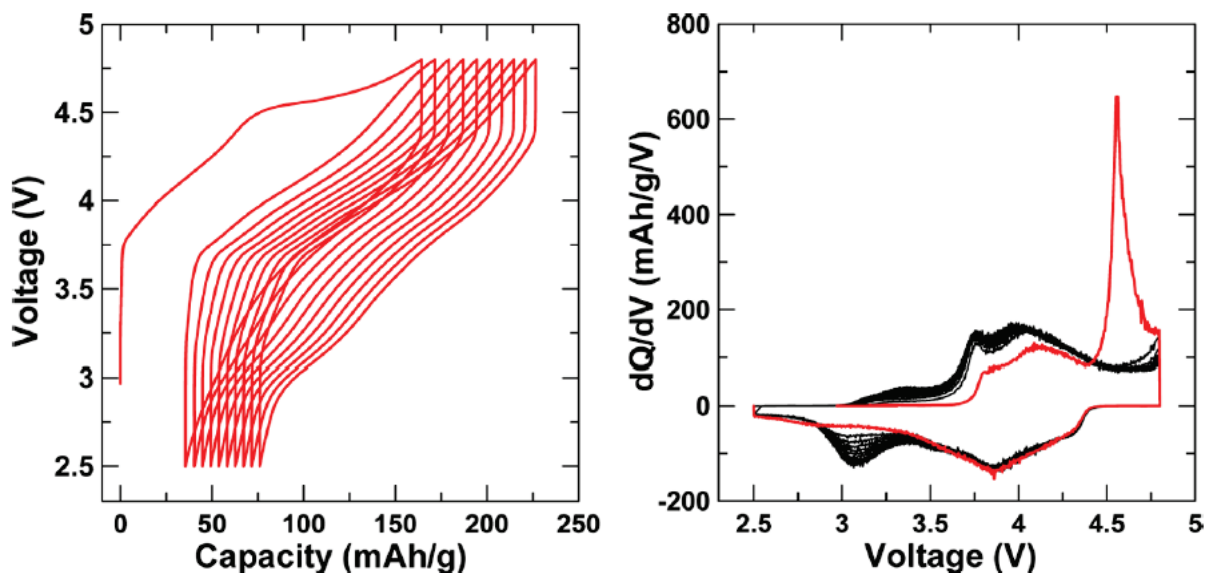


Figure 7.4 Left panel: Voltage-specific capacity profiles of  $\text{Li}[\text{Ni}_{1/6}\text{Mn}_{2/3}]\text{O}_2$  and right panel:  $dQ/dV$  vs.  $V$  plots for several cycles.

Reprinted with permission from (*Chem. Mater.*, **2013**, 25 (13), pp 2716–2721) (Ref.141) Copyright (2013) American Chemical Society.

accommodating Li ions back into the host structure. Hence, a study investigating the effect of metal-site vacancies residing in the TM layer on the first-cycle properties would be very interesting.

### 7.2.6 Layered NMC materials with metal-site vacancies

From the low-IRC materials search (Chapter 5), it was found that some materials (e.g. K2 and N2) were non-Li-rich as their Li/TM ratios were less than 1. Hence they should be treated as traditional layered materials with metal-site vacancies. Figure 7.5 shows the first cycle voltage-specific capacity profiles of the samples K2 and N2 compared with those of K1 and N1 respectively. Neither K2 nor N2 exhibited the 4.5 V plateau and hence the low-IRC behavior in K2 and N2 was not surprising. At the same time, they serve as new class of layered NMC materials, whose properties are not known



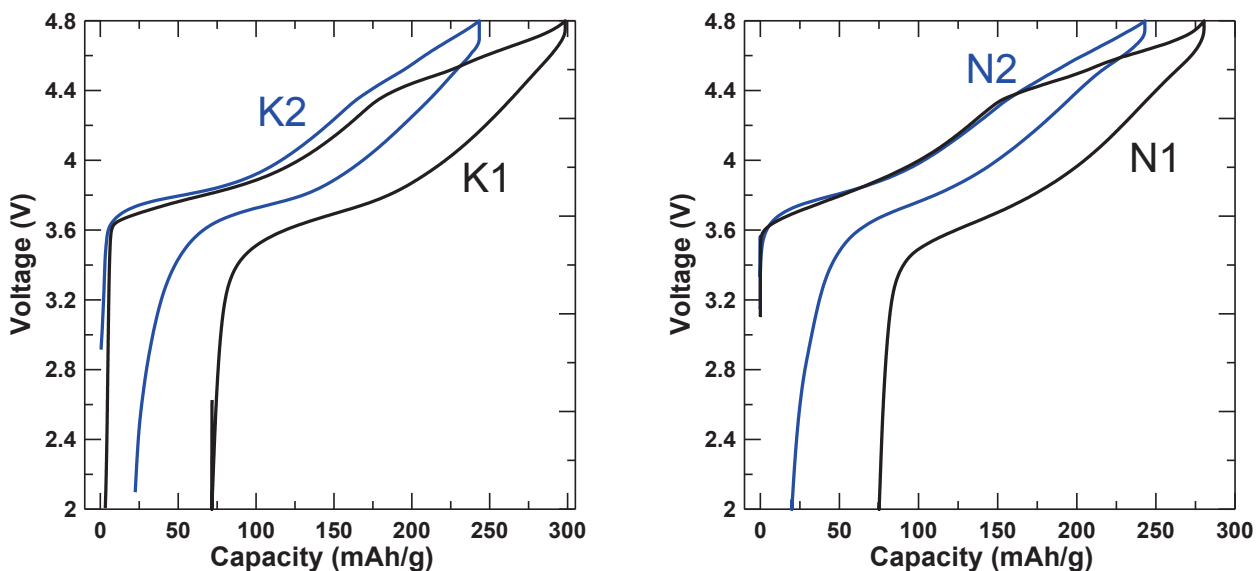


Figure 7.5 First cycle charge-discharge profiles of samples K1 and K2 (left panel) and N1 and N2 (right panel)

in detail. Hence, a detailed structural and electrochemical characterization of these materials would be an interesting future work.

### 7.2.7 Effect of metal-site vacancies on the reversible anionic redox properties

Recent work from Ceder's group<sup>142</sup> on the chemical origin of oxygen redox activity in LLRTMO materials was reported on the basis of the local environment of the O atoms. According to their theoretical predictions, those O atoms that are surrounded by specific Li-excess environments (Li-O-Li configuration) have a strong tendency to induce anionic redox. The top panel in Figure 7.6 shows the local Li-excess environments around O atoms in stoichiometric layered and the LLRTMO materials (as explained by Seo et al.<sup>142</sup>). The availability of Li-O-Li configuration in LLRTMO materials is one of the preliminary conditions for oxygen redox activity. The bottom panel in Figure 7.6 was created by adapting the same scenario as in the top panel but with metal-site vacancies around O atoms. In the light of the work by Seo et al.<sup>142</sup>, it is speculated that the Li-O-□

configuration, which is one of the possible configurations in single-phase low-IRC LLRTMO materials, would also affect the oxygen redox activity. So, similar DFT studies would be interesting to probe the anionic-redox tendency of LLRTMO materials with metal-site vacancies.

In the event of finding increased anionic redox activity in LLRTMO materials with metal-site vacancies, it can be verified by precisely measuring the oxygen release in

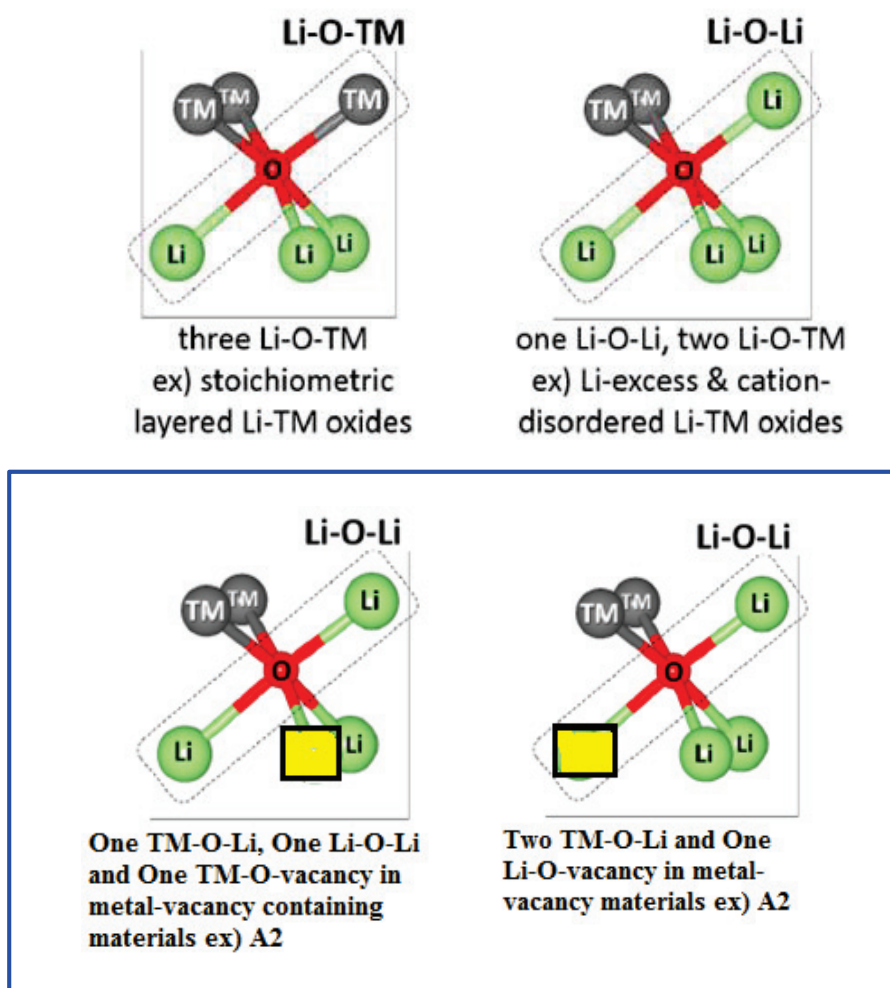


Figure 7.6 Local Li-excess environments around O atoms in LLRTMO materials (top panel) and LLRTMO with metal-site vacancies (bottom panels).

Metal-site vacancies are shown as yellow boxes.  
Adapted with permission from (*Nature Chemistry* **8**, 692–697 (2016)) Copyright (2016) Nature Publishing Group

different LLRTMO materials. Pouch cells should be made with LLRTMO materials with metal-site vacancies as working electrodes. The relative oxygen release during the first charge should be measured using Archimedes principle explained by Self et al<sup>143</sup>. Pouch cells with different active material mass loadings would be useful to confirm the amount of the released oxygen per unit mass of the active material. GS/MS could be used to monitor the composition of the evolved gas. Finally, the extent of oxygen redox with respect to the amount of metal-site vacancies can be estimated.

### **7.2.8 Eye to reality**

Volumetric energy density and electrode density for the all the materials should be measured and estimated to determine if any of these materials or future materials are competitive compared to high Ni content NMC, for example NMC 622, NMC 532, etc.,

## References

- (1) Xu, K. Electrolytes and Interphases in Li-Ion Batteries and Beyond. *Chem. Rev.* **2014**, *114* (23), 11503–11618.
- (2) Whittingham, M. S. Lithium Batteries and Cathode Materials. *Chem. Rev.* **2004**, *104* (10), 4271–4302.
- (3) Julien, C. M.; Mauger, A.; Zaghbi, K.; Groult, H. Comparative Issues of Cathode Materials for Li-Ion Batteries. *Inorganics* **2014**, *2* (1), 132–154.
- (4) Hy, S.; Liu, H.; Zhang, M.; Qian, D.; Hwang, B.-J.; Meng, Y. S. Performance and Design Considerations for Lithium Excess Layered Oxide Positive Electrode Materials for Lithium Ion Batteries. *Energy Environ. Sci.* **2016**, *9* (6), 1931–1954.
- (5) Venugopal, G.; Moore, J.; Howard, J.; Pendalwar, S. Characterization of Microporous Separators for Lithium-Ion Batteries. *J. Power Sources* **1999**, *77* (1), 34–41.
- (6) Lux, S. F.; Schappacher, F.; Balducci, A.; Passerini, S.; Winter, M. Low Cost, Environmentally Benign Binders for Lithium-Ion Batteries. *J. Electrochem. Soc.* **2010**, *157* (3), A320–A325.
- (7) L Fransson, T. E. Influence of Carbon Black and Binder on Li-Ion Batteries. *J. Power Sources* **2001**, *101* (1), 1–9.
- (8) Kikkawa, S.; Kanamaru, F.; Koizumi, M.; Rich, S. M.; Jacobson, A. Layered Intercalation Compounds. In *Inorganic Syntheses*; Jr, S. L. H., Ed.; John Wiley & Sons, Inc., 1984; pp 86–89.
- (9) Ohzuku, T.; Ueda, A. Why Transition Metal (Di) Oxides Are the Most Attractive Materials for Batteries. *Solid State Ion.* **1994**, *69* (3), 201–211.
- (10) Reddy, T. *Linden's Handbook of Batteries, 4th Edition*, 4 edition.; McGraw-Hill Education: New York, 2010.
- (11) Urban, A.; Seo, D.-H.; Ceder, G. Computational Understanding of Li-Ion Batteries. *Npj Comput. Mater.* **2016**, *2*, 16002.
- (12) Kinoshita, K.; Zaghbi, K. Negative Electrodes for Li-Ion Batteries. *J. Power Sources* **2002**, *110* (2), 416–423.
- (13) Park, O. K.; Cho, Y.; Lee, S.; Yoo, H.-C.; Song, H.-K.; Cho, J. Who Will Drive Electric Vehicles, Olivine or Spinel? *Energy Environ. Sci.* **2011**, *4* (5), 1621–1633.
- (14) Armand, M.; Tarascon, J.-M. Building Better Batteries. *Nature* **2008**, *451* (7179), 652–657.
- (15) Masquelier, C.; Croguennec, L. Polyanionic (Phosphates, Silicates, Sulfates) Frameworks as Electrode Materials for Rechargeable Li (or Na) Batteries. *Chem. Rev.* **2013**, *113* (8), 6552–6591.
- (16) Mizushima, K.; Jones, P. C.; Wiseman, P. J.; Goodenough, J. B. Mizushima, K.; Jones, P. C.; Wiseman, P. J.; Goodenough, J. B.  $\text{Li}_x\text{CoO}_2$  (*Mater. Res. Bull.* 1980, *15* (6), 783–789. *Mater. Res. Bull.* **1980**, *15* (6), 783–789.
- (17) Ozawa, K. Lithium-Ion Rechargeable Batteries with  $\text{LiCoO}_2$  and Carbon Electrodes: The  $\text{LiCoO}_2/\text{C}$  System. *Solid State Ion.* **1994**, *69* (3), 212–221.
- (18) Yabuuchi, N.; Yoshida, H.; Komaba, S. Crystal Structures and Electrode Performance of  $\alpha\text{-NaFeO}_2$  for Rechargeable Sodium Batteries. *Electrochemistry* **2012**, *80* (10), 716–719.
- (19) Delmas, C.; Fouassier, C.; Hagenmuller, P. Structural Classification and Properties of the Layered Oxides. *Phys. BC* **1980**, *99*, 81–85.

- (20) Dahn, J. R.; Sacken, U. von; Juzkow, M. W.; Al-Janaby, H. Rechargeable LiNiO<sub>2</sub> / Carbon Cells. *J. Electrochem. Soc.* **1991**, *138* (8), 2207–2211.
- (21) Rougier, A.; Gravereau, P.; Delmas, C. Optimization of the Composition of the Li<sub>1-z</sub>Ni<sub>1+z</sub>O<sub>2</sub> Electrode Materials: Structural, Magnetic, and Electrochemical Studies. *J. Electrochem. Soc.* **1996**, *143* (4), 1168–1175.
- (22) Dahn, J. R.; Fuller, E. W.; Obrovac, M.; von Sacken, U. Thermal Stability of Li<sub>x</sub>CoO<sub>2</sub>, Li<sub>x</sub>NiO<sub>2</sub> and λ-MnO<sub>2</sub> and Consequences for the Safety of Li-Ion Cells. *Solid State Ion.* **1994**, *69* (3), 265–270.
- (23) Mishra, S. K.; Ceder, G. Structural Stability of Lithium Manganese Oxides. *Phys. Rev. B* **1999**, *59* (9), 6120–6130.
- (24) Reimers, J. N.; Fuller, E. W.; Rossen, E.; Dahn, J. R. Synthesis and Electrochemical Studies of LiMnO<sub>2</sub> Prepared at Low Temperatures. *J. Electrochem. Soc.* **1993**, *140* (12), 3396–3401.
- (25) Paulsen, J. M.; Thomas, C. L.; Dahn, J. R. Layered Li-Mn-Oxide with the O<sub>2</sub> Structure: A Cathode Material for Li-Ion Cells Which Does Not Convert to Spinel. *J. Electrochem. Soc.* **1999**, *146* (10), 3560–3565.
- (26) Rougier, A.; Saadoune, I.; Gravereau, P.; Willmann, P.; Delmas, C. Effect of Cobalt Substitution on Cationic Distribution in LiNi<sub>1-y</sub>Co<sub>y</sub>O<sub>2</sub> Electrode Materials. *Solid State Ion.* **1996**, *90* (1–4), 83–90.
- (27) Ohzuku, T.; Yanagawa, T.; Kouguchi, M.; Ueda, A. Innovative Insertion Material of LiAl<sub>1/4</sub>Ni<sub>3/4</sub>O<sub>2</sub> (R-M) for Lithium-Ion (Shuttlecock) Batteries. *J. Power Sources* **1997**, *68* (1), 131–134.
- (28) Park, S. H.; Park, K. S.; Sun, Y. K.; Nahm, K. S.; Lee, Y. S.; Yoshio, M. Structural and Electrochemical Characterization of Lithium Excess and Al-Doped Nickel Oxides Synthesized by the Sol-gel Method. *Electrochimica Acta* **2001**, *46* (8), 1215–1222.
- (29) Guilnard, M.; Rougier, A.; Grüne, M.; Croguennec, L.; Delmas, C. Effects of Aluminum on the Structural and Electrochemical Properties of LiNiO<sub>2</sub>. *J. Power Sources* **2003**, *115* (2), 305–314.
- (30) Wang, Y.; Jiang, J.; Dahn, J. R. The Reactivity of Delithiated Li(Ni<sub>1/3</sub>Co<sub>1/3</sub>Mn<sub>1/3</sub>)O<sub>2</sub>, Li(Ni<sub>0.8</sub>Co<sub>0.15</sub>Al<sub>0.05</sub>)O<sub>2</sub> or LiCoO<sub>2</sub> with Non-Aqueous Electrolyte. *Electrochem. Commun.* **2007**, *9* (10), 2534–2540.
- (31) Robert, R.; Villeveille, C.; Novák, P. Enhancement of the High Potential Specific Charge in Layered Electrode Materials for Lithium-Ion Batteries. *J. Mater. Chem. A* **2014**, *2* (23), 8589–8598.
- (32) McCalla, E. *Consequences of Combinatorial Studies of Positive Electrodes for Li-Ion Batteries*; Springer Science & Business Media, 2014.
- (33) Makimura, Y.; Ohzuku, T. Lithium Insertion Material of LiNi<sub>1/2</sub>Mn<sub>1/2</sub>O<sub>2</sub> for Advanced Lithium-Ion Batteries. *J. Power Sources* **2003**, *119–121*, 156–160.
- (34) Venkatraman, S.; Choi, J.; Manthiram, A. Factors Influencing the Chemical Lithium Extraction Rate from Layered LiNi<sub>1-y-z</sub>Co<sub>y</sub>Mn<sub>z</sub>O<sub>2</sub> Cathodes. *Electrochem. Commun.* **2004**, *6* (8), 832–837.
- (35) Zhou, F.; Zhao, X.; Bommel, A. van; Xia, X.; Dahn, J. R. Comparison of Li [Li<sub>1/9</sub>Ni<sub>1/3</sub>Mn<sub>5/9</sub>]O<sub>2</sub>, Li [Li<sub>1/5</sub>Ni<sub>1/5</sub>Mn<sub>3/5</sub>]O<sub>2</sub>, LiNi<sub>0.5</sub>Mn<sub>1.5</sub>O<sub>4</sub>, and LiNi<sub>2/3</sub>Mn<sub>1/3</sub>O<sub>2</sub> as High Voltage Positive Electrode Materials. *J. Electrochem. Soc.* **2011**, *158* (2), A187–A191.
- (36) McCalla, E.; Rowe, A. W.; Shunmugasundaram, R.; Dahn, J. R. Structural Study of the Li-Mn-Ni Oxide Pseudoternary System of Interest for Positive Electrodes of Li-Ion Batteries. *Chem. Mater.* **2013**, *25* (6), 989–999.

- (37) Li, J.; Camardese, J.; Glazier, S.; Dahn, J. R. Structural and Electrochemical Study of the Li–Mn–Ni Oxide System within the Layered Single Phase Region. *Chem. Mater.* **2014**, *26* (24), 7059–7066.
- (38) Koyama, Y.; Makimura, Y.; Tanaka, I.; Adachi, H.; Ohzuku, T. Systematic Research on Insertion Materials Based on Superlattice Models in a Phase Triangle of LiCoO<sub>2</sub>–LiNiO<sub>2</sub>–LiMnO<sub>2</sub> I. First-Principles Calculation on Electronic and Crystal Structures, Phase Stability and New LiNi<sub>1/2</sub>Mn<sub>1/2</sub>O<sub>2</sub> Material. *J. Electrochem. Soc.* **2004**, *151* (9), A1499–A1506.
- (39) Abuzeid, H. A. M.; Hashem, A. M. A.; Abdel-Ghany, A. E.; Eid, A. E.; Mauger, A.; Groult, H.; Julien, C. M. De-Intercalation of Li<sub>x</sub>Co<sub>0.8</sub>Mn<sub>0.2</sub>O<sub>2</sub>: A Magnetic Approach. *J. Power Sources* **2011**, *196* (15), 6440–6448.
- (40) Lu, Z.; MacNeil, D. D.; Dahn, J. R. Layered Li [ Ni<sub>x</sub>Co<sub>1-2x</sub>Mn<sub>x</sub>]O<sub>2</sub> Cathode Materials for Lithium-Ion Batteries. *Electrochem. Solid-State Lett.* **2001**, *4* (12), A200–A203.
- (41) Gabrisch, H.; Yi, T.; Yazami, R. Transmission Electron Microscope Studies of LiNi<sub>1/3</sub>Mn<sub>1/3</sub>Co<sub>1/3</sub>O<sub>2</sub> before and after Long-Term Aging at 70 ° C. *Electrochem. Solid-State Lett.* **2008**, *11* (7), A119–A124.
- (42) Hy, S.; Cheng, J.-H.; Liu, J.-Y.; Pan, C.-J.; Rick, J.; Lee, J.-F.; Chen, J.-M.; Hwang, B. J. Understanding the Role of Ni in Stabilizing the Lithium-Rich High-Capacity Cathode Material Li[Ni<sub>x</sub>Li<sub>(1-2x)/3</sub>Mn<sub>(2-x)/3</sub>]O<sub>2</sub> (0 ≤ X ≤ 0.5). *Chem. Mater.* **2014**, *26* (24), 6919–6927.
- (43) Strobel, P.; Lambert-Andron, B. Crystallographic and Magnetic Structure of Li<sub>2</sub>MnO<sub>3</sub>. *J. Solid State Chem.* **1988**, *75* (1), 90–98.
- (44) Jarvis, K. A.; Deng, Z.; Allard, L. F.; Manthiram, A.; Ferreira, P. J. Atomic Structure of a Lithium-Rich Layered Oxide Material for Lithium-Ion Batteries: Evidence of a Solid Solution. *Chem. Mater.* **2011**, *23* (16), 3614–3621.
- (45) Meng, Y. S.; Ceder, G.; Grey, C. P.; Yoon, W.-S.; Jiang, M.; Bréger, J.; Shao-Horn, Y. Cation Ordering in Layered O3 Li[Ni<sub>x</sub>Li<sub>1/3-2x/3</sub>Mn<sub>2/3-x/3</sub>]O<sub>2</sub>(0 ≤ X ≤ 1/2) Compounds. *Chem. Mater.* **2005**, *17* (9), 2386–2394.
- (46) Johnson, C. S.; Kim, J.-S.; Lefief, C.; Li, N.; Vaughey, J. T.; Thackeray, M. M. The Significance of the Li<sub>2</sub>MnO<sub>3</sub> Component in “composite” xLi<sub>2</sub>MnO<sub>3</sub> · (1 - x)LiMn<sub>0.5</sub>Ni<sub>0.5</sub>O<sub>2</sub> Electrodes. *Electrochem. Commun.* **2004**, *6* (10), 1085–1091.
- (47) Yu, H.; Kim, H.; Wang, Y.; He, P.; Asakura, D.; Nakamura, Y.; Zhou, H. High-Energy “composite” Layered Manganese-Rich Cathode Materials via Controlling Li<sub>2</sub>MnO<sub>3</sub> Phase Activation for Lithium-Ion Batteries. *Phys. Chem. Chem. Phys.* **2012**, *14* (18), 6584–6595.
- (48) Lu, Z.; MacNeil, D. D.; Dahn, J. R. Layered Cathode Materials Li [ Ni<sub>x</sub>Li<sub>(1/3-2x/3)</sub>Mn<sub>(2/3-x/3)</sub>] O<sub>2</sub> for Lithium-Ion Batteries. *Electrochem. Solid-State Lett.* **2001**, *4* (11), A191–A194.
- (49) Shukla, A. K.; Ramasse, Q. M.; Ophus, C.; Duncan, H.; Hage, F.; Chen, G. Unravelling Structural Ambiguities in Lithium- and Manganese-Rich Transition Metal Oxides. *Nat. Commun.* **2015**, *6*, 8711.
- (50) McCalla, E.; Rowe, A. W.; Brown, C. R.; Hacquebard, L. R. P.; Dahn, J. R. How Phase Transformations during Cooling Affect Li-Mn-Ni-O Positive Electrodes in Lithium Ion Batteries. *J. Electrochem. Soc.* **2013**, *160* (8), A1134–A1138.
- (51) Shunmugasundaram, R.; Arumugam, R. S.; Dahn, J. R. A Study of Stacking Faults and Superlattice Ordering in Some Li-Rich Layered Transition Metal Oxide Positive Electrode Materials. *J. Electrochem. Soc.* **2016**, *163* (7), A1394–A1400.
- (52) Bareño, J.; Lei, C. H.; Wen, J. G.; Kang, S.-H.; Petrov, I.; Abraham, D. P. Local Structure of Layered Oxide Electrode Materials for Lithium-Ion Batteries. *Adv. Mater.* **2010**, *22* (10), 1122–1127.
- (53) Luo, K.; Roberts, M. R.; Hao, R.; Guerrini, N.; Pickup, D. M.; Liu, Y.-S.; Edström, K.; Guo, J.; Chadwick, A. V.; Duda, L. C.; Bruce, P. G. Charge-Compensation in 3d-Transition-Metal-



- Oxide Intercalation Cathodes through the Generation of Localized Electron Holes on Oxygen. *Nat. Chem.* **2016**, *8* (7), 684–691.
- (54) Arunkumar, T. A.; Wu, Y.; Manthiram, A. Factors Influencing the Irreversible Oxygen Loss and Reversible Capacity in Layered  $\text{Li}[\text{Li}_{1/3}\text{Mn}_{2/3}]\text{O}_2\text{-Li}[\text{M}]\text{O}_2$  ( $\text{M} = \text{Mn}_{0.5-y}\text{Ni}_{0.5-y}\text{Co}_{2y}$  and  $\text{Ni}_{1-y}\text{Co}_y$ ) Solid Solutions. *Chem. Mater.* **2007**, *19* (12), 3067–3073.
- (55) Oishi, M.; Fujimoto, T.; Takanashi, Y.; Orikasa, Y.; Kawamura, A.; Ina, T.; Yamashige, H.; Takamatsu, D.; Sato, K.; Murayama, H.; Tanida, H.; Arai, H.; Ishii, H.; Yogi, C.; Watanabe, I.; Ohta, T.; Mineshige, A.; Uchimoto, Y.; Ogumi, Z. Charge Compensation Mechanisms in  $\text{Li}_{1.16}\text{Ni}_{0.15}\text{Co}_{0.19}\text{Mn}_{0.50}\text{O}_2$  Positive Electrode Material for Li-Ion Batteries Analyzed by a Combination of Hard and Soft X-Ray Absorption near Edge Structure. *J. Power Sources* **2013**, *222*, 45–51.
- (56) Armstrong, A. R.; Holzapfel, M.; Novák, P.; Johnson, C. S.; Kang, S.-H.; Thackeray, M. M.; Bruce, P. G. Demonstrating Oxygen Loss and Associated Structural Reorganization in the Lithium Battery Cathode  $\text{Li}[\text{Ni}_{0.2}\text{Li}_{0.2}\text{Mn}_{0.6}]\text{O}_2$ . *J. Am. Chem. Soc.* **2006**, *128* (26), 8694–8698.
- (57) Lu, Z.; Dahn, J. R. Understanding the Anomalous Capacity of  $\text{Li} / \text{Li} [ \text{Ni}_x \text{Li}_{(1/3 - 2x/3)} \text{Mn}_{(2/3 - x/3)} ] \text{O}_2$  Cells Using In Situ X-Ray Diffraction and Electrochemical Studies. *J. Electrochem. Soc.* **2002**, *149* (7), A815–A822.
- (58) Fell, C. R.; Qian, D.; Carroll, K. J.; Chi, M.; Jones, J. L.; Meng, Y. S. Correlation Between Oxygen Vacancy, Microstrain, and Cation Distribution in Lithium-Excess Layered Oxides During the First Electrochemical Cycle. *Chem. Mater.* **2013**, *25* (9), 1621–1629.
- (59) Tran, N.; Croguennec, L.; Ménétrier, M.; Weill, F.; Biensan, P.; Jordy, C.; Delmas, C. Mechanisms Associated with the “Plateau” Observed at High Voltage for the Overlithiated  $\text{Li}_{1.12}(\text{Ni}_{0.425}\text{Mn}_{0.425}\text{Co}_{0.15})_{0.88}\text{O}_2$  System. *Chem. Mater.* **2008**, *20* (15), 4815–4825.
- (60) Shunmugasundaram, R.; Senthil Arumugam, R.; Dahn, J. R. High Capacity Li-Rich Positive Electrode Materials with Reduced First-Cycle Irreversible Capacity Loss. *Chem. Mater.* **2015**, *27* (3), 757–767.
- (61) Shunmugasundaram, R.; Senthil Arumugam, R.; Harris, K. J.; Goward, G. R.; Dahn, J. R. A Search for Low-Irreversible Capacity and High-Reversible Capacity Positive Electrode Materials in the Li–Ni–Mn–Co Pseudoquaternary System. *Chem. Mater.* **2016**, *28* (1), 55–66.
- (62) Jiang, M.; Key, B.; Meng, Y. S.; Grey, C. P. Electrochemical and Structural Study of the Layered, “Li-Excess” Lithium-Ion Battery Electrode Material  $\text{Li}[\text{Li}_{1/9}\text{Ni}_{1/3}\text{Mn}_{5/9}]\text{O}_2$ . *Chem. Mater.* **2009**, *21* (13), 2733–2745.
- (63) Koga, H.; Croguennec, L.; Ménétrier, M.; Mannesiez, P.; Weill, F.; Delmas, C. Different Oxygen Redox Participation for Bulk and Surface: A Possible Global Explanation for the Cycling Mechanism of  $\text{Li}_{1.20}\text{Mn}_{0.54}\text{Co}_{0.13}\text{Ni}_{0.13}\text{O}_2$ . *J. Power Sources* **2013**, *236*, 250–258.
- (64) Koga, H.; Croguennec, L.; Ménétrier, M.; Douhil, K.; Belin, S.; Bourgeois, L.; Suard, E.; Weill, F.; Delmas, C. Reversible Oxygen Participation to the Redox Processes Revealed for  $\text{Li}_{1.20}\text{Mn}_{0.54}\text{Co}_{0.13}\text{Ni}_{0.13}\text{O}_2$ . *J. Electrochem. Soc.* **2013**, *160* (6), A786–A792.
- (65) Li, J.; Shunmugasundaram, R.; Doig, R.; Dahn, J. R. In Situ X-Ray Diffraction Study of Layered Li–Ni–Mn–Co Oxides: Effect of Particle Size and Structural Stability of Core–Shell Materials. *Chem. Mater.* **2016**, *28* (1), 162–171.
- (66) Ohzuku, T.; Nagayama, M.; Tsuji, K.; Ariyoshi, K. High-Capacity Lithium Insertion Materials of Lithium Nickel Manganese Oxides for Advanced Lithium-Ion Batteries: Toward Rechargeable Capacity More than 300 mA h g<sup>-1</sup>. *J. Mater. Chem.* **2011**, *21* (27), 10179–10188.

- (67) Genevois, C.; Koga, H.; Croguennec, L.; Ménétrier, M.; Delmas, C.; Weill, F. Insight into the Atomic Structure of Cycled Lithium-Rich Layered Oxide  $\text{Li}_{1.20}\text{Mn}_{0.54}\text{Co}_{0.13}\text{Ni}_{0.13}\text{O}_2$  Using HAADF STEM and Electron Nanodiffraction. *J. Phys. Chem. C* **2015**, *119* (1), 75–83.
- (68) Sathiya, M.; Rousse, G.; Ramesha, K.; Laisa, C. P.; Vezin, H.; Sougrati, M. T.; Doublet, M.-L.; Foix, D.; Gonbeau, D.; Walker, W.; Prakash, A. S.; Ben Hassine, M.; Dupont, L.; Tarascon, J.-M. Reversible Anionic Redox Chemistry in High-Capacity Layered-Oxide Electrodes. *Nat. Mater.* **2013**, *12* (9), 827–835.
- (69) Sathiya, M.; Ramesha, K.; Rousse, G.; Foix, D.; Gonbeau, D.; Prakash, A. S.; Doublet, M. L.; Hemalatha, K.; Tarascon, J.-M. High Performance  $\text{Li}_2\text{Ru}_{1-y}\text{Mn}_y\text{O}_3$  ( $0.2 \leq Y \leq 0.8$ ) Cathode Materials for Rechargeable Lithium-Ion Batteries: Their Understanding. *Chem. Mater.* **2013**, *25* (7), 1121–1131.
- (70) McCalla, E.; Abakumov, A. M.; Saubanère, M.; Foix, D.; Berg, E. J.; Rousse, G.; Doublet, M.-L.; Gonbeau, D.; Novák, P.; Tendeloo, G. V.; Dominko, R.; Tarascon, J.-M. Visualization of O-O Peroxo-like Dimers in High-Capacity Layered Oxides for Li-Ion Batteries. *Science* **2015**, *350* (6267), 1516–1521.
- (71) van Bommel, A.; Krause, L. J.; Dahn, J. R. Investigation of the Irreversible Capacity Loss in the Lithium-Rich Oxide  $\text{Li}[\text{Li}_{1/5}\text{Ni}_{1/5}\text{Mn}_{3/5}]_{\text{O}_2}$ . *J. Electrochem. Soc.* **2011**, *158* (6), A731–A735.
- (72) Mohanty, D.; Sefat, A. S.; Li, J.; Meisner, R. A.; Rondinone, A. J.; Payzant, E. A.; Abraham, D. P.; Ili, D. L. W.; Daniel, C. Correlating Cation Ordering and Voltage Fade in a Lithium–manganese-Rich Lithium-Ion Battery Cathode Oxide: A Joint Magnetic Susceptibility and TEM Study. *Phys. Chem. Chem. Phys.* **2013**, *15* (44), 19496–19509.
- (73) Yu, X.; Lyu, Y.; Gu, L.; Wu, H.; Bak, S.-M.; Zhou, Y.; Amine, K.; Ehrlich, S. N.; Li, H.; Nam, K.-W.; Yang, X.-Q. Understanding the Rate Capability of High-Energy-Density Li-Rich Layered  $\text{Li}_{1.2}\text{Ni}_{0.15}\text{Co}_{0.1}\text{Mn}_{0.55}\text{O}_2$  Cathode Materials. *Adv. Energy Mater.* **2014**, *4* (5), n/a–n/a.
- (74) Zhou, F.; Zhao, X.; van Bommel, A.; Rowe, A. W.; Dahn, J. R. Coprecipitation Synthesis of  $\text{Ni}_x\text{Mn}_{1-x}(\text{OH})_2$  Mixed Hydroxides. *Chem. Mater.* **2010**, *22* (3), 1015–1021.
- (75) van Bommel, A.; Dahn, J. R. Analysis of the Growth Mechanism of Coprecipitated Spherical and Dense Nickel, Manganese, and Cobalt-Containing Hydroxides in the Presence of Aqueous Ammonia. *Chem. Mater.* **2009**, *21* (8), 1500–1503.
- (76) Kriegner, D.; Matěj, Z.; Kužel, R.; Holý, V. Powder Diffraction in Bragg–Brentano Geometry with Straight Linear Detectors. *J. Appl. Crystallogr.* **2015**, *48* (2), 613–618.
- (77) Todokoro, H.; Ezumi, M. Scanning Electron Microscope. US5872358 A, February 16, 1999.
- (78) Olesik, J. W. Elemental Analysis Using ICP-OES and ICP/MS. *Anal. Chem.* **1991**, *63* (1), 12A–21A.
- (79) Fagerlund, G. Determination of Specific Surface by the BET Method. *Matér. Constr.* **6** (3), 239–245.
- (80) Koh, K.; Wong-Foy, A. G.; Matzger, A. J. A Porous Coordination Copolymer with over 5000 m<sup>2</sup>/g BET Surface Area. *J. Am. Chem. Soc.* **2009**, *131* (12), 4184–4185.
- (81) Brunauer, S.; Emmett, P. H.; Teller, E. Adsorption of Gases in Multimolecular Layers. *J. Am. Chem. Soc.* **1938**, *60* (2), 309–319.
- (82) MacKenzie, K. J. D.; Smith, M. E. *Multinuclear Solid-State Nuclear Magnetic Resonance of Inorganic Materials*; Elsevier, 2002.
- (83) Grey, C. P.; Dupré, N. NMR Studies of Cathode Materials for Lithium-Ion Rechargeable Batteries. *Chem. Rev.* **2004**, *104* (10), 4493–4512.



- (84) Marks, T.; Trussler, S.; Smith, A. J.; Xiong, D.; Dahn, J. R. A Guide to Li-Ion Coin-Cell Electrode Making for Academic Researchers. *J. Electrochem. Soc.* **2011**, *158* (1), A51–A57.
- (85) Meng, Y. S.; Ceder, G.; Grey, C. P.; Yoon, W.-S.; Jiang, M.; Bréger, J.; Shao-Horn, Y. Cation Ordering in Layered O3  $\text{Li}[\text{Ni}_x\text{Li}_{1/3-2x/3}\text{Mn}_{2/3-x/3}]\text{O}_2$  ( $0 \leq X \leq 1/2$ ) Compounds. *Chem. Mater.* **2005**, *17* (9), 2386–2394.
- (86) Shannon, R. D. Revised Effective Ionic Radii and Systematic Studies of Interatomic Distances in Halides and Chalcogenides. *Acta Crystallogr. Sect. A* **1976**, *32* (5), 751–767.
- (87) Weill, F.; Tran, N.; Croguennec, L.; Delmas, C. Cation Ordering in the Layered  $\text{Li}_{1+x}(\text{Ni}_{0.425}\text{Mn}_{0.425}\text{Co}_{0.15})_{1-x}\text{O}_2$  Materials ( $X = 0$  and  $0.12$ ). *J. Power Sources* **2007**, *172* (2), 893–900.
- (88) Yoon, W.-S.; Iannopollo, S.; Grey, C. P.; Carlier, D.; Gorman, J.; Reed, J.; Ceder, G. Local Structure and Cation Ordering in O3 Lithium Nickel Manganese Oxides with Stoichiometry  $\text{Li}[\text{Ni}_x\text{Mn}_{(2-x)/3}\text{Li}_{(1-2x)/3}]\text{O}_2$  NMR Studies and First Principles Calculations. *Electrochem. Solid-State Lett.* **2004**, *7* (7), A167–A171.
- (89) Yoon, W.-S.; Kim, N.; Yang, X.-Q.; McBreen, J.; Grey, C. P. 6Li MAS NMR and in Situ X-Ray Studies of Lithium Nickel Manganese Oxides. *J. Power Sources* **2003**, *119–121*, 649–653.
- (90) Boulineau, A.; Croguennec, L.; Delmas, C.; Weill, F. Reinvestigation of  $\text{Li}_2\text{MnO}_3$  Structure: Electron Diffraction and High Resolution TEM. *Chem. Mater.* **2009**, *21* (18), 4216–4222.
- (91) Treacy, M. M. J.; Newsam, J. M.; Deem, M. W. A General Recursion Method for Calculating Diffracted Intensities from Crystals Containing Planar Faults. *Proc. R. Soc. Lond. Math. Phys. Eng. Sci.* **1991**, *433* (1889), 499–520.
- (92) Bréger, J.; Jiang, M.; Dupré, N.; Meng, Y. S.; Shao-Horn, Y.; Ceder, G.; Grey, C. P. High-Resolution X-Ray Diffraction, DIFFaX, NMR and First Principles Study of Disorder in the  $\text{Li}_2\text{MnO}_3\text{--Li}[\text{Ni}_{1/2}\text{Mn}_{1/2}]\text{O}_2$  Solid Solution. *J. Solid State Chem.* **2005**, *178* (9), 2575–2585.
- (93) Riou, A.; Lecerf, A.; Gerault, Y.; Cudennec, Y. Etude Structurale de  $\text{Li}_2\text{MnO}_3$ . *Mater. Res. Bull.* **1992**, *27* (3), 269–275.
- (94) Wang, R.; He, X.; He, L.; Wang, F.; Xiao, R.; Gu, L.; Li, H.; Chen, L. Atomic Structure of  $\text{Li}_2\text{MnO}_3$  after Partial Delithiation and Re-Lithiation. *Adv. Energy Mater.* **2013**, *3* (10), 1358–1367.
- (95) Yu, D. Y. W.; Yanagida, K.; Kato, Y.; Nakamura, H. Electrochemical Activities in  $\text{Li}_2\text{MnO}_3$ . *J. Electrochem. Soc.* **2009**, *156* (6), A417–A424.
- (96) Boulineau, A.; Croguennec, L.; Delmas, C.; Weill, F. Structure of  $\text{Li}_2\text{MnO}_3$  with Different Degrees of Defects. *Solid State Ion.* **2010**, *180* (40), 1652–1659.
- (97) Lu, Z.; Dahn, J. R. Effects of Stacking Fault Defects on the X-Ray Diffraction Patterns of T2, O2, and O6 Structure  $\text{Li}_{2/3}[\text{Co}_x\text{Ni}_{1/3-x}\text{Mn}_{2/3}]\text{O}_2$ . *Chem. Mater.* **2001**, *13* (6), 2078–2083.
- (98) McCalla, E.; Abakumov, A.; Rousse, G.; Reynaud, M.; Sougrati, M. T.; Budic, B.; Mahmoud, A.; Dominko, R.; Van Tendeloo, G.; Hermann, R. P.; Tarascon, J.-M. Novel Complex Stacking of Fully-Ordered Transition Metal Layers in  $\text{Li}_4\text{FeSbO}_6$  Materials. *Chem. Mater.* **2015**, *27* (5), 1699–1708.
- (99) Lu, Z.; Beaulieu, L. Y.; Donaberger, R. A.; Thomas, C. L.; Dahn, J. R. Synthesis, Structure, and Electrochemical Behavior of  $\text{Li}[\text{Ni}_x\text{Li}_{(1/3-2x/3)}\text{Mn}_{(2/3-x/3)}]\text{O}_2$ . *J. Electrochem. Soc.* **2002**, *149* (6), A778–A791.
- (100) Koga, H.; Croguennec, L.; Mannesiez, P.; Ménétrier, M.; Weill, F.; Bourgeois, L.; Duttine, M.; Suard, E.; Delmas, C.  $\text{Li}_{1.20}\text{Mn}_{0.54}\text{Co}_{0.13}\text{Ni}_{0.13}\text{O}_2$  with Different Particle Sizes as Attractive Positive Electrode Materials for Lithium-Ion Batteries: Insights into Their Structure. *J. Phys. Chem. C* **2012**, *116* (25), 13497–13506.

- (101) West, W. C.; Soler, J.; Smart, M. C.; Ratnakumar, B. V.; Firdosy, S.; Ravi, V.; Anderson, M. S.; Hrbacek, J.; Lee, E. S.; Manthiram, A. Electrochemical Behavior of Layered Solid Solution  $\text{Li}_2\text{MnO}_3\text{-LiMO}_2$  (M = Ni, Mn, Co) Li-Ion Cathodes with and without Alumina Coatings. *J. Electrochem. Soc.* **2011**, *158* (8), A883–A889.
- (102) Mohanty, D.; Huq, A.; Payzant, E. A.; Sefat, A. S.; Li, J.; Abraham, D. P.; Wood, D. L.; Daniel, C. Neutron Diffraction and Magnetic Susceptibility Studies on a High-Voltage  $\text{Li}_{1.20}\text{Mn}_{0.55}\text{Co}_{0.1}\text{Ni}_{0.15}\text{O}_2$  Lithium Ion Battery Cathode: Insight into the Crystal Structure. *Chem. Mater.* **2013**, *25* (20), 4064–4070.
- (103) Thackeray, M. M.; Kang, S.-H.; Johnson, C. S.; Vaughey, J. T.; Hackney, S. A. Comments on the Structural Complexity of Lithium-Rich  $\text{Li}_{1+x}\text{M}_{1-x}\text{O}_2$  Electrodes (M = Mn, Ni, Co) for Lithium Batteries. *Electrochem. Commun.* **2006**, *8* (9), 1531–1538.
- (104) Long, B. R.; Croy, J. R.; Dogan, F.; Suchomel, M. R.; Key, B.; Wen, J.; Miller, D. J.; Thackeray, M. M.; Balasubramanian, M. Effect of Cooling Rates on Phase Separation in  $0.5\text{Li}_2\text{MnO}_3\cdot 0.5\text{LiCoO}_2$  Electrode Materials for Li-Ion Batteries. *Chem. Mater.* **2014**, *26* (11), 3565–3572.
- (105) Yabuuchi, N.; Yamamoto, K.; Yoshii, K.; Nakai, I.; Nishizawa, T.; Omaru, A.; Toyooka, T.; Komaba, S. Structural and Electrochemical Characterizations on  $\text{Li}_2\text{MnO}_3\text{-LiCoO}_2\text{-LiCrO}_2$  System as Positive Electrode Materials for Rechargeable Lithium Batteries. *J. Electrochem. Soc.* **2013**, *160* (1), A39–A45.
- (106) Liu, Y.; Wang, Q.; Wang, X.; Wang, T.; Gao, Y.; Su, M.; Dou, A. Improved Electrochemical Performance of  $\text{Li}_{1.2}\text{Ni}_{0.2}\text{Mn}_{0.6}\text{O}_2$  Cathode Material with Fast Ionic Conductor  $\text{Li}_3\text{VO}_4$  Coating. *Ionics* **2015**, *21* (10), 2725–2733.
- (107) Mueller-Neuhaus, J. R.; Dunlap, R. A.; Dahn, J. R. Understanding Irreversible Capacity in  $\text{Li}_x\text{Ni}_{1-y}\text{Fe}_y\text{O}_2$  Cathode Materials. *J. Electrochem. Soc.* **2000**, *147* (10), 3598–3605.
- (108) Kang, S.-H.; Johnson, C. S.; Vaughey, J. T.; Amine, K.; Thackeray, M. M. The Effects of Acid Treatment on the Electrochemical Properties of  $0.5\text{Li}_2\text{MnO}_3 \cdot 0.5\text{LiNi}_{0.44}\text{Co}_{0.25}\text{Mn}_{0.31}\text{O}_2$  Electrodes in Lithium Cells. *J. Electrochem. Soc.* **2006**, *153* (6), A1186–A1192.
- (109) Zheng, J.; Deng, S.; Shi, Z.; Xu, H.; Xu, H.; Deng, Y.; Zhang, Z.; Chen, G. The Effects of Persulfate Treatment on the Electrochemical Properties of  $\text{Li}_{1.20}\text{Mn}_{0.54}\text{Co}_{0.13}\text{Ni}_{0.13}\text{O}_2$  Cathode Material. *J. Power Sources* **2013**, *221*, 108–113.
- (110) Gao, J.; Kim, J.; Manthiram, A. High Capacity  $\text{Li}[\text{Li}_{0.2}\text{Mn}_{0.54}\text{Ni}_{0.13}\text{Co}_{0.13}]\text{O}_2\text{-V}_2\text{O}_5$  Composite Cathodes with Low Irreversible Capacity Loss for Lithium Ion Batteries. *Electrochem. Commun.* **2009**, *11* (1), 84–86.
- (111) Gao, J.; Manthiram, A. Eliminating the Irreversible Capacity Loss of High Capacity Layered  $\text{Li}[\text{Li}_{0.2}\text{Mn}_{0.54}\text{Ni}_{0.13}\text{Co}_{0.13}]\text{O}_2\text{-V}_2\text{O}_5$  Cathode by Blending with Other Lithium Insertion Hosts. *J. Power Sources* **2009**, *191* (2), 644–647.
- (112) Wu, Y.; Murugan, A. V.; Manthiram, A. Surface Modification of High Capacity Layered  $\text{Li}[\text{Li}_{0.2}\text{Mn}_{0.54}\text{Ni}_{0.13}\text{Co}_{0.13}]\text{O}_2\text{-V}_2\text{O}_5$  Cathodes by  $\text{AlPO}_4$ . *J. Electrochem. Soc.* **2008**, *155* (9), A635–A641.
- (113) Reimers, J. N.; Fuller, E. W.; Rossen, E.; Dahn, J. R. Synthesis and Electrochemical Studies of  $\text{LiMnO}_2$  Prepared at Low Temperatures. *J. Electrochem. Soc.* **1993**, *140* (12), 3396–3401.
- (114) Lee, E.-S.; Huq, A.; Chang, H.-Y.; Manthiram, A. High-Voltage, High-Energy Layered-Spinel Composite Cathodes with Superior Cycle Life for Lithium-Ion Batteries. *Chem. Mater.* **2012**, *24* (3), 600–612.

- (115) McCalla, E.; Rowe, A. W.; Camardese, J.; Dahn, J. R. The Role of Metal Site Vacancies in Promoting Li–Mn–Ni–O Layered Solid Solutions. *Chem. Mater.* **2013**, *25* (13), 2716–2721.
- (116) Wang, J.; Yuan, G.; Zhang, M.; Qiu, B.; Xia, Y.; Liu, Z. The Structure, Morphology, and Electrochemical Properties of  $\text{Li}_{1+x}\text{Ni}_{1/6}\text{Co}_{1/6}\text{Mn}_{4/6}\text{O}_{2.25+x/}$  ( $0.1 \leq X \leq 0.7$ ) Cathode Materials. *Electrochimica Acta* **2012**, *66*, 61–66.
- (117) Verde, M. G.; Liu, H.; Carroll, K. J.; Baggetto, L.; Veith, G. M.; Meng, Y. S. Effect of Morphology and Manganese Valence on the Voltage Fade and Capacity Retention of  $\text{Li}[\text{Li}_{2/12}\text{Ni}_{3/12}\text{Mn}_{7/12}]\text{O}_2$ . *ACS Appl. Mater. Interfaces* **2014**, *6* (21), 18868–18877.
- (118) Park, Y. J.; Hong, Y.-S.; Wu, X.; Kim, M. G.; Ryu, K. S.; Chang, S. H. Synthesis and Electrochemical Characteristics of  $\text{Li}[\text{Co}_x\text{Li}_{(1/3-x/3)}\text{Mn}_{(2/3-2x/3)}]\text{O}_2$  Compounds. *J. Electrochem. Soc.* **2004**, *151* (5), A720–A727.
- (119) Kim, J.-M.; Chung, H.-T. The First Cycle Characteristics of  $\text{Li}(\text{Ni}_{1/3}\text{Co}_{1/3}\text{Mn}_{1/3})\text{O}_2$  Charged up to 4.7 V. *Electrochimica Acta* **2004**, *49* (6), 937–944.
- (120) Arunkumar, T. A.; Wu, Y.; Manthiram, A. Factors Influencing the Irreversible Oxygen Loss and Reversible Capacity in Layered  $\text{Li}[\text{Li}_{1/3}\text{Mn}_{2/3}]\text{O}_2\text{--Li}[\text{M}]\text{O}_2$  (M =  $\text{Mn}_{0.5-y}\text{Ni}_{0.5-y}\text{Co}_{2y}$  and  $\text{Ni}_{1-y}\text{Co}_y$ ) Solid Solutions. *Chem. Mater.* **2007**, *19* (12), 3067–3073.
- (121) Shao-Horn, Y.; Croguennec, L.; Delmas, C.; Nelson, E. C.; O’Keefe, M. A. Atomic Resolution of Lithium Ions in  $\text{LiCoO}_2$ . *Nat. Mater.* **2003**, *2* (7), 464–467.
- (122) Brown, C. R.; McCalla, E.; Watson, C.; Dahn, J. R. Combinatorial Study of the Li–Ni–Mn–Co Oxide Pseudoquaternary System for Use in Li–Ion Battery Materials Research. *ACS Comb. Sci.* **2015**, *17* (6), 381–391.
- (123) van Bommel, A.; Dahn, J. R. Analysis of the Growth Mechanism of Coprecipitated Spherical and Dense Nickel, Manganese, and Cobalt-Containing Hydroxides in the Presence of Aqueous Ammonia. *Chem. Mater.* **2009**, *21* (8), 1500–1503.
- (124) Genevois, C.; Koga, H.; Croguennec, L.; Ménétrier, M.; Delmas, C.; Weill, F. Insight into the Atomic Structure of Cycled Lithium-Rich Layered Oxide  $\text{Li}_{1.20}\text{Mn}_{0.54}\text{Co}_{0.13}\text{Ni}_{0.13}\text{O}_2$  Using HAADF STEM and Electron Nanodiffraction. *J. Phys. Chem. C* **2015**, *119* (1), 75–83.
- (125) Lu, Z.; Chen, Z.; Dahn, J. R. Lack of Cation Clustering in  $\text{Li}[\text{Ni}_x\text{Li}_{(1/3-2x/3)}\text{Mn}_{(2/3-x/3)}]\text{O}_2$  ( $0 < X \leq 1/2$ ) and  $\text{Li}[\text{Cr}_x\text{Li}_{(1-x/3)}\text{Mn}_{(2-2x/3)}]\text{O}_2$  ( $0 < X < 1$ ). *Chem. Mater.* **2003**, *15* (16), 3214–3220.
- (126) Qiu, B.; Zhang, M.; Wu, L.; Wang, J.; Xia, Y.; Qian, D.; Liu, H.; Hy, S.; Chen, Y.; An, K.; Zhu, Y.; Liu, Z.; Meng, Y. S. Gas–solid Interfacial Modification of Oxygen Activity in Layered Oxide Cathodes for Lithium-Ion Batteries. *Nat. Commun.* **2016**, *7*, 12108.
- (127) Cabana, J.; Johnson, C. S.; Yang, X.-Q.; Chung, K.-Y.; Yoon, W.-S.; Kang, S.-H.; Thackeray, M. M.; Grey, C. P. Structural Complexity of Layered-Spinel Composite Electrodes for Li-Ion Batteries. *J. Mater. Res.* **2010**, *25* (8), 1601–1616.
- (128) Yabuuchi, N.; Koyama, Y.; Nakayama, N.; Ohzuku, T. Solid-State Chemistry and Electrochemistry of  $\text{Li}(\text{Ni}_{1/3}\text{Co}_{1/3}\text{Mn}_{1/3})\text{O}_2$  for Advanced Lithium-Ion Batteries II. Preparation and Characterization. *J. Electrochem. Soc.* **2005**, *152* (7), A1434–A1440.
- (129) Choi, J.; Manthiram, A. Role of Chemical and Structural Stabilities on the Electrochemical Properties of Layered  $\text{Li}(\text{Ni}_{1/3}\text{Co}_{1/3}\text{Mn}_{1/3})\text{O}_2$  Cathodes. *J. Electrochem. Soc.* **2005**, *152* (9), A1714–A1718.
- (130) Grey, C. P.; Dupré, N. NMR Studies of Cathode Materials for Lithium-Ion Rechargeable Batteries. *Chem. Rev.* **2004**, *104* (10), 4493–4512.
- (131) Hung, I.; Zhou, L.; Pourpoint, F.; Grey, C. P.; Gan, Z. Isotropic High Field NMR Spectra of Li-Ion Battery Materials with Anisotropy  $>1$  MHz. *J. Am. Chem. Soc.* **2012**, *134* (4), 1898–1901.

- (132) Sathiya, M.; Abakumov, A. M.; Foix, D.; Rouse, G.; Ramesha, K.; Saubanère, M.; Doublet, M. L.; Vezin, H.; Laisa, C. P.; Prakash, A. S.; Gonbeau, D.; VanTendeloo, G.; Tarascon, J.-M. Origin of Voltage Decay in High-Capacity Layered Oxide Electrodes. *Nat. Mater.* **2015**, *14* (2), 230–238.
- (133) Alcántara, R.; Jumas, J. C.; Lavela, P.; Olivier-Fourcade, J.; Pérez-Vicente, C.; Tirado, J. L. X-Ray Diffraction, <sup>57</sup>Fe Mössbauer and Step Potential Electrochemical Spectroscopy Study of LiFe<sub>y</sub>Co<sub>1-y</sub>O<sub>2</sub> Compounds. *J. Power Sources* **1999**, *81–82*, 547–553.
- (134) McLaren, V. L.; West, A. R.; Tabuchi, M.; Nakashima, A.; Takahara, H.; Kobayashi, H.; Sakaebe, H.; Kageyama, H.; Hirano, A.; Takeda, Y. Study of the Capacity Fading Mechanism for Fe-Substituted LiCoO<sub>2</sub> Positive Electrode. *J. Electrochem. Soc.* **2004**, *151* (5), A672–A681.
- (135) van Bommel, A. Lithium-Rich Transition Metal Oxides as Positive Electrode Materials in Lithium-Ion Batteries. PhD Thesis, Dalhousie University, 2010.
- (136) Fell, C. R. Structural Factors Affecting Lithium Transport in Lithium-Excess Layered Cathode Materials. PhD Thesis, University of Florida, 2012.
- (137) Koga, H. Study of Li-Rich Lamellar Oxides as Positive Electrode Materials for Lithium-Ion Batteries. PhD Thesis, Université Sciences et Technologies - Bordeaux I, 2013.
- (138) Knight, J. C. Electrochemical Properties and Ion-Extraction Mechanisms of Li-Rich Layered Oxides and Spinel Oxides. PhD Thesis, University of Texas, Austin, 2015.
- (139) Ates, M. N. High Energy Density Cathode Active Materials for Lithium-Ion Batteries. PhD Thesis, Northeastern University, 2015.
- (140) Li, J.; Camardese, J.; Shunmugasundaram, R.; Glazier, S.; Lu, Z.; Dahn, J. R. Synthesis and Characterization of the Lithium-Rich Core–Shell Cathodes with Low Irreversible Capacity and Mitigated Voltage Fade. *Chem. Mater.* **2015**, *27* (9), 3366–3377.
- (141) Lee, E.-S.; Huq, A.; Chang, H.-Y.; Manthiram, A. High-Voltage, High-Energy Layered-Spinel Composite Cathodes with Superior Cycle Life for Lithium-Ion Batteries. *Chem. Mater.* **2012**, *24* (3), 600–612.
- (142) Seo, D.-H.; Lee, J.; Urban, A.; Malik, R.; Kang, S.; Ceder, G. The Structural and Chemical Origin of the Oxygen Redox Activity in Layered and Cation-Disordered Li-Excess Cathode Materials. *Nat. Chem.* **2016**, *8* (7), 692–697.
- (143) Self, J. In-Situ Volume Studies of Li-Ion Pouch Cells. Thesis, Dalhousie University, 2015.

## Appendix A: Two-phase behavior vs. stacking faults

In Chapter 3, it was concluded that  $\text{Li}[\text{Li}_{1/3-2x/3}\text{Ni}_x\text{Mn}_{2/3-x/3}]\text{O}_2$  materials were single phase materials and that they were solid-solutions between  $\text{Li}_2\text{MnO}_3$  and  $\text{Li}[\text{Ni}_{0.5}\text{Mn}_{0.5}]\text{O}_2$ . The peak broadening of the superlattice peaks of those materials was attributed to the presence of stacking faults. However, during the PhD defense, one of the examining committee members asked - whether the stacking faults can just exist in the  $\text{Li}_2\text{MnO}_3$  phase.

Figure 3.10 shows the diffraction pattern of the  $\text{Li}[\text{Li}_{1/3-2x/3}\text{Ni}_x\text{Mn}_{2/3-x/3}]\text{O}_2$  series. The (001) peak near  $19^\circ$  becomes broader as the Ni content increases. The examiner asked! Couldn't this happen if a  $\text{Li}_2\text{MnO}_3$  phase of fixed lattice constant coexisted with a  $\text{LiNi}_{0.5}\text{Mn}_{0.5}\text{O}_2$  phase of fixed lattice constant. As x increased, the peak would broaden and shift to the left as observed in the right panel of Figure 3.10.

In order to decide if this interpretation is correct, one must examine what happens to the superlattice peaks. The superlattice peaks become very broad, due to stacking faults. The examiner asked: what if the stacking faults are in the  $\text{Li}_2\text{MnO}_3$  (second) phase Figure A1 shows the calculated 020 superlattice peak of  $\text{Li}_2\text{MnO}_3$  as a function of stacking fault probability. Figure A1 shows that this peak shifts to the right as the stacking faults probability increases. By contrast, Figure 3.11 shows that this 020 peak shifts to the left as Ni content increases. In addition, the 020 peak shifts in concert with the 001 peak as shown in Figure 3.12. Therefore, the postulate of the examiner cannot be correct. Instead, the conclusion of chapter 3 are deemed correct.

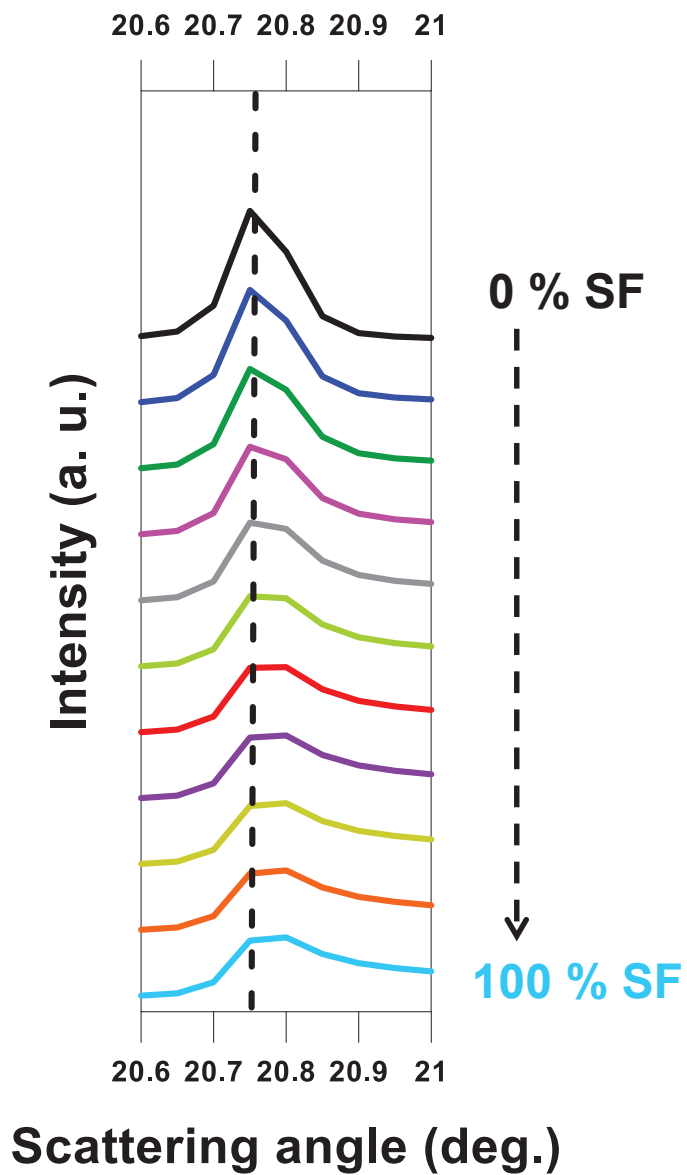


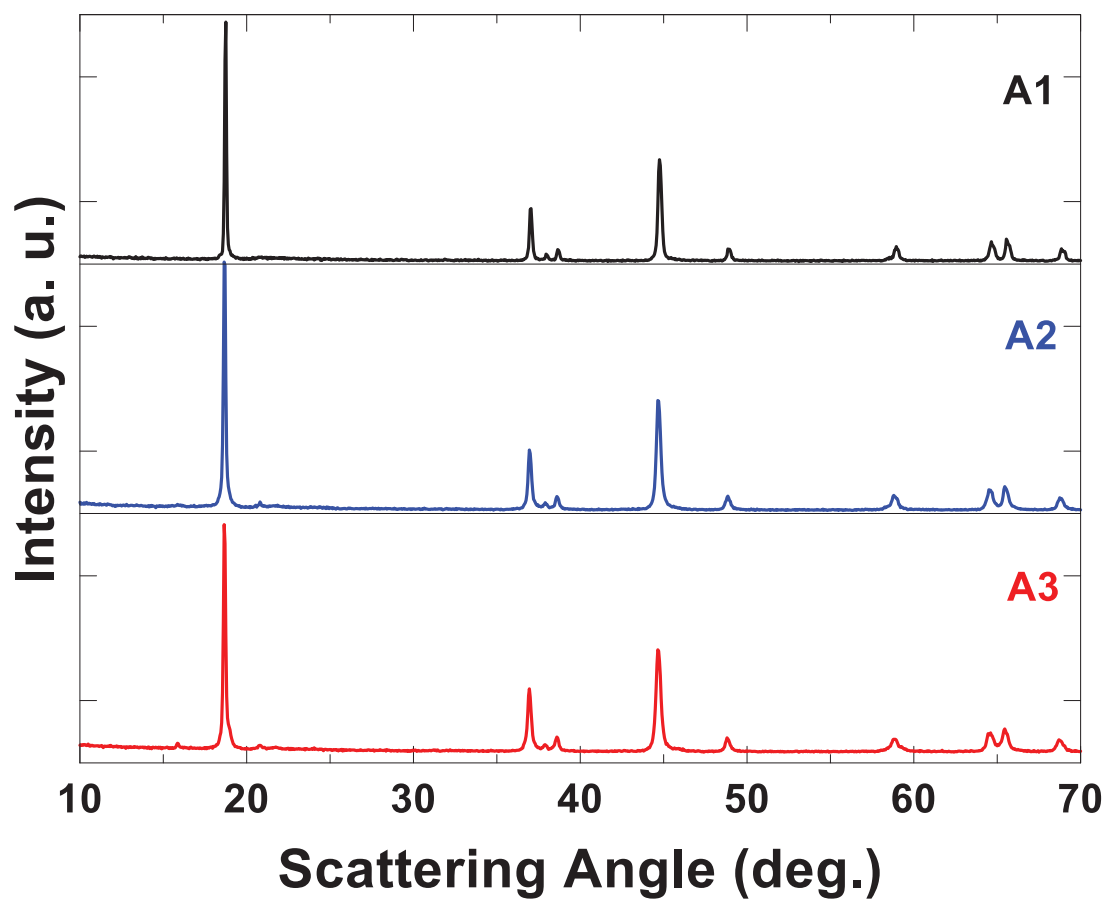
Figure A1. XRD pattern between 20.6° and 21° showing the first superlattice peak obtained from FAULTS simulation

## **Appendix B: Rietveld refinement of the XRD patterns**

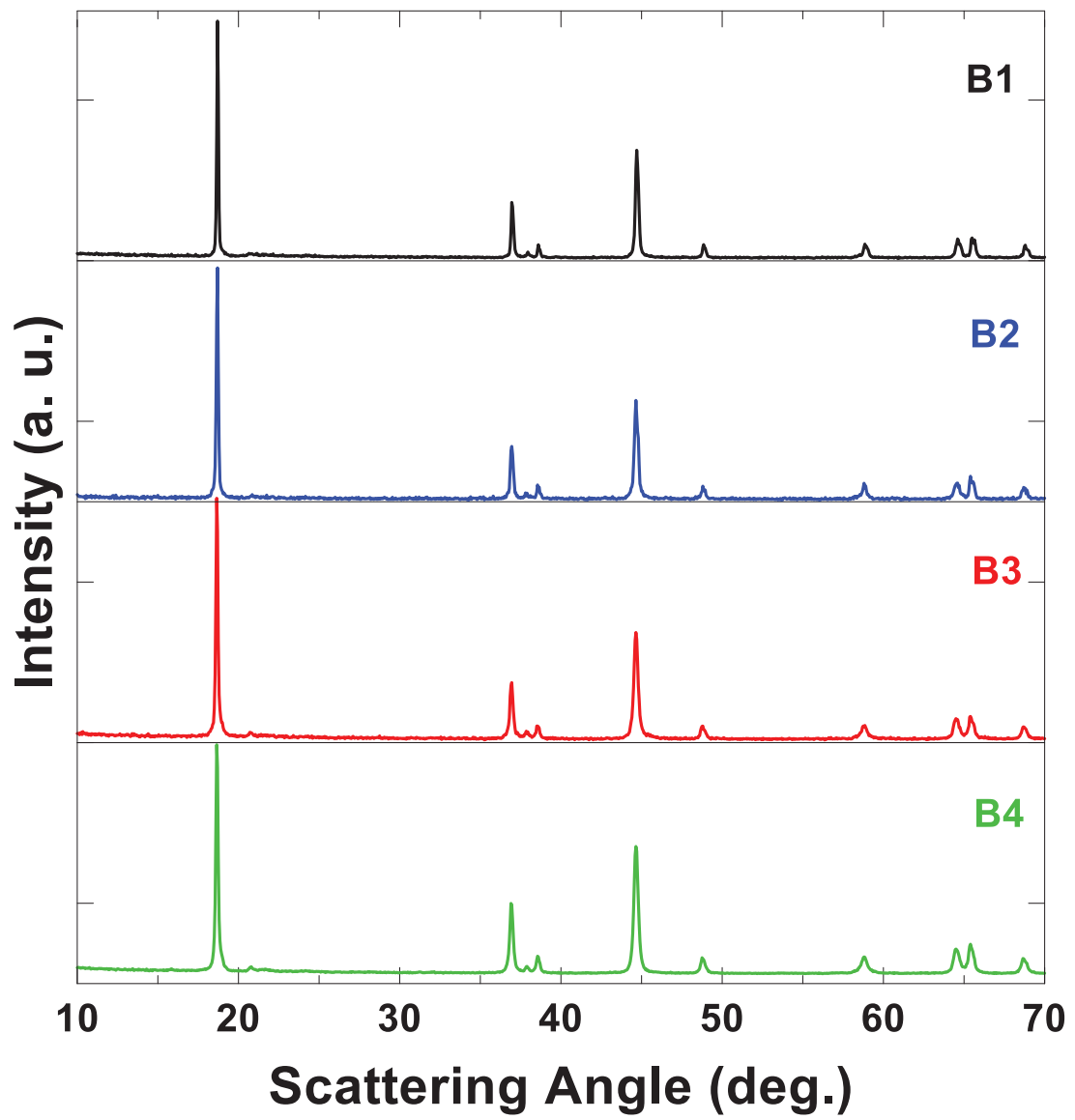
The XRD patterns of the single-phase materials with and without metal-site vacancies were fitted using Rietveld refinement. The parameters used in the model are explained as follows. For convenience, the superlattice peaks were excluded in the refinement and the space group  $R\bar{3}m$  (hexagonal unit cell) was used. The metal-ratios obtained from the ICP-OES analysis were normalized to 2 and hence the total oxygen was fixed to 2. In the case of materials with metal-site vacancies, the total metal content was less than 2. The location of metal-site vacancies was assumed either in the Li layer or TM layer according to the  $^7\text{Li}$  NMR results.

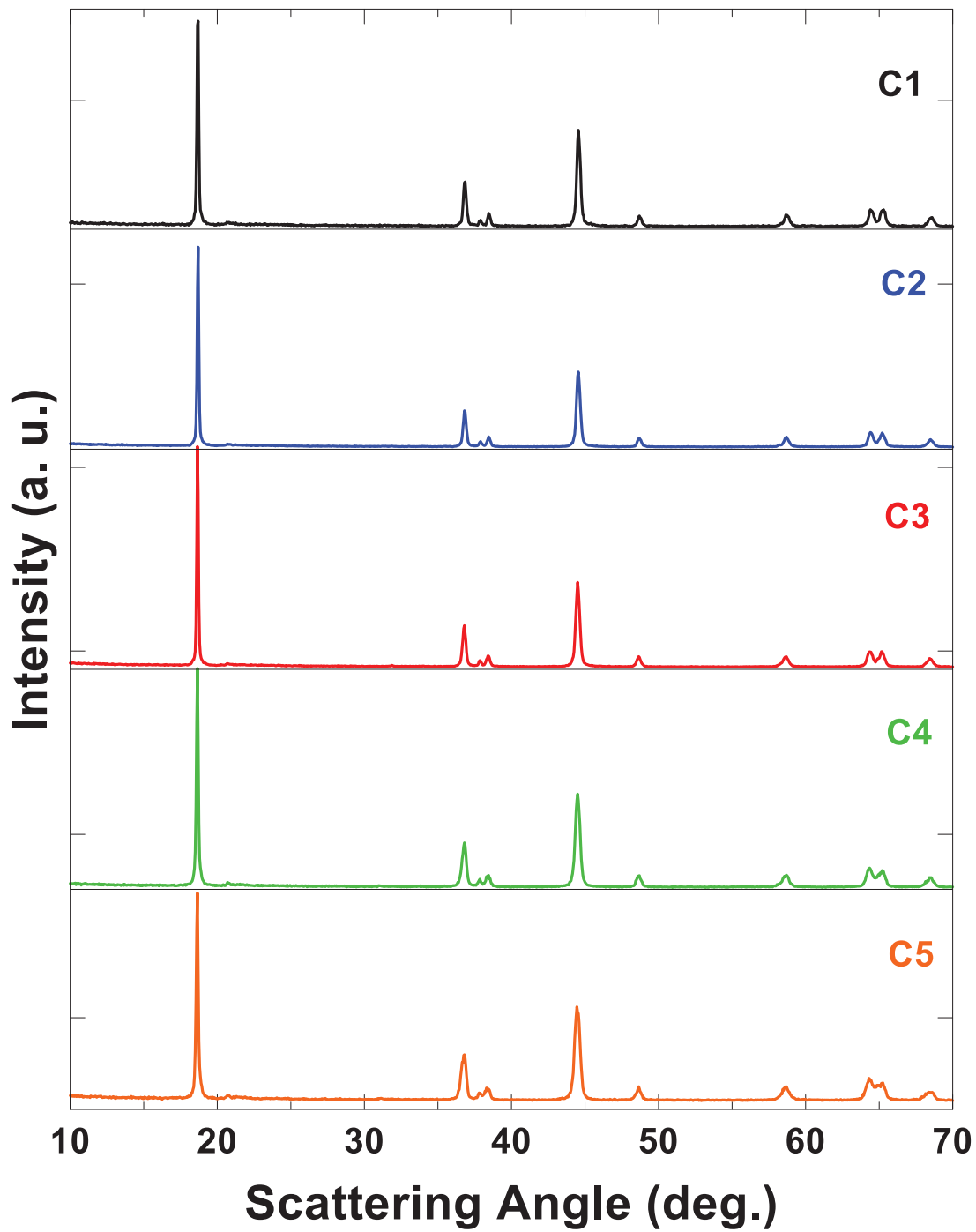
In the refinement, the lattice parameters  $a$  and  $c$ , the scale factor, the position of oxygen in the hexagonal unit cell and the parameters for the background (fifth order polynomial function) were adjustable parameters. The peak shape was defined using pseudo-voigt function and the variation of the FWHM was defined by the Caglioti function and hence the  $u$ ,  $v$  and  $w$  were adjustable parameters. Constraints for the exchange of Li and Ni between the Li layer and TM layers were imposed in such a way the total metal content in each layer is always equal to 1. In the case of materials with metal-site vacancies, the metal ions were fixed according to the  $^7\text{Li}$  NMR results.

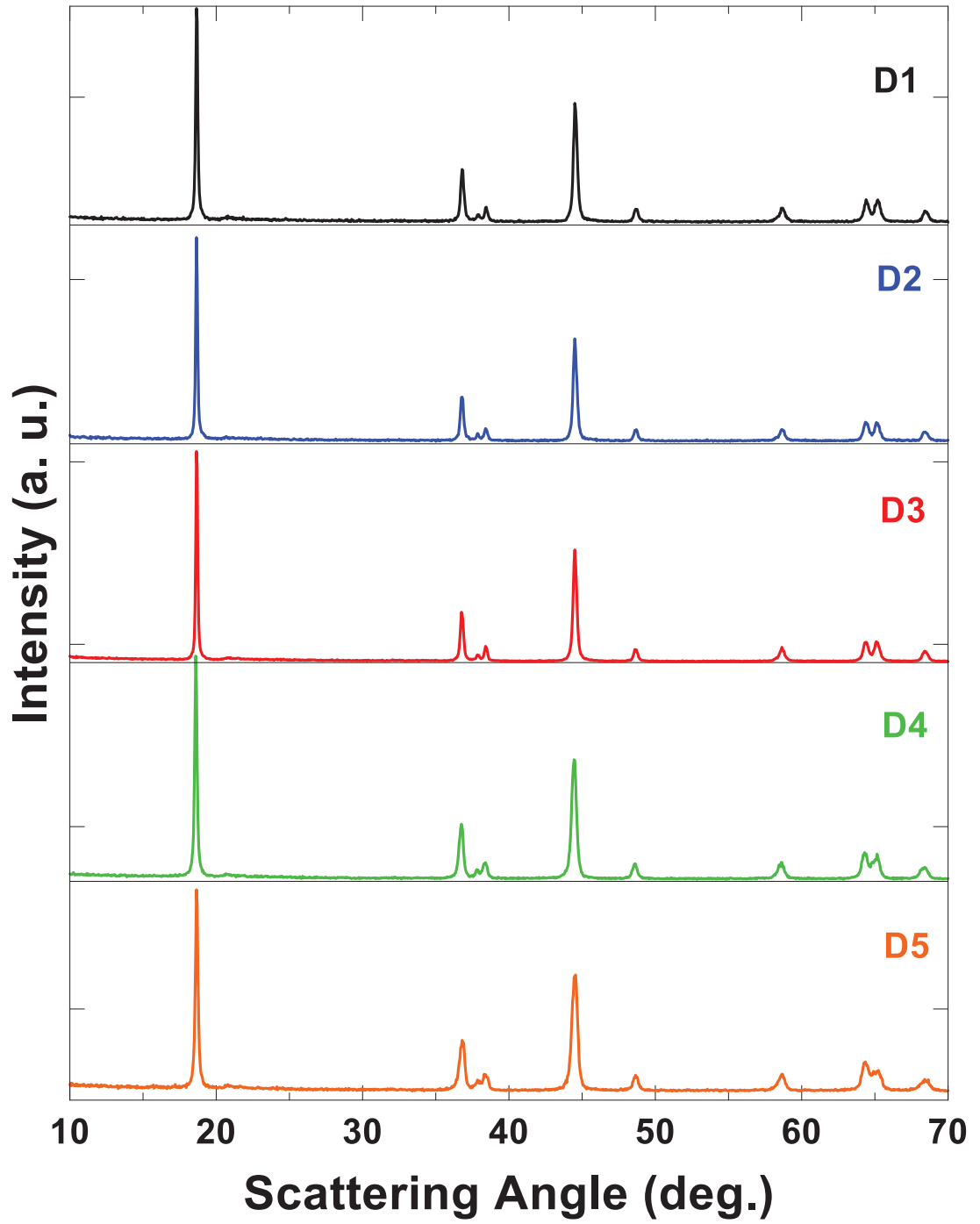
Appendix C: XRD patterns of samples A1 to O2

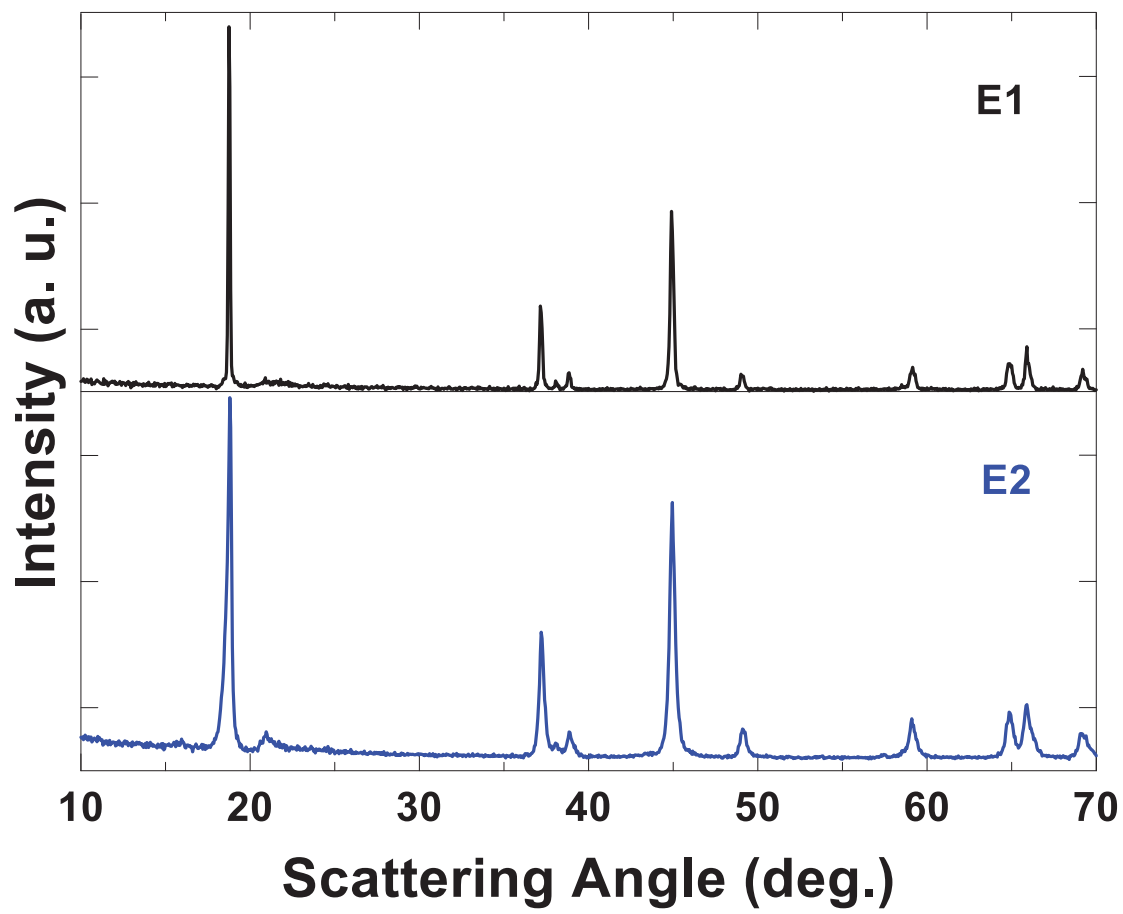


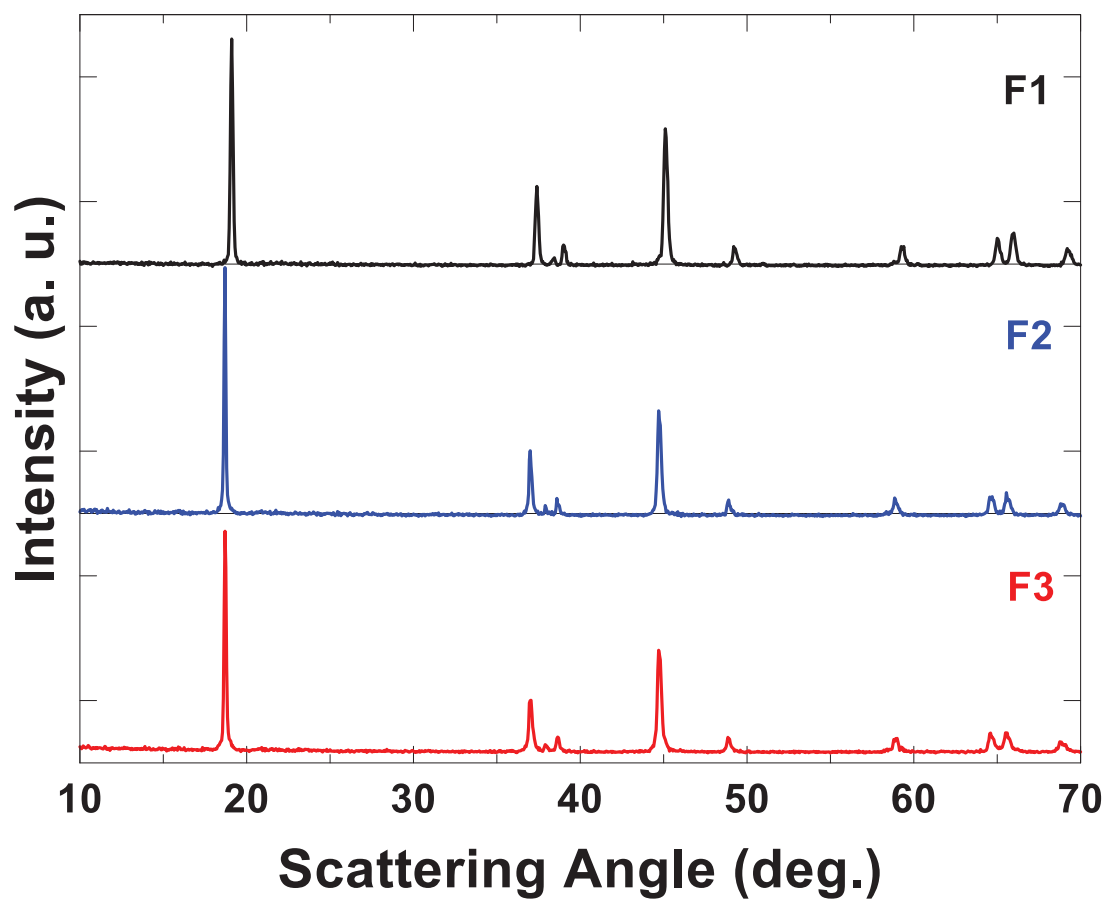


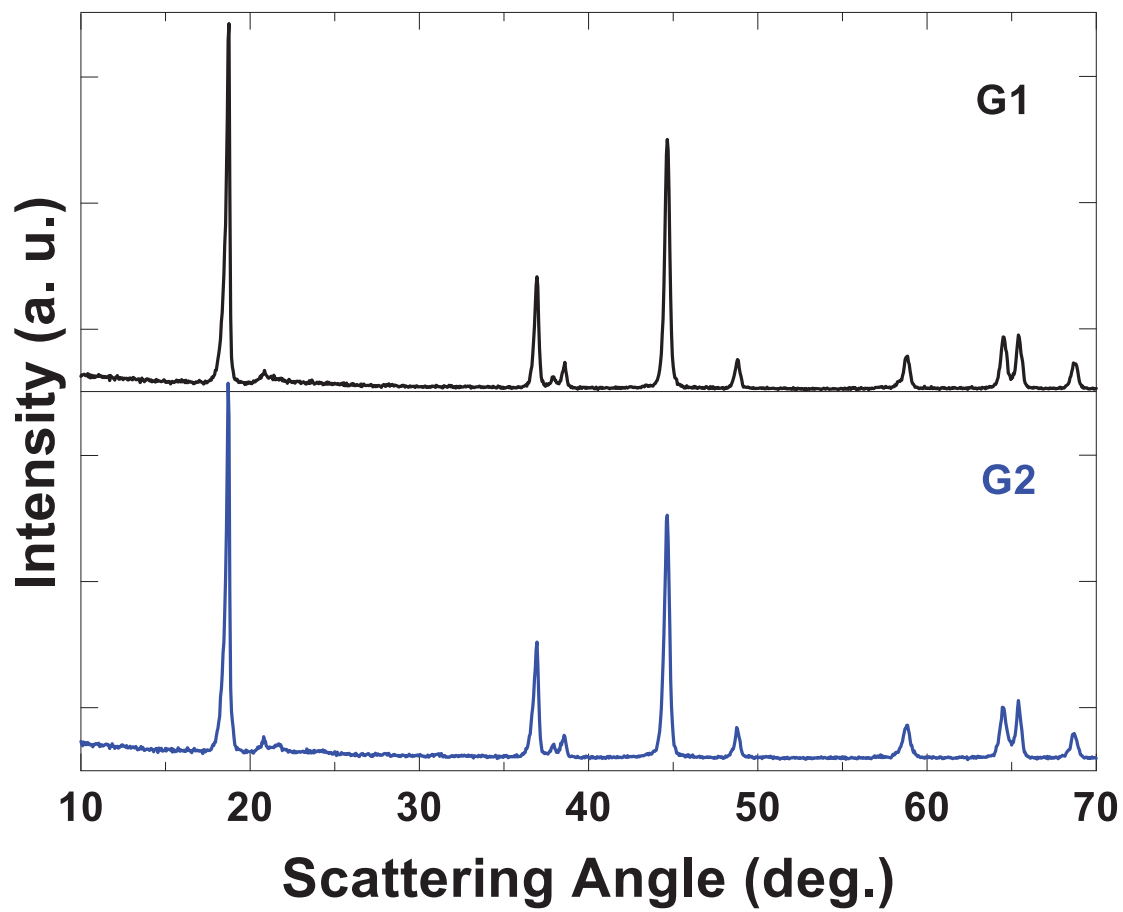


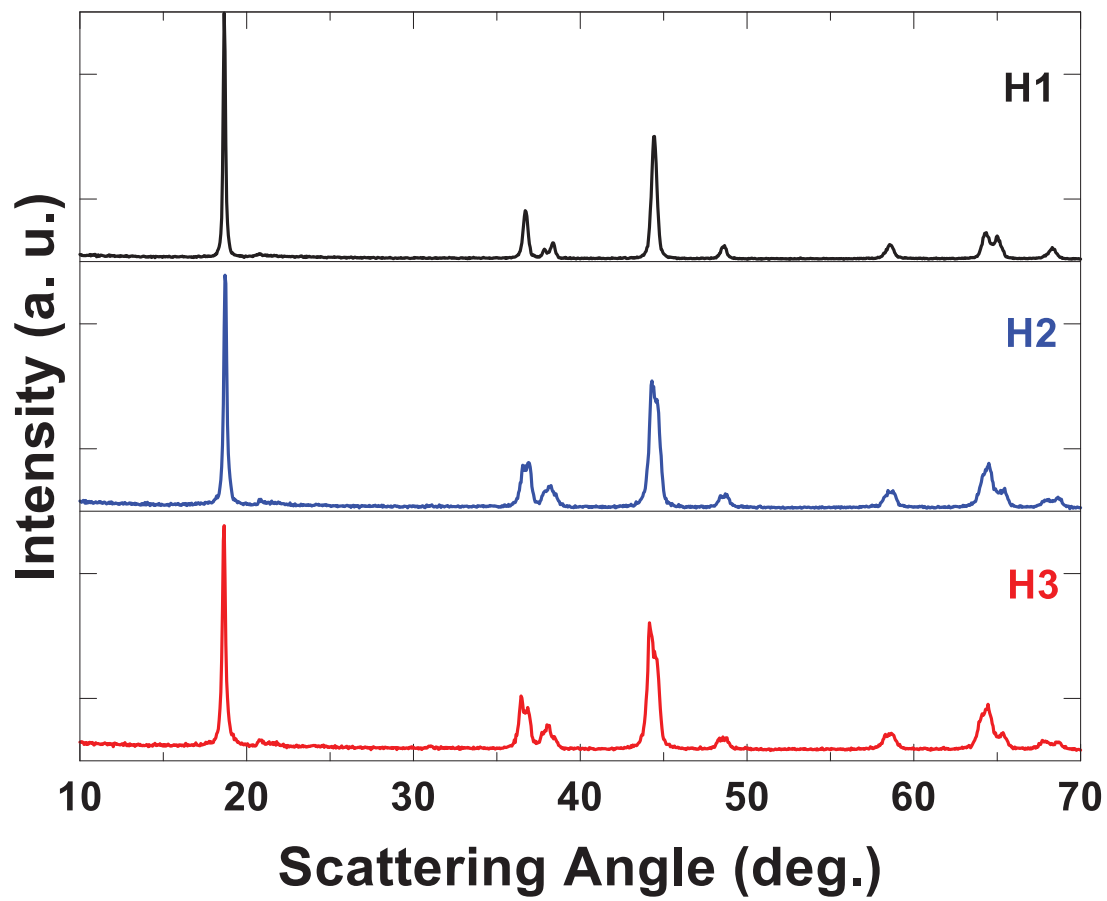


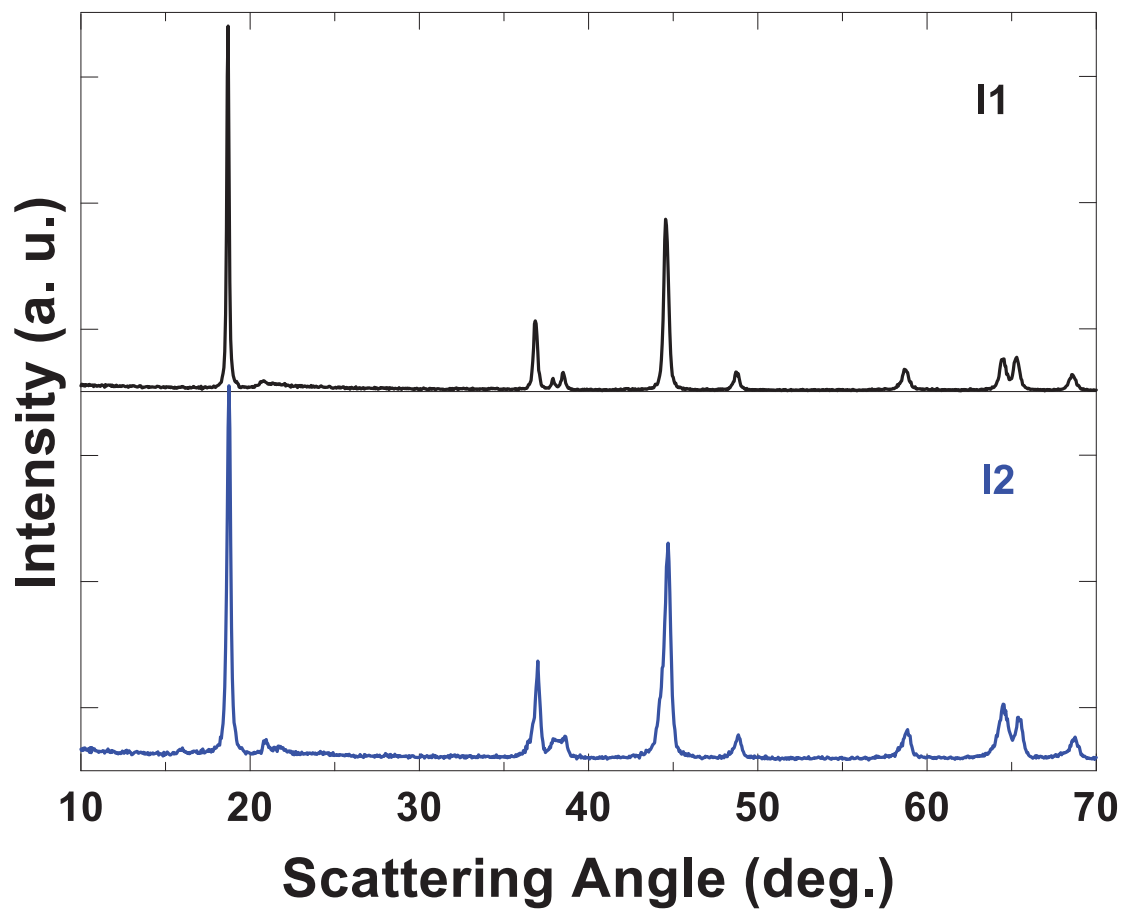




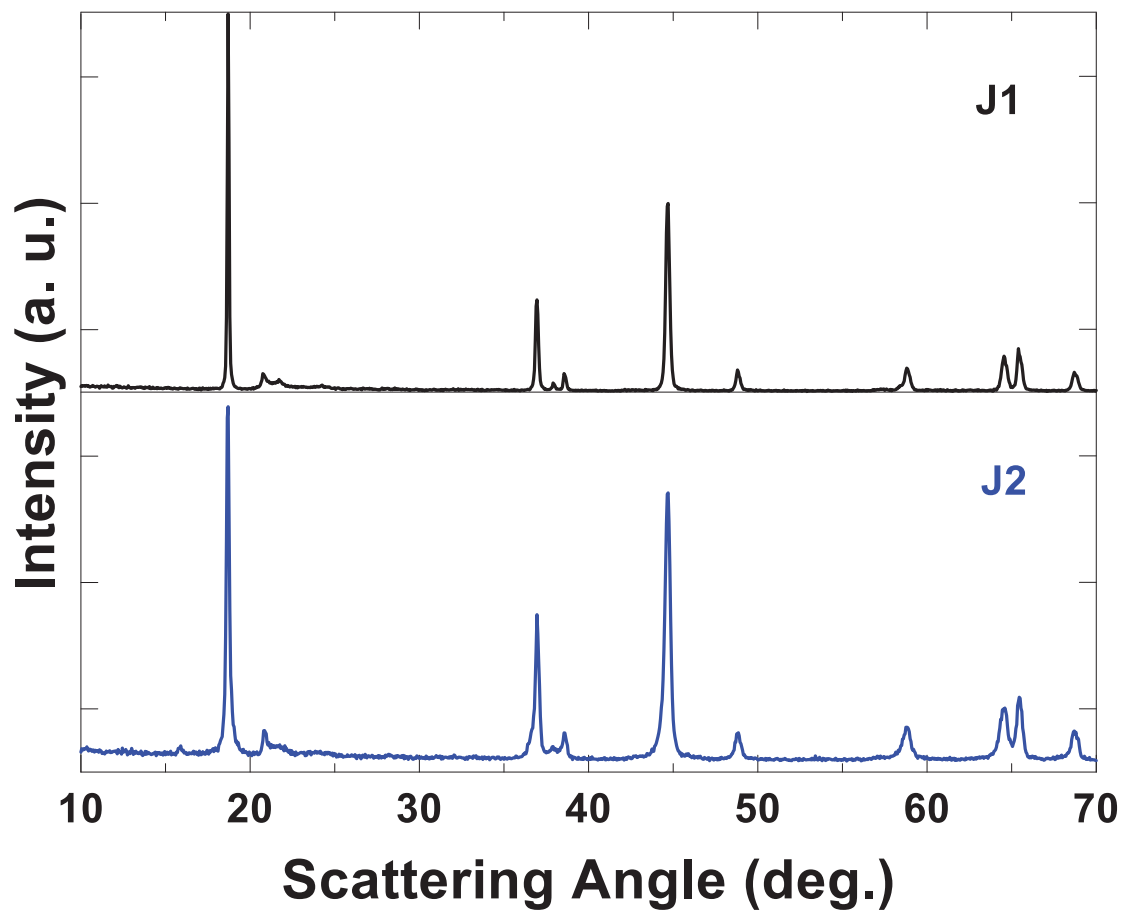


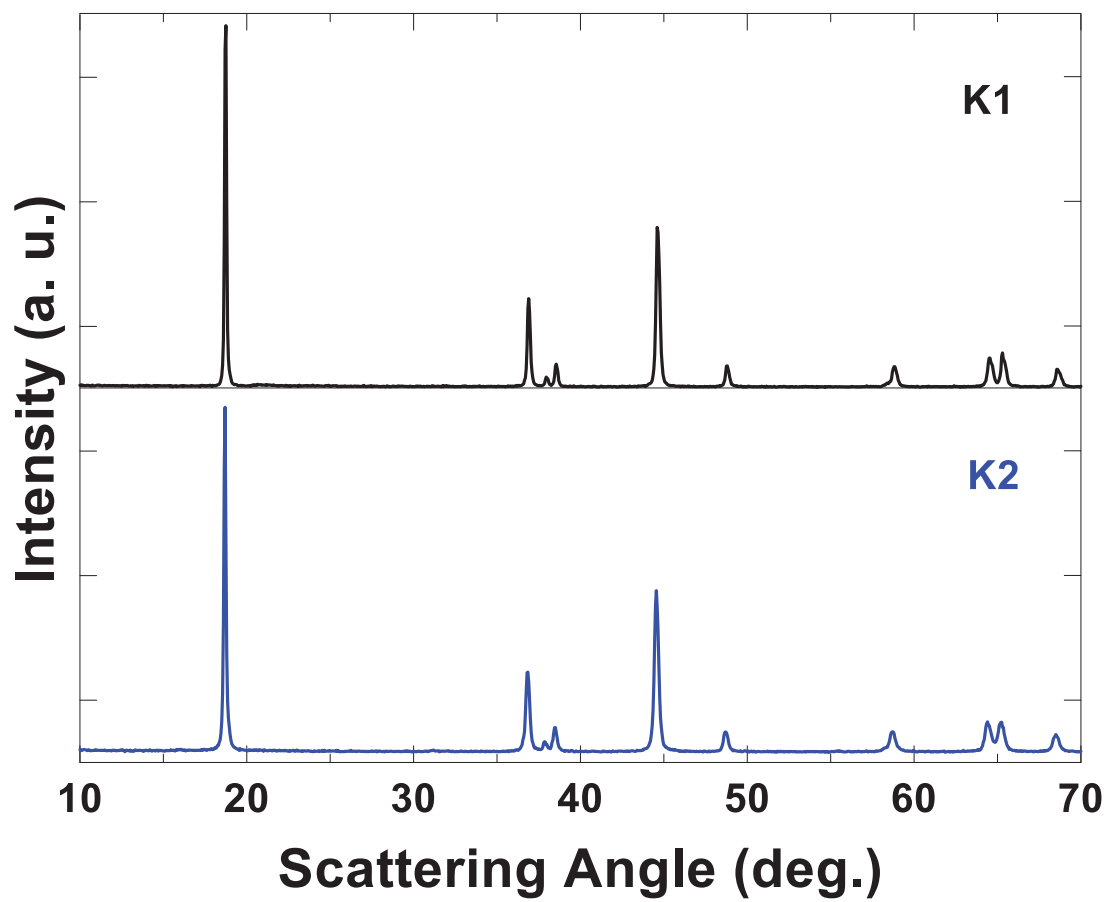


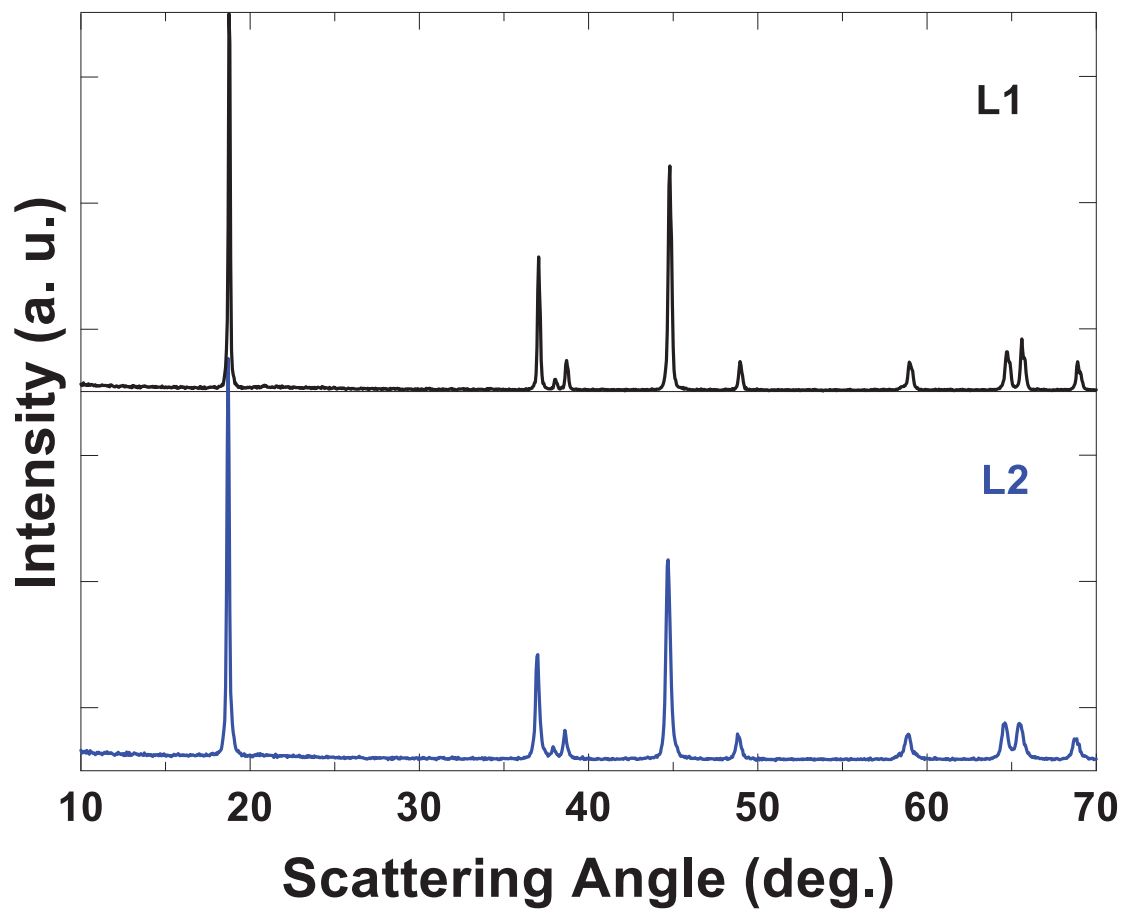


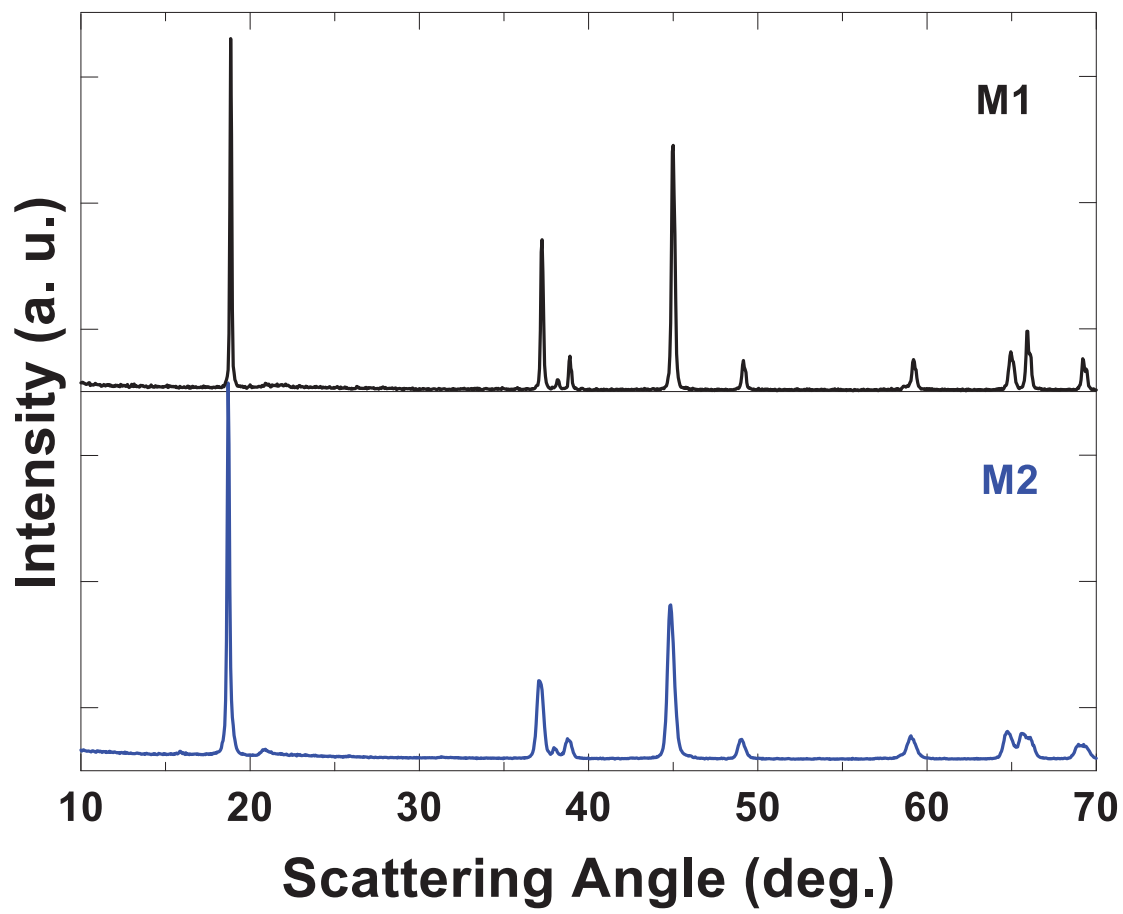


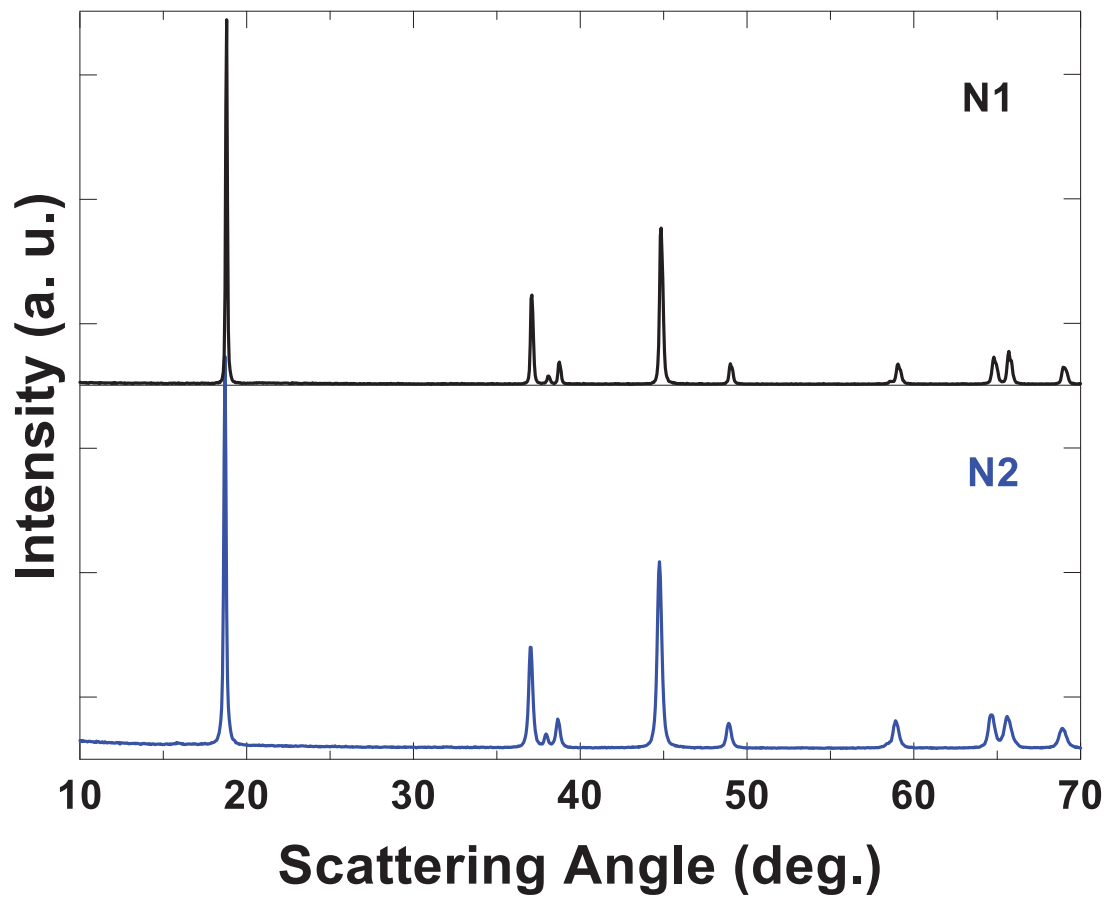


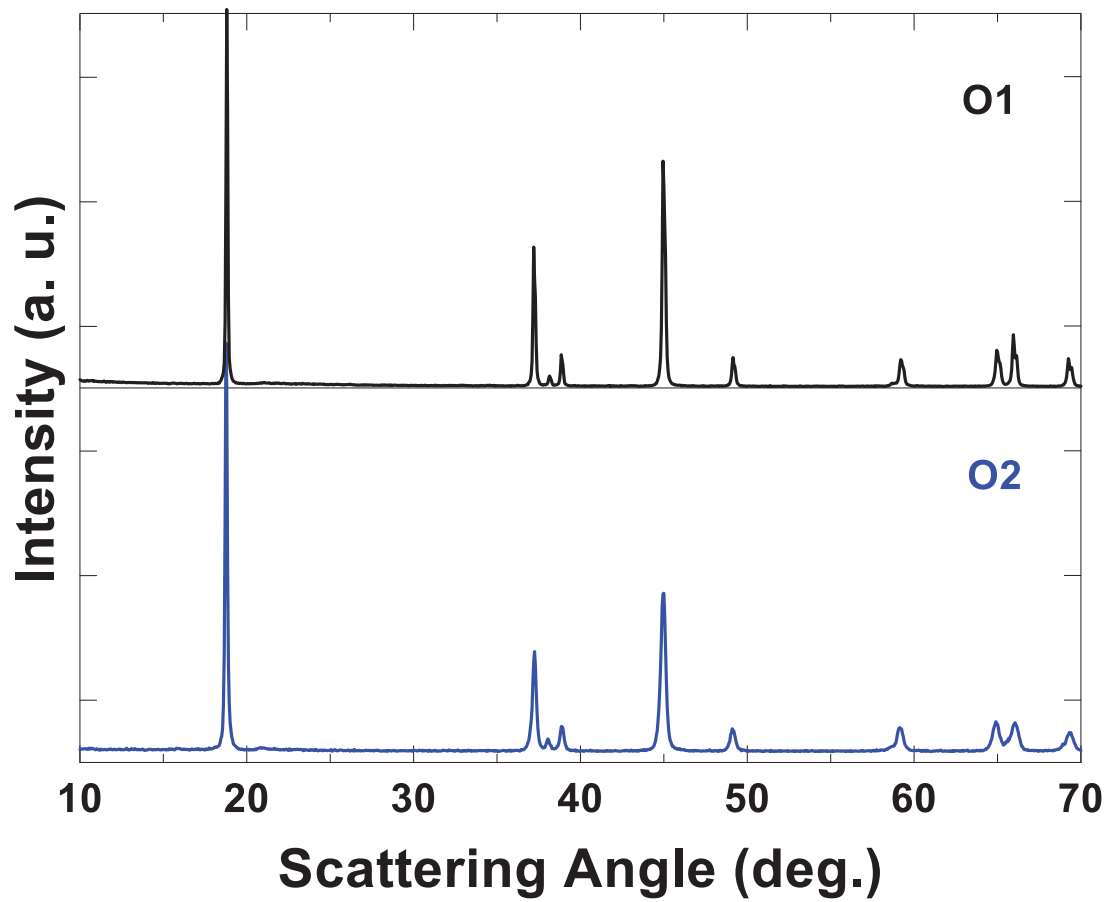












**Appendix D: Table of lattice constants of samples A1 to O2**

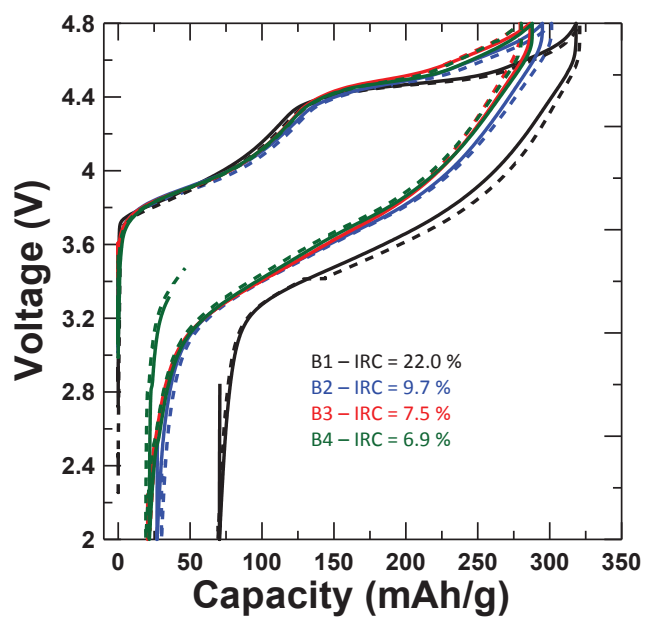
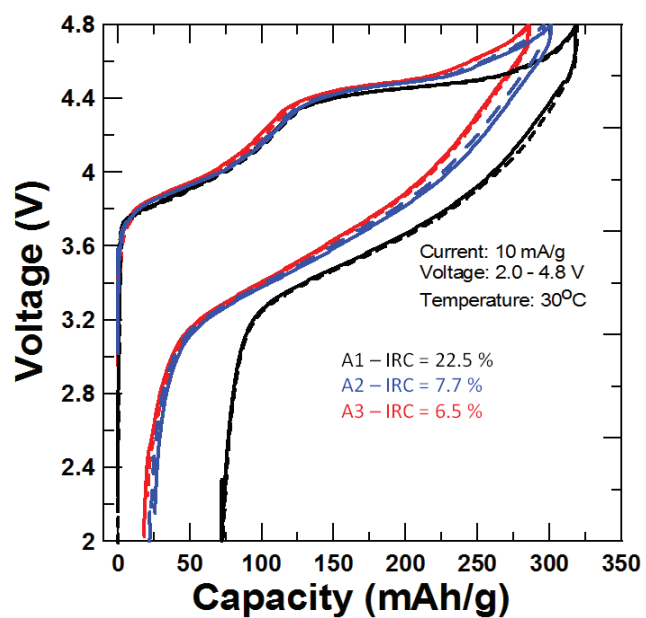
Sample	$a(\text{Å})$	$c(\text{Å})$
A1	2.8452(3)	14.213(4)
A2	2.8476(6)	14.235(2)
A3*	2.8483(3)	14.243(1)
B1	2.8481(1)	14.208(4)
B2	2.8514(4)	14.239(3)
B3	2.8511(1)	14.244(8)
B4	2.8518(8)	14.247(2)
C1	2.8597(3)	14.239(2)
C2	2.8625(3)	14.252(8)
C3	2.8634(9)	14.259(1)
C4	2.8635(6)	14.261(6)
C5*	2.8648(4)	14.262(8)
D1	2.8613(4)	14.243(8)
D2	2.8635(1)	14.258(4)
D3	2.8644(3)	14.263(7)
D4	2.8653(3)	14.276(3)
D5*	2.8609(2)	14.279(3)
E1	2.8346(3)	14.208(2)
E2*	2.8331(8)	14.20(7)
F1	2.8477(7)	14.223(5)
F2	2.8455(1)	14.21(5)
F3	2.8462(6)	14.233(4)
G1	2.8564(5)	14.258(1)
G2	2.8572(3)	14.259(6)

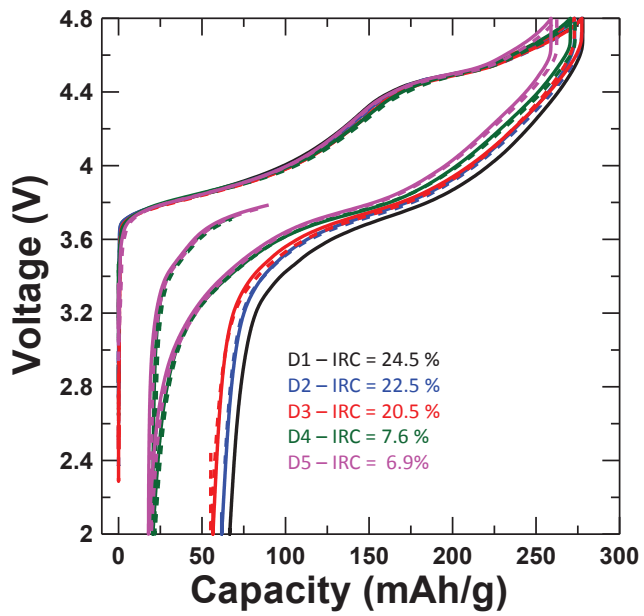
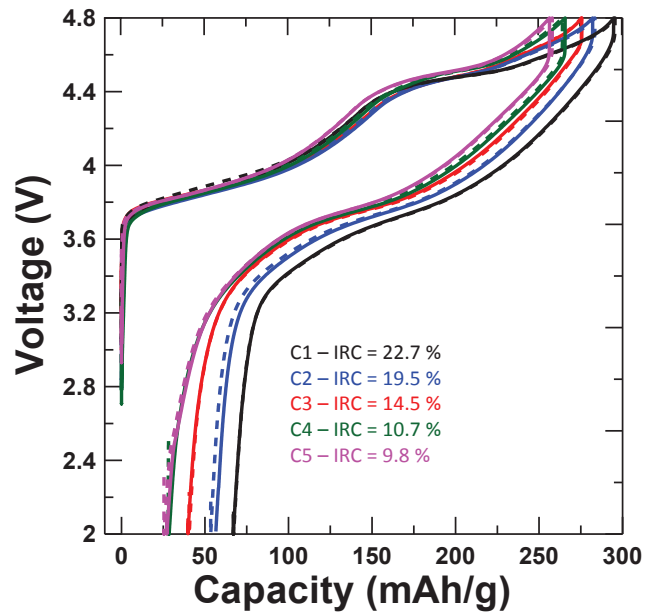
Sample	$a(\text{Å})$	$c(\text{Å})$
H1	2.8702(9)	14.270(3)
H2*	2.8762(7)	14.295(2)
H3*	2.8811(3)	14.267(9)
I1	2.8582(2)	14.244(4)
I2*	2.8597(6)	14.279(2)
J1	2.8522(5)	14.232(7)
J2*	2.8513(6)	14.248(3)
K1	2.8549(6)	14.225(2)
K2	2.8592(2)	14.242(7)
L1	2.8453(1)	14.200(8)
L2	2.8496(7)	14.229(7)
M1	2.8345(6)	14.173(3)
M2*	2.8362(3)	14.201(2)
N1	2.8423(3)	14.184(6)
N2	2.8439(3)	14.219(5)
O1	2.8316	14.155(5)
O2*	2.8304(2)	14.192(1)

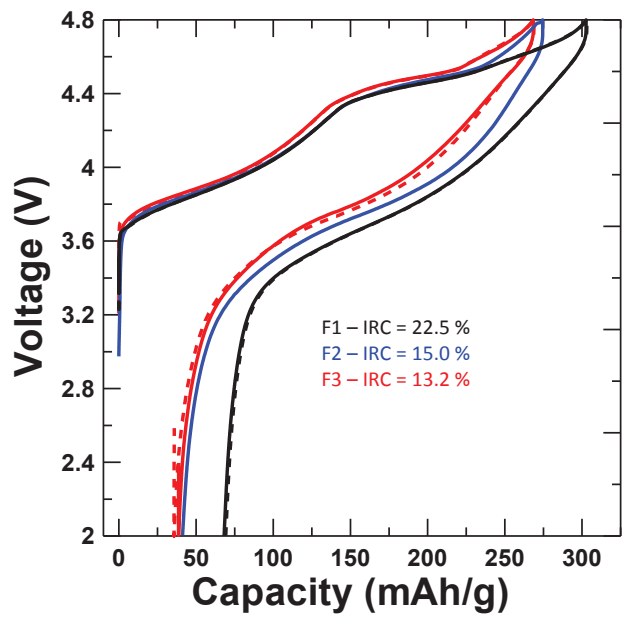
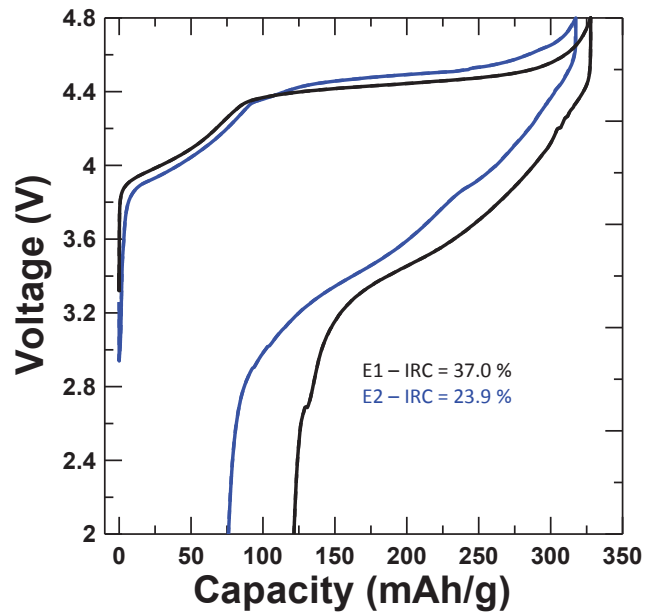
**\*Refinement done only for the major phase ( $R-3m$ )**

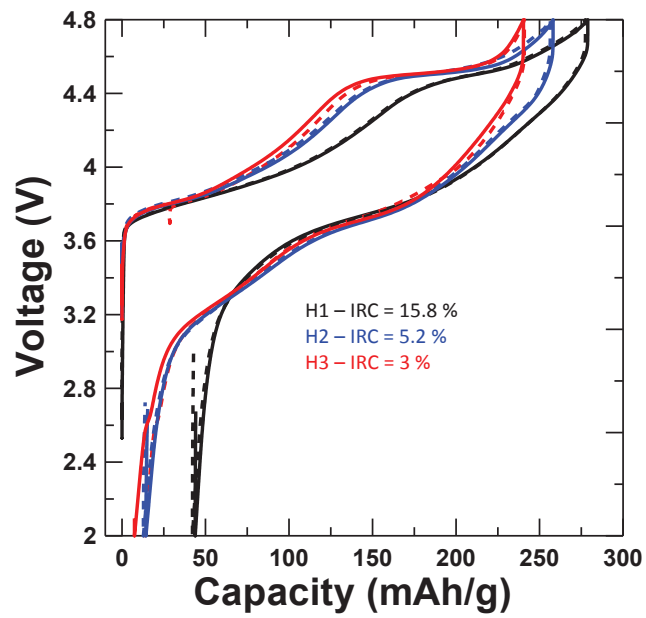
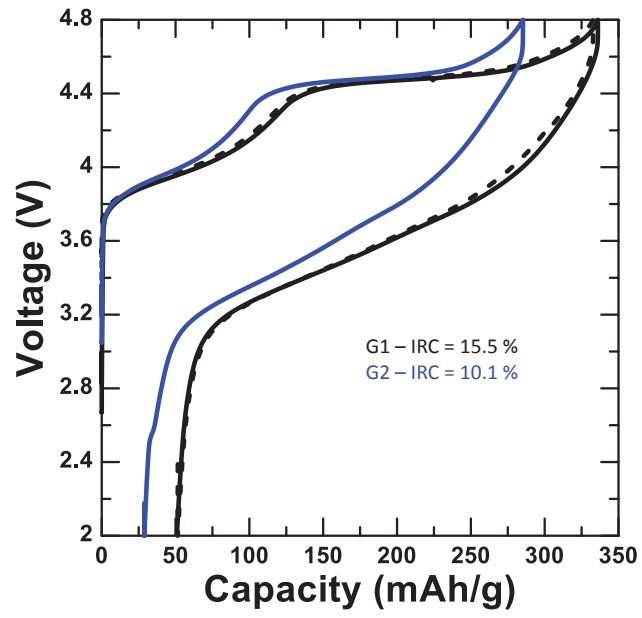


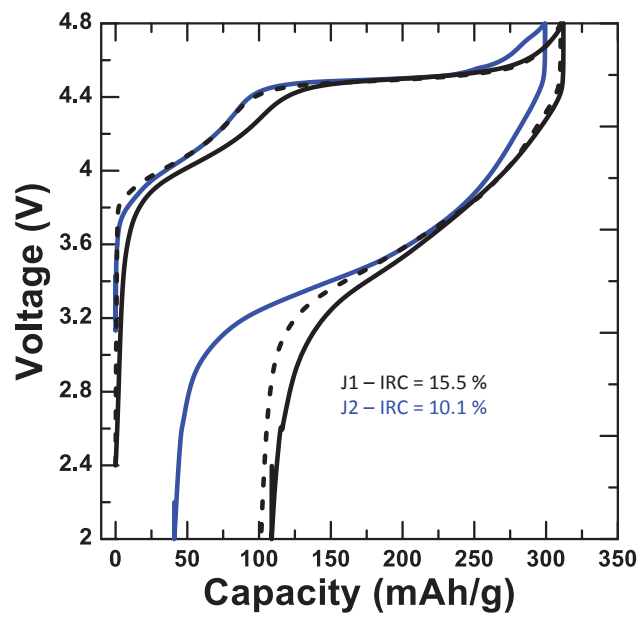
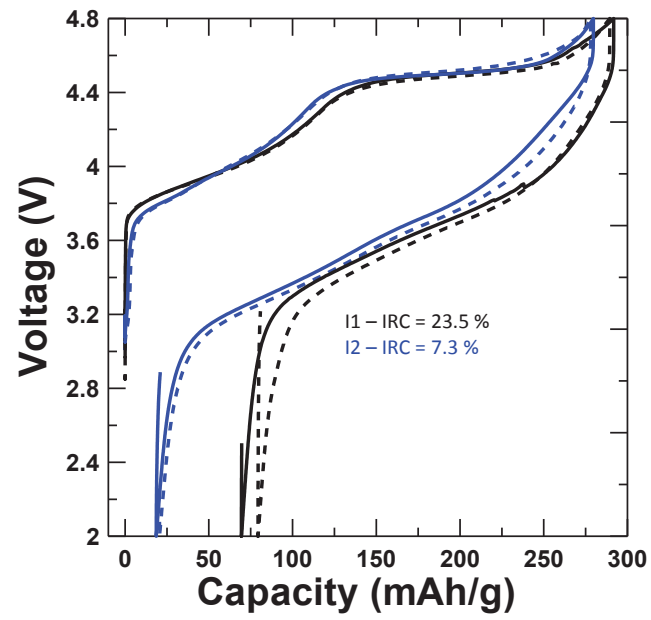
Appendix E: First charge-discharge profiles of samples A1 to O2

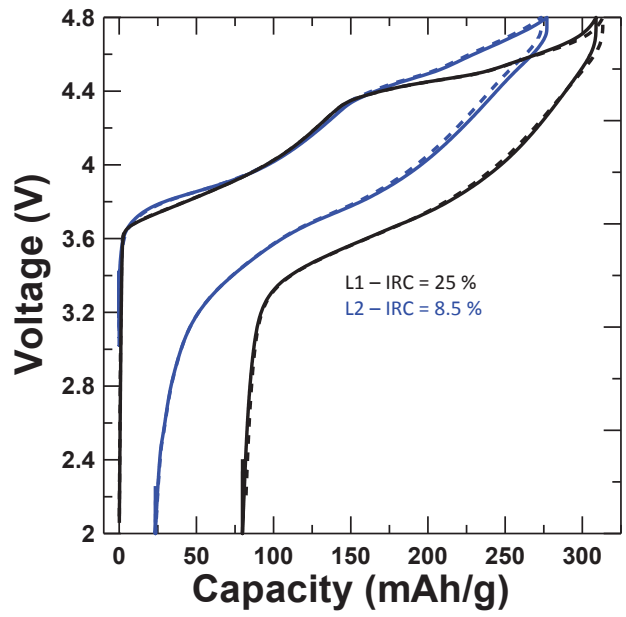
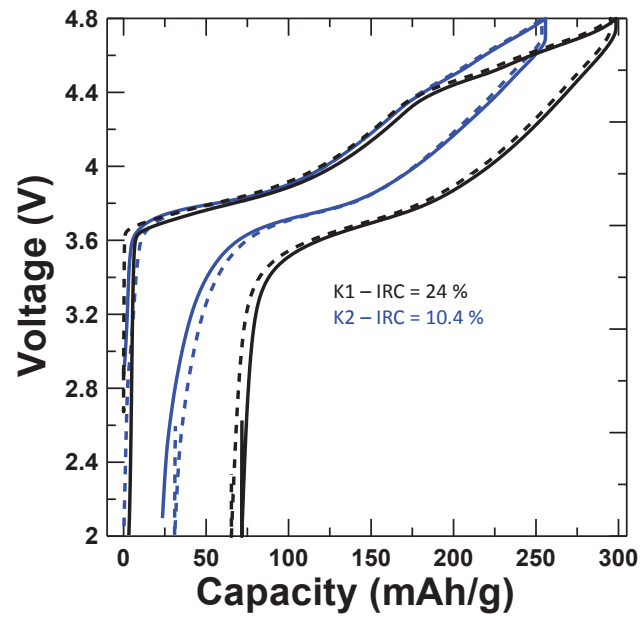


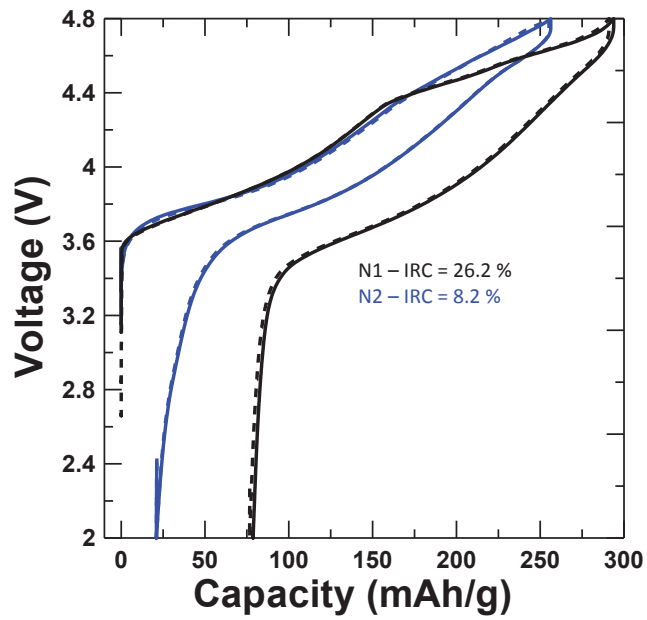
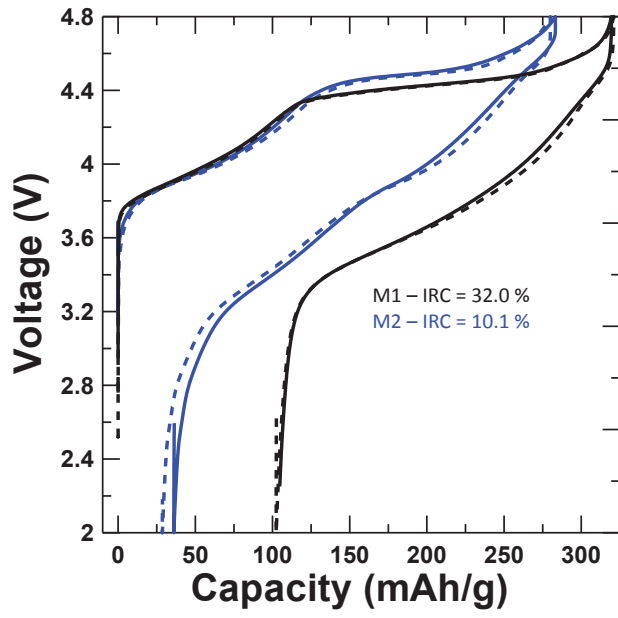


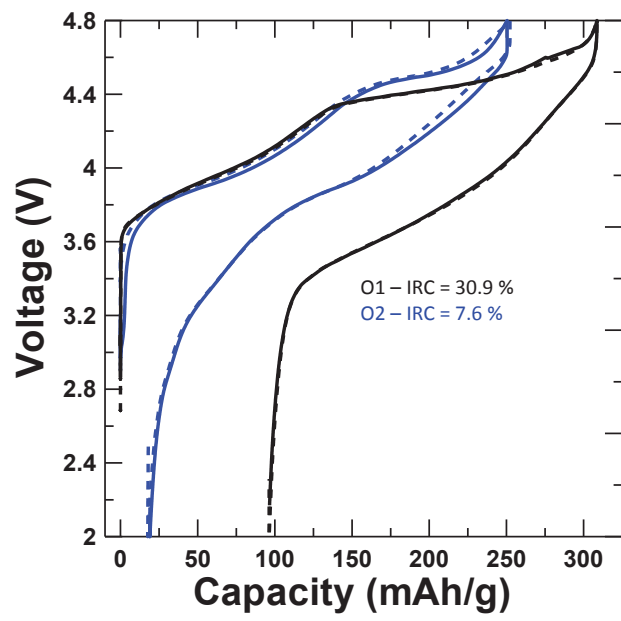

















## Appendix F: Copyright information


### Permission for Figure 1.6

9/11/2016 Rightslink® by Copyright Clearance Center

 **Copyright Clearance Center**

 **RightsLink®**

[Home](#) [Create Account](#) [Help](#)  [Live Chat](#)

 **ACS Publications** Most Trusted. Most Cited. Most Read.

**Title:** Atomic Structure of a Lithium-Rich Layered Oxide Material for Lithium-Ion Batteries: Evidence of a Solid Solution

**Author:** Karalee A. Jarvis, Zengqiang Deng, Lawrence F. Allard, et al

**Publication:** Chemistry of Materials

**Publisher:** American Chemical Society

**Date:** Aug 1, 2011

Copyright © 2011, American Chemical Society

[LOGIN](#)

If you're a [copyright.com](#) user, you can login to RightsLink using your [copyright.com](#) credentials. Already a [RightsLink](#) user or want to [learn more?](#)

#### PERMISSION/LICENSE IS GRANTED FOR YOUR ORDER AT NO CHARGE

This type of permission/license, instead of the standard Terms & Conditions, is sent to you because no fee is being charged for your order. Please note the following:

- Permission is granted for your request in both print and electronic formats, and translations.
- If figures and/or tables were requested, they may be adapted or used in part.
- Please print this page for your records and send a copy of it to your publisher/graduate school.
- Appropriate credit for the requested material should be given as follows: "Reprinted (adapted) with permission from (COMPLETE REFERENCE CITATION). Copyright (YEAR) American Chemical Society." Insert appropriate information in place of the capitalized words.
- One-time permission is granted only for the use specified in your request. No additional uses are granted (such as derivative works or other editions). For any other uses, please submit a new request.

If credit is given to another source for the material you requested, permission must be obtained from that source.

[BACK](#)

[CLOSE WINDOW](#)

Copyright © 2016 [Copyright Clearance Center, Inc.](#) All Rights Reserved. [Privacy statement](#). [Terms and Conditions](#). Comments? We would like to hear from you. E-mail us at [customercare@copyright.com](mailto:customercare@copyright.com)

## Permission for Figure 1.7

RightsLink Printable License

<https://s100.copyright.com/App/PrintableLicenseFrame.jsp?publisherID...>

### NATURE PUBLISHING GROUP LICENSE TERMS AND CONDITIONS

Sep 11, 2016

This Agreement between Ramesh Shunmugasundaram ("You") and Nature Publishing Group ("Nature Publishing Group") consists of your license details and the terms and conditions provided by Nature Publishing Group and Copyright Clearance Center.

License Number	3946080075316
License date	Sep 11, 2016
Licensed Content Publisher	Nature Publishing Group
Licensed Content Publication	Nature Chemistry
Licensed Content Title	Charge-compensation in 3d-transition-metal-oxide intercalation cathodes through the generation of localized electron holes on oxygen
Licensed Content Author	Kun Luo, Matthew R. Roberts, Rong Hao, Niccoló Guerrini, David M. Pickup, Yi-Sheng Liu
Licensed Content Date	Mar 21, 2016
Licensed Content Volume Number	8
Licensed Content Issue Number	7
Type of Use	reuse in a dissertation / thesis
Requestor type	academic/educational
Format	electronic
Portion	figures/tables/illustrations
Number of figures/tables /illustrations	1
High-res required	no
Figures	Figure 1.7
Author of this NPG article	no
Your reference number	
Title of your thesis / dissertation	A study on the properties of layered lithium transition metal oxide positive electrode materials for lithium-ion batteries
Expected completion date	Oct 2016
Estimated size (number of pages)	200
Requestor Location	Ramesh Shunmugasundaram 1205-1094 Wellington Street  Halifax, NS B3H2Z9 Canada Attn: Ramesh Shunmugasundaram
Billing Type	Invoice

Billing Address Ramesh Shunmugasundaram  
Department of Chemistry  
Dalhousie University  
  
Halifax, NS B3H2Z9  
Canada  
Attn: Ramesh Shunmugasundaram

Total 0.00 USD

[Terms and Conditions](#)**Terms and Conditions for Permissions**

Nature Publishing Group hereby grants you a non-exclusive license to reproduce this material for this purpose, and for no other use, subject to the conditions below:

1. NPG warrants that it has, to the best of its knowledge, the rights to license reuse of this material. However, you should ensure that the material you are requesting is original to Nature Publishing Group and does not carry the copyright of another entity (as credited in the published version). If the credit line on any part of the material you have requested indicates that it was reprinted or adapted by NPG with permission from another source, then you should also seek permission from that source to reuse the material.
2. Permission granted free of charge for material in print is also usually granted for any electronic version of that work, provided that the material is incidental to the work as a whole and that the electronic version is essentially equivalent to, or substitutes for, the print version. Where print permission has been granted for a fee, separate permission must be obtained for any additional, electronic re-use (unless, as in the case of a full paper, this has already been accounted for during your initial request in the calculation of a print run). NB: In all cases, web-based use of full-text articles must be authorized separately through the 'Use on a Web Site' option when requesting permission.
3. Permission granted for a first edition does not apply to second and subsequent editions and for editions in other languages (except for signatories to the STM Permissions Guidelines, or where the first edition permission was granted for free).
4. Nature Publishing Group's permission must be acknowledged next to the figure, table or abstract in print. In electronic form, this acknowledgement must be visible at the same time as the figure/table/abstract, and must be hyperlinked to the journal's homepage.
5. The credit line should read:  
Reprinted by permission from Macmillan Publishers Ltd: [JOURNAL NAME] (reference citation), copyright (year of publication)  
For AOP papers, the credit line should read:  
Reprinted by permission from Macmillan Publishers Ltd: [JOURNAL NAME], advance online publication, day month year (doi: 10.1038/sj.[JOURNAL ACRONYM].XXXXX)

**Note: For republication from the *British Journal of Cancer*, the following credit lines apply.**

Reprinted by permission from Macmillan Publishers Ltd on behalf of Cancer Research UK: [JOURNAL NAME] (reference citation), copyright (year of publication) For AOP papers, the credit line should read:  
Reprinted by permission from Macmillan Publishers Ltd on behalf of Cancer Research UK: [JOURNAL NAME], advance online publication, day month year (doi: 10.1038/sj.[JOURNAL ACRONYM].XXXXX)

6. Adaptations of single figures do not require NPG approval. However, the adaptation should be credited as follows:

Adapted by permission from Macmillan Publishers Ltd: [JOURNAL NAME] (reference citation), copyright (year of publication)

**Note: For adaptation from the *British Journal of Cancer*, the following credit line**

**applies.**

Adapted by permission from Macmillan Publishers Ltd on behalf of Cancer Research UK:  
[JOURNAL NAME] (reference citation), copyright (year of publication)

7. Translations of 401 words up to a whole article require NPG approval. Please visit <http://www.macmillanmedicalcommunications.com> for more information. Translations of up to a 400 words do not require NPG approval. The translation should be credited as follows:

Translated by permission from Macmillan Publishers Ltd: [JOURNAL NAME] (reference citation), copyright (year of publication).

**Note: For translation from the *British Journal of Cancer*, the following credit line applies.**

Translated by permission from Macmillan Publishers Ltd on behalf of Cancer Research UK:  
[JOURNAL NAME] (reference citation), copyright (year of publication)

We are certain that all parties will benefit from this agreement and wish you the best in the use of this material. Thank you.

Special Terms:

v1.1

Questions? [customercare@copyright.com](mailto:customercare@copyright.com) or +1-855-239-3415 (toll free in the US) or +1-978-646-2777.



## Permission for Figure 2.8



RightsLink®

Home

Create Account

Help



ACS Publications  
Most Trusted. Most Cited. Most Read.

**Title:** NMR Studies of Cathode Materials for Lithium-Ion Rechargeable Batteries  
**Author:** Clare P. Grey, Nicolas Dupré  
**Publication:** Chemical Reviews  
**Publisher:** American Chemical Society  
**Date:** Oct 1, 2004

Copyright © 2004, American Chemical Society

LOGIN

If you're a [copyright.com](#) user, you can login to RightsLink using your [copyright.com](#) credentials. Already a [RightsLink](#) user or want to [learn more?](#)

### PERMISSION/LICENSE IS GRANTED FOR YOUR ORDER AT NO CHARGE

This type of permission/license, instead of the standard Terms & Conditions, is sent to you because no fee is being charged for your order. Please note the following:

- Permission is granted for your request in both print and electronic formats, and translations.
- If figures and/or tables were requested, they may be adapted or used in part.
- Please print this page for your records and send a copy of it to your publisher/graduate school.
- Appropriate credit for the requested material should be given as follows: "Reprinted (adapted) with permission from (COMPLETE REFERENCE CITATION). Copyright (YEAR) American Chemical Society." Insert appropriate information in place of the capitalized words.
- One-time permission is granted only for the use specified in your request. No additional uses are granted (such as derivative works or other editions). For any other uses, please submit a new request.

If credit is given to another source for the material you requested, permission must be obtained from that source.

BACK

CLOSE WINDOW

Copyright © 2016 [Copyright Clearance Center, Inc.](#) All Rights Reserved. [Privacy statement.](#) [Terms and Conditions.](#)

Comments? We would like to hear from you. E-mail us at [customercare@copyright.com](mailto:customercare@copyright.com)

## ECS Copyright and Permissions

### Guidelines for Use of ECS Material

#### Fees

#### How to Ask for Permission

#### Permission Request Form (PDF)

#### Credit Lines

#### Permission to Reproduce Full Articles

---

### Permission Requests Key Points

- To request permission, please [submit this form](#) with full bibliographic information and figure/table numbers to [copyright@electrochem.org](mailto:copyright@electrochem.org).
- Our normal turnaround times for permission requests are 4–5 working days for figure and/or table requests, and 4–6 working days for full articles.
- ECS does not hold the copyright on the Open access articles published in its journals. Please follow reuse instructions that correspond with the Creative Commons license on the paper.
- Authors may use their own tables and figures in other scholarly research papers that they write, without writing to ECS for permission. Full credit to the original source should be given.

### Guidelines for Use of Open Access Materials from ECS Publications

**ECS does not hold the copyright on the Open Access articles published in its journals.** The copyright is held by the author(s). Please follow reuse instructions given by Creative Commons for its various licenses. ECS articles are published using either CC BY or CC BY-NC-ND licenses, here are links for more information:

CC BY: <http://creativecommons.org/licenses/by/4.0/>

CC BY-NC-ND: <http://creativecommons.org/licenses/by-nc-nd/4.0/>

Best Practices for Citing CC Licensed Articles:

[https://wiki.creativecommons.org/Best\\_practices\\_for\\_attribution](https://wiki.creativecommons.org/Best_practices_for_attribution)

### Guidelines for Use of Materials from ECS Publications

\*\*Before submitting your request, please note our normal turnaround times are 4–5 working days for figure and/or table requests, and 4–6 working days for full article requests. We will try our best to meet your deadline; but please plan to submit your request with these times in mind.

Before using ECS material or requesting to reproduce ECS material, please see the [ECS Transfer of Copyright Form](#) for the rights retained by authors and employers. **For example, authors may use their own tables and figures in other scholarly research papers that they write, without writing to ECS for permission.** Full credit to the original source should be given, for example, "Reproduced with permission from *J. Electrochem. Soc.*, **150**, H205 (2003). Copyright 2003, The Electrochemical Society."

## Permission for Figures in chapter 4



RightsLink®

Home

Create Account

Help



ACS Publications  
Most Trusted. Most Cited. Most Read.

**Title:** High Capacity Li-Rich Positive Electrode Materials with Reduced First-Cycle Irreversible Capacity Loss

**Author:** Ramesh Shunmugasundaram, Rajalakshmi Senthil Arumugam, J. R. Dahn

**Publication:** Chemistry of Materials

**Publisher:** American Chemical Society

**Date:** Feb 1, 2015

Copyright © 2015, American Chemical Society

LOGIN

If you're a [copyright.com](#) user, you can login to RightsLink using your [copyright.com](#) credentials. Already a [RightsLink](#) user or want to [learn more?](#)

### PERMISSION/LICENSE IS GRANTED FOR YOUR ORDER AT NO CHARGE

This type of permission/license, instead of the standard Terms & Conditions, is sent to you because no fee is being charged for your order. Please note the following:

- Permission is granted for your request in both print and electronic formats, and translations.
- If figures and/or tables were requested, they may be adapted or used in part.
- Please print this page for your records and send a copy of it to your publisher/graduate school.
- Appropriate credit for the requested material should be given as follows: "Reprinted (adapted) with permission from (COMPLETE REFERENCE CITATION). Copyright (YEAR) American Chemical Society." Insert appropriate information in place of the capitalized words.
- One-time permission is granted only for the use specified in your request. No additional uses are granted (such as derivative works or other editions). For any other uses, please submit a new request.

BACK

CLOSE WINDOW

Copyright © 2016 [Copyright Clearance Center, Inc.](#) All Rights Reserved. [Privacy statement](#). [Terms and Conditions](#). Comments? We would like to hear from you. E-mail us at [customer-care@copyright.com](mailto:customer-care@copyright.com)



## Permission for Figures in chapter 5



RightsLink®

Home

Create Account

Help



ACS Publications  
Most Trusted. Most Cited. Most Read.

**Title:** A Search for Low-Irreversible Capacity and High-Reversible Capacity Positive Electrode Materials in the Li-Ni-Mn-Co Pseudoquaternary System  
**Author:** Ramesh Shunmugasundaram, Rajalakshmi Senthil Arumugam, Kristopher J. Harris, et al  
**Publication:** Chemistry of Materials  
**Publisher:** American Chemical Society  
**Date:** Jan 1, 2016

Copyright © 2016, American Chemical Society

LOGIN

If you're a [copyright.com](#) user, you can login to RightsLink using your [copyright.com](#) credentials. Already a [RightsLink](#) user or want to [learn more](#)?

### PERMISSION/LICENSE IS GRANTED FOR YOUR ORDER AT NO CHARGE

This type of permission/license, instead of the standard Terms & Conditions, is sent to you because no fee is being charged for your order. Please note the following:

- Permission is granted for your request in both print and electronic formats, and translations.
- If figures and/or tables were requested, they may be adapted or used in part.
- Please print this page for your records and send a copy of it to your publisher/graduate school.
- Appropriate credit for the requested material should be given as follows: "Reprinted (adapted) with permission from (COMPLETE REFERENCE CITATION). Copyright (YEAR) American Chemical Society." Insert appropriate information in place of the capitalized words.
- One-time permission is granted only for the use specified in your request. No additional uses are granted (such as derivative works or other editions). For any other uses, please submit a new request.

BACK

CLOSE WINDOW

Copyright © 2016 [Copyright Clearance Center, Inc.](#) All Rights Reserved. [Privacy statement.](#) [Terms and Conditions.](#) Comments? We would like to hear from you. E-mail us at [customercare@copyright.com](mailto:customercare@copyright.com)



## Permission for Figure 7.1

9/3/2016

Rightslink® by Copyright Clearance Center



# RightsLink®

Home

Create Account

Help



**Title:** Effect of Morphology and Manganese Valence on the Voltage Fade and Capacity Retention of Li[Li<sub>2</sub>/12Ni<sub>3</sub>/12Mn<sub>7</sub>/12]O<sub>2</sub>

**Author:** Michael G. Verde, Haodong Liu, Tyler J. Carroll, et al

**Publication:** Applied Materials

**Publisher:** American Chemical Society

**Date:** Nov 1, 2014

Copyright © 2014, American Chemical Society

**LOGIN**

If you're a [copyright.com](http://copyright.com) user, you can login to RightsLink using your [copyright.com](http://copyright.com) credentials. Already a RightsLink user or want to learn more?

### PERMISSION/LICENSE IS GRANTED FOR YOUR ORDER AT NO CHARGE

This type of permission/license, instead of the standard Terms & Conditions, is sent to you because no fee is being charged for your order. Please note the following:

- Permission is granted for your request in both print and electronic formats, and translations.
- If figures and/or tables were requested, they may be adapted or used in part.
- Please print this page for your records and send a copy of it to your publisher/graduate school.
- Appropriate credit for the requested material should be given as follows: "Reprinted (adapted) with permission from (COMPLETE REFERENCE CITATION). Copyright (YEAR) American Chemical Society." Insert appropriate information in place of the capitalized words.
- One-time permission is granted only for the use specified in your request. No additional uses are granted (such as derivative works or other editions). For any other uses, please submit a new request.

If credit is given to another source for the material you requested, permission must be obtained from that source.

BACK

CLOSE WINDOW

Copyright © 2016 [Copyright Clearance Center, Inc.](http://Copyright Clearance Center, Inc.) All Rights Reserved. [Privacy statement](#). [Terms and Conditions](#). Comments? We would like to hear from you. E-mail us at [customercare@copyright.com](mailto:customercare@copyright.com)

## Permission for Figures 7.3 and 7.4

9/11/2016

Rightslink® by Copyright Clearance Center



# RightsLink®

Home

Create Account

Help



**ACS Publications** Title: Most Trusted. Most Cited. Most Read.

The Role of Metal Site Vacancies in Promoting Li-Mn-Ni-O Layered Solid Solutions

**Author:** E. McCalla, A. W. Rowe, J. Camardese, et al

**Publication:** Chemistry of Materials

**Publisher:** American Chemical Society

**Date:** Jul 1, 2013

Copyright © 2013, American Chemical Society

LOGIN

If you're a [copyright.com](#) user, you can login to RightsLink using your [copyright.com](#) credentials. Already a [RightsLink](#) user or want to [learn more?](#)

### PERMISSION/LICENSE IS GRANTED FOR YOUR ORDER AT NO CHARGE

This type of permission/license, instead of the standard Terms & Conditions, is sent to you because no fee is being charged for your order. Please note the following:

- Permission is granted for your request in both print and electronic formats, and translations.
- If figures and/or tables were requested, they may be adapted or used in part.
- Please print this page for your records and send a copy of it to your publisher/graduate school.
- Appropriate credit for the requested material should be given as follows: "Reprinted (adapted) with permission from (COMPLETE REFERENCE CITATION). Copyright (YEAR) American Chemical Society." Insert appropriate information in place of the capitalized words.
- One-time permission is granted only for the use specified in your request. No additional uses are granted (such as derivative works or other editions). For any other uses, please submit a new request.

If credit is given to another source for the material you requested, permission must be obtained from that source.

BACK

CLOSE WINDOW

Copyright © 2016 [Copyright Clearance Center, Inc.](#) All Rights Reserved. [Privacy statement](#), [Terms and Conditions](#). Comments? We would like to hear from you. E-mail us at [customercare@copyright.com](mailto:customercare@copyright.com)

## Permission for Figure 7.6

RightsLink Printable License

<https://s100.copyright.com/App/PrintableLicenseFrame.jsp?publisherID...>

### NATURE PUBLISHING GROUP LICENSE TERMS AND CONDITIONS

Sep 11, 2016

This Agreement between Ramesh Shunmugasundaram ("You") and Nature Publishing Group ("Nature Publishing Group") consists of your license details and the terms and conditions provided by Nature Publishing Group and Copyright Clearance Center.

License Number	3946071406610
License date	Sep 11, 2016
Licensed Content Publisher	Nature Publishing Group
Licensed Content Publication	Nature Chemistry
Licensed Content Title	The structural and chemical origin of the oxygen redox activity in layered and cation-disordered Li-excess cathode materials
Licensed Content Author	Dong-Hwa Seo, Jinhyuk Lee, Alexander Urban, Rahul Malik, ShinYoung Kang, Gerbrand Ceder
Licensed Content Date	May 30, 2016
Licensed Content Volume Number	8
Licensed Content Issue Number	7
Type of Use	reuse in a dissertation / thesis
Requestor type	academic/educational
Format	electronic
Portion	figures/tables/illustrations
Number of figures/tables /illustrations	1
High-res required	no
Figures	Figure 7.6
Author of this NPG article	no
Your reference number	
Title of your thesis / dissertation	A study on the properties of layered lithium transition metal oxide positive electrode materials for lithium-ion batteries
Expected completion date	Oct 2016
Estimated size (number of pages)	200
Requestor Location	Ramesh Shunmugasundaram 1205-1094 Wellington Street  Halifax, NS B3H2Z9 Canada Attn: Ramesh Shunmugasundaram
Billing Type	Invoice

**Billing Address** Ramesh Shunmugasundaram  
Department of Chemistry  
Dalhousie University  
  
Halifax, NS B3H2Z9  
Canada  
Attn: Ramesh Shunmugasundaram

**Total** 0.00 USD

**Terms and Conditions****Terms and Conditions for Permissions**

Nature Publishing Group hereby grants you a non-exclusive license to reproduce this material for this purpose, and for no other use, subject to the conditions below:

1. NPG warrants that it has, to the best of its knowledge, the rights to license reuse of this material. However, you should ensure that the material you are requesting is original to Nature Publishing Group and does not carry the copyright of another entity (as credited in the published version). If the credit line on any part of the material you have requested indicates that it was reprinted or adapted by NPG with permission from another source, then you should also seek permission from that source to reuse the material.
2. Permission granted free of charge for material in print is also usually granted for any electronic version of that work, provided that the material is incidental to the work as a whole and that the electronic version is essentially equivalent to, or substitutes for, the print version. Where print permission has been granted for a fee, separate permission must be obtained for any additional, electronic re-use (unless, as in the case of a full paper, this has already been accounted for during your initial request in the calculation of a print run). NB: In all cases, web-based use of full-text articles must be authorized separately through the 'Use on a Web Site' option when requesting permission.
3. Permission granted for a first edition does not apply to second and subsequent editions and for editions in other languages (except for signatories to the STM Permissions Guidelines, or where the first edition permission was granted for free).
4. Nature Publishing Group's permission must be acknowledged next to the figure, table or abstract in print. In electronic form, this acknowledgement must be visible at the same time as the figure/table/abstract, and must be hyperlinked to the journal's homepage.
5. The credit line should read:  
Reprinted by permission from Macmillan Publishers Ltd: [JOURNAL NAME] (reference citation), copyright (year of publication)  
For AOP papers, the credit line should read:  
Reprinted by permission from Macmillan Publishers Ltd: [JOURNAL NAME], advance online publication, day month year (doi: 10.1038/sj.[JOURNAL ACRONYM].XXXXX)

**Note: For republication from the *British Journal of Cancer*, the following credit lines apply.**

Reprinted by permission from Macmillan Publishers Ltd on behalf of Cancer Research UK: [JOURNAL NAME] (reference citation), copyright (year of publication) For AOP papers, the credit line should read:  
Reprinted by permission from Macmillan Publishers Ltd on behalf of Cancer Research UK: [JOURNAL NAME], advance online publication, day month year (doi: 10.1038/sj.[JOURNAL ACRONYM].XXXXX)

6. Adaptations of single figures do not require NPG approval. However, the adaptation should be credited as follows:

Adapted by permission from Macmillan Publishers Ltd: [JOURNAL NAME] (reference citation), copyright (year of publication)

**Note: For adaptation from the *British Journal of Cancer*, the following credit line**

**applies.**

Adapted by permission from Macmillan Publishers Ltd on behalf of Cancer Research UK:  
[JOURNAL NAME] (reference citation), copyright (year of publication)

7. Translations of 401 words up to a whole article require NPG approval. Please visit <http://www.macmillanmedicalcommunications.com> for more information. Translations of up to a 400 words do not require NPG approval. The translation should be credited as follows:

Translated by permission from Macmillan Publishers Ltd: [JOURNAL NAME] (reference citation), copyright (year of publication).

**Note: For translation from the *British Journal of Cancer*, the following credit line applies.**

Translated by permission from Macmillan Publishers Ltd on behalf of Cancer Research UK:  
[JOURNAL NAME] (reference citation), copyright (year of publication)

We are certain that all parties will benefit from this agreement and wish you the best in the use of this material. Thank you.

Special Terms:

v1.1

Questions? [customercare@copyright.com](mailto:customercare@copyright.com) or +1-855-239-3415 (toll free in the US) or +1-978-646-2777.

---